Long Non-Coding RNA Sarrah:

Staying Young at Heart

Dissertation
zur Erlangung des Doktorgrades
der Naturwissenschaften

vorgelegt beim Fachbereich Biowissenschaften (FB15)
der Johann Wolfgang Goethe-Universität
in Frankfurt am Main

von
Dorotée Julia Trembinski
aus Geesthacht

Frankfurt am Main (2019)

(D 30)

vom Fachbereich Biowissenschaften (FB15)

der Johann Wolfgang Goethe-Universität als Dissertation angenommen.

Dekan: Prof. Dr. Sven Klimpel

Gutachter: Prof. Dr. Stefanie Dimmeler

Prof. Dr. Michaela Müller-McNicoll

Datum der Disputation:

We're all someone's daughter

We're all someone's son

– John Farnham, “You’re the Voice”

Wujkowi Zydze

Disclaimer:

While completing this work, a major proportion of the presented results and figures has been under revision as a research article by Trembinski et al. in Nature Communications under the title "Sarrah is an Aging-Regulated Anti-Apoptotic Long Non-Coding RNA in Cardiomyocytes that Augments Recovery from Acute Myocardial Infarction". The author refrains from citation of her own publication for reasons of readability and text esthetics.

Contents

1. Introduction

1.1 The Mammalian Cardiovascular System

1.1.1 Overview of the Mammalian Cardiovascular System

Mammalian anatomy in all its tissue diversity, twisty structure and, compared with other organism classes, oftentimes large size requires a nutrient and oxygen supply that is sufficiently branched and efficient to ensure simultaneous maintenance and function of all organs at all times. This demanding task is carried out by the cardiovascular system, a complex network of blood vessels connected to the lungs and the heart that function as gas station and transport pump, respectively.

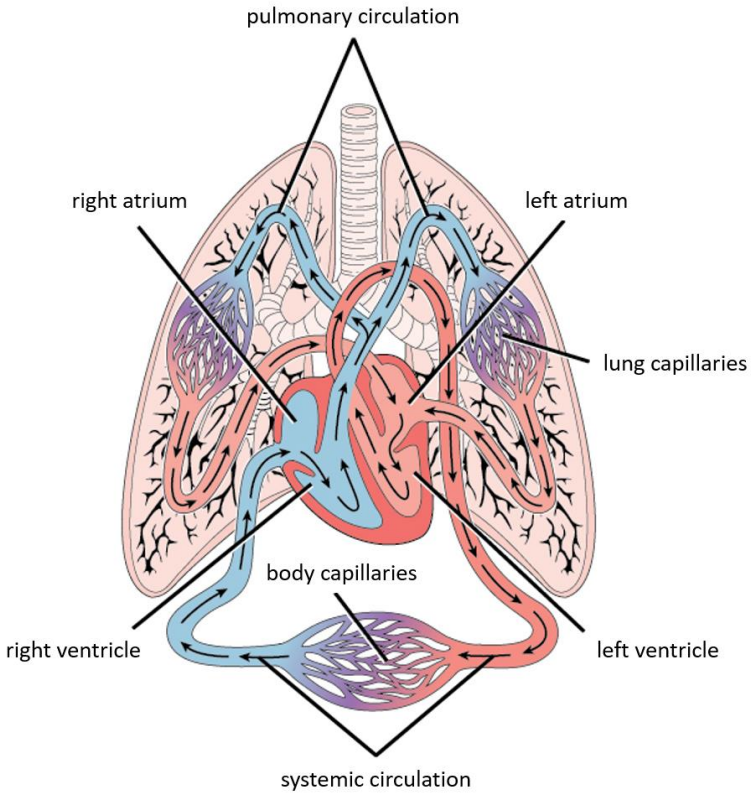

Figure 1: The human cardiovascular system. The cardiovascular system in mammals forms a closed network that supplies all organs as well as the heart via the coronary system with nutrients and oxygens. Oxygenated blood is pumped from the left heart ventricle through the vessels of the systemic circuit. From there, it enters the right heart ventricle in a deoxygenated state and is pumped into the pulmonary circuit where it is oxygenated again. (Modified from OpenStax CNX, licensed under CC BY 4.0.)

A second network of lymph vessels specialized in interstitial fluid drainage from tissues, immune cell trafficking and fat absorption supports the cardiovascular system in nutrient and waste circulation[1]. While the lymphatic system constitutes an open network, the cardiovascular system is closed in itself and organized in three subdivisions: the systemic circuit, the pulmonary circuit and the coronary circuit[2]. Systemic circulation supplies virtually all organs and tissues with oxygenated blood through arteries from the heart and returns deoxygenated blood through veins. Deoxygenated blood from the

heart is transported through arteries of the pulmonary circuit to the lungs to be oxygenated in lung alveoli and brought back to the heart through pulmonary veins[3]. The coronary circuit embraces the outer surface of the heart and secures the autonomy of heart muscle supply, which is of major importance for all other organ systems. It consists of a distinct set of coronary arteries that deliver nutrients and oxygen to the myocardium as well as coronary veins that drain away deoxygenated blood. Nutrients and oxygen are exchanged between tissues and blood in the capillaries, in which arteries transition to veins (figure 1).

Blood vessels are divided by size and structure into arteries, arterioles, capillaries, venules and veins[4]. Their specific structure is adapted to the hemodynamic forces each vessel type is exposed to. In contrast to arteries, veins are equipped with valves that prevent blood flowing backwards. Arteries and veins both consist of three layers. The tunica externa with connective tissue, collagen fibers and extracellular matrix (ECM) anchors the vessel to surrounding tissue and represents the thickest layer of veins. The tunica media is composed of smooth muscle cells interlaced with elastic fibers and regulates vasoconstriction and -dilation; it is the thickest layer in arteries where blood pressure is substantially higher than in veins. The tunica intima consist of an endothelial cell layer and, in large arteries, an internal elastic membrane[5]. Capillaries are composed of an endothelial cell layer that directly contact pericytes embedded in a basement membrane. Pericytes act as mural elements that confer stability to the vessel.

1.1.2 The Mammalian Heart

1.1.2.1 Heart Development

During embryonic development, the heart is the first organ to be formed[6]. At embryonic day (E) 7.5, mesodermal cardiac progenitor cells first give rise to the primary heart field and later to the secondary heart field (cardiac crescents)[7]. The primary heart field forms the heart tube at E8.5, which together with the secondary heart field expands and loops into primitive atria and ventricles at E9.5. The left ventricle arises from the primary heart field, the right ventricle and the outflow tract from the secondary[8]. Epicardial cells enclose the major portion of the ventricular surface at E10. By E15, a septum in atria and ventricles and a valve are formed and a four-chambered heart adopts its role as a blood pumping hollow organ (figure 2).

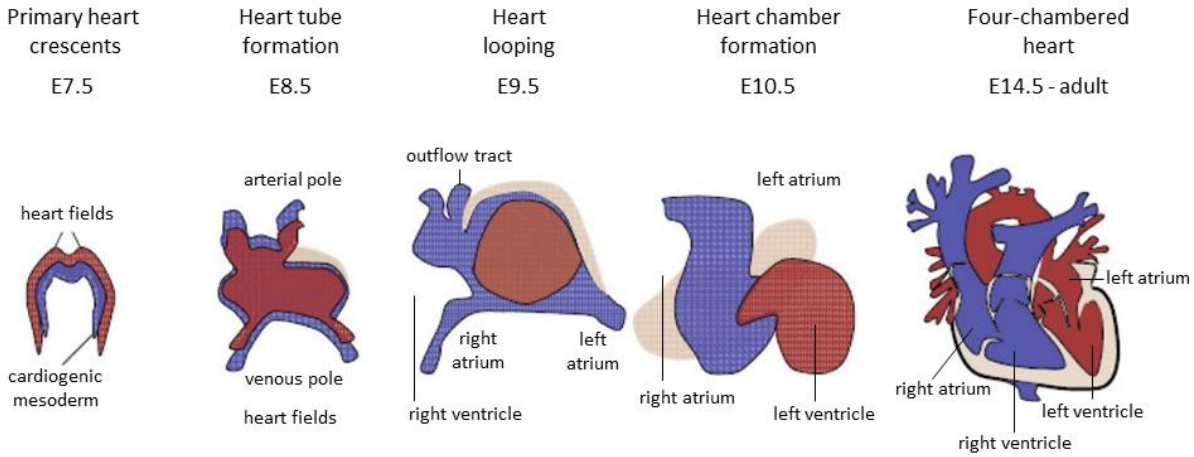

Figure 2: Development of the human heart. During early embryonic development, mesodermal cells give rise to the primary heart crescents that later form the heart tube, which loops and develops into the four-chambered mammalian heart. (Modified from Nandi et al., Harnessing fetal and adult genetic reprograming for therapy of heart disease, J Nat Sci. 2015.)

1.1.2.2 Heart Structure

Evolutionary, the structure of the adult heart in placental mammals has remained strikingly conserved compared to other organs. Differences in heart structure between mammalian species can mostly be ascribed to scaling in order to account for changes in body size[9].

The mammalian heart is located within the thoracic cavity, sheathed by the pericardium and organized in four asymmetrical chambers that are separated by valves and the atrioventricular septum[10] (figure 3). The right and left atrium receive blood while the right and left ventricle pump it into the circulation circuits by muscular contraction. The right atrium receives blood from the superior and the inferior vena cava, which collect it from multiple veins and venules, as well as from the coronary sinus, which drains blood from the heart itself. Passing through the tricuspid valve, deoxygenated blood reaches the right ventricle. Since the right ventricle pushes blood into the pulmonary circuit, it is considerably smaller than the left ventricle that pushes blood into the much larger systemic circuit. After passing through the pulmonary arteries with the pulmonary valve, the blood is reoxygenated in the lungs before being pumped into the left atrium and from there through the mitral valve into the left ventricle. It exits the heart through the aorta, the major artery of the body, whose aortic valve prevents blood backflow into the heart[11].

On a histological level, the heart is composed of three layers[12] (figure 3). The epicardium is linked to the parietal and fibrous pericardial structures. Together, they stabilize the heart and reduce friction at the interface to the surrounding tissue during heart movement. The myocardium represents the bulk of the heart wall. It comprises collagenous fibers, blood vessels, nerve fibers and, most importantly, the sophisticatedly patterened heart muscle that enables contraction and that the differences in thickness between right and left ventricle are derived from. The endocardium consists of a specialized

endothelial cell layer that lines the inner heart wall. It is continuous with the endothelial lining of the blood vessels and participates in modulation of cardiac contractility[13].

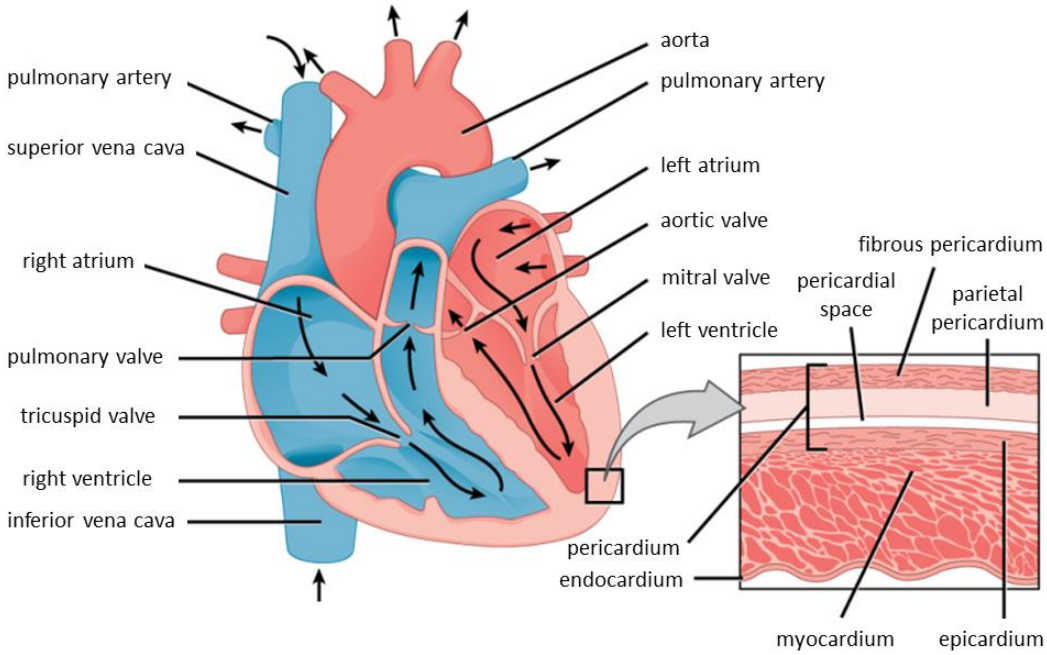

Figure 3: Structure of the human heart. Blood is pumped through four chambers of the heart. The right atrium receives blood through the vena cava and pushes it into the right ventricle. After reoxygenation in the lungs, it reaches the left atrium, is transported into the left ventricle and exits the heart via the aorta. The heart is located within the pericardium and histologically consists of the epicardium, the myocardium and the endocardium. (Modified from OpenStax CNX, licensed under CC BY 4.0.)

1.1.2.3 The Cardiac Cycle

The cardiac cycle is a rhythmic sequence of pressure changes within the heart chambers. It is driven by coordinated myocardial contraction and relaxation and ensures steady blood supply of all organs. In humans, the heart contracts at a rate of 60 to 100 beats per minute[14].

Electrochemical signals effected by calcium ions entering cardiomyocytes cause the myocardium to contract during systole and thereby to move blood through the heart and the whole body[15]. When the myocardium relaxes during diastole, the heart is filled with blood again. The electrical signals originate from the sinoatrial node and cause both atria to contract simultaneously. They spread to the atrioventricular node, the bundle of His and through the heart septum. From here, the Purkinje fibers conduct the pulse from the heart apex up the walls of both ventricles that contract in consequence. At the atrioventricular node, the signal pauses shortly due to a time gap between eletrical conduction and myocardial force development. This allows complete atrial emtyping and sufficient ventricular filling[16] (figure 4). Two widely used methods to visualize parameters of cardiac wall motion and contractility are echocardiograophy, an ultrasound-based technique, and magnetic resonance imaging (MRI).

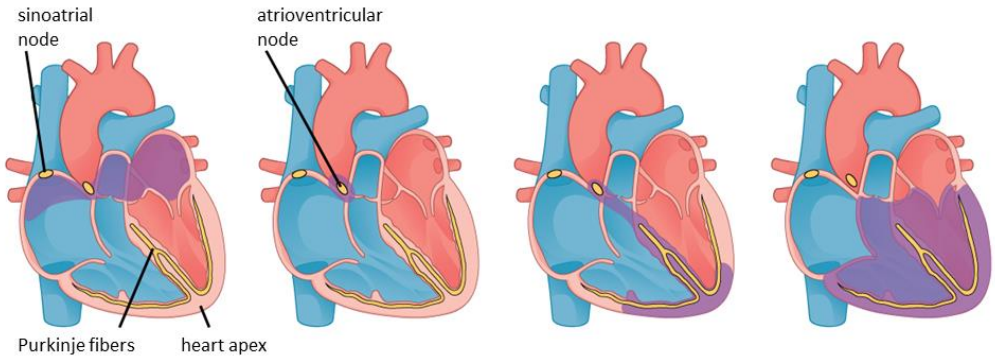

Figure 4: Electrical excitation of the heart. An electrical signal originating from the sinoatrial node causes the atria to contract. It spreads to the atrioventricular node, pauses shortly and arrives at the apex via Purkinje fibers. From here, it reaches the ventricular walls that now contract. (Modified from OpenStax CNX, licensed under CC BY 4.0.)

1.1.2.4 Cellular Composition of the Heart

Between 70 and 85 percent of heart volume are composed of cardiomyocytes[17,18,19,20]. Like in skeletal muscle cells, actin and myosin filaments in cardiac myocytes are arranged in sarcomeres, the contractile units that confer a striated appearance to the tissue[21]. However, in their self-regulated involuntary contractions, cardiomyocytes resemble smooth muscle cells[22]. A feature unique of cardiac myocytes is their coupling by so-called intercalated discs that are comprised of adherens junctions and thereby synchronize the contraction of cardiac tissue[23].

Cardiomyocytes are the cells that enable the heart to perform its main function, namely contraction and blood transport throughout the body. However, cardiac non-myocytes are crucial for homeostasis, extracellular matrix production, intercellular communication and vascularization. Although they represent only a small share of volume in the heart, proportions shift when considering absolute cell numbers (figure 5). In human and mouse, endothelial cells are the most abundant cardiac cell type comprising approximately half of all cells[18]. They regulate vascular homeostasis and form new blood vessels after myocardial infarction to limit further tissue damage[24]. Myocytes represent almost a third of cardiac cells. Recently, after having been overestimated in many studies[25], fibroblasts have been reported to make up 13 percent of cells in the mouse heart[18]. Their primary functions are secretion of ECM components and scar formation after myocardial infarction to maintain heart integrity[26].

Additionally, smaller numbers of smooth muscle cells, neurons, leukocytes, macrophages and pericytes have homeostatic functions in the heart. For example, macrophages perform phagocytosis[27] and facilitate electrical conduction[28] while pericytes participate in vessel stabilization and maturation[29].

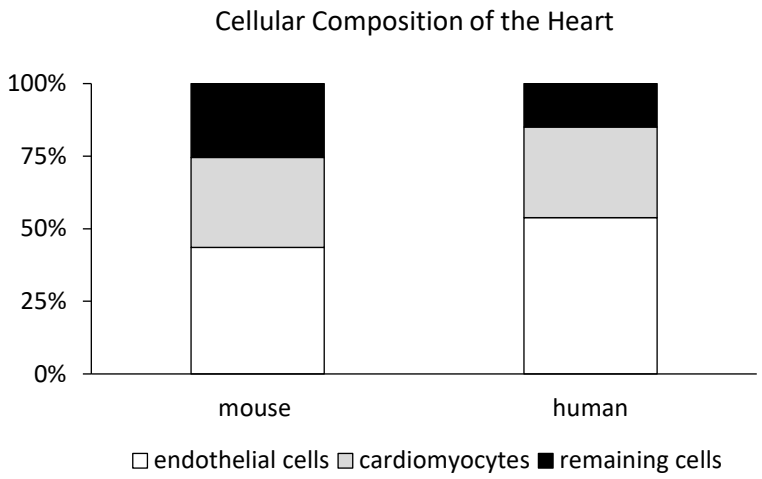

Figure 5: Cellular composition of the mammalian heart. Both in mouse and human, endothelial cells represent the most abundant cell type in the heart (44 % and 54 %, respectively). Cardiac myocytes make up approximately one third of cardiac cells (31 %). Among the remaining cells, fibroblasts are most numerous. (Data from Pinto et al., Revisiting Cardiac Cellular Composition, Circ Res. 2016.)

Intense cell-cell interactions between different cell types modulate their functioning. For example, angiogenesis depends on the crosstalk between endothelial cell with pericytes and macrophages[30,31], but also between fibroblasts with endothelial cells and macrophages[24]. For this work, communication between cardiomyocytes and endothelial cells is of particular interest. Information between them is exchanged bidirectionally and via different channels[32]. Besides physical coupling by gap junctions between cardiomyocytes and endothelial cells[33], they also communicate via secretion of exosomes or microvesicles that transport among others non-coding RNAs as signaling effectors[34]. Furthermore, endothelial cells talk to cardiomyocytes via paracrine signaling, specifically via secretion of nitric oxide, prostaglandins or angiotensin II[35]. Cardiomyocytes in turn secrete thirty to sixty different proteins and peptides that affect endothelial and other cells[36]. The best known cardiokine that signals to endothelial cells is vascular endothelial growth factor (VEGF). It induces endothelial cell proliferation and thereby promotes angiogenesis[37].

1.2 Systemic and Cardiac Aging

1.2.1 Systemic Aging

Aging refers to the accumulation of biological changes within an organism over time and is usually accompanied by a progressive impairment of organ function, a decline in fertility as well as an increasing vulnerability to disease and death[38,39,40,41]. Typical syndromes that develop during aging, but frequently also occur in pathological conditions include immunodeficiency, oxidative stress, endogenous intoxication, maladjustment to environmental challenge and tissue sclerosis[41].

Although many of these characteristics are heavily influenced by genetics, evolutionary considerations suggest that the underlying cause of aging is not genetically programmed, but depends on the laws of thermodynamics. Organisms are far from thermodynamic equilibrium and tend to fall apart unless great efforts are undertaken to counteract this thermodynamical striving for a growth of entropy at all structural levels of the body[40,41]. Put simply, organisms are not programmed to die, they are programmed to live. Aging is part of life and can be understood as failure of living systems to maintain themselves due to a fundamental principle of physics.

On a cellular level, aging is characterized by a set of hallmarks that meet the following criteria: present in natural aging, accelerating aging when externally induced and delaying aging when inhibited[42,43,44] (figure 6). López-Ontín et al. summarize them in three categories (figure 6).

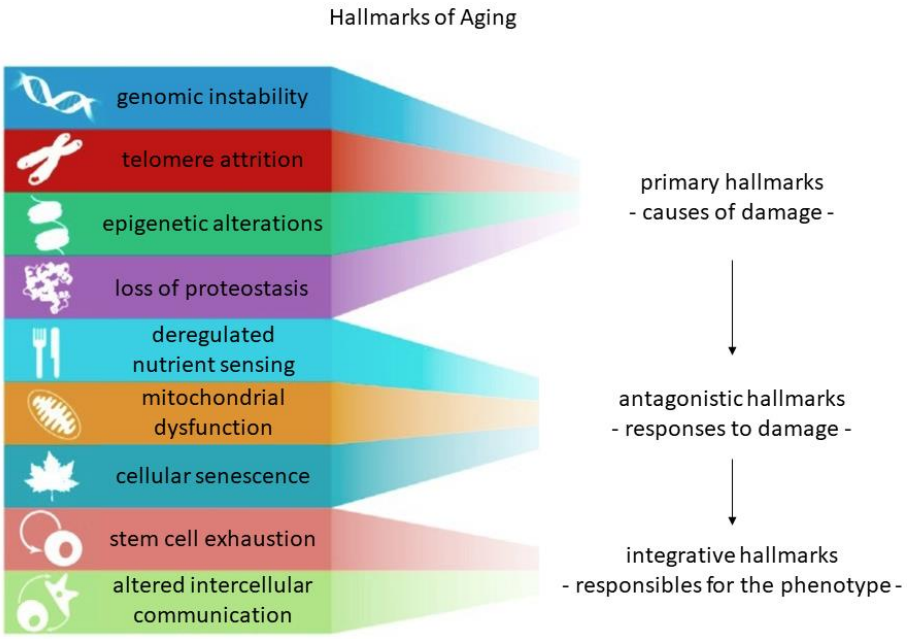

Figure 6: Hallmarks of aging. Primary hallmarks of aging deteriorate cellular function and induce the onset of antagonistic hallmarks in order to compensate for this deterioration. Antagonistic hallmarks contribute to further functional decline when present at excess and lead to the occurrence of integrative hallmarks. (Modified from López-Ontín et al., The Hallmarks of Aging, Cell 2016.)

Genomic instability, telomere attrition, epigenetic alterations and loss of proteostasis have been postulated as primary hallmarks. Genomic instability affects both nuclear and mitochondrial DNA. It encompasses not only somatic mutations, but also chromosomal abberations and nuclear lamina defects. They can arise spontaneously or due to external factors like ultraviolet radiation and disintegrate the genetic architechture. A particular type of genomic instability is driven by telomere attrition. Notably, telomeres are particularly susceptible to age-related DNA damage accumulation compared with other chromosomal regions[45]. Due to the lacking capacity of the physiological, non-oncogenic cellular machinery to completely replicate the ends of linear DNA, telomeres shorten over time in mammals. Examples of epigenetic perturbations that contribute to aging are histone

methylation, loci-specific DNA hypo- or hypermethylation, chromatin remodeling concomitant with heterochromatin loss and increasing transcriptional noise. Protein homeostasis is gradually lost due to impaired expression of chaperones and collapsing proteolytic systems.

The three antagonistic hallmarks are deregulated nutrient sensing, mitochondrial dysfunction and cellular senescence. Deregulated nutrient sensing manifests among others in enhanced anabolism and attenuated insulin and IGF-1 signaling during aging. Consistently, dietary restriction can extend life span in various animal models and humans[46]. Consequences of mitochondrial dysfunction include increased production of reactive oxygen species, reduced biogenesis of mitochondria and defective bioenergetics. The number of senescent cells that per definition undergo a stable cell cylcle arrest increases during aging and exhausts the regenerative capacity of a tissue.

Stem cell exhaustion and altered intercellular communication are defined as integrative hallmarks of aging. Like an increase in the number of senescent cells, a loss of stem cells lowers the regenerative capacity of a tissue. Aging-associated alterations of intercellular communication take place mostly on the endocrine, neuroendocrine or neuronal level and increase inflammation, jeopardize immunosurveillance against pathogens and tumor cells and impact the cellular microenvironment. An example of a microenvironmental change leading to aging are senescent cells that induce senescence in neighboring cells via gap junctions[47].

The primary hallmarks have unambigiously negative consequences for the cell, the organism and longevity. In contrast, the impact of antagonistic hallmarks is dose-dependent. Their effects can be inversed when changing their extent, which is illustrated when considering senesence, a mechanism that initially protects cells from oncogenic transformation, but in excessive amounts ages the whole tissue. López-Ontín et al. suggest that the primary hallmarks trigger the anatgonistic ones in an attempt to rescue organ changes, which are finally consolidated by the integrative hallmarks.

1.2.2 Cardiac Aging

1.2.2.1 Clinical Implications of Cardiovascular Aging

Aging is the major risk factor for cardiovascular diseases[48,49]. Every year, almost 18 million people die from heart disease or stroke, which makes up approximately one third of deaths worldwide[50,51] (figure 7). Although more than 75 percent of cardiovascular disease-related deaths occur in low- and middle-income countries, cardiovascular disease is the leading cause of death in many countries of the Western world, among others in the United States of America (USA)[52] and in Germany[53], where 37.2 percent of all deaths in 2016 were caused by cardiovascular disease. In the USA, heart diease alone was at the pole position of the leading causes of death in 2016[54]. Specifically, the aging heart and

vasculature become more and more susceptible to conditions including arrhythmias[55], hypertrophy, diminished left ventricular systolic reserve capacity, increased arterial stiffness, atherosclerosis, hypertension, left ventricular diastolic dysfunction and myocardial infarction[56,57], of which the latter two are of special interest for this study.

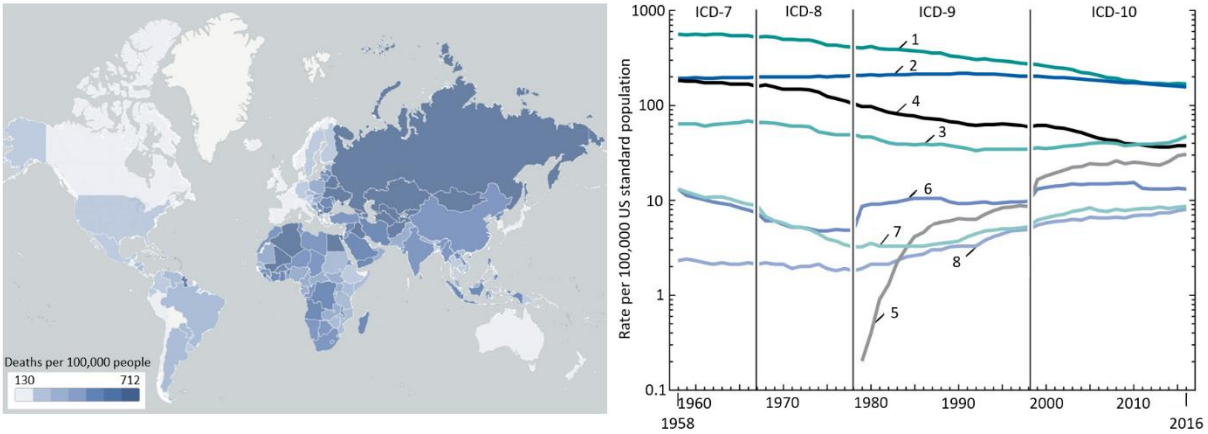

Figure 7: Cardiovascular disease is among the leading causes of death worldwide. Left: World map showing death rates from cardiovascular disease in 2012. Death rates from cardiovascular disease are highest in Asian and African low-income countries. (Modified from the World Health Organization.) Right: Age-adjusted death rates for selected leading causes of death in the USA from 1958 to 2016. Heart disease has been the leading cause of death each year. Death rates from two other cardiovascular death causes, cerebrovascular disease and hypertension, also range among the highest. ICD: International Classification of Diseases; 1: heart disease; 2: malignant neoplasms; 3: accidents; 4: cerebrovascular disease; 5: Alzheimer's disease; 6: kidney disease; 7: hypertension; 8: Parkinson's disease. (Modified from the US National Vital Statistics Reports on Death 2016.)

In a typical time course, a characteristic of the aging heart at an early stage is impaired diastolic filling of the left ventricle. In a compensation attempt, atrial contraction is increased to sustain stroke volume and ejection fraction[58,59]. Over time, however, left ventricular contractility and ejection fraction decrease in the aging heart[56]. As a result, the diminished cardiac output stimulates the myocardium to counteract this functional decline by increasing muscle mass, which in turn leads to hypertrophy. Being initially beneficial by increasing cardiac output, hypertrophic heart remodeling has detrimental effects on cardiac function in the long term[60]. In consequence, heart rate and cardiac output decrease[61]. The blood volume pumped through the systemic and coronary circuits is not sufficient to properly provide oxygen and nutrients to the organs of the body, also not the heart. In a vicious circle, the heart becomes ischemic and its functional parameters further deteriorate.

Also the cellular structure and composition of the heart are affected by aging. The underlying basis for hypertrophy is an enlargement of individual cardiomyocytes, which is irreversible under pathological conditions[62]. Simultaneously, the absolute number of cardiomyocytes decreases as a consequence of apoptosis and necrosis[63]. The remaining cardiomyocytes become increasingly vulnerable to oxidative stress that is augmented due to an increase in mitochondrial dysfunction, one of the hallmarks of aging. More reactive oxygen species contribute to further cardiomyocyte loss. This process can

become partially self-propagating when cardiomyocytes die of necrosis, which creates a pro-inflammatory and pro-fibrotic environment and thereby increases the probability of further necrotic events. Finally, aging also facilitates cardiomyocyte senescence[64] that is related to DNA damage[65], two other hallmarks of aging.

These processes are partially caused by profound changes on the genetic level[66,67]. In mice, 10 percent of cardiac transcripts have been reported to be differentially regulated during aging[68]. Altered patterns of gene expression include a general downregulation of mitochondrial gene transcription[69], which is in line with the aging hallmark of mitochondrial dysfunction. This transcriptional downregulation can be attributed to the physical proximity of mitochondria to reactive oxygen species that they produce[70]. Furthermore, levels of transcripts associated with extracellular matrix production and cell growth rise supporting previous findings that extracellular matrix deposition, fibrosis and cardiomyocyte hypertrophy increase in the aging heart[66]. In both mouse and human, transcript levels of sarcomeric α-actin and sarco-/endoplasmic reticulum calcium ATPase 2 (SERCA2) drop with aging, which leads to decreased calcium ion sequestration by the sarcoplasmic reticulum and reduced myocardial contractility[67,71,72].

Overall, structural, cellular and genetic alterations represent interconnected origins of cardiac aging. They cause pathological changes that reach epidemic dimensions in Western countries and emphasize the great societal relevance and need for treatment of heart and vascular diseases.

1.2.2.2 Myocardial Infarction

Myocardial infarction (MI) is a cardiac emergency oftentimes leading to death or disability[73]. The risk to die from MI dramatically increases with age. In Germany, 48,669 people died after suffering an MI in 2016, 37,110 of them being older than 70 years. The MI death rate was even higher in the age group between 80 and 90 years than in the age group between 70 and 80 years although life expectancy in Germany was 80.64 years in 2016[74] (figure 8).

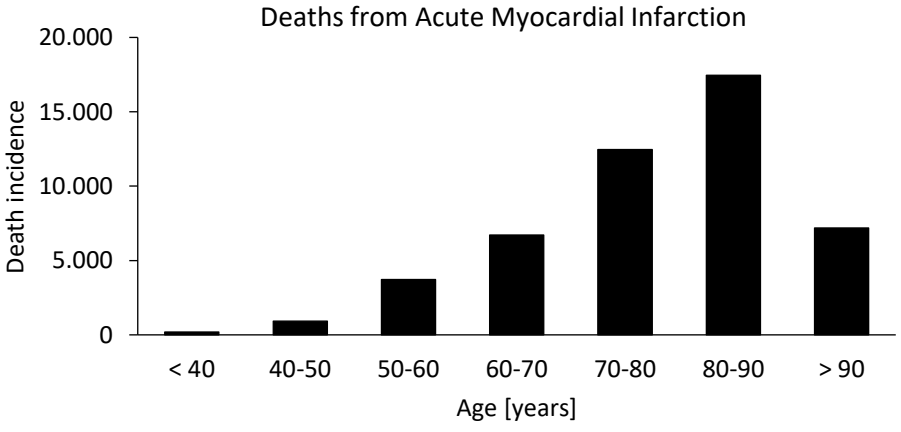

Figure 8: Death rates from myocardial infarction in Germany in 2016 by age group. Death rates from myocardial infarction rise with increasing age, peaking in the age group between 80 and 90 years that is beyond the mean life expectancy of 80.64 years. (Data from Deutsche Herzstiftung, Deutscher Herzbericht 2018.)

Per definition, MI refers to any myocardial necrosis in the setting of myocardial ischemia[75]. It results from an imbalance between oxygen supply and demand and within minutes entails myocardial dysfunction, cell death and healing by fibrosis several weeks later. After the onset of regional myocardial hypoperfusion and ischemia, cardiomyocytes undergo necrosis within 20 minutes. This can be detected by measuring levels of biomarkers in blood, preferrably of cardiac troponin, which is highly and almost exclusively expressed in cardiomyocytes. Cardiac troponin elevations in blood reflect a disintegration of the contractile apparatus and thereby indicate injury and necrosis of myocardial cells[76]. Additionally, MI is diagnosed by electrocardiographic abnormalities. Beside necrosis, cardiomyocyte loss after MI is also attributed to apoptosis in the border region surrounding the infarcted area. Here, ischema is limited, but still sufficient to damage the cells and trigger apoptosis[77,78].

With respect to temporal resolution, MI events are classified as acute or chronic. The presence of edema is indicative of acute MI (AMI) that has occurred very recently and has not healed yet. Fibrosis characterizes chronic MI (CMI) that has occurred at least several weeks earlier[79]. Causal classification of MI[75] differentiates between spontaneous MI or type 1 MI that is in most cases the primary manifestation of coronary artery disease with atherosclerotic plaque rupture or other coronary artery pathology. Type 2 MI is a secondary consequence of an ischemic imbalance that originates form a condition other than coronary artery disease, for instance coronary endothelial dysfunction, bradyarrhythmia, anemia or hypotension[80]. Cardiac death due to MI with symptoms suggestive of myocardial ischemia is categorized as type 3 MI. Types 4a, 4b and 5 encompass all MI events associated with revascularization procedures and are further subdivided into MI related to percutaneous coronary intervention, MI related to stent thrombosis and MI related to coronary artery bypass grafting, respectively. A differential diagnosis of MI is myocardial injury detectable by histological methods. It occurs in consequence of non-ischemic pathology such as pulmonary embolism or myocarditis[81].

Echocardiography and magnetic resonance imaging (MRI) are commonly used MI imaging techniques. Echocardiographic measurements are particularly suitable for assessment of cardiac structure and function based on myocardial thickness and motion[82] and perform better in distinguishing between acute and chronic MI[83]. However, MRI represents the current gold standard for cardiac imaging after MI with its enhanced tissue contrast and precise volume measurements[84]. Left ventricular ejection fraction values after AMI typically drop below 40 percent[85] compared with 55 to 75 percent in the healthy heart[86].

Prophylaxis of AMI focuses on treatment of underlying diseases, most importantly coronary artery disease. Within the scope of preventive, antithrombotic therapies both anti-platelet and anti-coagulant agents are prescribed[73]. In case of AMI that results from a coronary vessel occlusion, ischemic myocardium that is in the process of becoming infarcted has to be reperfused as soon as possible, latest within few hours. Coronary vessels are opened by percutaneous coronary intervention (PCI) that can be accomplished by angioplasty or stenting. Alternatively, instead of PCI, intravenous fibrinolytic therapy can be applied. Reperfusion therapy has substabtially improved patient outcome by lowering mortility after AMI from 20 to 5 percent[87].

Cardiomyocyte death is the main cause of the detrimental consequences of MI that is attempted to be contained by reperfusion therapy. It occurs due to both necrosis and apoptosis, the former of which peaks at 24 h after AMI induction in rats, while apoptosis reaches its maximum already at 4.5 h[88].

Necrosis happens as a consequence of nutrient deprivation or injury as it occurs in the infarct core during myocardial ischemia[89]. It is defined by loss of plasma membrane integrity and depletion of cellular ATP[90]. Necrotic cells appear initially swollen and release cellular components into the extracellular space upon membrane damage, thereby triggering an inflammatory response in their environment. Although necrosis has long been considered as uncontrolled, emerging evidence suggests that it may partially be programmed[91,92].

In contrast, apoptotic cells appear shrunken[93] and are characterized by plasma membrane blebbing, nuclear condensation and fragmentation into apoptotic bodies that are cleared by phagocytosis, thereby avoiding an inflammatory response[90]. The process is genetically programmed and orchestrated by a variety of precisely tuned signaling molecules that can initiate apoptosis via two distinct, but interconnected pathways. The extrinsic pathway is activated via binding of, for example, the Fas ligand to cell surface receptors, whereas the intrinsic pathway induces the release of apoptogenic proteins, most prominently cytochrome c,[94] as well as calcium ions[95] from mitochondria or the endoplasmic reticulum (ER), respectively. Both signaling cascades converge in caspase activation, a hallmark of apoptosis[96]. The intrinsic pathway is activated upon stimuli that include hypoxia and oxidative or nutrient stress and is therefore more relevant to the ischemic heart[97]. In this context, intrinsic apoptotic signaling to the mitochondria and ER is transduced by pro-apoptotic Bcl-2 proteins, which finally leads to permeabilization of the outer mitochondrial membrane[90]. Nevertheless, apoptotic signaling has also been shown to be transduced via the extrinsic cascade with the Fas ligand constituting the major effector in the setting of MI-induced apoptosis[98].

In rodents, AMI can be induced by permanent ligation of the left anterior descending (LAD) coronary artery, which models type 1 MI (figure 9)[99]. Heart tissue distal to the ligation becomes ischemic, cardiac troponin levels in blood are elevated and the animals develop electrocardiographic alterations typical

of MI. *Post mortem*, the infarcted tissue can often be identified macroscopically by its pale appearance. The model can be modified to mimic MI followed by successful revascularization, as it is the case for most patients, by applying the suture only transiently for 20 to 60 minutes[100]. Typically, AMI surgery in mice results in an apical infarction of the left ventricular wall involving approximately 40 percent of left ventricular circumference. The infarcted area becomes characteristically thin and inable to contract, which results in left ventricular dilatation[101].

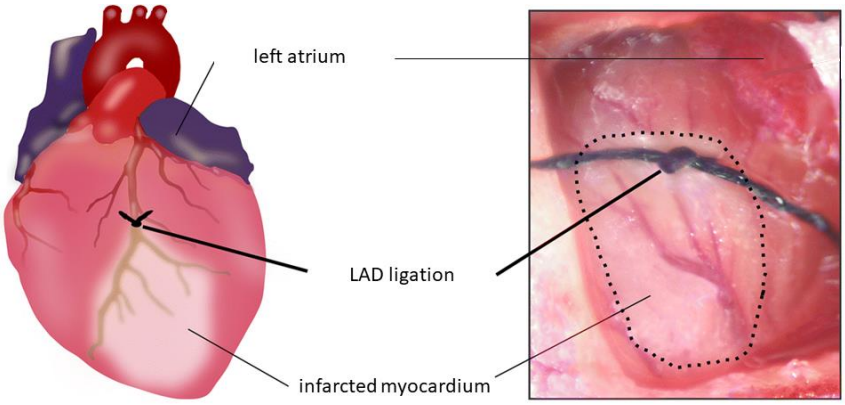

Figure 8: Acute myocardial infarction mouse model. AMI can be modeled in mice by permanent ligation of the left anterior descending coronary artery. Upon artery suture, the distal tissue is not sufficiently supplied with blood, becomes ischemic and turns pale. (Modified from Bacmeister et al., Inflammation and fibrosis in murine models of heart failure, Basic Research in Cardiology 2019.)

1.2.2.3 Heart Failure with Preserved Ejection Fraction

Heart failure with preserved ejection fraction (HFpEF) is the most common form of heart failure[102]. The risk to develop HFpEF increases with age[103,104] leading to a prevalence of 10 percent in the population over 75 years old[105], with women being affected more often than men. Even when treated, HFpEF remains a leading cause of mortality and morbidity especially among the elderly and increases the likelihood of rehospitalization, thereby severely compromising life quality of patients and posing a significant burden to health care services[106].

Beside aging, risk factors for HFpEF are hypertension, coronary artery disease, diabetes mellitus, obesity, anemia, chronic kidney disease, atrial fibrillation and chronic obstructive pulmonary disease[103,105]. But even without a history of the mentioned conditions, the aging heart undergoes a number of structural changes that in many cases pave the way for HFpEF development. These include increased arterial and myocardial stiffness, decreased diastolic myocardial relaxation, increased left ventricle mass, decreased coronary flow reserve and decreased capacity to enhance adenosine triphosphate (ATP) production and cardiac output at demand[107].

A fully developed HFpEF phenotype is characterized by left ventricular diastolic dysfunction[108] that leads to compensatory structural heart remodeling at the expense of raised left ventricular filling pressures[109] (figure 9). Concomitant haemodynamic features vary and require appropriate corresponding treatment. A common HFpEF characteristic independent of disease etiology is a dramatically reduced stroke volume below 35 ml[110] compared with physiological 60 to 100 ml[111]. This is due to extremely small absolute volumes both in diastole and in systole, although the fraction of ejected blood is preserved and comparable to a healthy heart. In response to the reduction in stroke volume, the heart tries to compensate the inefficient cardiac output by increasing the heart rate, which leads to self-perpetuating ventricular hypertrophy, a characteristic of cardiac aging. The cellular basis for ventricular hypertrophy is hypertrophy of individual cardiomyocytes[112].

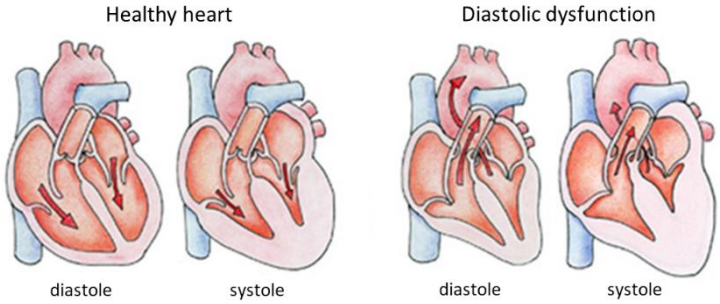

Figure 9: Heart remodeling upon diastolic dysfunction. Diastolic dysfunction, a characteristic of heart failure with preserved ejection fraction, results in elevated left ventricular diastolic pressure and reduced stroke volume. In consequence, the heart fails to adequately respond to circulatory demands of the body. (Modified from eesom AG, https://www.eesom.com/herz-kreislauf/herzschwaeche/, accessed May 8, 2019.)

One of the pathophysiological mechanisms underlying HFpEF is arterial stiffening[113] that contributes to left ventricular diastolic pressure elevation. This usually entails left atrial hypertension that can be targeted therapeutically using a transcatheter interatrial shunt device[114]. Another fearture that develops due to increased left ventricular diastolic pressure is pulmonary venous congestion and consequent pulmonary hypertension. This in turn often causes right ventricular dysfunction[115]. In patients who present with such disease etiology, treatment targeting the pulmonary vasculature is preferential[116]. In a subgroup of patients, HFpEF has been reported to develop due to plasma volume expansion[117]. It is associated with right heart dilation and increased total heart volumes, which raises left ventricular diastolic pressure[118]. Addressing plasma volume expansion with diuretics has been shown to be beneficial[119].

Several molecular mechanisms have been proposed to account for the pathophysiological changes that lead to HFpEF. For example, impaired myocardial energetics following a reduced mitochondrial membrane potential and opening of membrane permeability pores has been observed[120]. Other studies indicate decreased ATP synthesis and therefore insufficient energy supply of cardiomyocytes[121]. Also, intracellular calcium overload due to impaired SERCA2 function contributes

to HFpEF development[122]. In line with SERCA2 impairment, myocardial stiffness is recongnized as one of the molecular origins of HFpEF. On the one hand, cardiomyocytes become stiff due to titin hypophosphorylation[123,124]. On the other hand, non-cardiomyocytes secrete extracellular matrix components of altered composition and in higher amounts, which secondarily contributes to cardiac stiffness[125]. Crosstalk between the cell types further reinforces these changes in a reciprocal manner[126]. In addition, HFpEF is associated with an inflammatory state of the microvasculature that promotes microvascular ischemia and fibrosis due to endothelial to mesenchymal transition, which further reduces cardiac contractility and contributes to diastolic dysfunction[127]. Also the coronary microvascular endothelium is significantly affected by inflammation[128]. In consequence, the myocardium is perfused less efficiently and cardiomyocytes and other cells die from apoptosis[129,130], although cardiomyocyte apoptosis is usually not reported in HFpEF. Additionally, myocardial ischemia has been described to play a role in HFpEF development by inducing myocardial hypertrophy and changing the extracellular matrix composition[131]. Conversely, diastolic dysfunction itself contributes to ischemia in the myocardium by compromising diastolic coronary filling[132].

A wide range of rodent strains modeling HFpEF is described in the literature[133]. Different models use different triggers to induce HFpEF by one or several comorbidities observed in humans, for example aging or hypertension. A rat model in which HFpEF is induced by obesity achieved through high fat diet feeding is the Zucker fatty spontaneously hypertensive heart failure F1 hybrid (ZSF1) strain. The model is a crossing of rats with two different leptin receptor mutations: the lean female Zucker diabetic fatty rat and the lean male spontaneously hypertensive heart failure rat[134]. The phenotype manifests between 10 and 20 weeks of age when the animals develop a number of characteristics typical of HFpEF including hypertension, diastolic dysfunction, pulmonary congestion, increased arterial stiffness as well as on the cellular level cardiomyocyte hypertrophy, fibrosis and increased cardiomyocyte stiffness resulting from titin hypophosphorylation[135,136,137].

Overall, like myocardial infarction, HFpEF is a heart disease occuring predominantly in the elderly that affects a substantial proportion of the population and involves ischemic heart injury and potentially, remaining to be further evidenced though, cardiomyocyte apoptosis. Moreover, small ischemic myocardial injuries contribute to inflammation, fibrosis and cardiac remodeling in the development of HFpEF[112].

1.2.2.4 Heart Regeneration

Over time, aging itself, cardiovascular disease and ischemic heart injury lead to a loss of myocardial cells. Unlike skeletal muscle[138], the mammalian heart only has poor regenerative potential[139]. Since the

bulk mass of the myocardium consists of cardiac myocytes, the cells which confer contractility to the heart, cardiac contractile function gradually deteriorates and oftentimes necessitates heart transplantation as the only suitable treatment[140]. Endogenous mechanisms of cardiac regeneration as well as therapeutic strategies to boost it are a topic of ongoing research in order to counteract the high morbidity and mortality of cardiovascular disease.

Although traditionally considered postmitotic, cardiomyocytes in the rodent heart are capable of cell division within a time window of one week after birth[141]. Also in humans, a subpopulation of incompletely differentiated cardiomyocytes is able to re-enter the cell cycle and undergo division[142]. However, the rate of cardiomyocyte turnover ranges between 0.5 and two percent annually in humans and mice[143,144], a negligible scale in the context of injured heart regeneration. Postnatal growth of the mammalian heart is primarily achieved by an increase in cardiomyocyte size[145] concomitant with genome duplication, but not nuclear division[146] – a mechanism contributing rather to cardiac hypertrophy than regeneration[147].

However, injury augments the regenerative potential of the myocardium. Resident stem cells and myocyte precursor cells proliferate to partially replace adult cardiomyocytes lost due to ischemia, but not during normal aging[148]. These cells also differentiate into other cells types, but with a proliferation rate below 0.01 percent per year, their overall contribution is very minor[149]. Beside restricted proliferative capacities, the adult myocardium faces environmental challenges that impede regeneration. Following injury, blood supply is limited and immune cells invade the tissue hampering regenerative progress[150]. Moreover, fibroblasts rapidly infiltrate the tissue and create a scar that stiffens the myocardium[151].

To significantly improve cardiac repair after injury, the regenerative potential has been tried to be enhanced via different approaches including fibroblast reprogramming, cell therapy and stimulation of endogenous cardiomyocyte proliferation as well as revascularization. Fibroblast reprogramming was first achieved through activation of transcription factors known to drive cardiomyocyte differentiation during development. The resulting cardiomyocyte-like cells express genes conferring contractility[152]. When delivered by a viral system and injected directly into the injured tissue, these transcription factors are able to reprogram fibroblasts in the border zone that form part of the post-injury scar into cardiomyocytes, thereby reducing scar size and improving left ventricular contractility[153,154]. Consistently, targeting pathways that contribute to secretion of fibrotic scar components attenuates cardiac remodeling[155,156].

Cell therapeutic strategies have tested the infusion, injection and transplantation of cells of diverse origins and indicate that both direct cardiomyocyte replacement and facilitation of endogenous cardiomyocyte renewal may confer an improved outcome[157]. Studies with infused bone marrow-

derived stem cells suggest that the cells themselves have low cardiomyogenic potential displaying very limited long-term engraftment and differentiation rates. Still, enhanced heart function has been observed and attributed to paracrine signaling that improves tissue survival and neovascularization[158]. Promisingly, when human induced pluripotent stem cell (hiPSC)-derived cardiomyocytes were transplanted[159,160], they engrafted, coupled electrically and beat in synchrony with the host myocardium. Also with hiPSC-derived cardiomyocytes, paracrine effects may play a secondary role. Engraftment could be further supported using synthetic or natural tissue scaffolds[161]. Of note, introducing tissue into the myocardium, even with beneficial results for contractility, increases the risk to develop arrhythmias.

Endogenous cardiomyocyte proliferation can be stimulated by targeting the cell cycle[162], redox regulators[163] or growth factors. For example, intravenous infusion of the growth factor neuregulin 1 that is essential for cardiomyocyte proliferation and maturation has yielded an improved left ventricular ejection fraction in patients with heart failure[164]. Alternatively, the Hippo pathway can be manipulated to disinhibit cardiomyocyte proliferation and thereby reduce scar size as shown in mice[150]. Another approach to augment the proliferative capacity of cardiomyocytes might be regulated hypoxia[165].

In addition, treatment of myocardial injury with human cardiac stem cell-derived exosomes also has been shown to enhance cardiac contractility[166,167]. Investigations to develop a method to restore lost myocardium by boosting the small subpopulation of resident dividing cardiomyocytes is ongoing, taking model organisms with high cardiac regenerative potential like neonatal mice or zebrafish as examples[139]. These models are also studied to decipher the underlying mechanisms, for instance vascular endothelial growth factor (VEGF) expression, required for revascularization of infarcted tissue[168].

1.3 The Non-Coding Transcriptome

1.3.1 The Human Genome and its Coding Potential

In the mid 20th century, the scientific view of what is considered a gene was shaped by a posit that later became known as the central dogma of molecular biology. A gene was defined by its potential to encode an RNA that can be translated into an amino acid sequence, usually a protein. The view was at the latest challenged in 2003 when completion of the Human Genome Project[169,170] revealed that the human genome contains approximately 22,300 protein-coding genes – a number that is being continuously downscaled since with current estimates around 20,000 protein-coding genes, which is within the same range as other mammalian genomes[171,172]. Counterintuitively, some plant genomes,

for example that of grapes, contain more than 30,000 protein-coding genes. Thus, the number of protein-coding genes does not seem to correlate with an organism's complexity. In contrast, the more complex a species is, the higher is the proportion of non-coding genomic shares[173]. In fact, while protein-coding genes only constitute around two percent of the total human genome, more than 90 percent are transcribed into ribonucleic acid (RNA) molecules. After having been disregarded as junk DNA and transcriptional noise for some time, accumulating evidence advocates that they are functional themselves, appear in diverse forms and perform a great variety of tasks[174].

Roughly, non-coding RNAs (ncRNAs) can be categorized into small and longer RNAs of less or more than 200 nucleotides, respectively[175]. To name only a few classes, small ncRNAs include transfer RNAs (tRNAs), small nuclear RNAs (snRNAs), small nucleolar RNAs (snoRNAs), microRNAs (miRNAs) and small interfering RNAs (siRNAs). Longer ncRNAs encompass among others ribosomal RNAs (rRNAs), enhancer RNAs (eRNAs), circular RNAs (circRNAs) and long non-coding RNAs (lncRNAs).

Though only between 70 and 90 nucleotides long, tRNAs are the most abundant RNA in moles among all cellular RNAs. The human genome harbors at least 610 tRNA encoding genes[176] whose products function as adaptors connecting a messenger RNA (mRNA) codon with an amino acid during protein synthesis on the ribosome. They are highly modified and characteristically fold into a cloverleaf secondary structure[177].

The existence of snRNAs that are between 100 and 300 nucleotides long emerged in the 1980s. Assisting in precursor messenger RNA splicing, they reside within the cell nucleus, oftentimes in clusters, are relatively conserved across species and extensively modified, mainly by 2'-O-methylation and pseudouridylation. The mechanisms behind these modifications are both protein only-directed and RNA-guided and play a crucial role in the biogenesis of snRNA-protein complexes and spliceosome assembly[178,179].

Most of the 70 nucleotides long snoRNAs in vertebrates are processed intron fragments[180]. They guide the site-specific 2'-O-methylation of precursor rRNAs or their processing during ribosome biogenesis, a function conserved in Archaea and all eukaryotes[181]. Processing of snoRNAs enables them to perform additional, non-canonical functions like erasure of the m^7G cap and the poly(A) tail on mRNAs[182,183].

Since their discovery in the early 2000s in nematodes, miRNAs and particularly their biogenesis have been well characterized. MiRNAs are transcribed as precursor molecules and subsequently cleaved to 22 nucleotides by the endoribonucleases Drosha and Dicer before binding the protein Ago in the mature state to form the RNA-induced silencing complex (RISC). In the RISC complex, miRNAs bind a target mRNA via base pairing at the 5' end and thereby induce deadenylation and decay or translational regulation of the mRNA[184,185].

A relative of miRNAs are siRNAs. Originally observed during virus-induced silencing in plants[186], endogenous genomic loci like centromeres, transposons and other repetitive sequences were identified as siRNA precursor sources in the beginning of the 21st century[187]. Dicer cleavage of these double-stranded RNAs yields two complementary 22 nucleotides long siRNA molecules, one of which is integrated into the RISC complex. The other strand guides and aligns the RISC complex on a perfectly complementary mRNA target to induce its cleavage by an Ago protein[188].

Among the longer ncRNAs, rRNAs have become the most firmly established class since their discovery in the 1950s. They represent the principal elements of the small or large ribosomal subunits and are, in humans, 120, 160 and 1,868 nucleotides long. RRNAs cluster at functionally important sites of the ribosome, such as the peptidyltransferase center and the decoding site, where they catalize protein synthesis. Their secondary structure is stabilized by RNA modifications. Environmental cues as well as developmental and pathologic events can trigger changes in the rRNA modification pattern[189]. Ribozymes, which are RNA molecules with enzymatic activity, are also classified as rRNAs[180].

Enhancers that long have been thought to exclusively function as distal genomic regulatory elements are the site of pervasive eRNA transcription yielding eRNA molecules of 200 to 500 nucleotides in length, some even larger. The levels of eRNA transcription tightly correlate with the corresponding enhancer activity. Transcripts can be functional to activate target genes both on their own and through the act of transcription[190].

CircRNAs are covalently closed RNAs of cyclic structure equipping them with high stability due to their resistance to exonucleases. They are generated by precursor mRNA back-splicing and divided into exonic circRNAs, intronic circRNAs and exon-intron circRNAs so that they often share a sequence overlap with the corresponding mRNA. Although expressed at low levels, circRNAs can function as microRNA sponges and, often together with protein interaction partners, modulators of alternative splicing, transcription or translation[191,192].

1.3.2 Long Non-Coding RNAs

1.3.2.1 Characteristics of Long Non-Coding RNAs

Long non-coding RNAs are defined as RNA molecules of at least 200 nucleotides length from which no peptide or protein is translated. Compared with proteins or some other RNA classes, lncRNA characterization and functional classification are still in their infancy. According to the most recent GENCODE version, the human and mouse genomes contain around 16,000 and 13,000 lncRNA genes, respectively, that are transcribed by RNA polymerase II[193].

Table 1: LncRNA Statistics according to GENCODE Version 30

Species	LncRNA Genes	LncRNA Transcripts
Human	16,193	30,369
Mouse	13,374	18,930

Particularly in humans, the number of transcripts generated from these loci greatly exceeds the gene number (table 1), indicating that similarly to protein-coding genes, many lncRNA genes are spliced. Unlike protein-coding trancripts, lncRNAs are disproportionately often spliced into transcript with two exons. The histone modification profiles, canonical splicing signals and lengths of exons and introns are similar to those of protein-coding genes, though. LncRNAs can be capped and polyadenylated, but lack a 3' untranslated region (UTR)[194]. They reside in the nucleus, the cyoplasm or both, with a strikingly large number of lncRNAs localizing to chromatin. Despite being equally stable, they are approximately 90 percent lower expressed than mRNAs[195,196], but exhibit a higher tissue-specificity with the majority of tissue-specific lncRNAs being expressed in the brain[197]. Sequence-conservation is rather poor among lncRNAs, whereas many are locus-conserved[198] and sequences of lncRNA promoter regions even display a degree of conservation comparable to that of protein-coding gene promoters[199]. Secondary structure predictions of lncRNAs suggest that they resemble mRNAs in terms of the number of paired nucleotides folding into hairpins or similar structural elements[200]. Enhancer RNAs and circular RNAs are sometimes categorized as lncRNA subclasses. Some lncRNAs have been suggested to be processed into small ncRNAs, mostly snoRNAs, but also tRNAs, miRNAs and snRNAs[197].

Since lncRNA functions have not been investigated on a large scale to date, the molecules are classified based on their genomic locus in relation to neighboring protein-coding genes[175] (figure 10). Intergenic lncRNA genes are located between two protein-coding genes that they do not share any overlap with. Intronic lncRNA genes lie within an intron. Sense and antisense lncRNA genes overlap with intronic or exonic elements or both of protein-coding genes and are transcribed in the same or reverse direction, respectively. Both genes often share the same promoter, which may account for the correlation of expression between a lncRNA and its antisense gene.

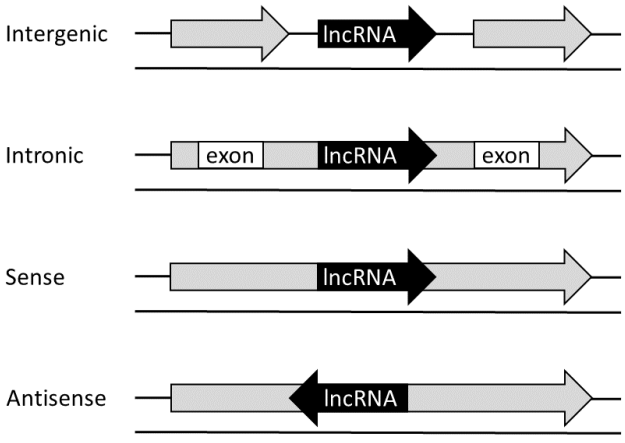

Figure 10: Classification of long non-coding RNAs. Most commonly, long non-coding RNAs are classified according to their genomic locus with regard to protein-coding genes. Long non-coding RNA genes can be located between two genes, between two exons of the same gene or overlap with a protein-coding gene and be transcribed in sense or antisense direction. Gray arrows indicate protein-coding sequences, arrow heads point in the direction of transcription.

Even when mechanistic data will be available for a majority of lncRNAs, functional classification will remain a challenge because many lncRNAs are long enough to contain several functional domains that might involve them in multiple time- and tissue-specific cellular processes[180].

1.3.2.2 Mechanisms of Long Non-Coding RNAs

Although only a fraction of annotated lncRNAs has been characterized, they have already been implicated in a great variety of cellular functions exerted through an equally diverse range of mechanisms. For example, lncRNAs have been demonstrated to modulate imprinting, regulate gene expression in *cis* and *trans*, shape the nuclear architecture, intervene in splicing and act as a sponge, scaffold or decoy for multiple other cellular components. Molecular mechanisms encompass interactions with other RNAs, proteins and chromatin, for example via triple helix formation with genomic DNA (gDNA; figure 11).

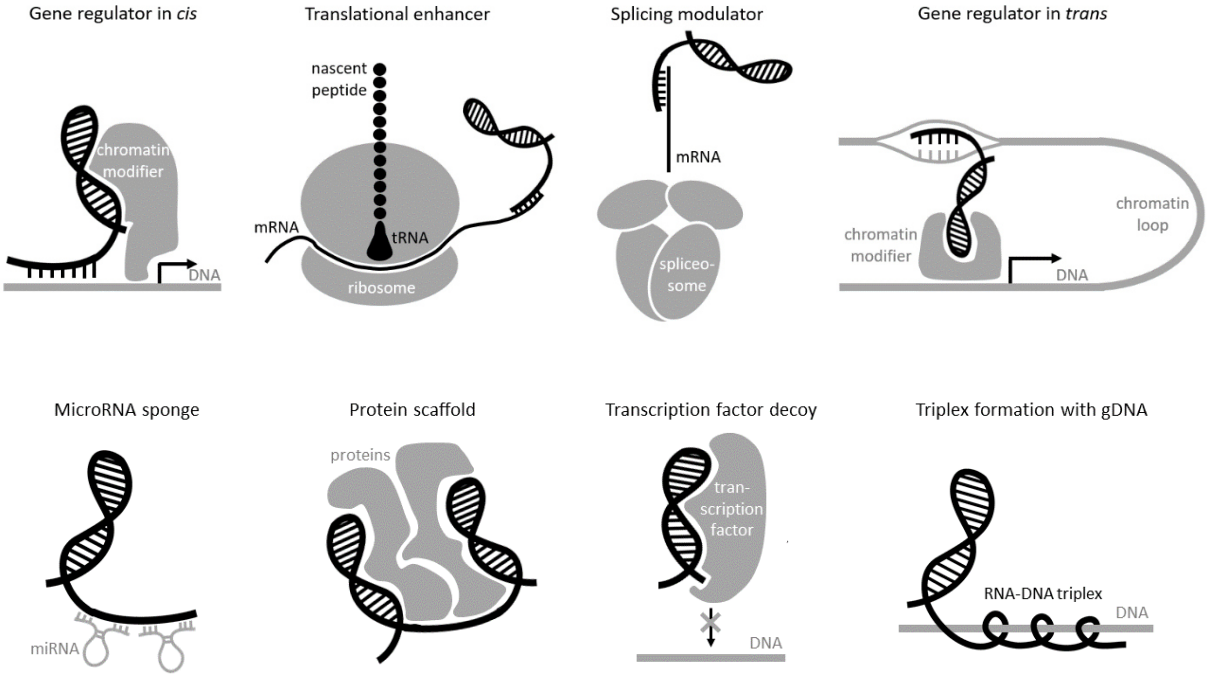

Figure 11: Mechanisms of long non-coding RNAs. Long non-coding RNAs have been shown to act via a plethora of mechanisms that include interactions with proteins, RNA and DNA. For example, long non-coding RNAs can activate gene expression in *cis* and *trans*, enhance translation, impede splicing, act as a sponge for microRNAs or scaffold or decoy for proteins and bind to genomic DNA via triple helix formation.

The first mechanistically described lncRNA was Xist in 1969[201], which is involved in imprinting, the epigenetic repression of one allele. Xist is essential for imprinting of one X chromosome in female

mammals for dosage compensation of transcripts encoded on the X chromosome. Its transcripts spread across the entire chromosome and recruit the transcriptional repressor SHARP that binds to a repetitive sequence element on Xist. Consequently, the chromosome is located to the nuclear periphery and its histones are deacetylated to silence genes transcription[202]. This repression of genes that are localized in proximity to the Xist gene itself represents an example for gene regulation in *cis*.

Another lncRNA regulating genes in *cis*, but on post-transcriptional level, is antisense Uchl1. Translation of Uchl1, the protein encoded by an overlapping gene, is enhanced by binding of the 5' UTR of the mRNA to a SINE element within antisense Uchl1, which facilitates association of the mRNA to polyribosomes[203].

In contrast, lncRNA HOTAIR regulates gene expression in *trans* by repressing the distant HOXD gene locus. HOTAIR binds to the HOXD gene and thereby recruits components of the polycomb repressive complex 2 (PRC2) that catalyzes the chromatin modification H3K27me3[204]. However, more recent studies question this model and postulate a mechanism independent of PRC2 recruitment[205]. Analogously, lncRNA HOTTIP has been reported to epigenetically enhance expression of the distally located HOXA gene cluster. Chromosomal looping spatially approximates HOTTIP to the gene loci where histone modifier WDR5 is recruited by HOTTIP to catalyze the activating H3K4me3 mark[206].

A more indirect form of gene regulation is exerted by NEAT1, a lncRNA that shapes nuclear architecture. It interacts with several proteins that are localized to specialized nuclear compartments, so-called paraspeckles[207], and involved in transcription and RNA processing. NEAT1 is required for paraspeckle formation and maintenance and has been proposed to direct them into proximity of actively transcribed gene loci[208].

Furthermore, lncRNAs can affect splicing as shown for Zeb2. The lncRNA Zeb2-NAT is transcribed from the locus antisense to the Zeb2 5' UTR and interferes with spliceosome assembly by base-pairing with the Zeb2 precursor mRNA. This prevents the splicing of an intron within the Zeb2 5' UTR that contains an internal ribosomal entry site. Retention of the intron therefore augments Zeb2 translation[209].

LncRNAs have also been demonstrated to act as sponges for both miRNAs and proteins. For instance, linc-MD1 competes for binding of miRNA-133 and miRNA-135 and thereby regulates transcription factors involved in myoblast differentiation[210]. In analogy, lncRNA NORAD sequesters PUMILIO proteins and thereby prevents them from inducing genomic instability[211]. Notably, lncRNAs acting as sponges are usually more abundant than lncRNAs regulating gene expression because sponging is a dose-dependent mechanism, wherease regulation of transcription or translation can usually be amplified at multiple levels and does not require high expression of all signaling molecules[175].

Another dose-dependent function of lncRNAs is scaffolding as described for TERC that serves as an adaptor to join telomerase subunits into a complex[212]. Strictly, also Xist and HOTAIR act as scaffolds for epigenetic modifiers. An example of a lncRNA that functions as protein decoy and whose mechanism consequently is also dose-dependent is Gas5. The RNAs binds to the glucocorticoid receptor via a secondary structural hairpin motif that resembles the DNA-binding site of the receptor. Upon growth factor starvation, Gas5 is induced to sequester the receptor from target gene loci to inhibit metabolic gene transcription[213]. NORAD, which sequesters PUMILIO proteins, can also be classified as a decoy.

1.3.2.3 Triplex Formation between Long Non-Coding RNAs and Genomic DNA

An only recently proposed mechanism for lncRNAs is triple helix formation with genomic DNA. In triplex structures, a single-stranded nucleic acid, which can be DNA or RNA, inserts into the major groove of the DNA double helix with high sequence specificity. Hereby, the Watson-Crick base pair interacts with the third base of the single strand via Hoogsteen hydrogen bonding or reverse Hoogsteen hydrogen bonding[214,215]. The two possible triplex types differ in the orientation of the third strand, whose sequence dictates whether a parallel or an antiparallel triplex is formed. In case of the third strand being an RNA, parallel structures form between TA-U, CG-C^+ and CG-G triplets while antiparallel structures result from TA-A, TA-U and CG-G triplets, with the hyphen indicating a Hoogsteen hydrogen bond (figure 12). Consistently, RNA molecules with high CU-content preferentially form parallel triplexes, such with high AG-content tend to form antiparallel triplexes and such with high GU-content are capable of forming triplexes of both orientations. Acidic conditions facilitate formation of parallel triplexes because protonated cytosines undergo triplex structures more efficiently[216].

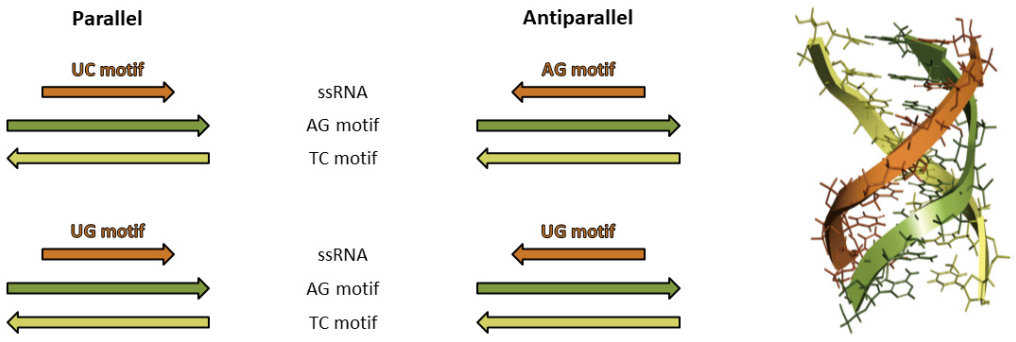

Figure 12: Triplex formation between single-stranded RNA and double-stranded DNA. RNA molecules can form triple helices with double-stranded DNA molecules by binding to the major groove of the double helix in either parallel or antiparallel orientation. Usually, RNAs with CU motifs preferentially form parallel triplexes, RNAs with AG motifs form antiparallel triplexes and RNAs with GU motifs can form triplexes of both orientations. (Modified from Li et al., RNA-DNA triplex formation by long noncoding RNAs, Cell Chem. Biol. 2016.)

Although Hoogsteen hydrogen bonding is weaker than Watson-Crick hydrogen bonding and in some cases requires an acidic environment, DNA-RNA triplexes have been demonstrated to form *in vivo*. Studies using antibodies[217] or fluorescent molecules[218] specifically binding to triplex structures indicate triplex formation in the nucleus, with stronger evidence for DNA-RNA than DNA-DNA structures. Computational predictions suggest that triplex-prone motifs exist across the genome and accumulate in regulatory regions, particularly gene promoters[219], interestingly omitting transcription factor binding sites. The vast majority of annotated human lncRNAs predicted to form triplexes are either antisense or intergenic transcripts[220].

Direct evidence supporting triplex formation between lncRNAs with genomic DNA *in vivo* has emerged through a handful of examples acting in both *cis* and *trans*. The first was described in 2007 when promoter-associated RNA (pRNA) of DHFR was reported to form a triplex with the DHFR promoter, bind to the transcription factor TFIIB and thereby inhibit DHFR transcription[221]. Transcription of rRNA genes is also silenced by pRNAs through triplex formation within rRNA promoters. In this case, pRNAs form triplexes within a transcription factor binding site, thereby impeding efficient binding of the transcription factor TTF-1. Additionally, they recruit DNA methyltransferase DNMT3b that hypermethylates rRNA gene promoters and thus promotes heterochromatin formation in this region[222]. The pRNA PARTICLE in turn recruits PRC2 to the promoter of its antisense gene MAT2A, thereby acting as a transcriptional repressor in *cis*[223]. Three examples of lncRNAs regulating expression of *trans* genes are Fendrr[224], MEG3[225] and HOTAIR[226]. Like PARTICLE, they all recruit PRC2 to silence expression of their respective numerous distant target genes. Fendrr is additionally capable of recruiting MLL1, a histone methylase complex that positively regulates gene transcription. The only lncRNA exclusively activating gene expression that has so far been described is Khps1. It forms a triplex with the promoter of its antisense gene, the proto-oncogene SPHK1, and recruits histone acetyltransferases p300 and CBP. Notably, triplex formation by Khps1 *in vivo* does not require an acidic environment[227].

All of these examples, particularly the studies on MEG3 and HOTAIR[228] that showed that these lncRNAs preferentially occupy AG-rich DNA motifs across the genome, suggest that DNA-RNA triplex formation may be a general mechanism of lncRNAs to recognize genome-wide target sites in a sequence-specific manner and epigenetically regulate gene expression by recruitment of chromatin modifiers[216].

1.3.2.4 Long Non-Coding RNAs in Cardiovascular Disease and Aging

Genomde-wide association studies have revealed that 88 percent of human disease-associated genetic variants occur in non-coding regions of the genome, highlighting the relevance of non-coding RNAs for pathophysiology[229,230]. LncRNAs have been linked among others to cancer, diabetes, neurological and

cardiovascular diseases. RNA deep sequencing of the myocardial transcriptome of heart failure patients revealed that sets of 679 and 570 lncRNAs are differentially expressed upon ischemic and non-ischemic heart failure, respectively. Left ventricular assist devices partially normalized lncRNA expression patterns. Moreover, lncRNA profiles were more specific to the type of heart failure than miRNA or mRNA profiles. These findings indicate that lncRNAs participate in disease etiology and bear unexplored diagnostic and therapeutic potential[231].

An example of a lncRNA associated with ischemia and myocardial infarction is MIAT. Genome-wide association studies found six single-nucleotide polymorphisms (SNPs) within the MIAT gene that increase the risk for myocardial infarction. One of the SNPs increases MIAT expression levels and affinity for nuclear protein binding, thereby suggesting a potential role of the SNP in myocardial infarction pathogenesis[232]. Similarly, genetic variation within the genes encoding H19, a lncRNA that binds miRNAs of the let-7 family[233,234], and ANRIL, a lncRNA regulating gene transcription through recruitment of polycomb repressive complexes[235,236], increase the risk for coronary artery disease and and myocardial infarction, whereas a SNP within the lincRNA-p21 gene has been reported to decrease coronary atery diseases susceptibility[237]. Truncation of the lncRNA KCNQ1OT1 that is an antisense transcript to a potassium channel gene has been reported to be associated with myocardial infarction in mice[238]. Consistently, patients display higher ANRIL, but lower KCNQ1OT1 levels in blood upon myocardial infarction[239]. Levels of two other lncRNAs, MALAT1 and HIF1A-AS2, were also found to be decreased upon myocardial infarction. HIF1A-AS2 is an antisense transcript to hypoxia-inducible factor 1-alpha (HIF1A), a major transcription factor regulating the cellular reponse to hypoxia. It destabilizes HIF1A mRNA and is overexpressed in the failing heart[240]. Another lncRNA with altered expression levels upon myocardial infarction in humans in UCA1[241]. In rats, UCA1 promotes cardiomyocyte apoptosis and thereby exacerbates cardiac injury following ischemia and reperfusion[242]. Myocardial infarction model in mice revealed two lncRNAs, Mirt1 and Mirt2, to be upregulated after heart injury. Their expression correlated with genes levels protective against left ventricular remodeling, suggesting some therapeutic potential for Mirt1 and Mirt2[243]. Ischemic injury and reperfusion in mice also increase levels of lncRNA APF, which regulates autophagy, a process that can be both protective and detrimental for cardiomyocyte survival[244], by sponging miRNA-188-3p[245]. Another study of murine lncRNA profiles after myocardial infarction identified several novel lncRNAs suppressed following AMI surgery[231]. The human ortholog of one of them, Novlnc6, was also downregulated in humans with dilative cardiomyopathy.

This already implies that also other cardiac disease phenotypes are influenced by specific lncRNAs. The lncRNA Carl was generally associated with cardiomyocyte apoptosis. Under physiological conditions, it sponges miRNA-539, which plays a role in mitochondrial homeostasis[246]. Also lncRNA MEG3

contributes to apoptosis of cardiomyocytes[247]. LIPCAR, a circulating lncRNA, is downregulated early after acute myocardial infarction, but upregulated at later stages in patients developing cardiac remodeling and heart failure. It is therefore of potential use as a biomarker predicting patient survival[248]. Fibrosis in the heart is modulated by the pro-fibrotic lncRNAs MIAT[249] in humans as well as by H19[250], NR024118 and Cdkn1c[251] in rats. Cardiac hypertrophy was found to be aggrevated by pressure overload-induced downregulation of Myheart levels, a lncRNA transcribed antisense to the locus of the myosin heavy chain 7 (MYH7) gene. Restoring Myheart levels protected the heart from hypetrophy and heart failure[252]. The opposite function was described for Chast[253] and Chaer[254], two species-conserved lncRNAs that both contribute to development of cardiac hypertrophy. In mice, hypertrophy followed by heart failure is associated with a significant H19 upregulation[255] whereas lncRNA CHRF attenuates the hypertrophic response by sponging miRNA-489[256]. Murine heart development in turn is disturbed upon inhibition of lncRNAs Braveheart[257] or Fendrr[258] that both epigenetically regulate expression of cardiac transcription factors to promote cardiomyocyte differentation. Fendrr orthologues are also found in humans and rats.

Besides, lncRNAs have been linked to the etiology of many vascular diseases, some of which overlap with cardiac conditions. Among many others, ANRIL has been implicated in atherosclerosis[259], hypertension[239] as well as intracranial and abdominal aortic aneurysms[260]. H19 is involved in aortic aneurysms[261], atherosclerosis[262] and calcific aortic valves[263]. MALAT1 has been well characterized as a regulator of angiogenesis in endothelial cells[264], but is also linked to atherosclerotic plaques[265], coronary atherosclerotic disease[266] and pulmonary arterial hypertension[267]. MEG3 levels are decreased in patients with coronary artery disease[268] or pulmonary arterial hypertension[269], but increased upon heart failure[247]. Both MALAT1 and MEG3 expression is stimulated by hypoxia, a trigger for angiogenesis[264]. Expression of lincRNA-p21 is decreased in coronary tissue with diseased arteries[270] as well as in atherosclerotic plaques[271], but increased in thoracic aortic aneurysms[272]. Genetic variants of Gas5 have been shown to be associated with a higher risk for atherosclerosis[273], while a decrease in Gas5 levels is implicated in hypertension[274]. The lncRNA TUG1 contributes to atherosclerosis[275], hypertension[276] and ischemic stroke[277].

The overlap of cardiovascular diseases that are regulated by the same lncRNAs illustrates that one lncRNA can perform multiple functions in different tissues or different pathological contexts. Many of the described disease-associated lncRNAs are differentially regulated during aging in a tissue- or cell line-specific manner. For example, senescent fibroblasts exhibit reduced MIAT levels[278], but augmented HOTAIR levels[279]. ANRIL expression in turn increases in aging rodents[204], but decreases in high passages of several cell lines, which induces a senescent phenotype[280]. H19 levels drop in the endothelium of aged mice[281]. Also, MEG3 is differentially and tissue-specifically regulated. While being

upregulated in the aged human atrial myocardium and in senescent human umbilical vein endothelial cells[282], it is downregulated in the brain during some aging-related neurodegenerative disorders like Huntington's disease[283]. Murine Gas5 expression rises in the hippocampus[284], but drops in other brain regions and ovaries[285]. Cellular senescence has been linked to depletion of MALAT1[286] and Xist[278], but, conversely, also to enhanced UCA1[287] and lncRNA-p21[288] transcription as well as to the presence of TUG1[289].

A considerable number of other lncRNAs whose role in the cardiovascular system has not been investigated yet has been reported to be associated with aging-related disorders in multiple organ systems and to be differentially regulated in tissues and cell lines during aging or passaging[290,291,292]. These aging-dependent lncRNA expression patterns underline the link between cardiovascular or other diseases and aging on a molecular level and the need for further investigations to achieve a deeper understanding of lncRNA implication in cardiovascular disease etiology and their therapeutic potential.

2. Objective

Cardiovascular diseases are a leading cause of morbidity and mortality worldwide, severly compromising life quality of patients and straining health care services. Two continuously increasing variables converge into a medical challenge that constantly aggravates the burden on either side: human life expectancy and the risk to develop cardiovascular diseases during aging. A more thorough understanding of disease etiology and molecular mechanistics is indispensable to develop novel therapies that improve patient outcome in a sustainable manner, especially in view of the limited regenerative potential of the heart.

Since a major proportion of disease-associated genetic loci is located within transcribed, non-coding regions, RNA molecules represent a promising starting point in the search of such therapeutic strategies. The last two decades have spawned the functional analysis of a handful of long non-coding RNAs and emerging evidence supports the hypothesis that they are of potential use as therapeutic targets. Still, the vast majority of long non-coding RNAs remains to be characterized in the cardiovascular context.

Against this background, this study aims to

(1) identify and functionally characterize a novel long non-coding RNA in the heart,
(2) decipher the molecular mechanism via which it exerts its function,
(3) identify interaction partners that participate in the performed mechanism,
(4) elucidate its role in the settings of aging and cardiovascular disease, particularly ischemia,
(5) and assess its potential to contribute to myocardial regeneration.

3. Materials and Methods

3.1 Materials

Table 2: Consumables

Item	Manufacturer
¼" ceramic spheres	MP Biomedicals (Illkirch, France)
384-well qRT-PCR plates	Life Technologies
5 ml polystyrene round-bottom tubes	BD Biosciences (Erembodegen, Belgium)
96-well black polystyrene microplate	Corning (Big Flats, NY, USA)
96-well polystrene round buttom microplate	Life Technologies (Carlsbad, CA, USA)
96-well qRT-PCR plates	Life Technologies (Carlsbad, CA, USA)
Cell culture dishes (3 cm, 6 cm, 10 cm, 15 cm)	Greiner Bio-One GmbH (Frickenhausen, Germany)
Cell culture flasks, TC-treated (T25, T75, T175)	Greiner Bio-One GmbH (Frickenhausen, Germany)
Cell culture inserts (6 well, 1 µm pore size)	Greiner Bio-One GmbH (Frickenhausen, Germany)
Cell culture multiwell plates (96 wells, 48 wells, 24 wells, 12 wells, 6 wells)	Greiner Bio-One GmbH (Frickenhausen, Germany)
Cell scrapers	Greiner Bio-One GmbH (Frickenhausen, Germany)
Cell strainers (40 µm, 70 µm, 100 µm)	PluriSelect (Leipzig, Germany)
Combitips (0.1 ml, 0.5 ml, 2.5 ml, 5 ml, 10 ml)	Eppendorf (Hamburg, Germany)
Costar stripette serological pipettes (2 ml, 5 ml, 10 ml, 25 ml, 50 ml)	Corning (Big Flats, NY, USA)
CryoPure tubes (1.8 ml)	Sarstedt (Nümbrecht, Germany)
DNA LoBind tubes (1.5 ml)	Eppendorf (Hamburg, Germany)
Filter Tips TipOne RPT (10 µl, 20 µl, 100 µl, 200 µl, 1,000 µl)	Starlab (Ahrensburg, Germany)
GeneChIP Human Exon 1.0 ST arrays	Affymetrix (Santa Clara, CA, USA)
GentleMACS C Tubes	Miltenyi Biotec (Bergisch Gladbach, Germany)
Microlance cannulas	VWR (Leicestershire, UK)
Mini Protean precast SDS gels	Bio-Rad (Munich, Germany)
NucleoCasette (Cell Counting)	ChemoMetec A/S (Allerød, Denmark)
Optical 96 well reaction plates	Applied Biosystems (Foster City, CA, USA)
Optical adhesive covers	Applied Biosystems (Foster City, CA, USA)
Polypropylene falcon tubes (15 ml and 50 ml)	Greiner Bio-one GmbH (Frickenhausen, Germany)
Polypropylene microtubes 2 ml	Sarstedt (Nümbrecht, Germany)
Protein LoBind tubes (1.5 ml)	Eppendorf (Hamburg, Germany)
Rotiprotect-NITRIL evo gloves	Carl Roth (Karlsruhe, Germany)
Safe-lock tubes (0.5 ml, 1.5 and 2 ml)	Eppendorf (Hamburg, Germany)
Suture material (6-0, 8-0)	Ethicon (Norderstedt, Germany)
Syringes (1 ml, 5 ml, 10 ml)	VWR (Leicestershire, UK)
Syringes with needle (1 ml)	BD Biosciences (Erembodegen, Belgium)
Tissue embedding cassettes	VWR (Leicestershire, UK)
Ultra centrifugal filter devices 100K Amicon	Millipore (Billerica, MA, USA)

Table 3: Equipment

Instrument	Model	Manufacturer
Adjustable volume pipettes	Research plus	Eppendorf (Hamburg, Germany)
Autoclave	DX-23	Systec (Linden, Germany)
Autoclave	VX-75	Systec (Linden, Germany)
Cell counter	Nucleocounter NC-200	ChemoMetec A/S (Allerød, Denmark)
Cell framing adapter	CFA300	IonOptix (Westwood, MA, USA)

Cell freezing container	CoolCell LX	Biocision (Chelmsford, MA, USA)
Cell stimulator	MyoPacer	IonOptix (Westwood, MA, USA)
Centrifuge (falcons, plates)	Centrifuge 5804	Eppendorf (Hamburg, Germany)
Centrifuge (falcons)	Rotina 420R	Hettich (Tuttlingen, Germany)
Centrifuge, benchtop	Centrifuge 5424	Eppendorf (Hamburg, Germany)
Centrifuge, tabletop	Galaxy Mini	VWR (Leicestershire, UK)
Chemistry analyzer	Cobas Fara II	Roche (Basel, Switzerland)
CO_2 incubator	Galaxy 170S	Eppendorf (Hamburg, Germany)
Confocal microscope	LSM 780	Zeiss (Jena, Germany)
Disc rotator	SU1010	Sunlab (Mannheim, Germany)
Dissociator	gentleMACS	Miltenyi Biotec (Bergisch Gladbach, Germany)
EHT contractility analysis instrument	A0001	EHT Technologies GmbH (Hamburg, Germany)
Flow cytometer	BD FACSCanto II	BD Biosciences (Erembodegen, Belgium)
Fluorescence system interface	FSI-700	IonOptix (Westwood, MA, USA)
High-speed contractility camera	MyoCam-S	IonOptix (Westwood, MA, USA)
Homogenizer	FastPrep24	MP Biomedicals (Solon, OH, USA)
Hotplate stirrer	peqMIX Plus	VWR (Leicestershire, UK)
Hypoxia incubator	C16	Labotect (Rosdorf, Germany)
Hypoxia incubator	CB 150	Binder (Tuttlingen, Germany)
Imaging system	ChemiDoc Touch	Bio-Rad (Munich, Germany)
Individually ventilated cage	SealSafe PLUS AERO	Tecniplast (Hohenpeißenberg, Germany)
Inhalation anesthesia device	Trajan 808	Dräger Medical Deutschland GmbH (Lübeck, Germany)
Inverted microscope	AE31 Elite	Motic (Wetzlar, Germany)
Ion source	Nanospray Flex	Thermo Fisher (Waltham, MA, USA)
Light source	HyperSwitch	IonOptix (Westwood, MA, USA)
Liquid chromatography unit	Dionex Ultimate 3000	Thermo Fisher (Waltham, MA, USA)
Magnetic rack	DynaMag-2	Thermo Fisher (Waltham, MA, USA)
Mass Spectrometer	Q Exactive Plus	Thermo Fisher (Waltham, MA, USA)
Microplate multimode reader	GloMax-Multi+with Instinct	Promega, (Madison, WI, USA)
Microscope	Axio Observer Z1	Zeiss (Jena, Germany)
Microscope	Axiovert 100	Zeiss (Jena, Germany)
Microscope	Eclipse Ci	Nikon (Düsseldorf, Germany)
Microtome	Microm HM 430	Microm International (Walldorf, Germany)
Micro-ultrasound imaging system	Vevo 2100	VisualSonics (Toronto, Canada)
Mini gel electrophoresis setup	Protean Tetra	Bio-Rad (Munich, Germany)
MRI gradient system	B-GA 9S HP	Bruker BioSpin (Ettlingen,Germany)
MRI scanner	7 Tesla MR system	Bruker BioSpin (Ettlingen,Germany)
Multipipette	XStream	Eppendorf (Hamburg, Germany)
NMR spectrometer	Ascend 800 MHz	Bruker Corporation (Billerica, MA, USA)
Pacing adapter	P0002	EHT Technologies GmbH (Hamburg, Germany)
Pacing electrode	P0001	EHT Technologies GmbH (Hamburg, Germany)
PH meter	Φ 340	Beckman (Fullerton, CA, USA)
Pipetting aid	PIPETBOY acu 2	Integra Biosciences (Zizers, Switzerland)
Power supply	MyoCam-S Power Supply	IonOptix (Westwood, MA, USA)
Power supply	Powerpac HC	Bio-Rad (Munich, Germany)
Precision scales	AEJ-CM	Kern (Balingen, Germany)
Razor	Aesculap Isis	B. Braun Vet Care (Tuttlingen, Deutschland)
Real time PCR system	StepOnePlus	Applied Biosystems (Foster City, CA, USA)

Real time PCR system	Viia 7	Applied Biosystems (Foster City, CA, USA)
Refrigerated/heating circulator	F12-MA	Julabo (Seelbach, Germany)
Safety cabinet	Hera safe	Heraeus (Hanau, Germany)
Safety cabinet	ScanLaf Mars Pro Cytosafe Class 2	LaboGene (Allerød, Denmark)
Scales	SE1202	VWR (Leicestershire, UK)
Shaker	DOS-10L	Neolab (Heidelberg, Germany)
Shaking incubator	3033	GFL GmbH (Burgwedel, Germany)
Silicone rack	C0001	EHT Technologies GmbH (Hamburg, Germany)
Sonicator	Bioruptor Plus	Diagenode (Seraing, Belgium)
Spectrophotometer	Nanodrop 2000	Thermo Fisher (Waltham, MA, USA)
Surgical lamp	NovaFlex	World Precision Instruments (Sarasota, FL, USA)
Teflon spacer	C0002	EHT Technologies GmbH (Hamburg, Germany)
Temperature controller	mTCII	Cell MicroControls (Norfolk, VA, USA)
Thermocycler	Mastercycler nexus	Eppendorf (Hamburg, Germany)
Thermocycler	Mastercycler nexus X2e	Eppendorf (Hamburg, Germany)
Thermocycler	Mastercycler pro S	Eppendorf (Hamburg, Germany)
Thermomixer compact	ThermoMixer C	Eppendorf (Hamburg, Germany)
Thermomixer lid	ThermoTop	Eppendorf (Hamburg, Germany)
Tissue embedding system	TPC 15 Duo/Trio	Medite GmbH (Burgdorf, Germany)
Triple resonance NMR probe	CPTCI 5 mm	Bruker Corporation (Billerica, MA, USA)
UV Trans illuminator	T2201	Sigma-Aldrich (St. Louis, MO, USA)
Ventilator	MiniVent TYPE 845	Harvard Apparatus (March, Germany)
Vortexer	Vortex Genie 2	Scientific Industries (Bohemia, NY, USA)
Water bath	1008	GFL (Burgwedel, Germany)

Table 4: Chemicals and Reagents

Product	**Manufacturer**
7-AAD	BD Biosciences (Erembodegen, Belgium)
10x PCR buffer	Applied Biosystems (Foster City, CA, USA)
Acetic acid	Carl Roth (Karlsruhe, Germany)
Acetoacetyl-CoA	Sigma-Aldrich (St. Louis, MO, USA)
Acetone	Sigma-Aldrich (St. Louis, MO, USA)
Acrylamide	AppliChem (Darmstadt, Germany)
Agarose	AppliChem (Darmstadt, Germany)
Ammonium per sulphate (APS)	Carl Roth (Karlsruhe, Germany)
Annexin V Binding Buffer	BD Biosciences (Erembodegen, Belgium)
Annexin V-V450	BD Biosciences (Erembodegen, Belgium)
Biotinylated isolectin B4	Vector Laboratories (Burlingame, CA, USA)
Bis-Tris SDS-PAGE 4-12% gradient gel	Invitrogen (San Diego, CA, USA)
Bovine Serum Albumin (BSA) Fraction V	PAA laboratories (Paching, Austria)
Calcium chloride ($CaCl_2$)	Merck (Darmstadt, Germany)
Chloroform	J T Baker (Phillipsburg, NJ, USA)
Citric acid	Carl Roth (Karlsruhe, Germany)
CutSmart buffer	New England Biolabs (Frankfurt, Germany)
DAPI	Roche (Basel, Switzerland)
DiaMag protein A and G coated magnetic beads	Diagenode (Seraing, Belgium)
Dimethyl sulfoxide (DMSO)	Sigma-Aldrich (St. Louis, MO, USA)
Dithiothretol (DTT)	AppliChem (Darmstadt, Germany)
DL-Dithiothreitol solution	Sigma-Aldrich (St. Louis, MO, USA)

DNase and RNase-free water	Gibco, Invitrogen (Darmstadt, Germany)
dNTP Mix, 10 mM	Invitrogen (Carlsbad, CA, USA)
Dulbecco´s phosphate buffer saline (PBS)	Life Technologies (Carlsbad, CA, USA)
Dynabeads MyOne Streptavidin C1	Invitrogen (San Diego, CA, USA)
Dynabeads sheep anti-rat IgG	Invitrogen (San Diego, CA, USA)
Epson salt ($MgSO_4$*7 H_20)	Sigma-Aldrich (St. Louis, MO, USA)
Ethanol absolute	Sigma-Aldrich (St. Louis, MO, USA)
Ethylene glycol-bis(2-aminoethylether)-N N N'N'-tetraacetate (EGTA)	AppliChem (Darmstadt, Germany)
Ethylenediaminetetraacetate (EDTA)	AppliChem (Darmstadt, Germany)
Fast SYBR green mix	Applied Biosystems (Foster City, CA, USA)
Formaldehyde (16 %), methanol-free	Thermo Fisher (Waltham, MA, USA)
GeneRuler 1 kb DNA ladder	Thermo Fisher (Waltham, MA, USA)
GeneRuler 100 bp DNA ladder	Thermo Fisher (Waltham, MA, USA)
Glycerol	AppliChem (Darmstadt, Germany)
Glycine	AppliChem (Darmstadt, Germany)
Glycogen	Invitrogen (San Diego, CA, USA)
Goat serum	Thermo Fisher (Waltham, MA, USA)
GSL I isolectin B4	Linaris (Dossenheim, Germany)
Halt Protease Inhibitor Cocktail, 100x	Thermo Fisher (Waltham, MA, USA)
Histofix, 4 %	Carl Roth (Karlsruhe, Germany)
Hoechst	AnaSpec (Fremont, CA)
Hydrochloric acid (HCl)	Sigma-Aldrich (St. Luis, MO, USA)
Iodoacetamide	Sigma-Aldrich (St. Louis, MO, USA)
Isopropanol	Sigma-Aldrich (St. Louis, MO, USA)
Laemmli buffer	Bio-Rad (Munich, Germany)
MagnaBind protein G beads	Thermo Fisher (Waltham, MA, USA)
Magnesium chloride ($MgCl_2$)	Sigma-Aldrich (St. Louis, MO, USA)
Magnesium sulfate ($MgSO_4$)	Sigma-Aldrich (St. Louis, MO, USA)
Manganese dichloride ($MnCl_2$)	Sigma-Aldrich (St. Louis, MO, USA)
Methanol	Sigma-Aldrich (St. Louis, MO, USA)
Methylcellulose	Sigma-Aldrich (St. Louis, MO, USA)
Midori Green	Biozym (Hessisch Oldendorf, Germany)
Mounting medium	DAKO (Jena, Germany)
N,N dimethylformamide	Sigma-Aldrich (St. Louis, MO, USA)
Nonidet P-40 (NP-40)	Sigma-Aldrich (St. Louis, MO, USA)
PageRuler Plus Prestained Protein Ladder	Thermo Fisher (Waltham, MA, USA)
Paraformaldehyde (PFA; 37 %)	AppliChem (Darmstadt, Germany)
PERTEX mounting medium	VWR (Leicestershire, UK)
Phenol-Chlorophorm-Isoamylalcohol	AppliChem (Darmstadt, Germany)
Picric acid	Sigma-Aldrich (St. Louis, MO, USA)
Potassium bicarbonate	Sigma-Aldrich (St. Louis, MO, USA)
Potassium chloride (KCl)	AppliChem (Darmstadt, Germany)
Potassium dihydrogenphosphate (KH_2PO_4)	Sigma-Aldrich (St. Louis, MO, USA)
Protease Inhibitor Cocktail Tablets	Roche (Basel, Switzerland)
ProteaseMax Surfactant	Promega (Madison, WI, USA)
QIAzol	Qiagen (Hilden, Germany)
Random hexamer primers	Thermo Fisher (Waltham, MA, USA)
Reverse transcriptase buffer	Invitrogen (Carlsbad, CA, USA)
Silver nitrate ($AgNO_3$)	Sigma-Aldrich (St. Louis, MO, USA)
Sirius red	Waldeck (Münster, Germany)
Sodium azide (NaN_3)	Sigma-Aldrich (St. Louis, MO, USA)
Sodium bicarbonate ($NaHCO_3$)	Sigma-Aldrich (St. Louis, MO, USA)
Sodium carbonate (Na_2CO_3)	Merck (Darmstadt, Germany)
Sodium chloride (NaCl)	Sigma-Aldrich (St. Louis, MO, USA)

Sodium deoxycholate ($C_{24}H_{39}NaO_4$)	Sigma-Aldrich (St. Louis, MO, USA)
Sodium dodecyl sulfate (SDS)	Carl Roth (Karlsruhe, Germany)
Sodium hydrogen phosphate (Na_2HPO_4)	Sigma-Aldrich (St. Louis, MO, USA)
Sodium hydroxide (NaOH)	Carl Roth (Karlsruhe, Germany)
Sodium succinate dibasic hexahydrate	Sigma-Aldrich (St. Louis, MO, USA)
Sodium thiosulfate ($Na_2S_2O_3$)	Sigma-Aldrich (St. Louis, MO, USA)
Staurosporine	Sigma-Aldrich (St.Louis, MO, USA)
Streptavidin, Alexa Fluor 488 conjugate	Invitrogen (Carlsbad, CA, USA)
Sulfuric acid (H_2SO_4)	Sigma-Aldrich (St. Louis, MO, USA)
SYBR Green	Applied Biosystems (Foster City, CA, USA)
TBE buffer	Sigma-Aldrich (St. Louis, MO, USA)
TE buffer	Promega (Madison, WI, USA)
TEMED	AppliChem (Darmstadt, Germany)
Tris(hydroxymethyl)aminomethane	AppliChem (Darmstadt, Germany)
Triton X-100	Sigma-Aldrich (St. Louis, MO, USA)
Trypsin (sequening grade)	Promega (Madison, WI, USA)
Tween 20	Sigma-Aldrich (St. Louis, MO, USA)
Wheat germ agglutinin, Alexa Fluor 647 conjugate	Invitrogen (Carlsbad, CA, USA)
Xylene	Carl Roth (Karlsruhe, Germany)
Yeast tRNA	Sigma-Aldrich (St. Louis, MO, USA)

Table 5: Kits

Kit	Manufacturer
Apo-ONE Homogeneous Caspase-3/7 Kit	Promega (Madison, WI, USA)
BrdU Flow Kit	BD Biosciences (Heidelberg, Germany)
CytoTune-iPS Sendai Reprogramming Kit	Life Technologies (Carlsbad, CA, USA)
Direct-zol RNA Microprep	Zymo Research (Freiburg, Germany)
Direct-zol RNA Miniprep	Zymo Research (Freiburg, Germany)
Gateway LR Clonase II Enzyme Mix	Invitrogen (San Diego, CA, USA)
In Situ Cell Death Detection Kit TMRed	Roche (Basel, Switzerland)
Magna RIP RNA-Binding Protein Immunoprecipitation Kit	Millipore (Billerica, MA, USA)
Neonatal Heart Dissociation Kit	Miltenyi Biotec (Bergisch Gladbach, Germany)
Plasmid Maxi Kit	Qiagen (Hilden, Germany)
QIAprep Spin Miniprep Kit	Qiagen (Hilden, Germany)
QIAquick PCR Purification Kit	Qiagen (Hilden, Germany)
RNase-Free DNase Set	Qiagen (Hilden, Germany)
RNeasy Micro Kit	Qiagen (Hilden, Germany)
RNeasy Mini Kit	Qiagen (Hilden, Germany)
TruChIP Chromatin Shearing Kit	Covaris (Woburn, MA, USA)
TruSeq RNA Sample Preparation Kit	Illumina (San Diego, CA, USA)

Table 6: Plasmids

Plamid name	Manufacturer
pCMVΔR8.91	Thermo Fisher (Waltham, MA, USA)
pENTR4	Invitrogen (San Diego, CA, USA)
pKLV2.2	Addgene (Watertown, MA, USA)
pLenti4/V5	Invitrogen (San Diego, CA, USA)
pLentiCRISPRv2_neo	Addgene (Watertown, MA, USA)
pMD2.G	Addgene (Watertown, MA, USA)
psPAX2	Addgene (Watertown, MA, USA)

Table 7: Enzymes

Enzyme name	Manufacturer
AsiSI	New England Biolabs (Frankfurt, Germany)
Chondroitinase ABC	Sigma-Aldrich (St. Louis, MO, USA)
Collagenase II	Merck (Darmstadt, Germany)
Dispase II	Life Technologies (Darmstadt, Germany)
DNase I (grade II)	Sigma-Aldrich (St. Louis, MO, USA)
DsDNA Shearase Plus	Zymo Research (Freiburg, Germany)
Liberase Blendzyme 1	Roche (Basel, Switzerland)
LR clonase	Invitrogen (San Diego, CA, USA)
MultiScribe reverse transcriptase	Thermo Fisher (Waltham, MA, USA)
MuLV reverse transcriptase	Applied Biosystems (Foster City, CA, USA)
Proteinase K	Diagenode (Seraing, Belgium)
Proteinase K	New England Biolabs (Frankfurt, Germany)
RNase H	New England Biolabs (Frankfurt, Germany)
RNase inhibitor	Applied Biosystems (Foster City, CA, USA)

Table 8: Antibodies

Antibody	Species	Manufacturer	Catalog number	Use
Alexa Fluor 488-rabbit IgG	Goat	Invitrogen	A-11088	Histological staining
Alexa Fluor 555-rabbit IgG	Goat	Invitrogen	A-21428	Histological staining
BrdU-V450	Mouse	BD Biosciences	560810	Cell staining for flow cytometry
DNA-RNA hybrids (S9.6 antibody)	Mouse	Kerafast	ENH001	RNA and chromatin immunoprecipitation
Human acetylated histone H3K27	Rabbit	abcam	4729	RNA immunoprecipitation
Human CRIP2	Rabbit	Novus Bio	NBP2-59094	RNA immunoprecipitation
Human histone H3	Rabbit	abcam	1791	RNA immunoprecipitation
Human p300	Mouse	active motif	61401	RNA immunoprecipitation
Mouse CD31	Rat	ThermoFisher Scientific	14-0311-82	Endothelial cell isolation
Mouse IgG	Mouse	Santa Cruz	2025	RNA immunoprecipitation
Mouse phospho-histone H3 (Ser10)	Rabbit	Merck	6570	Histological staining
Phospho-histone H2AX (Ser139)	Mouse	Merck	05-636	Histological staining
Rabbit IgG	Rabbit	Diagenode	15410206	RNA and chromatin immunoprecipitation
Rabbit IgG	Rabbit	Millipore	12-370	RNA immunoprecipitation

Table 9: Bacterial Media

Medium	Composition	Manufacturer
LB agar capsules	1 % tryptone, 0.5 % yeast extract, 1 % NaCl, 1.5 % agar B	MP Biomedicals (Irvine, CA, USA)
LB medium capsules	1 % tryptone, 0.5 % yeast extract, 1 % NaCl; pH = 6.7	MP Biomedicals (Irvine, CA, USA)
SOC medium	2 % tryptone, 0.5 % yeast extract, 10 mM NaCl, 2.5 mM KCl, 10 mM $MaCl_2$, 10 mM $MgSO_4$, 20 mM glucose	Invitrogen (San Diego, CA, USA)

Table 10: Cell Culture Solutions and Supplements

Product	Manufacturer
2,3-butanedione monoxime	Sigma-Aldrich (St. Louis, MO, USA)
Aprotinin	Sigma-Aldrich (St. Louis, MO, USA)
AutoMACS Rinsing Solution	Miltenyi Biotec (Bergisch Gladbach, Germany)
Bovine collagen type I	Sigma-Aldrich (St. Louis, MO, USA)
Bovine serum albumin (BSA)	CarlRoth (Karlsruhe, Germany)
Claycomb medium	Sigma-Aldrich (St. Louis, MO, USA)
Desferrioxamine (DFO) mesylate	Sigma-Aldrich (St. Louis, MO, USA)
Dimethyl sulfoxide (DMSO)	Sigma-Aldrich (St. Louis, MO, USA)
Distilled water	Sigma-Aldrich (St. Louis, MO, USA)
DMEM high glucose	BioConcept (Allschwil, Switzerland)
DMEM low glucose with GlutaMAX	Life Technologies (Carlsbad, CA, USA)
EGM single quots	Lonza (Verviers, Belgium)
Endothelial basal medium (EBM)	Lonza (Verviers, Belgium)
Fetal Bovine Serum (FBS)	Invitrogen (San Diego, CA, USA)
Fibronectin from human plasma (0.1 % solution)	Sigma-Aldrich (St. Louis, MO, USA)
Gelatin (0.1 % solution)	Millipore (Billerica, MA, USA)
GeneJuice transfection reagent	Millipore (Billerica, MA, USA)
Glucose	Sigma-Aldrich (St. Louis, MO, USA)
GlutaMAX	Life Technologies (Carlsbad, CA, USA)
Insulin, human	Sigma-Aldrich (St. Louis, MO, USA)
Hank's Balanced Salt Solution with Ca^{2+} and Mg^{2+} ($HBSS^{+/+}$)	Life Technologies (Carlsbad, CA, USA)
HEPES	Invitrogen (San Diego, CA, USA)
Horse serum (HS)	BioConcept (Allschwil, Switzerland)
L-Ascorbic acid	Sigma-Aldrich (St. Louis, MO, USA)
L-Glutamine	Sigma-Aldrich (St. Louis, MO, USA)
Lipofectamine 2000	Invitrogen (San Diego, CA, USA)
Lipofectamine RNAiMAX	Invitrogen (San Diego, CA, USA)
M199	Sigma-Aldrich (St. Louis, MO, USA)
M199 with Earle's Balanced Salts (EBS)	BioConcept (Allschwil, Switzerland)
Myocyte Growth Medium	PromoCell GmbH (Heidelberg, Germany)
Norepinephrine bitartrate salt	Sigma-Aldrich (St. Louis, MO, USA)
Opti-MEM	Invitrogen (San Diego, CA, USA)
Penicillin/streptomycin (500x)	Roche (Basel, Switzerland)
Phenol red	Sigma-Aldrich (St. Louis, MO, USA)
Poly-L-lysine	Sigma-Aldrich (St. Louis, MO, USA)
Rat tail collagen type I	Millipore (Billerica, MA, USA)
Red Blood Cell Lysis Solution	Miltenyi Biotec (Bergisch Gladbach, Germany)
ROCK inhibitor Y-27632	Sigma-Aldrich (St. Louis, MO, USA)
RPMI medium	Sigma-Aldrich (St. Louis, MO, USA)
Sodium pyruvate	Life Technologies (Paisley, UK)
Supplement Mix C	PromoCell GmbH (Heidelberg, Germany)
Taurine	Sigma-Aldrich (St. Louis, MO, USA)
Trypsin-EDTA, 2.5 %	Life Technologies (Carlsbad, CA, USA)
Vascular endothelial growth factor, human (VEGF)	R&D Systems GmbH (Wiesbaden, Germany)

Table 11: Drugs

Substance	Trade name	Manufacturer
Ampicillin	Ampicillin ratiopharm	Ratiopharm (Ulm, Germany)
Bupivacaine	Bupivacain 0.25 %	Jenapharm (Jena, Germany)
Buprenorphine	Temgesic	Schering-Plough (Kenilworth, NJ, USA)

Carprofen	Rimadyl	Zoetis (Berlin, Germany)
Dexpanthenole	Bepanthen eye and nose ointment	Bayer (Leverkusen, Germany)
Iodine and potassium iodide	Iodine tincture Hetterich	Teofarma Srl. (Valle Salimbene, Italy)
Isoflurane	Forene	AbbVie (Wiesbaden, Germany)

Table 12: Bacteria

Strain	Manufacturer
One Shot Stbl3 chemically competent *E. coli*	Invitrogen (San Diego, CA, USA)
One Shot TOP10 chemically competent *E. coli*	Invitrogen (San Diego, CA, USA)

Table 13: Primary Cells and Cell Lines

Name	Species	Source	Supplier
HEK293FT	*Homo sapiens*	Kidney	Clontech (Mountain View, CA, USA)
HL-1	*Mus musculus*	Heart	Prof. W. Claycomb (New Orleans, LA, USA)
Human cardiomyocytes (hCM)	*Homo sapiens*	Heart	PromoCell (Heidelberg, Germany)
Human umbilical vein endothelial cells (HUVEC)	*Homo sapiens*	Umbilical cord	Lonza (Verviers, BEL)

Table 14: Animals

Species	Strain	Age	Supplier
Mouse	C57BL/6	8 weeks, 12 weeks, 18 months	Charles River Laboratories (Sulzfeld, Germany)
Rat	Sprague Dawley	1 day	Charles River Laboratories (Sulzfeld, Germany)
Rat	Wistar-Kyoto	20 weeks	Charles River Laboratories (Barcelona, Spain)
Rat	ZSF1 lean	20 weeks	Charles River Laboratories (Barcelona, Spain)
Rat	ZSF1 obese	20 weeks	Charles River Laboratories (Barcelona, Spain)

Table 15: Human Primers for qRT-PCR

Primer name	Pimer forward sequence	Primer reverse sequence
GAPDH	ATGGAAATCCCATCACCATCTT	CGCCCCACTTGATTTTGG
RPLP0	TCGACAATGGCAGCATCTAC	ATCCGTCTCCACAGACAAGG
Sarrah	CCTGGACTGCGTTCACGTTT	CTGCAAGCCTTGTTGCTCAC
VEGF	CCCTGATGAGATCGAGTACA	AGCAAGGCCCACAGGGATTT
OXCT1	GCAACAATGCAGGGGTTGAC	ATCCTCTCTGCAAGTGTGCC
FBXO4	GCCGGTACAGTGTGATTCCA	CAGCCTCTGTATCCTGGACTTTTA
c5orf51	GTGTGGTGAGACGAGTGGAA	AAGTGATCATCTTCACCGGCA
CHMP4C	AGAAAACCAGGCATGTCGTC	CCCAAGCTGCCAATTGTTTG
ZNF280A	TGAAGAGACCAGTGGCTTCA	GTACATGCTCCACCCCAACA
GPRC5A	GAAGCAGCACCAAGTTCACG	CTGTTGGAGTCCTGCACCTT
BEX1	GCTGGTGAATACTGTGTGCC	ATCCTTGCCTGTGGTTCTCC
SPINK1	TGCACCAAGATATATGACCCTGT	GTTCTCAGCAAGGCCCAGAT
GPC6	TCACTCGGCCTGACACTTTC	AACTCAAACTCCGTGGGACA
DPYD	GATGCCCCGTGTCAGAAGAG	AATGGGTCCCTCTTCAGTGG
PSD3	AGGAGAAAGCTAACGGAACACA	TCCGAGCCAAGAATCCACTT
KMT2C	AGAACCCAGCTGAAGGACTG	GTCCGTTTGCTTCGCTGTTT
NEK10	CTTTGGCCTGGCAAAGCAAA	CCCCATACGGCTCACTCTTC

PDE3A	GCAGACCCTTCTCTTCCACC	ACTCGTCTCAACAAGCCAGG
ITPR2	GCCAACCCTCCCAAGAAGTT	TGTGGTTCCCTTGTTTGGCT
PARP8	GGGGATGTGTTCAAGGCAAG	GCAGTCCTTCTCAGCTCTGG
SSBP2	TGGGATCTCTACTGTGCAGC	CTAGCACTGGACTGGGAGC
U4 snRNA	GCCAATGAGGTTTATCCGAGG	TCAAAAATTGCCAATGCCG
GAPDH promoter	TGGTGTCAGGTTATGCTGGGCCAG	GTGGGATGGGAGGGTGCTGAACAC
GPC6 promoter	TGTTGCTTCTGTGGTCTGGT	ATGGGTGGCAGAGCACAATC
PDE3A promoter	CTGAAGTAGGAAGAGACCCCG	CGGGCAGAAACGATCAGGAT
ITPR2 promoter	AGTAGGAAGAGACCCCGGAG	AAGGCTAGCACGCTCAAGTT
PARP8 promoter	GGCTTGAACCTGTCCTACCC	TCCACTGCAGCCTTTGATGT
SSBP2 promoter	TTCCACACACACACAGCTTT	TCTCGACCTCTCACTTTTGCT

Table 16: Mouse Primers for qRT-PCR

Primer name	Pimer forward sequence	Primer reverse sequence
GAPDH	CATCTGAGGGCCCACTGAAG	GTTGCTGTTGAAGTCGCAGG
RPLP0	GCGTCCTGGCATTGTCTGT	GAAGGCCTTGACCTTTTCAGTAA
Sarrah	GCCCAATGGCTGATAGTGTT	GTGGAGACCCAGAGCAGAAG
VEGF	CACGACAGAAGGAGAGCAGA	GGCAGTAGCTTCGCTGGTAG
Oxct1	GGACGGCATGTACGCTAACT	TCCGCATCAGCTTCGTCTTT
Fbxo4	TCAGCCTACAGAGTGAGGGG	TTGCCATTCATGACGTCGGT
Cdh5	AGCGCAGCATCGGGTACT	TCGGAAGAATTGGCCTCTGT
Tnnt2	TGAAGAAGCCAAAGATGCTG	CCTGCTGGGCTTGGGTTT
GPC6	GACAGTGGGCAGAGAGGTTG	AAGGTCTCACAGTGGGCAAG
PDE3A	TCCAAGCGCCTGAGAAGAAG	GGCAGAGGTGGTAGTTGTCC
ITPR2	CCTGACGGTGAACAAGAGGT	TGCAGCATCCAGTGACACTC
PARP8	GGGGAGGAGTCAAGGCAAAA	GCTGAGGGTGCTTGTGTAGT
SSBP2	TGCCTGGAATGAACATGGGT	AGGAGACGCTGAGGAGTAGG
Sarrah TH region	CTGGAACCGGAGTCCCAAC	CGAGGAGGAGAGGAGACAGAC
Antisense probe pos. ctrl.	CCAAATCGCCCTCTGGAATGA	GAGTTGTGGGTGTTGGGGTT
Antisense probe 1	GGAGCCTGGAGTCTGTAGGA	AGGCTCTGTGTACCAAAGCC
Antisense probe 2	GGAGCCTGGAGTCTGTAGGA	GTCGAGGCTCTGTGTACCAA
Antisense probe 3	CAGATGCCAGATCCCCGAC	CGGCTCTCAAACTCCTGTCC
Antisense probe 4	GCAAGGCTTGGCATCAACC	AGAGAGTTGTGGGTGTTGGG
Antisense probe 5	TTCCAAATCGCCCTCTGGAA	GTGGGTGTTGGGGTTGAGAA
Antisense probe 6	TTCTCAACCCCAACACCCAC	TCATGAGGGTCAGTCAGCAC
Antisense probe 7	GTGCTGACTGACCCTCATGA	GGACTCCGGTTCCAGGAAAA
Antisense probe 8	GGCAAGAGGCTCTAAGAAAGCA	GTTTCATGGATCTCTCTAGGCACA

Table 17: Rat Primers for qRT-PCR

Primer name	Pimer forward sequence	Primer reverse sequence
HPRT1	CCTCCTCCGCCAGCTT	GTCATAACCTGGTTCATCATCACT
Sarrah	TAGGGGAAGGCAGGCATTTG	AGAAGCTAGACAGGGAGGGG

Table 18: Locked Nucleic Acid (LNA) GapmeRs for Cell Transfection

LNA GapmeR name	LNA GapmeR sequence
GapmeR negative control A	AACACGTCTATACGC
Mouse GapmeR Sarrah	TTGGAAAGGTGAGCTG
Human GapmeR Sarrah	GGTTGCATCTTTAGTA

Rat GapmeR Sarrah	TGAAGGTCGCCAATCC

Table 19: SiRNAs for Cell Transfection

SiRNA name	SiRNA forward sequence	SiRNA reverse sequence
siRNA firefly luciferase GL2	CGUACGCGGAAUACUUCGA[dT][dT]	UCGAAGUAUUCCGCGUACG[dT][dT]
siSarrah_1 (mouse)	UUCUGCCGAAAGUAUCCAG[dT][dT]	CUGGAUACUUUCGGCAGAA[dT][dT]
siSarrah_2 (mouse)	UCCCAAUGCUCCUUAUCUC[dT][dT]	GAGAUAAGGAGCAUUGGGA[dT][dT]
siOXCT1 (mouse)	GAGUUUAACGGUCAGCACU[dT][dT]	AGUGCUGACCGUUAAACUC[dT][dT]
siGPC6 (human)	CUCCGUGUGAUGACCAACAAA[dT][dT]	UUUGUUGGUCAUCACACGGAG [dT][dT]
siPDE3A (human)	UACAGUGAGGUACAUUGUUAA[dT][dT]	UUAACAAUGUACCUCACUGUA[dT][dT]
siITPR2 (human)	UACAGUAAUGUUAUACAACUA[dT][dT]	UAGUUGUAUAACAUUACUGUA[dT][dT]
siPARP8 (human)	AUCCCUUACUGCAAUGGGUUA[dT][dT]	UAACCCAUUGCAGUAAGGGAU[dT][dT]
siSSBP2 (human)	CGGGUCCAAAUGUGAUUCAAA[dT][dT]	UUUGAAUCACAUUUGGACCCG[dT][dT]

Table 20: Oligonucleotides for Nuclear Magnetic Resonance Experiments

Oligonucleotide name	Nucleic acid type	Oligonucleotide sequence
human Sarrah TH	RNA	CCCCCUUCUCUUCUC
human GPC6 promoter_s	DNA	CACCTCCCTTCCCCC
human GPC6 promoter_as	DNA	GGGGGAAGGGAGGTG
mouse Sarrah TH	RNA	UGUCUCCUCUCCUCC
mouse GPC6 promoter_s	DNA	AGAAAGGAGGGGAGG
mouse GPC6 promoter_as	DNA	CCTCCCCTCCTTTCT

Table 21: SgRNAs for CRISPR/Cas9-Mediated Genome Editing

SgRNA name	SgRNA sequence #1	SgRNA sequence #2
sgRNA mock	TCAACCCCAGCGCACCGTTG	GCAATGCAATCGCAGGAGCA
sgRNA SarrahΔTH	TGTTGTATAATTCCCCTCAC	GAGTCCCAACAATTCCAGAA

Table 22: 2'O-Methyl-RNA Probes for RNA Affinity Purification

Probe name	Probe sequence
scrambled	mAmGmUmGmUmUmAmCmGmGmUmCmGmAmCmCmAmAmCmAmA-iSp9-rArCrGrArUrC-3deSBioTEG
Sarrah antisense #5	mAmGmGmAmGmAmAmUmCmUmUmUmAmUmCmAmGmUmGmAmCmC-iSp9-rArCrGrArUrC-3deSBioTEG
Sarrah antisense #8	mUmUmUmCmAmUmGmGmAmUmCmUmCmUmCmUmAmGmGmCmA-iSp9-rArCrGrArUrC-3deSBioTEG

Table 23: Software and Web Tools

Name	Provider	Use
Andromeda	Mattias Mann (Max-Planck-Institute of Biochemistry Martinsried, Germany)	Identification of mass spectrometry peptide sequences by fragmentation spectra

ApE 2.0.49	M. Wayne Davis (University of Utah, USA)	Sequence alignment
AxioVision SE64 Rel. 4.9.1	Zeiss (Jena, Germany)	Histological image acquisition
Azimuth 2.0	Microsoft Research (Redmond, WA, USA)	SgRNA design
CPAT	Wei Li (Mayo Clinic College of Medicine, Rochester, MN, USA)	Sarrah coding potential assessment
Cufflinks 2.1	Cole Trapnell (University of Washington, USA)	RNA deep sequencing data analysis
Database for Annotation, Visualization and Integrated Discovery (DAVID) 6.7	Laboratory of Human Retrovirology and Immunoinformatics (LHRI)	Gene ontology analysis
EHT Technologies software	EHT Technologies	EHT contractility analysis
Ensembl Genome Browser	Ensembl Project	Sequence download for primer design
Excel 2013	Microsoft Office	Analysis of qRT-PCR, caspase assay and other data
FACSDiva	BD Biosciences (Erembodegen, Belgium)	Flow cytometry data acquisition
FASTA Sequence Comparison software	University of Virginia, USA	Sequence homology analysis
GraphPad Prism 5	GraphPad Software	Statistical data analysis
Image Lab 5.2.1	Bio-Rad (Munich, Germany)	Agarose and silver gel image acquisition
ImageJ 1.4.3.67	Wayne Rasband (NIH, Bethesda, MD, USA)	Histological image analysis
IonWizard	IonOptix (Westwood, MA, USA)	Cardiomyocyte contractility measurement
MaxQuant 1.6.1.0	Computational Systems Biochemistry	Mass spectrometry data analysis
MatLab R2014a	MathWorks (Natick, MA, USA)	Magnetic resonance image analysis
NanoDrop 2000/2000c software	Thermo Fisher (Waltham, MA, USA)	Nucleid acid concentration measurement
Perseus 1.6.1.3	Computational Systems Biochemistry	Mass spectrometry data analysis
Primer3 4.1.0	ELIXIR	qRT-PCR primer design
QuantStudio Real-Time PCR	Applied Biosystems (Foster City, CA, USA)	Acquisition of qRT-PCR data
Segment 1.8	Medviso (Lund, Sweden)	Magnetic resonance image analysis
SnapGene	GSL Biotech LLC (Chicago, IL, USA)	*In silico* restriction digest and cloning
Stellaris Probe Designer	Biosearch Technologies (Novato, CA, USA)	RNA affinity purification probe design
StepOne 2.3	Applied Biosystems (Foster City, CA, USA)	Acquisition of qRT-PCR data
Triplex Domain Finder	Ivan G. Costa (RWTH Aachen University, Germany)	Prediction of triplex formation between Sarrah and gene promoters
UCSC Genome Browser	UC Santa Cruz	Sequence alignment and *in silico* PCR
Vevo LAB 1.7.0	VisualSonics (Toronto, Canada)	Echocardiographic data acquisition and analysis
ZEN 2.3 lite	Zeiss (Jena, Germany)	Histological image analysis

3.2 Methods

3.2.1 Cell Culture

3.2.1.1 Cell Cultivation

Cells of the murine atrial cardiomyocyte cell line HL-1 were obtained from William Claycomb's laboratory (New Orleans, LA, USA) and cultured in Claycomb medium (Sigma-Aldrich) supplemented with 10 % fetal bovine serum (FBS; Invitrogen), 100 µg/ml penicillin/streptomycin (Roche), 0.1 mM norepinephrine (Sigma-Aldrich) and 2 mM GlutaMAX (Thermo Fisher) in flasks coated for at least 30 min at 37 °C with 0.02 % gelatin (Millipore) and 0.1 % fibronectin from human plasma (Sigma-Aldrich). Primary ventricular human cardiomyocytes (hCMs) were purchased from PromoCell and cultured in Myocyte Growth Medium (PromoCell) with the supplier's Supplement Mix C and 100 µg/ml penicillin/streptomycin. HEK293FT (HEK) cells were purchased from Clontech and cultured in Dulbecco's Modified Eagle's Medium (DMEM) with low glucose and GlutaMAX (Life Technologies) supplemented with 10 % heat-inactivated FBS (30 min at 56 °C), sodium pyruvate (Life Technologies) and 100 µg/ml penicillin/streptomycin. Human umbilical vein endothelial cells (HUVECs) were purchased from Lonza and cultured in endothelial basal medium (EBM) supplemented with 10 % FBS (Invitrogen) and EGM SingleQuots (Lonza) containing bovine brain extract, hydrocortisone, epidermal growth factor, gentamycin sulfate, ascorbic acid and amphotericin B. All cells were cultured at 37 °C and 5 % CO_2.

3.2.1.2 Co-Cultivation of HCMs and HUVECs

For co-culturing hCMs with HUVECs, hCMs were seeded on transwell inserts with 1 µM pore size (Greiner Bio-One) in full Myocyte Growth Medium. HUVECs were seeded in cell culture plates and cultured in full EBM. 24 h after HUVECs were seeded, inserts with hCMs were washed with phosphate-buffered saline (PBS) and transferred to cell culture plates with HUVECs so that both were cultured in full EBM. Experiments were performed after 48 h of co-cultivation. Alternatively, Myocyte Growth Medium on hCMs was replaced with EBM 4 h after locked nucleic acid (LNA) GapmeR transfection and conditioned EBM from hCMs was transferred to HUVECs 48 h after transfection and incubated for 24 h before HUVECs were used for downstream applications.

3.2.1.3 Cell Splitting and Seeding

For splitting and seeding, cells were washed with PBS, detached using trypsin-EDTA (Life Technologies) for 3 min (10 min for HL-1 cells) at 37 °C, pelletted in a 1:1 mixture of trypsin-EDTA and growth medium

at 500 g for 5 min and resuspended in growth medium. At confluency, HL-1 cells and hCMs were split 1:5 and 1:4, respectively, for passaging. For seeding, cells were counted with a NucleoCounter NC-200 (ChemoMetec). Cells were seeded in cell culture plates and dishes at the densities listed in table 24.

Table 24: Cell Seeding Densities

Format	HL-1 cell number	hCM number	HUVEC number
6 cm-dish	750,000	400,000	
6-well plate	300,000	200,000	100,000
12-well plate	125,000	100,000	
24-well plate	65,000	50,000	
96-well plate	12,000	7,000	

3.2.1.4 Induction of Hypoxia and Cell Transfection

For induction of hypoxia, cells were cultured at 1 % (HL-1 cells) or 0.2 % (hCMs) O_2 at 37 °C and 5 % CO_2 for 24 h or treated with 300 µM desferrioxamine (DFO) mesylate (Sigma-Aldrich) for 24 h. For transfection, cells were seeded as specified in table 24 and grown for 24 h until reaching approximately 70 % confluency. Medium was changed to Claycomb medium supplemented with 10 % fetal bovine serum and 2 mM glutamine (HL-1 cells) or full Myocyte Growth Medium (hCMs) before transfection. Cells were transfected with 100 nM (HL-1 cells) or 25 nM (hCMs) LNA GapmeRs (Exiqon; table 18) or 50 nM small interfering RNAs (siRNAs; Qiagen; table 19) using lipofectamine RNAiMAX (Thermo Fisher). Briefly, 0.45 % (v/v) of RNAiMAX were added to 7.5 % (v/v) serum-reduced Opti-MEM medium (Life Technologies), mixed and incubated for 5 min at room temperature (RT). GapmeRs or siRNAs were added to 7.5 % (v/v) of Opti-MEM, mixed with RNAiMAX in Opti-MEM and incubated for 20 min at RT before addition to the cells. 100 % refer to total culture volume. Same concentrations of LNA GapmeR negative control A (Exiqon) and siRNA against firefly luciferase (Sigma-Aldrich) were used as controls. Experiments were performed 48 h after transfection unless otherwise indicated.

3.2.1.5 Virus Particle Production

For production of lentiviral particles from pLenti4 constructs, HEK cells were cultured to reach 70 % confluency in T175 flasks on the day of transfection. 47 µl GeneJuice (Millipore) were added to 1,853 µl Opti-MEM, mixed and incubated at RT for 10 min. 8 µg overexpression plasmid (pLenti4-mock or pLenti4-hSarrah), 2 µg of packaging plasmid pMD2.G and 6 µg of packaging plasmid pCMVΔR8.91 were diluted in 100 µl Opti-MEM, mixed with GeneJuice in Opti-MEM and incubated at RT for 20 min. The transfection mix was added to HEK cells in 18 ml full growth medium. 12 h after transfection, medium was changed to fresh full growth medium. 36 h and 60 h after transfection, medium was collected,

pooled and virus particles were concentrated by centrifugation at 690 g using Amicon filter devices (Millipore).

For production of mixed lentiviral particles from pKLV2.2 and pLentiCRISPRv2_neo constructs, 1,000,000 HEK cells were seeded in wells of a 6-well-plate for transfection in the evening. 21 µl Lipofectamine 2000 (Invitrogen) were added to 179 µl Opti-MEM and mixed. 1.65 µg of each overexpression plasmid (pKLV2.2-mock or pKLV2.2-SarrahΔTH and pLentiCRISPRv2_neo), 2.7 µg of packaging plasmid pPAX2 and 1 µg of packaging plasmid pMD2.G were added directly afterwards and the mixture was incubated at RT for 30 min. The transfection mix was added to HEK cells in 2 ml full growth medium. 12 h after transfection, medium was changed to fresh full growth medium. 36 h and 60 h after transfection, medium containing virus particles was collected and pooled.

3.2.1.6 Cell Transduction

250,000 hCMs per T25 flask were transduced with pLenti4 constructs; 150,000 HL-1 cells per well were transduced in 6-well-plates with a pKLV2.2 construct together with a pLentiCRISPRv2_neo construct. 250 µl of pLenti4 concentrated lentiviral supernatant (hCMs) or 250 µl of pKLV2.2/pLentiCRISPRv2_neo lentiviral supernatant (HL-1) were added to the cells in 3 ml or 2 ml growth medium, respectively. Cells were washed three times with PBS and three times with growth medium in alternating order 24 h and 72 h after transduction and used for downstream applications six days (HL-1) or ten days (hCMs) after transduction. Cells were not selected resulting in a cell pool of wildtype cells and mutant cells.

3.2.1.7 Differentiation of Human Induced Pluripotent Stem Cells to Cardiomyocytes

Human induced pluripotent stem cells (hiPSCs) were differentiated into cardiomyocytes as described elsewhere[293] by Marc Hirt and Kaja Yorgan (Department of Experimental Pharmacology and Toxicology, University Medical Center Hamburg-Eppendorf, Germany). The differentiation procedure is an imitation of distinct stages of embryonic development and mesodermal germline commitment. Briefly, hiPSCs were obtained by reprogramming of fibroblasts from a healthy donor with Yamanaka factors using the Sendai virus based Kit (CytoTune, Life Technologies). HiPSCs were expanded under hypoxic conditions for seven days and dissociated into single cells. Subsequently, cells were cultured overnight in stirred spinner flasks with glass bulb impellers to propagate spontaneous formation of embryoid bodies. Mesoderm was induced by addition of the cytokines bFGF, BMP-4 and activin A in an RPMI-based medium composition under hypoxic conditions over three days. Cardiac differentiation was conducted under normoxic conditions with the IWR-1 analog and WNT antagonist DS-I-7 for three days and additional insulin from day 4. Onset of spontaneous beating was observed between days 8

and 10. The WNT antagonist was omitted after day 11. After 17 days, hiPSC-cardiomyocytes were dissociated into single cells and used for generation of engineered heart tissue (EHT) organoids.

3.2.2 Molecular Biology

3.2.2.1 RNA Isolation

Total ribonucleic acid (RNA) was isolated using the RNeasy Micro or Mini Kit combined with the RNase-Free DNase Set by Qiagen (cellular and tissue samples; phenol-chloroform extraction method) or the Direct-zol RNA MicroPrep or MiniPrep Kit by Zymo Research (cellular samples; Direct-zol™ method without phase separation or nucleic acid precipitation) according to manufacturers' instructions. Adherent cells were washed with PBS before lysis and detachment with QIAzol (Qiagen). Pelleted cells were resuspended in small volumes of PBS before lysis in QIAzol. Tissue samples were immersed in QIAzol directly after collection and homogenized using ceramic spheres (MP Biomedicals) and the FastPrep24 homogenizer (MP Biomedicals) for 20 s at 20 m/s twice prior to RNA isolation. DNase digestion was performed during all RNA extractions. RNA was eluted in 15 to 50 µl water and stored at -80 °C.

3.2.2.2 Nucleic Acid Concentration Measurement

RNA and deoxyribonucleic acid (DNA) concentrations were determined in ng/µl using the spectrophotometer NanoDrop 2000 (Thermo Fisher). The spectrophotometer was blanked with 1 µl of the respective solvent (water in case of RNA, water or elution buffer in case of DNA) before 1 µl of RNA or DNA solution was added onto the optical pedestal, which was wiped after every measurement.

3.2.2.3 Reverse Transcription of RNA

100 to 1,000 ng of total RNA were reversely transcribed into complementary DNA (cDNA) using 50 units of MulV (Applied Biosystems) or MultiScribe reverse transcriptase (Thermo Fisher). For samples from RNA affinity purification and RNA immunprecipitation experiments, equal volumes of isolated RNA were used for reverse transcription (1 µl of input samples, 10 µl of all other samples). 400 ng of random hexamer primers (Thermo Fisher), 1x PCR Buffer (Thermo Fisher), 5 mM $MgCl_2$ (Thermo Fisher), 1 mM of each dNTP (dATP, dCTP, dGTP and dTTP; Thermo Fisher) and 10 units RNase inhibitor (Thermo Fisher) to inhibit RNase activity were added to the reaction that was performed at 20 °C for 10 min, 43 °C for 75 min and 95 °C for 5 min. For RNA affinity purification and RNA immunprecipitation

experiments, a negative control without reverse transcriptase was included. Reversely transcribed cDNA was diluted to 2.5 to 5 ng/µl in water and stored at -20 °C.

3.2.2.4 Quantitative Real-Time PCR

To determine messenger RNA (mRNA) or long non-coding RNA (lncRNA) levels, quantitative real-time polymerase chain reaction (qRT-PCR) with 6.25 to 25 ng cDNA per reaction as template was performed with Fast SYBR Green Master Mix (Applied Biosystems) in StepOne Plus (10 µl Fast SYBR Green Master Mix per reaction, final volume of 20 µl) or Viia 7 instruments (5 µl Fast SYBR Green Master Mix per reaction, final volume of 10 µl; both Applied Biosystems). Forward and reverse primers were designed using the freely available web tool Primer3 4.1.0 with RNA sequences from the Ensembl Genome Browser as template and checked for specificity using the *in silico* polymerase chain reaction (PCR)-tool of the UCSC Genome Browser. Primers (tables 15 to 17) were purchased from Sigma-Aldrich as DNA oligonucleotides and added to the qRT-PCR at a final concentration of 1 mM. Reactions were performed in triplicates. Negative controls with water instead of cDNA were included in duplicates for every primer pair. Relative gene expression levels were analyzed using to the $2^{-\Delta CT}$ method, according to which housekeeping gene levels are substracted from the levels of the gene of interest for normalization. Glyceraldehyde-3-phosphate dehydrogenase (GAPDH; human and mouse), ribosomal protein, large, P0 (RPLP0; human and mouse) or hypoxanthine-guanine phosphoribosyltransferase 1 (HPRT1; rat) were used as housekeeping genes. Threshold was set to 0.4 (StepOne Plus) or 0.2 (Viia 7) for comparability between experiments. For analysis of Sarrah levels in RNA affinity purification experiments, the baseline start cycle was increased from 3 to 5.

3.2.2.5 RNA Accessibility Assay

To identify accessible Sarrah regions in HL-1 cells in order to design probes for RNA affinity purification, an RNA accessibility assay was performed by RNase H-mediated cleavage of DNA-RNA hybrids. Probes were designed using the Stellaris Probe Designer and purchased as DNA oligonucleotides from Sigma-Aldrich. Two confluent T75 flasks of HL-1 cells were washed twice with cold PBS, detached by scraping in 1 ml PBS and pelleted at 500 g for 5 min at 4 °C. Cells were lysed for 30 min on ice in lysis buffer (50 mM Tris, 150 mM NaCl, 0.5 % NP-40, 1x protease inhibitor; pH = 8) and centrifuged at 21,000 g for 8 min at 4 °C. The supernatant was adjusted to a pH of 8.3 and final concentrations of 60 mM NaCl, 50 mM Tris, 75 mM KCl, 3 mM $MgCl_2$ and 10 mM DTT in a volume of 1.5 ml. 3 µl RNase inhibitor were added. 100 pmol of probe as DNA oligonucleotide were added to 100 µl of adjusted supernatant and incubated for 2 h at 4 °C under rotation. Supernatant without any probe was used as negative control

while supernatant with the murine LNA GapmeR sequence targeting Sarrah as DNA oligonucleotide was used as positive control. Subsequently, 2.5 units of RNase H (NEB) were added and incubated for 20 min at 37 °C and 350 rotations per minute (rpm) to induce RNase H-mediated cleavage of DNA-RNA hybrids. QIAzol (Qiagen) was added to all samples for RNA isolation.

3.2.2.6 RNA Affinity Purification

To identify proteins interacting with Sarrah, RNA affinity purification followed by mass spectrometry analysis was performed. DNA or Protein LoBind tubes (Eppendorf) were used during all steps. Two confluent 15 cm-dishes of HL-1 cells were washed with cold PBS, detached by scraping in 1 ml PBS, pelleted at 500 g for 5 min at 4 °C, washed with cold PBS again and lysed in 200 µl lysis buffer per reaction (50 mM Tris, 150 mM NaCl, 1 mM EDTA, 1 % NP-40, 1x protease inhibitor; pH = 8) for 30 min on ice. After centrifuging at 21,130 g for 10 min at 4 °C, supernatants were adjusted to a pH of 8.3 and final concentrations of 150 mM NaCl, 50 mM Tris, 75 mM KCl, 3 mM $MgCl_2$, 10 mM DTT and 1x protease inhibitor in a volume of 1.1 ml per reaction. 8 µl RNase inhibitor were added per reaction. 10 % input was mixed with 300 µl QIAzol (Qiagen) and stored for RNA isolation. For binding of RNA-protein complexes, lysates were pre-cleared for 2 h at 4 °C under rotation with washed and blocked streptavidin C1 beads (Thermo Fisher; 50 µl beads per reaction; washing: three times before and after blocking with wash buffer (50 mM Tris, 150 mM NaCl, 1 mM EDTA, 0.05 % NP-40; pH = 8); blocking: for 2 h at 4 °C under rotation with yeast tRNA and glycogen, both 0.2 mg/ml) and subsequently incubated with 200 pmol 2'O-methyl-RNA probes (table 22) overnight at 4 °C under rotation. RNA-protein-complexes were captured by addition of precleared lysate-probe-mix to 100 µl washed and blocked streptavidin C1 beads for 1 h at 37 °C. Subsequently, beads were washed twice with mild wash buffer (20 mM Tris, 10 mM NaCl, 1 mM EDTA, 0.05 % NP-40; pH = 8), twice with wash buffer (50 mM Tris, 150 mM NaCl, 1 mM EDTA, 0.05 % NP-40; pH = 8), once with mass spectrometry buffer (10 mM Tris, 50 mM NaCl; pH = 7.5) and finally resuspended in 200 µl water. RNA and proteins were eluted by incubation at 95 °C for 5 min and cooling on ice. The eluate was collected and elution was repeated. Both eluates and the beads fractions resuspended in 200 µl were split for RNA isolation (16 µl) together with 10 % input, SDS gel run and silver staining (24 µl) and mass spectrometry analysis (160 µl). Samples for RNA isolation were resuspeded in 300 µl QIAzol, DNase digestion was performed during RNA extraction. Samples for SDS gel run were mixed with Laemmli buffer (final concentration: 1x) and, together with samples for mass spectrometry, shock-frozen in liquid nitrogen and stored at -80 °C.

3.2.2.7 Mass Spectrometry

Mass spectrometry and corresponding data analysis was performed by Ilka Wittig (Functional Proteomics, Goethe University Frankfurt, Germany). Proteins of RNA affinity purification samples from first elution and beads fractions were separated by Bis-Tris SDS-PAGE in a short run (2 cm). SDS gels were fixed in 50 % (v/v) methanol, 10 % (v/v) acetic acid and 10 mM ammonium acetate for 30 min. Proteins were reduced in 10 mM DTT, 50 mM ABC for 1 h at 56 °C and alkylated for 45 min in 30 mM iodoacetamid. Samples were digested for 16 h with trypsin (sequencing grade, Promega) at 37 °C in 50 mM ABC, 0.01 % Protease Max (Promega) and 1 mM $CaCl_2$. Peptides were eluted in 30 % acetonitrile and 3 % formic acid, dried and resolved in 1 % acetonitrile and 0.5 % formic acid. Liquid chromatography-mass spectrometry was performed on a Thermo Scientific™ Q Exactive Plus equipped with a Dionex Ultimate 3000 ultra-high performance liquid chromatography unit (Thermo Fisher) and a Nanospray Flex ion source (Thermo Fisher). Peptides were separated using a gradient from 4 % to 50 % acetonitrile with 0.1 % formic acid for 30 min with a flow rate 400 nl/min. Mass spectrometry data were recorded by data-dependent acquisition in profile mode. Peptide sequences were identified by their fragmentation spectra using the search engine Andromeda[294]. Data were analyzed using MaxQuant 1.6.1.0[295] and Perseus 1.6.1.3[296]. N-terminal acetylation (+42.01) and oxidation of methionine (+15.99) were set as variable modifications and carbamidomethylation (+57.02) on cysteines as fixed modification. Uniprot mouse reference proteome (February 2018, 52,538 entries) was used to identify peptides and proteins with a false discovery rate of less than 1 %.

3.2.2.8 SDS Gel Electrophoresis

Equal volumes (32 µl) of RNA affinity purification elution and beads fractions were mixed with 8 µl 4x Laemmli buffer (Bio-Rad) and incubated at 95 °C for 10 min to denature proteins. Samples were subsequently cooled on ice, loaded on Mini Protean precast SDS gels (Bio-Rad) without beads and separated by sodium dodecyl sulfate (SDS) gel electrophoresis in electrophoresis buffer (Bio-Rad; 100 mM Tris, 100 mM tricine, 0.1 % SDS; pH = 8.3) in a Protean Tetra mini gel electrophoresis setup (Bio-Rad) at 100 V constant. 15 µl PageRuler Plus Prestained Protein Ladder (Fermentas) were loaded as molecular weight marker. Gels were used for silver staining.

3.2.2.9 Silver Staining

SDS gels with separated proteins from RNA affinity purification elution and beads fractions were fixed in fixing solution (50 % (v/v) methanol, 12 % (v/v) acetic acid, 0.03 % formaldehyde) for at least 2 h. After three 15 min washing steps with 50 % ethanol, gels were incubated for 2 min in solution A

(preparation: dissolve 100 mg $Na_2S_2O_3$*5 H_2O in 500 ml water). After washing three times for 40 s in water, gels were stained for 40 min in freshly prepared solution B (preparation: dissolve 300 mg $AgNO_3$ in 125 ml water and add 100 µl 37 % formaldehyde). Washing with water was repeated and the staining was developed in solution C (preparation: dissolve 15 g Na_2Co_3 in 122 ml water and add 70 µl 37 % formaldehyde and 2.5 ml solution A) until protein bands became visible. The reaction was stopped by addition of 3 % (v/v) acetic acid for 5 min. Gels were washed twice in water for 30 min before documentation using the ChemiDoc Touch imaging system.

3.2.2.10 RNA Immunoprecipitation with Protein-Binding Antibodies

For RNA immunoprecipitation, 5 µg antibody (serotype control antibody and antibody binding protein of interest) was coupled overnight to 50 µl protein G beads (Thermo Fisher) per reaction. Beads had been blocked with blocking solution (preparation: 970 µl binding buffer, 5 µl glycogen (20 mg/ml), 5 µl BSA (20 mg/ml), 10 µl ytRNA (13 mg/ml), 10 µl 1 M DTT) at 4 °C under rotation and washed three times with binding buffer (50 mM Tris, 150 mM KCl, 10 mM $MgCl_2$, 0.05 % NP-40, 1 mM EDTA; pH = 8) before and after blocking. Two confluent 15 cm-dishes of human cardiomyocytes per condition were washed with cold PBS, detached by scraping in 1 ml PBS, pelleted at 4 °C and 500 g for 5 min and lysed in 100 µl lysis buffer per reaction (50 mM Tris, 150 mM KCl, 10 mM $MgCl_2$, 0.5 % NP-40, 1x protease inhibitor; pH = 8) for 15 min on ice. Lysates were centrifuged for 10 min at 4 °C and 12,500 g and 1 ml lysis buffer without NP-40 per condition was added. 10 % input was mixed with 300 µl QIAzol (Qiagen) and stored for RNA isolation. For preclearing, lysates were incubated with 25 µl blocked and washed beads for 2 h at 4 °C under rotation. For immunoprecipitation, 1 ml precleared lysate was incubated with blocked and washed antibody-coupled beads for 4 h at 4 °C under rotation. Beads were washed three times with was buffer (50 mM Tris, 300 mM KCl, 10 mM $MgCl_2$, 0.05 % NP-40, 1 mM EDTA; pH = 8), twice with NaCl buffer (50 mM Tris, 300 mM NaCl, 0.05 % NP-40, 1 mM EDTA; pH = 8) and treated with 1.7 µl proteinase K (NEB) for 30 min at 50 °C in protease K buffer (preparation: 400 µl 1 M Tris (pH = 8.0), 100 µl 0.5 M EDTA, 600 µl 1 M NaCl, 400 µl 10 % SDS, 500 µl water). Finally, samples were resuspeded in 300 µl QIAzol for RNA isolation together with 10 % input. DNase digestion was performed during RNA extraction.

3.2.2.11 RNA Immunoprecipitation with DNA-RNA Hybrid Binding Antibody

To identify DNA-associated RNAs, RNA immunoprecipitation experiments with a DNA-RNA hybrid binding antibody were performed by Matthias Leisegang (Institute of Cardiovascular Physiology, Goethe University Frankfurt, Germany). Human cardiomyocytes were crosslinked with ultraviolet light

at 254 nm and detached by scraping. Nuclei were isolated with the truChIP Chromatin Shearing Kit (Covaris) according to the manufacturer's instructions, but without sonication. Dilution buffer (20 mM Tris, 100 mM NaCl, 2 mM EDTA, 0.5 % Triton X-100, 1x protease inhibitor; pH = 7.4) was added to washed lysates that were subsequently precleared with 20 µl DiaMag protein A- and protein G-coated magnetic beads (Diagenode) for 30 min at 4 °C. The samples were incubated overnight at 4 °C with anti-DNA-RNA hybrid S9.6 antibody[297] (Kerafast). Complexes were captured with 50 µl DiaMag protein A- and protein G-coated magnetic beads (Diagenode) for 3 h at 4 °C. Subsequently, beads were washed three times for 10 min in dilution buffer, incubated with 10 units of RNase H for 60 min at 37 ° (NEB), washed again in dilution buffer and treated with proteinase K (Diagenode). QIAzol was added to the samples for RNA isolation together with 5 % input.

3.2.2.12 Chromatin Immunoprecipitation with DNA-RNA Hybrid Binding Antibody

To identify RNA-associated DNA fragments, chromatin immunoprecipitation experiments with a DNA-RNA hybrid antibody were performed by Matthias Leisegang (Institute of Cardiovascular Physiology, Goethe University Frankfurt, Germany). Human cardiomyocytes were crosslinked with UV light at 254 nm, detached by scraping and washed. Nuclei were isolated with the truChIP Chromatin Shearing Kit (Covaris) according to the manufacturer's instructions. Nuclei were resuspended and genomic DNA was fragmented using 25 mU/µl dsDNA Shearase Plus (Zymo Research) for 5 min at 37 °C before washing with wash buffer from the truChIP Chromatin Shearing Kit. After sonication with the Bioruptor Plus (10 cycles, 30 s on, 90 s off, 4 °C; Diagenode), cell debris was removed by centrifugation and dilution buffer (20 mM Tris, 100 mM NaCl, 2 mM EDTA, 0.5 % Triton X-100, 1x protease inhibitor; pH = 7.4) was added to lysates (1:3) before preclearing with 20 µl DiaMag protein A- and protein G-coated magnetic beads (Diagenode) for 45 min at 4 °C. Anti-DNA-RNA hybrid S9.6 antibody[297] (Kerafast) was added overnight at 4 °C. Complexes were captured with 50 µl DiaMag protein A- and protein G-coated magnetic beads (Diagenode) for 3 h at 4 °C, subsequently washed twice for 5 min with each of the wash buffers 1, 2 and 3 (1: 20 mM Tris, 150 mM NaCl, 0.1 % SDS, 2 mM EDTA, 1 % Triton X-100; pH = 7.4; 2: 20 mM Tris, 500 mM NaCl, 2 mM EDTA, 1 % Triton X-100; pH = 7.4; 3: 10 mM Tris, 1 % NP-40, 1 % $C_{24}H_{39}NaO_4$, 1 mM EDTA; pH = 7.4). For RNase H treatment[298], 10 units of RNase H (NEB) were added for 60 min at 37 °C. Subsequently, samples were washed with TE buffer (pH = 8.0) and eluted in elution buffer (0.1 M $NaHCO_3$, 1 % SDS) containing 1x proteinase K (Diagenode) shaking at 600 rpm for 1 h at 55 °C, 1 h at 62 °C and 10 min at 95 °C. After removal of the beads, the eluate was purified with the QIAquick PCR Purification Kit (Qiagen) together with 5 % input.

3.2.2.13 Cloning

To obtain a lentiviral Sarrah overexpressing construct, the Gateway pENTR4 Dual Selection Vector was purchased from Thermo Fisher. The human Sarrah sequence (OXCT1-AS1) was introduced by the company Eurofins (Hamburg, Germany) using a sequence- and ligation-independent cloning[299] protocol. 500 ng plasmid were linearized with 0.5 µl of the restriction enzyme AsiSI (NEB) in 1x CutSmart buffer (NEB) in a total volume of 10 µl at 37 °C for 1 h. The reaction was inactivated at 80 °C for 20 min. 50 ng of both the circular and linear plasmid were analyzed on an agarose gel to verify linearization. To introduce the Sarrah sequence into the pLenti4/V5 vector, the Gateway LR Clonase II Enzyme Mix (Invitrogen) was used according to the manufacturer's instructions. Briefly, 100 ng of linear pENTR4-Sarrah were mixed with 150 ng pLenti4/V5-DEST in TE buffer. 2 µl of LR Clonase II were added and incubated at 25 °C for 2 h. 1 µl proteinase K was added and incubated at 37 °C for 10 min. 2 µl of the reaction were transformed into One Shot Stbl3 chemically competent *Escherichia coli*. Isolated plasmid DNA was sequenced with CMV forward (5'-CGCAAATGGGCGGTAGGCGTG-3') and V5(C-term) reverse (5'-ACCGAGGAGAGGGTTAGGGAT-3') primers (sequences provided by Invitrogen) and used for virus particle production.

Single guide RNAs (sgRNAs) for clustered regularly interspaced short palindromic repeats (CRISPR) / CRISPR-associated protein 9 (Cas9)-mediated genome editing were designed and cloned by Manuel Kaulich (Institute of Biochemistry, Goethe University Frankfurt, Germany). To design sgRNAs for excision of the mouse homolog of the triple helix domain in Sarrah, the annotated sequence (ENSMUST00000140003) together with 200 5' and 3' adjacently located nucleotides was used as input sequence for the RS2/Azimuth 2.0 gRNA-scoring algorithm[300]. Proposed sgRNAs were selected based on their RS2 score and proximity to the triple helix forming domain. The lentiviral CRISPR/Cas9 sgRNA-expressing vector pKLV2.2 (Addgene)[301] was used to sequentially introduce sgRNAs (table 21) targeting a region containing the murine Sarrah triple helix domain. A vector containing control sgRNAs was used as control. Positive cloning was sequentially confirmed by clonal Sanger sequencing.

Cloning of AAV9 vectors for *in vivo* overexpression of green fluorescent protein (GFP) or the murine Sarrah sequence (ENSMUST00000140003) driven by a cytomegalovirus (CMV) promoter was performed by Stanislas Werfel and Stefan Engelhardt (Institute of Pharmacology and Toxicology, Technical University Munich, Germany). Vectors containing the GFP sequence served as controls. Constructs were cloned into a single-stranded AAV9-vector backbone. Recombinant AAV9 vectors were produced using helper plasmid co-transfection and purified on iodixanol gradients as described elsewhere[302].

3.2.2.14 Transformation and Culture of Bacteria

For amplification, plasmid DNA was transformed into one vial of One Shot TOP10 or Stbl3 chemically competent *Escherichia coli* (both Invitrogen) according to the manufacturer's instructions. Briefly, bacteria were thawed on ice, 1 to 2 µl plasmid DNA were added, stirred carefully and incubated for 30 min on ice. Bacteria were heat-shocked at 42 °C (TOP10: 45 s, Stbl3: 30 s) and cooled for 2 min on ice. After addition of 250 µl SOC medium (Invitrogen), the culture was horizontally shaken at 225 rpm and 37 °C for 1 h. 200 µl and 50 µl of the culture were plated on LB agar (MP Biomedicals) plates containing 100 µg/ml ampicillin and incubated at 37 °C overnight. Single bacterial colonies were picked and grown in LB medium (MP Biomedicals) containing 100 µg/ml ampicillin overnight and used for plasmid DNA isolation.

3.2.2.15 Plasmid DNA Isolation

Bacterial cultures were pelleted by centrifugation at 6,000 g for 15 min at 4 °C. Plasmid DNA was isolated using the QIAprep Spin Miniprep Kit (1 to 5 ml cultures) or the Plasmid Maxi Kit (100 to 500 ml cultures; both Qiagen) accoring to the manufacturer's instructions. Briefly, bacteria were lysed. Subsequently, DNA was purified via a QIAprep spin column, washed and eluted in water (QIAprep Spin Miniprep Kit) or precipitated, washed and dissolved in water (Plasmid Maxi Kit) and stored at -20 °C.

3.2.2.16 Agarose Gel Electrophoresis

DNA was separated by size using agarose gel electrophoresis. 1 % agarose gels were prepared by boiling and solidification from agarose and 0.5x TBE buffer (45 mM Tris, 45 mM borate und 1 mM EDTA; pH = 8) containing 5 µl Midori Green (Biozym) per 100 ml. 6x DNA loading dye (Thermo Fisher) was added to the samples, which were loaded on the gel and separated at 120 V constant. 5 µl GeneRuler 1 kb or 100 bp DNA ladder (Thermo Fisher) were loaded as molecular weight marker. Gels were documented using the ChemiDoc Touch imaging system.

3.2.2.17 Fractionation of Nuclear and Cytoplasmic RNA

RNA fractionation was adapted from a protocol described elsewhere[303]. Mouse or human cardiomyocytes from one confluent T75 flask were washed twice with cold PBS, detached by scraping in 1 ml PBS, pelleted at 500 g and 4 °C and lysed in 200 µl lysis buffer A (10 mM Tris (pH = 7.5), 10 mM NaCl, 3 mM $MgCl_2$ and 0.5 % NP-40) for 5 min on ice. After centrifugation at 1,000 g and 4 °C for 3 min, the supernatant was collected as cytoplasmic fraction, to which QIAzol (Qiagen) was added for RNA

isolation. The pellet was washed twice with lysis buffer A and lysed in 200 µl lysis buffer B (10 mM Tris (pH = 7.5), 150 mM NaCl, 3 mM $MgCl_2$) for 5 min on ice. The nuclear fraction was pelleted by centrifugation at 1,000 g and 4 °C for 3 min and resuspended in QIAzol for RNA isolation.

3.2.3 *In vitro* Assays

3.2.3.1 Caspase Assay

Caspase-3/7 activity was assessed in mouse and human cardiomyocytes and HUVECs using the Apo-ONE Homogeneous Caspase-3/7 Kit (Promega) according to the manufacturer's instructions 48 h after treatment or 4 h after seeding when no treatment was applied (transduced HL-1 cells). Shortly, caspase substrate Z-DEVD-R110 was diluted 1:100 in Apo-ONE Homogenous Caspase-3/7 buffer. The mixture was diluted 1:2 with growth medium (HL-1 cells and HUVECs) or PBS (hCMs) and incubated with the cells for 1 h at 37 °C and 5 % CO_2. For induction of apoptosis, H_2O_2 was added to the cells at a final concentration of 100 µM 4 h before substrate addition. Fluorescence was measured at the GloMax-Multi Detection System (Promega) at 521 nm wavelength. A substrate dilution mixed with growth medium or PBS served as a blank control and was substracted from measured values.

3.2.3.2 Annexin V-Staining

Flow cytometry-based cell death assays were performed 24 h or 48 h after transfection with LNA GapmeR control or LNA GapmeR Sarrah to measure early or late apoptosis, respectively. HL-1 cells were seeded and transfected in 6 cm-dishes. Before washing the cells twice with PBS, the supernatant containing dead cells was collected. Cells were detached with trypsin-EDTA and the reaction was stopped with the earlier collected supernatant. After pelleting at 4 °C, cells were washed twice with cold binding buffer (BD Biosciences) and resuspended in 100 µl binding buffer (amount per 6 cm-dish) containing 5 µl annexin V-V450 (BD Biosciences) and 5 µl 7-AAD (BD Biosciences). The staining reaction was incubated for 15 min at RT in the dark, 200 µl binding buffer were added and samples were analyzed with a BD FACSCanto II (BD Biosciences). Single-stained cells (annexin V-V450 or 7-AAD only) were used to adjust laser settings. Data acquisition was terminated after 20,000 events per 6 cm-dish.

3.2.3.3 Rat Cardiomyocyte Contractility Measurements

Rat cardiomyocytes were isolated from neonatal Sprague Dawley pups according to the Neonatal Heart Dissociation protocol by Miltenyi Biotec as described in section 3.2.5.3. Isolated cells were plated on glass coverslips (250,000 cells per coverslip) that had been coated with poly-L-lysine (Sigma-Aldrich)

for 1 h, with 1 mg/ml type I bovine collagen (Sigma-Aldrich) for 5 min and washed with PBS. After 24 h, medium was changed to maintenance medium (DMEM high glucose (BioConcept) supplemented with 10 % M199 with Earle's Balanced Salts (EBS; BioConcept), 1 % horse serum (HS; BioConcept) and 4 mM L-glutamine (Thermo Fisher)). For LNA GapmeR treatment of neonatal rat cardiomyocytes, no transfection reagent was used. Instead, 325 nM LNA GapmeRs were added to maintenance medium and contractility of individual cardiomyocytes was measured 72 h later using the IonOptix Myocyte Contractility Recording System following the manufacturer's instructions. Briefly, cardiomyocytes were placed in a chamber mounted on the stage of an inverted microscope, perfused with warm (37 °C) modified Tyrode's buffer (137 mM NaCl, 5 mM KCl, 15 mM glucose, 1.3 mM $MgSO_4$, 1.2 mM NaH_2PO_4, 20 mM HEPES, 1 mM $CaCl_2$; pH = 7.4) and field-stimulated at a frequency of 1 Hz. Monotonic contractility transients of ten cells per coverslip were recorded within 20 min and analyzed using the IonWizard software.

3.2.3.4 Engineered Heart Tissue Organoids

Engineered heart tissue (EHT) organoids were generated from hiPSC-cardiomyocytes and HUVECs by Marc Hirt and Kaja Yorgan (Department of Experimental Pharmacology and Toxicology, University Medical Center Hamburg-Eppendorf, Germany), the analysis was performed by the author. Rectangular casting molds for EHT organoids in a 24-well format were obtained by dipping polytetrafluoroethylene spacers into warm liquid agarose and removing them upon solidification. Subsequently, silicone racks with two flexible silicone posts were placed to protrude into each casting mold. Each EHT was composed of 1,000,000 hiPSC-cardiomyocytes and 300,000 HUVECs. The cells were mixed with matrigel basement membrane matrix, fibrinogen and thrombin at a final volume of 100 µl and pipetted into the casting molds. After 90 minutes, EHT organoids were transferred into growth medium (DMEM supplemented with 10 % inactivated HS, penicillin/streptomycin, insulin and aprotinin to prevent rapid fibrin degradation) in cell culture dishes. 4 µM LNA GapmeRs and 10 µM ROCK/apoptosis-inhibitor Y-27632 were added to the medium. From day 3, EHT medium was changed three times a week containing 10 µM Y-27632 until day 8. After two days, first areas in EHT organoids started to beat spontaneously, and after six days, all tissue beat coherently. EHT organoid beating was recorded three times per week. Contractile force and fractional shortening were analyzed using the EHT contractility analysis instrument from EHT Technologies[304]. After 22 days in culture, EHT organoids were fixed for 24 h in acid-free, phosphate-buffered formaldehyde solution (4 %) stabilized with methanol for histology.

3.2.3.5 SCOT1 Enzymatic Activity Assay

To assess whether succinyl-CoA:acetoacetate transferase (SCOT1) enzymatic activity is affected by Sarrah, HL-1 cells were transfected with LNA GapmeR control and LNA GapmeR Sarrah in a 6-well-format. Cell pellets were prepared 48 h after transfection by washing with cold PBS, collecting by scraping in PBS and pelleting at 4 °C and 500 g for 15 min. Subsequently, the pellets were homogenized and used for the assay by Riekelt Houtkooper (Laboratory Genetic Metabolic Diseases, Academic Medical Center Amsterdam, the Netherlands). SCOT1 activity was measured as succinate-induced decrease in absorbance at 303 nm using a medium of the following composition: 100 mM Tris-H_2SO_4 (pH = 8.05), 25 mM $MgSO_4$, 50 µM acetoacetyl-CoA (Sigma-Aldrich) and 0.1 % (w/v) Triton X-100. Reactions were started by addition of sodium succinate at a final concentration of 50 mM and absorbance at 303 nm was subsequently followed in time on a COBAS-FARA-centrifugal analyzer (Hoffmann-LaRoche).

3.2.3.6 Nuclear Magnetic Resonance

Nuclear magnetic resonance (NMR) spectra were recorded by Christopher Johnson (Vanderbilt University Medical Center, Nashville, TN, USA) to model triple helix formation between Sarrah and gene promoters *in vitro*. Sequences of mouse and human Sarrah triple helix forming domains and binding sites in the GPC6 promoter in the respective genome (table 20) were purchased as RNA and DNA single-stranded oligonucleotides, respectively, from Sigma-Aldrich. 1 mM solutions of each strand were prepared by hydrating the oligonucleotides in 10 mM $NaPO_4$, 50 mM NaCl and 3 mM EGTA at pH = 7.4. The pH was measured using a Beckman Φ 340 pH meter and adjusted to 7.4 by addition of HCl. For NMR, 100 µM DNA duplex were prepared in a volume of 500 µl containing 15 µl D_20 for a lock signal. Spectra were measured with an 800 MHz magnet (Bruker) equipped with a 5 mm CPTCI probe using a 1-1 jump and return pulse protocol. Equal molar ratios of RNA were added to the DNA duplex samples and mixed by inversion. Spectra were recorded at 288, 298 and 320 K with 288 K yielding the best signal dispersion. All spectra were processed using a sinc window multiplication function.

3.2.3.7 Cell Proliferation Assay

HUVEC proliferation was assessed from BrdU incorporation during mitosis in a flow cytometry-based assay. The experiment was designed as a co-culture of HUVECs and hCMs that had either been transduced or transfected with LNA GapmeRs (see section 3.2.1.2) to mimic the interactions taking place *in vivo* between endothelial cells and myocytes in the heart. BrdU staining was performed after 48 h of co-cultivation using the BrdU Flow Kit (BD Biosciences) according to the manufacturer's

instructions. Briefly, HUVECs were incubated with BrdU in full growth medium at 37 °C (transduced hCMs: 30 min, transfected hCMs: 45 min), washed with PBS, detached with trypsin-EDTA, fixed with Cytofix/Cytoperm for 30 min, permeabilized with CytopermPlus for 10 min on ice, fixed with Cytofix/Cytoperm for 5 min on ice and washed with PermWash buffer between all steps. Finally, cells were treated with DNase for 1 h at 37 °C to expose incorporated BrdU, washed with PermWash buffer and stained with 2.5 µl V450-anti-BrdU antibody (BD Biosciences) for 20 min and 20 µl 7-AAD (BD Biosciences) for 10 min per well diluted in PermWash buffer. Samples were diluted with PBS and analyzed with a BD FACSCanto II (BD Biosciences). Cells that had not been incubated with BrdU were used to adjust laser settings. Data acquisition was terminated after 20,000 events per well.

3.2.3.8 Spheroid Sprouting Assay

Angiogenesis was modeled *in vitro* using an endothelial cell spheroid sprouting assay. Spheroid generation is described elsewhere[305]. Briefly, 400 HUVECs were incubated in a methylcellulose solution (6 g methylcellulose (Sigma-Aldrich) autoclaved in 250 ml full EBM, stirred at 60° C for 40 min before addition of another 250 ml full EBM, stirred overnight at 4 °C, centrifuged for 2 h at 2,000 rpm and stored at 4° C until use) in a 96-well-plate with non-adhesive U-bottoms at 37 °C and 5 % CO_2 to form spheroids. After 24 h, spheroids were collected by centrifugation at 200 g for 3 min, resuspended in 500 µl methylcellulose supplemented with FCS (4:1) per 50 spheroids and embedded in 500 µl of a collagen gel (5 ml of collagen solution contain 500 µl 10x M199 medium, 90 µl 1 M HEPES, 4 ml rat tail collagen type I (BD Biosciences) and 0.2 M NaOH to turn the color to pink) in a 24-well-plate. After 30 min of gel polymerization at 37 °C and 5 % CO_2, spheroids were treated with 100 µl conditioned medium from LNA GapmeR-transfected human cardiomyocytes. After 24 h, spheroids were fixed with 4 % formaldehyde in PBS and documented using an Axio Observer Z1.0 microscope (Zeiss) at 5-fold magnification. Cumulative sprout length of each spheroid was measured using the AxioVision SE64 Rel. 4.9.1 software.

3.2.4 Histological Methods

For histological stainings, mouse hearts were fixed for 24 h in acid-free, phosphate-buffered formaldehyde solution (4 %), embedded in paraffin, cut into 4 µm thick sections using the microtome Microm HM 430 (Micron International) and dried overnight at 37 °C. Engineered heart tissue (EHT) organoids were fixed for 24 h in acid-free, phosphate-buffered formaldehyde solution (4 %) stabilized with methanol and stained as whole mount specimens. Prior to all stainings, sections and organoids were deparaffinized by incubation in xylene for 10 min twice, in ethanol of decreasing concentrations

(100 %, 95 %, 80 %, 70 %, 50 %), water and PBS for 5 min each. Prior to deparaffinization, sections and organoids for fluorescence stainings were heated to 60 °C for 30 min. Sirius red stainings were imaged at the Nikon Eclipse Ci microscope, fluorescence stainings at the Zeiss LSM 780 confocal microscope.

3.2.4.1 Collagen Staining

Collagen staining was performed on heart sections to visualize fibrosis, which indicates infarcted myocardium. After deparaffinization, sections were stained for 1 h in 0.1 % sirius red (Waldeck) in saturated aqueous picric acid solution (Sigma-Aldrich). Subsequently, sections were washed in 0.5 % acetic acid twice, dehydrated in three changes of 100 % ethanol, cleared with xylene and mounted with PERTEX mounting medium (VWR). Infarct size was quantified as mean of epicardial and endocardial ratio of infarct length to left ventricle circumference on five serial sections.

3.2.4.2 Apoptosis Staining

Apoptosis staining was performed on heart sections and EHT organoids by TdT-mediated dUTP-biotin nick end labeling (TUNEL) using the In Situ Cell Death Detection Kit TMRed (Roche). After deparaffinization, specimens were treated with proteinase K for 7 min at 37 °C, washed in PBS for 5 min and stained with the TUNEL enzyme in dilution reagent for 1 h at 37 °C. After three times washing with PBS, specimens were mounted with mountung medium (DAKO) containing Hoechst (AnaSpec) to visualize all cell nuclei.

3.2.4.3 DNA Damage Staining

DNA damage staining was performed on heart sections by immunostaining of DNA double strand break marker phosphorylated histone H2AX (H2AXγ). After deparaffinization, sections were boiled in citrate buffer (10 mM citric acid, 0.05 % Tween 20; pH = 6) for 90 s for antigen retrieval and cooled by rinsing with water. After washing three times with 0.8 % NaCl in PBS-T, 5 min each, sections were blocked with 5 % goat serum in PBS for 30 min. Anti-phospho-histone H2AX (Ser139) antibody solution (1:300 in PBS) was incubated on the sections at 4 °C overnight. The next day, sections were washed three times for 5 min with 0.8 % NaCl in PBS-T and incubated with anti-rabbit Alexa 555 antibody solution (1:200) for 1 h at RT. Subsequently, washing with PBS-T was repeated and sections were mounted with mounting medium (DAKO) containing Hoechst (AnaSpec) to visualize cell nuclei.

3.2.4.4 Hypertrophy Staining

Hypertrophy staining was performed on heart sections by staining of wheat germ agglutinin (WGA) to visualize cardiomyocyte cell membranes. After deparaffinization, sections were washed for 5 min in PBS-T and blocked with 1 % BSA and 2 % goat serum in PBS-T for 30 min. Alexa Fluor 647-coupled wheat germ agglutinin was diluted 1:300 in PBS-T and added for 1 h at RT. Subsequently, sections were washed three times with PBS-T for 5 min and mounted with mounting medium (DAKO).

3.2.4.5 Proliferation Staining

Proliferation staining was performed on heart sections by immunostaining of mitosis marker phospho-histone H3 at serine 10. After deparaffinization, sections were washed twice with PBS, boiled in citrate buffer (10 mM citric acid, 0.05 % Tween 20; pH = 6) for 20 min and cooled for 30 min at RT. After washing with PBS, sections were blocked with 2 % goat serum and incubated with anti-phospho-histone H3 antibody solution (1:100 in PBS) at 4 °C overnight. The next day, sections were washed three times for 5 min with 0.1 % Tween 20 in PBS (PBS-T) and incubated with anti-rabbit Alexa 488 antibody solution (1:200) for 1 h at RT. Subsequently, washing with PBS-T was repeated and sections were mounted with mounting medium (DAKO) containing Hoechst (AnaSpec) to visualize all cell nuclei.

3.2.4.6 Endothelial Cell Staining

Endothelial cell staining was performed on heart sections by immunostaining of endothelial cell marker isolectin B4. After deparaffinization, sections were boiled in citrate buffer (10 mM citric acid, 0.05 % Tween 20; pH = 6) for 90 s for antigen retrieval. After washing once with PBS and three times with PBS-T, 5 min each, sections were blocked with 1 % BSA in PBS-T for 1 h. Biotinylated isolectin B4 (Linaris) diluted 1:100 in PBlec buffer (1 mM $MgCl_2$, 1 mM $CaCl_2$, 0.1 mM $MnCl_2$, 1 % Triton X-100 in PBS; pH = 6.9) was incubated on the sections at 4 °C overnight. Sections were washed three times with PBS-T for 5 min and stained with Alexa Fluor 488-coupled streptavidin (Invitrogen) at RT for 1 h. Washing with PBS-T was repeated before sections were mounted with mounting medium (DAKO) containing Hoechst (AnaSpec) to visualize all cell nuclei.

3.2.5 Animal Experiments

Animal experiments were performed in accordance with the principles of laboratory animal care as well as German national laws and have been approved by the ethics committee of the regional council (Regierungspräsidium Darmstadt, Hesse, Germany). All mice and rats were obtained from Charles River

and kept in individually ventilated cages (Tecniplast). Water and ssniff R/M-H complete feed (ssniff Spezialdiäten, Soest, Deutschland) were fed *ad libitum*.

3.2.5.1 Langendorff Heart Preparation

Young (8 weeks) and aged (18 months) male C57BL/6 mice were sacrificed and their hearts were isolated, perfused and digested according to the Langendorff method (http://www.signaling-gateway.org/data/cgi-bin/ProtocolFile.cgi?pid=PP00000125; April 27, 2019) by Reinier Boon (Institute of Cardiovascular Regeneration, Goethe University Frankfurt, Germany) in order to separate cardiomyocytes from remaining cell types. Briefly, pulmonary vessels and the aorta were cut and hearts were immediately perfused with perfusion buffer (113 mM NaCl, 4.7 mM KCl, 0.6 mM KH_2PO_4, 0.6 mM Na_2HPO_4, 1.2 mM $MgSO_4$*7 H_20, 0.032 mM phenol red, 12 mM $NaHCO_3$, 10 mM $KHCO_3$, 10 mM HEPES, 30 mM taurine, 10 mM 2,3-butanedione monoxime, 5.5 mM glucose; pH = 7.46) for 4 min and subsequently with digestion buffer (0.25 mg/ml Liberase Blendzyme 1 (Roche), 0.14 mg/ml trypsin and 12.5 µM $CaCl_2$ in 1x perfusion buffer) for 10 min to enzymatically separate cardiac cells. Digested heart tissue was dissociated mechanically. Cardiomyocytes were separated from other heart cells by density centrifugation. RNA from both fractions was isolated and used for RNA deep sequencing.

3.2.5.2 Isolation of Cardiac Cell Populations

Male 10 weeks old C57BL/6 mice were sacrificed for isolation of cardiac cell populations by Kosta Theodorou (Institute of Cardiovascular Regeneration, Goethe University Frankfurt, Germany). Hearts were flushed with Hank's Balanced Salt Solution with Ca^{2+} and Mg^{2+} ($HBSS^{+/+}$) and heart atria were removed. The tissue was minced and treated with dispase II (Merck), collagenase II (Thermo Fisher) and DNase I (Sigma-Aldrich) for 1 h at 37 °C. The digested hearts were sifted through a cell strainer of 100 µm pore size (PluriSelect) into isolation buffer (PBS with 0.5 % BSA and 2 mM EDTA), washed with DMEM with 10 % FBS and centrifuged at 30 g and 4 °C for 3 min to pellet cardiomyocytes, which were washed with PBS and centrifuged at 300 g and 4 °C for 5 min. Supernatants from both centrifugation steps were pooled, sifted through a cell strainer of 40 µm pore size (PluriSelect), washed with DMEM with 10 % FBS, centrifuged at 300 g and 4 °C for 5 min and washed with isolation buffer. Endothelial cells were isolated from the pellet by incubation with a CD31 antibody (1.25 µl per heart, Thermo Fisher) and Dynabeads (sheep anti-rat IgG, 6 µl per heart, Invitrogen) for 30 minutes at 4°C under rotation in isolation buffer. The beads had been coupled to the antibody for 30 min at 4 °C under rotation and washed three times with isolation buffer before and after coupling. The remaining cells were pelleted at 300 g and 4 °C for 5 min, resuspended in DMEM with 10 % FBS and incubated in a cell

culture dish at 37 °C and 5 % CO_2 for 40 min to let fibroblasts adhere before washing with isolation buffer. All cell fractions were resuspended in QIAzol (Qiagen) for RNA extraction.

3.2.5.3 Isolation of Neonatal Rat Cardiomyocytes

Rat cardiomyocytes were isolated from neonatal Sprague Dawley pups according to the Neonatal Heart Dissociation protocol by Miltenyi Biotec[306] using the gentleMACS Dissociator (Miltenyi Biotec) by Corinne Bischof (Institute of Cardiovascular Regeneration, Goethe University Frankfurt, Germany). Briefly, hearts were isolated, washed with $HBSS^{-/-}$ supplemented with 2,3-butanedione monoxime and minced before enzymatic digestion. Cells were dissociated using the gentleMACS Program m_neoheart_01. Cardiomyocytes were enriched in the cell suspension by centrifugation at 80 g for 5 min. The pellet was resuspended in plating medium (DMEM high glucose (BioConcept) containing 17 % M199 with EBS (BioConcept), 10 % horse serum (BioConcept), 5 % FBS, 4 mM L-glutamine and 100 µg/ml penicillin/streptomycin) and plated on glass coverslips that had been coated with 1 mg/ml type I bovine collagen (Sigma-Aldrich) for 24 h. After 1 h and 40 min, the supernatant was collected and centrifuged at 80 g for 5 min. The pelleted cardiomyocytes were resuspended in plating medium and plated for contractility measurements (see section 3.2.3.3).

3.2.5.4 Rat Model of Heart Failure with Preserved Ejection Fraction

Myocardial samples of 30 weeks old male Zucker fatty spontaneously hypertensive heart failure F1 hybrid (ZSF1) lean, ZSF1 obese and Wistar-Kyoto rats were kindly provided by Nazha Hamdani (Department of Cardiovascular Physiology, Ruhr University Bochum, Germany). All groups had been fed Purina diet 5008. Additionally, a subgroup of ZSF1 obese rats had received high fat diet D12468 (Research Diet Inc.). ZSF1 obese rats on both diets have been described to develop heart failure with preserved ejection fraction (HFpEF)[135]. Samples were used for RNA isolation and gene expression analysis by qRT-PCR.

3.2.5.5 Adenovirus-Associated Viral Overexpression

For overexpression of Sarrah or a GFP control construct, $6x10^{11}$ adeno-associated virus serotype 9 (AAV9) particles (see section 3.2.2.13) were diluted in PBS in a total volume of 200 µl. The particles were injected into tail veins of mice by Ariane Fischer (Institute of Cardiovascular Regeneration, Goethe University Frankfurt, Germany) two weeks before acute myocardial infarction was provoked by surgery.

3.2.5.6 Acute Myocardial Infarction Surgery

Acute myocardial infarction (AMI) surgery was performed by permanent ligation of the left anterior descending (LAD) coronary artery by Ariane Fischer (Institute of Cardiovascular Regeneration, Goethe University Frankfurt, Germany). Analysis of echocardiographic recordings was performed by the author. Briefly, mice were anesthetized with isoflurane, given buprenorphine (0.1 mg/kg) and bupivacaine (0.25 %, 1 mg/kg) for analgesia, intubated and provided with artificial respiration (200 breath intakes/min, 250 µl/intake; Harvard Apparatus). The thorax was opened between the fifth and sixth rib. After penetrating the pericardium, the LAD coronary artery was ligated using a 8-0 suture (Ethicon) at the height of the middle of the heart to induce heart ischemia and thereby a myocardial infarction. All structures were sewed and mice were intraperitoneally injected with 1 ml of 0.09 % NaCl in water. Buprenorphine (0.1 mg/kg) and carprofen (5 mg/kg) were intraperitoneally injected twice a day for analgesia and ampicillin (100 mg/kg) was added to drinking water over a period of six days after surgery to prevent infections. Induction of AMI was verified by echocardiography in the evening of the day of surgery.

3.2.5.7 Echocardiography

Echocardiographic measurements of mouse hearts after AMI were performed several hours, seven days or 14 days after surgery by Ariane Fischer (Institute of Cardiovascular Regeneration, Goethe University Frankfurt, Germany) to assess cardiac contractility. To this end, the Vevo 2100 imaging system (VisualSonics) and the corresponding software were used according to the manufacturer's instructions. Mice were anesthetized by isoflurane and hearts were recorded in both M mode and B mode. Left ventricular function parameters were assessed from M mode using Simpson's method while wall motion score index (WMSI) was assessed from B mode.

3.2.5.8 Magnetic Resonance Imaging

Magnetic resonance imaging (MRI) of infarcted mouse hearts was performed 14 days after surgery by Tijna Alekseeva (Institute of Tumor Biology and Experimental Therapy, Georg Speyer House Frankfurt, Germany) and Christoph Schürmann (Institute of Cardiovascular Physiology, Goethe University Frankfurt, Germany) to assess cardiac left ventricular function. Analysis of MRI recordings was performed by the author. Mice were anesthetized by isoflurane and scanned in a 7.0 Tesla magnetic resonance tomograph (Bruker) equipped with a B-GA 9S HP gradient system. The imaging plane was localized using 2- and 4-chamber view scout images of the heart. Images were acquired in short axis view using the IntraGate self-gating technique and the gradient echo method (repetition time = 6.2

ms; echo time = 1.6 ms; field of view = 2.20 * 2.20 cm; slice thickness = 1.0 mm; matrix = 128 * 128; oversampling = 100). Nine to ten contiguous short axis slices were imaged for complete coverage of the left ventricle. The Segment 1.8 software (Medviso) was used to analyze ejection fraction, ventricular volumes and wall thickness.

3.2.6 Bioinformatics

3.2.6.1 RNA Deep Sequencing Data Analysis

500 ng of total RNA from young and aged mouse cardiomyocytes and remaining heart cells were used for RNA deep sequencing by Wei Chen (Max Delbrück Center for Molecular Medicine, Berlin, Germany). RNA was fragmented and primed for cDNA synthesis. Libraries were constructed using the TruSeq RNA Sample Preparation Kit according to the manufacturer's instructions, pooled and sequenced with the HiSeq 2000 Sequencing System (Illumina, San Diego, CA, USA). Gene expression was estimated using Cufflinks version 2.1 with default parameters by Reinier Boon and David John (Institute of Cardiovascular Regeneration, Goethe University Frankfurt, Germany).

3.2.6.2 Coding Potential Analysis

The coding potential of human and mouse Sarrah was assessed by Tamer Ali (Institute of Cardiovascular Regeneration, Goethe University Frankfurt, Germany) using the Coding Potential Assessment Tool (CPAT) based on genome hg38 for human and genome mm10 for mouse sequences as described elsewhere[307]. Briefly, the logistic regression model underlying CPAT integrates four sequence features: open reading frame size, open reading frame coverage, Fickett TESTCODE statistic and hexamer usage bias.

3.2.6.3 Sequence Homology Alignment

To identify sequence conserved stretches between human and mouse Sarrah, sequence homology alignment was performed using the LALIGN DNA:DNA tool of the FASTA Sequence Comparison software published by the University of Virginia[308] with default parameters and scoring matrix +5/-4.

3.2.6.4 Microarray Analysis

Microarray data from GeneChIP Human Exon 1.0 ST arrays (Affymetrix) of human cardiomyocyte RNA from cells transfected in 6 cm-dishes were analyzed by gene set enrichment analysis (GSEA)[309] by

Reinier Boon (Institute of Cardiovascular Regeneration, Goethe University Frankfurt, Germany). Briefly, an enrichment score that indicates the degree of overrepresentation of a set of genes belonging to a specific cellular pathway in the list of all up- and downregulated genes was calculated. Statistical significance of the enrichment score was assessed by an empirical phenotype-based permutation test procedure. To eventually account for multiple hypothesis testing, the estimated significance level was adjusted by normalizing the enrichment score according to the gene set size and calculating the false discovery rate. As a second means of analyzing microarray data, gene ontology analysis of gene sets up- and downregulated in human cardiomyocytes after Sarrah silecing was performed by the author using the Functional Annotation Tool of the Database for Annotation, Visualization and Integrated Discovery (DAVID)[310,311].

3.2.6.5 Triplex Domain Finder Analysis

Triple helix formation between Sarrah and gene promoters was predicted by Chao-Chung Kuo and Ivan Costa (Institute for Computational Genomics, RWTH Aachen University, Germany) using the Triplex Domain Finder (TDF)[312]. The analysis was run on the human and mouse Sarrah sequences (OXCT1-AS1 and ENSMUST00000140003, respectively) and gene sets up- and downregulated by Sarrah silencing identified in the microarray. Sarrah DNA binding domains (DBDs) were identified by the promoter test with promoters being defined as regions 1 kb upstream of the transcription start site (TSS) based on GENCODE[313] version 24 and genome hg38 for human data or GENCODE version 4 and genome mm10 for mouse data. TDF parameters were set to indicate all DBDs with at least 120 DNA target sites and a significant enrichment with p-value < 0.05.

3.2.7 Statistical Analysis

Statistical analysis was performed using GraphPad Prism 5 software. Data are displayed as means ± SEM. Gaussian distribution was determined with Kolmogorov-Smirnov test. For comparison between two normally distributed groups with normal data distribution, two-tailed paired or unpaired Student's t-tests were performed; for multiple comparisons, one-way analysis of variance (ANOVA) followed by Bonferroni's correction was used. If normality of the data could not be confirmed, Mann-Whitney tests were used. Strength and direction of association between ranked variables were assessed by Spearman's rank-order correlation. Significant outliers within a group ($p < 0.05$) were detected by Grubbs' outlier test and excluded from the analysis. Data were considered statistically significant below a p-value of 0.05 (*), 0.01 (**) or 0.001 (***).

4. Results

4.1 Identification of the Novel Long Non-Coding RNA Sarrah in the Heart

To identify cardiac long non-coding RNAs (lncRNAs) that are differentially regulated during aging, mouse hearts from 8 weeks and 18 months old mice were isolated and processed according to the Langendorff method to separate cardiomyocytes from remaining cell types by enzymatic dispersion and differential centrifugation. RNA from both the cardiomyocyte and the other cell fraction was isolated and polyadenylated RNA was sequenced by next generation sequencing (figure 13 A). The sequencing results revealed 29,150 transcripts expressed in the cardiomyocyte fraction. 5,439 of these transcripts were annotated as lncRNAs (figure 13 B).

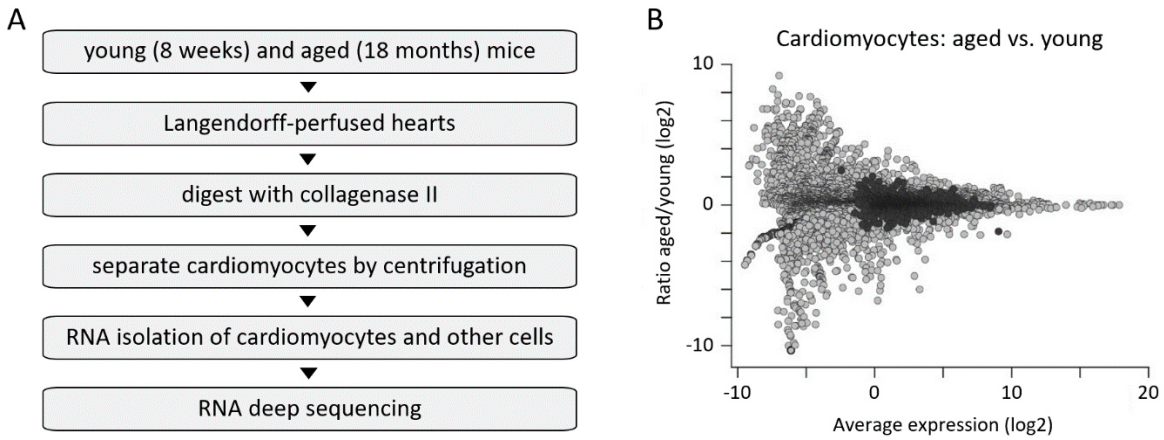

Figure 13: Identification of cardiac aging-regulated long non-coding RNAs. (A) Flow chart illustrating the procedure of primary mouse cardiomyocyte isolation and RNA deep sequencing. (B) Expression of polyadenylated RNA from young (8 weeks) and aged (18 months) mice was analyzed by RNA deep sequencing on the Illumina Hiseq platform (n = 3). Protein-coding and non-coding transcripts are depicted in gray or black, respectively.

For 76 of the annotated lncRNAs, expression in the heart was rated as reliable based on reads in a genome viewer and confirmed by quantitative real-time polymerase chain reaction (qRT-PCR) using RNA from cells of the atrial HL-1 mouse cardiomyocyte line as well as from adult mouse hearts (figure 14 A). Since myocardial loss is of particular relevance in the context of cardiac disease and one of its underlying causes is apoptosis of individual cardiomyocytes, it was assessed whether the 76 candidate lncRNAs are involved in apoptosis in an small interfering RNA (siRNA)-based screening (figure 14 B). Therefore, caspase-3/7 activity, a hallmark of apoptosis[314], was measured in siRNA-transfected mouse cardiomyocytes in standard cell culture conditions and following induction with hydrogen peroxide, which triggers apoptosis[315].

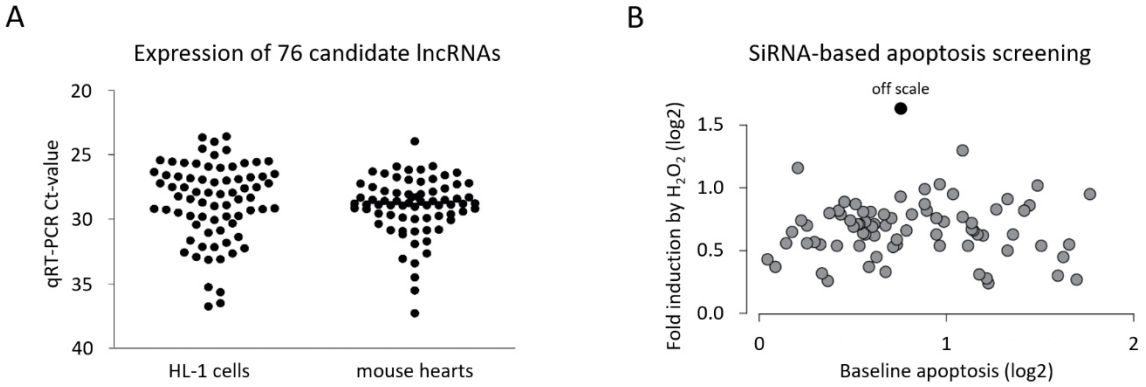

Figure 14: Identification of cardiac long non-coding RNAs that regulate apoptosis. (A) Expression of 76 candidate lncRNAs was confirmed by qRT-PCR in the murine HL-1 cardiomyocyte line and in adult mouse heart tissue. (B) Two different siRNAs against each of the 76 candidate lncRNAs were transfected in HL-1 cells, the average for both is displayed (n = 3). Apoptosis was assessed by measuring caspase-3/7 activity in standard cell culture conditions as well as after induction with 100 µM hydrogen peroxide. LncRNA Sarrah (black) is plotted off scale because measurements were precluded by potent induction of cell death upon knockdown.

The screening revealed that several lncRNAs promote or reduce apoptosis. Knockdown of one of them (black dot in figure 14 B) induced such massive apoptosis after hydrogen peroxide treatment that measurements were precluded. Its gene is annotated as "ENSMUST00000140003" in mouse and located antisense to the 3-oxoacid CoA-transferase 1 (OXCT1) gene, which encodes the enzyme SCOT1, so that the transcript was renamed "SCOT1-antisense RNA regulated during aging in the heart" ("Sarrah"). RNA deep sequencing results of Sarrah suggest that Sarrah is cardiomyocyte-enriched and downregulated during aging (figure 15).

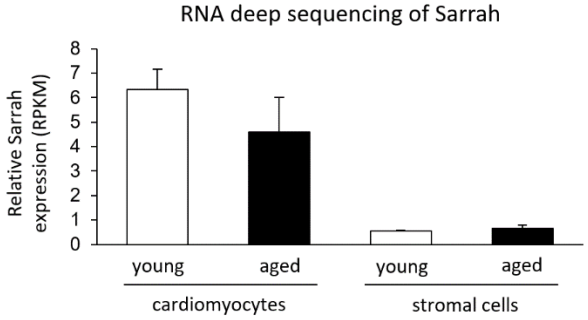

Figure 15: Cardiac Sarrah expression profile according to RNA deep sequencing data. Sarrah levels were determined in cardiac myocytes and stromal cells isolated from young (8 weeks) and aged (18 months) mice by RNA deep sequencing (RPKM: reads per kilobase million; n = 3).

The Sarrah locus overlaps with the OXCT1 transcription start site and is conserved across several species including humans, rats and pigs with the human ortholog being annotated as "OXCT1-AS1" (figure 16 A). Although unusual for lncRNAs, also the Sarrah sequence contains stretches conserved between mouse and human (figure 16 B).

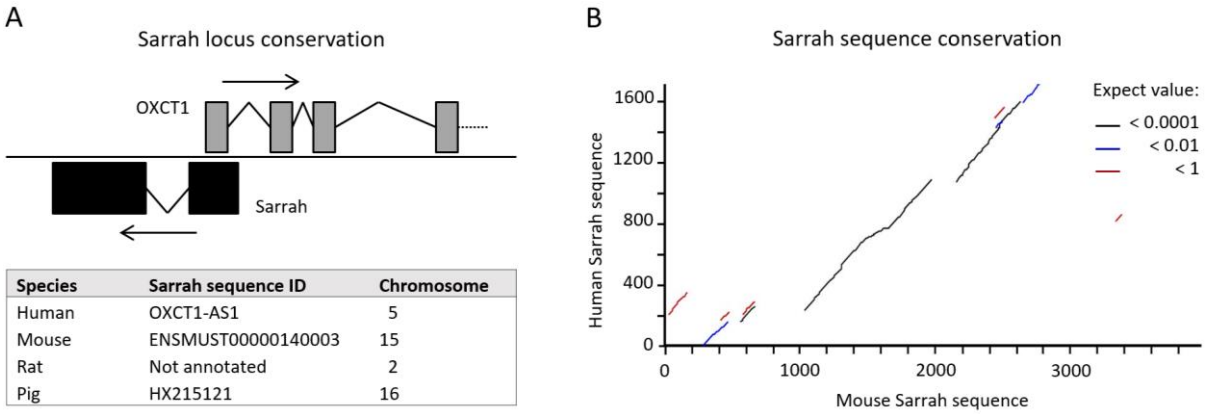

Species	Sarrah sequence ID	Chromosome
Human	OXCT1-AS1	5
Mouse	ENSMUST00000140003	15
Rat	Not annotated	2
Pig	HX215121	16

Figure 16: Sarrah conservation across species. (A) Top: Scheme illustrating the Sarrah locus, which is antisense to the OXCT1 gene and overlaps with its first exon. In mouse, the transcription start site of Sarrah is located within the first OXCT1 intron. Bottom: Table summarizing the sequence identifiers and chromosomes of the Sarrah gene in different species. (B) Sequence alignment of the human and mouse Sarrah sequences using the LALIGN DNA:DNA tool of the FASTA Sequence Comparison software of the University of Virginia reveals conserved stretches. The lower the expect value is, the more unlikely is it that the nucleotide sequences of a given length align by chance.

To ensure that the annotated sequences do not encode a protein or peptide, the coding probabilities of the human and mouse sequences were assessed using a coding potential analysis tool (CPAT, tables 25 A and B). For comparison, the sequences of two well characterized lncRNAs, Xist and MALAT1, whose functionality as RNA molecules is recognized in the literature, were included as positive controls and the messenger RNA (mRNA) sequences of the neighboring genes of Sarrah as negative controls. In both species, the coding potential of Sarrah is very low and comparable to that of Xist and MALAT1, whereas the mRNA coding probability of the protein coding genes OXCT1, FBXO4, c5orf51 and Plcxd3 is exactly or nearly 100 percent. It can therefore be excluded that Sarrah encodes any peptides.

Table 25: Coding Potential Analysis of the Human and Mouse Sarrah Sequences

Human					Mouse			
Gene	**RNA [nt]**	**ORF [nt]**	**Coding Probability**		**Gene**	**RNA [nt]**	**ORF [nt]**	**Coding Probability**
Sarrah	1,731	300	0.05		Sarrah	3,990	279	0.23
MALAT1	8,779	213	0.01		MALAT1	8,779	213	0.07
Xist	19,275	411	0.03		Xist	17,918	519	0.04
OXCT1	3,388	1,563	1.00		OXCT1	3,496	1,563	1.00
FBXO4	1,682	1,164	1.00		FBXO4	3,479	1,158	0.99
c5orf51	5,241	885	0.99		PLCXD3	1,905	966	0.99

The RNA deep sequencing analysis suggested that Sarrah was 9.04-fold enriched in cardiomyocytes over stromal heart cells. However, when 10 weeks old mouse hearts were isolated and enzymatically dispersed to purify the cardiomyocyte, endothelial cell and fibroblast populations, Sarrah was present at approximately equal levels in all fractions with only a 1.05-fold enrichment over endothelial cells and a 2.46-fold enrichment over fibroblasts (figure 16 A). Purity of the cell fractions was assessed by measuring the cell type-specific markers Tnnt2 for cardiomyocytes and Cdh5 for endothelial cells

(figure 17 A). Taking into consideration that the fractions were not perfectly pure and especially some endothelial cell contamination was detectable in the cardiomyocyte fraction, it is likely that Sarrah enrichment in cardiomyocytes over endothelial cells is higher than 1.05-fold, but does not reach the level of enrichment suggested by the initial RNA deep sequencing analysis.

Since Sarrah is still highest expressed in cardiomyocytes of all cardiac cell types, human and mouse cardiomyocytes were used for subcellular fractionation of nuclear and cytoplasmic RNA (figure 17 B). In both species, Sarrah is predominantly localized in the nucleus with 31.5 percent in the cytoplasm in human and only 7.9 percent in mouse.

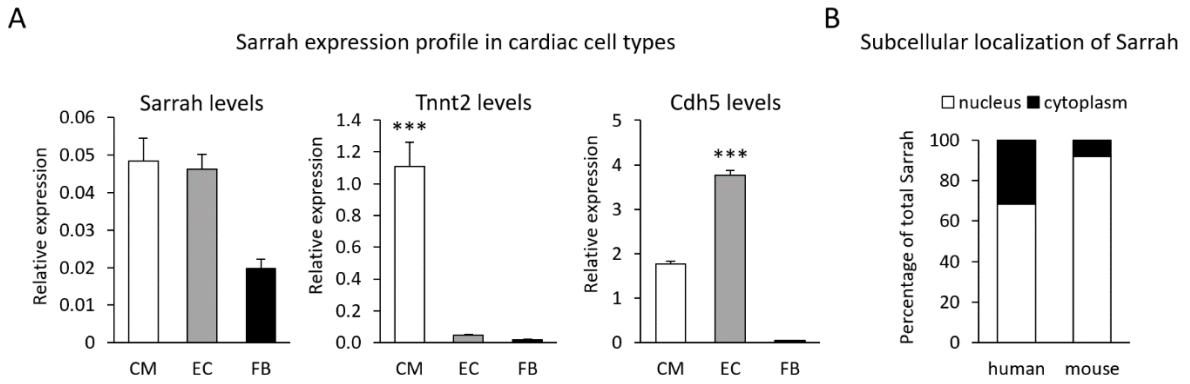

Figure 17: Cellular and subcellular Sarrah expression profiles. (A) Hearts of 10 weeks old mice were isolated and fractionated into cardiomyocytes (CM), endothelial cells (EC) and fibroblasts (FB). Levels of Sarrah, the cardiomyocyte marker Tnnt2 and the endothelial cell marker Cdh5 were measured by qRT-PCR (n = 5; SEM; *** t-test $p < 0.001$). (B) Primary human cardiomyocytes and mouse HL-1 cardiomyocytes were used for fractionation of cytoplasmic and nuclear RNA. Sarrah levels were measured by qRT-PCR (n = 3).

Taken together, lncRNA Sarrah was identified to be aging-regulated in the heart, to be locus- and partially sequence-conserved, to lack any coding potential and to be expressed in the nucleus of cardiomyocytes, where Sarrah silencing induced apoptosis, as well as in other cardiac cell types.

4.2 Sarrah is Downregulated during Aging and under Aging-Related Conditions

According to the initial RNA deep sequencing data, Sarrah is downregulated during aging (figure 15). This was confirmed in hearts of a separate cohort of young and aged mice, which displayed significantly reduced Sarrah levels in the aged group compared with young mice (figure 18).

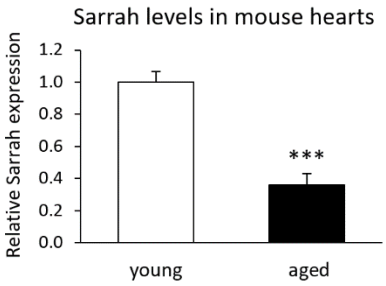

Figure 18: Sarrah is downregulated during aging. Sarrah levels were measured by qRT-PCR in whole-heart tissue from young (8 weeks) and aged (20 months) mice (n = 6; SEM; *** t-test $p < 0.001$).

Since aging is a major risk factor to suffer an acute myocardial infarction (AMI) and to develop heart failure with preserved ejection fraction (HFpEF), two highly prevalent cardiovascular conditions in the elderly, it was investigated whether Sarrah is regulated after AMI and upon HFpEF in two rodent models. AMI was induced in mice by ligation of the left anterior descending (LAD) coronary artery. In comparison to sham-operated control mice, Sarrah levels were significantly reduced in AMI mice in the infarct region on days 3, 7 and 14 after AMI as well as in the border region on days 1, 3 and 7 after AMI. In a remote control region, Sarrah levels were not affected by AMI (figure 19 A). Two obese ZSF1 rat groups that were fed either standard or high fat diet (HFD) served as a HFpEF model. In both groups, Sarrah levels were significantly lower than in the wildtype (WT) control and the hypertensive control groups (figure 19 B).

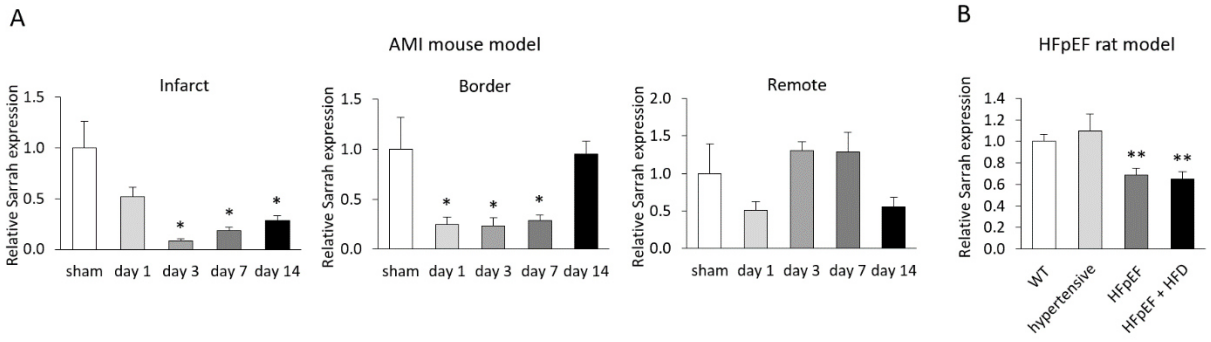

Figure 19: Sarrah is downregulated after AMI and upon HFpEF in rodents. (A) AMI was induced in mice by LAD ligation. Sarrah levels were measured by qRT-PCR in the infarct, border and remote region of sham-operated and AMI mouse hearts on days 1, 3, 7 and 14 after surgery (n = 3; SEM; * t-test $p < 0.05$). (B) Sarrah levels were measured by qRT-PCR in whole-heart tissue from male 20 weeks old Wistar-Kyoto WT rats, lean hypertensive ZSF1 rats without HFpEF phenotype and obese ZSF1 rats fed either a standard of high fat diet, both with HFpEF phenotype (n = 5-6; SEM; ** t-test $p < 0.01$).

A hallmark of the aging heart is ischemia in the myocardium, which plays an essential role in AMI, but also HFpEF. To mimic the setting of ischemia *in vitro*, human and mouse cardiomyocytes were cultured under hypoxic conditions for 24 hours (figure 20 A). As an alternative means to induce hypoxia, cells were treated with desferrioxamine (DFO), an iron ion chelating compound that prevents degradation of the hypoxia-responsive transcription factor HIF1A by inhibiting the activity of iron ion-dependent

hydroxylases[316] (figure 20 B). In both experiments, induction of hypoxia was verified by measuring an increase in vascular endothelial grwoth factor (VEGF), one of the targets of HIF1A[317]. Both under hypoxic cell culture conditions and upon DFO treatment, Sarrah levels were significantly downregulated in human and mouse cardiomyocytes.

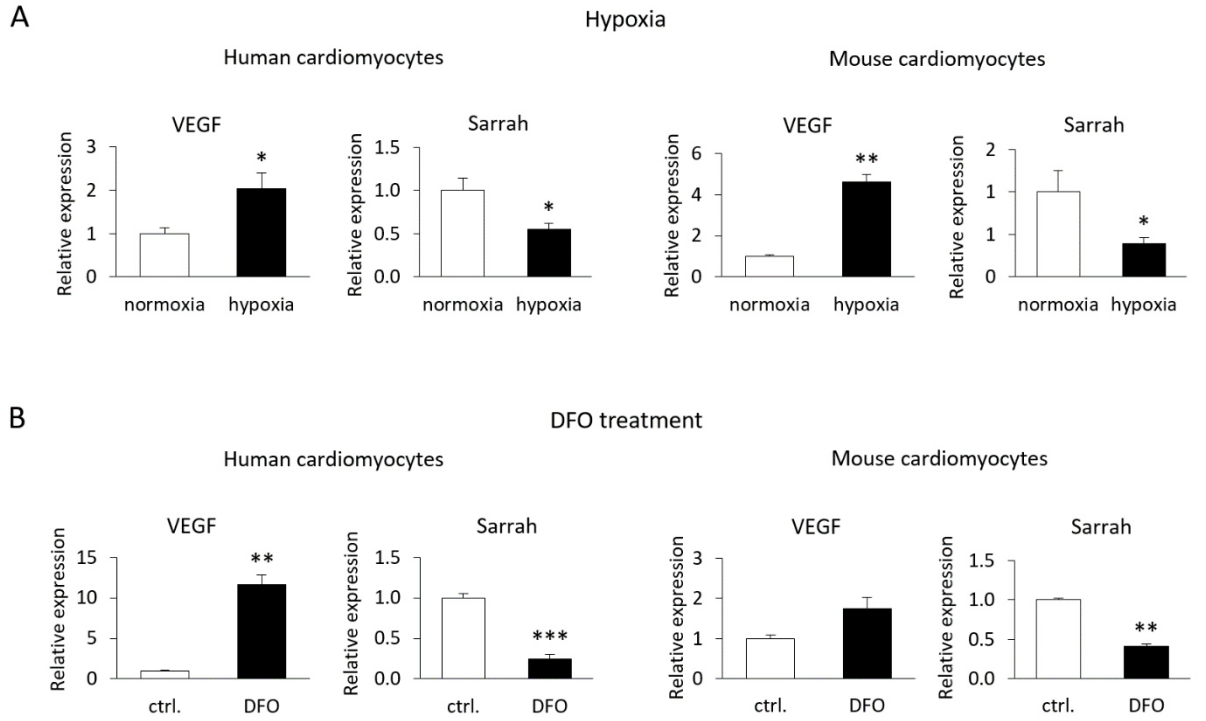

Figure 20: Sarrah is downregulated upon hypoxia and DFO treatment *in vitro*. (A) Primary human cardiomyocytes and mouse HL-1 cardiomyocytes were cultured at 0.2 percent oxygen (human) or 1 percent oxygen (mouse), respectively, for 24 h. RNA was isolated and Sarrah levels were measured by qRT-PCR. VEGF mRNA levels were quantified to confirm induction of hypoxia (n = 3; SEM; * t-test $p < 0.05$; ** t-test $p < 0.01$). (B) Primary human cardiomyocytes and mouse HL-1 cardiomyocytes were treated with 300 µM DFO for 24 h. RNA was isolated and Sarrah levels were measured by qRT-PCR. VEGF mRNA levels were quantified to confirm induction of hypoxia (n = 3; SEM; ** t-test $p < 0.01$; *** t-test $p < 0.001$).

These results demonstrate that in rodents, Sarrah is downregulated during aging alone, but also under pathological conditions after AMI or during HFpEF that are more likely to occur with increasing age. Besides, modeling ischemic conditions by inducing or chemically mimicking hypoxia in cell culture downregulated Sarrah in both human and mouse cardiomyocytes.

4.3 Sarrah is Anti-Apoptotic in Mouse and Human Cardiomyocytes

Sarrah was identified in an siRNA-based apoptosis screening (figure 14 B). But since caspase-3/7 measurements were precluded because of cell death of all cardiomyocytes upon treatment with siRNAs against Sarrah, it remained to be confirmed that Sarrah depletion induces apoptosis rather than a different type of cell death. To this end, caspase-3/7 activity measurements after Sarrah silencing were repeated without induction by hydrogen peroxide. This time, as the major proportion of Sarrah

is localized in the nucleus, which cannot be entered by siRNAs, locked nucleic acid (LNA) GapmeRs were used to pharmacologically deplete Sarrah by RNase H cleavage[318]. In both mouse and human cardiomyocytes, transfection of LNA GapmeRs targeting Sarrah resulted in a significant reduction of Sarrah levels (figure 21 A), which augmented caspase-3/7 activity as suggested by the initial apoptosis screening (figure 21 B). Conversely, when human Sarrah was overexpressed in human cardiomyocytes using lentivirus particles (figure 21 C), caspase-3/7 activity was dramatically reduced (figure 21 D), indicating that Sarrah is an anti-apoptotic lncRNA.

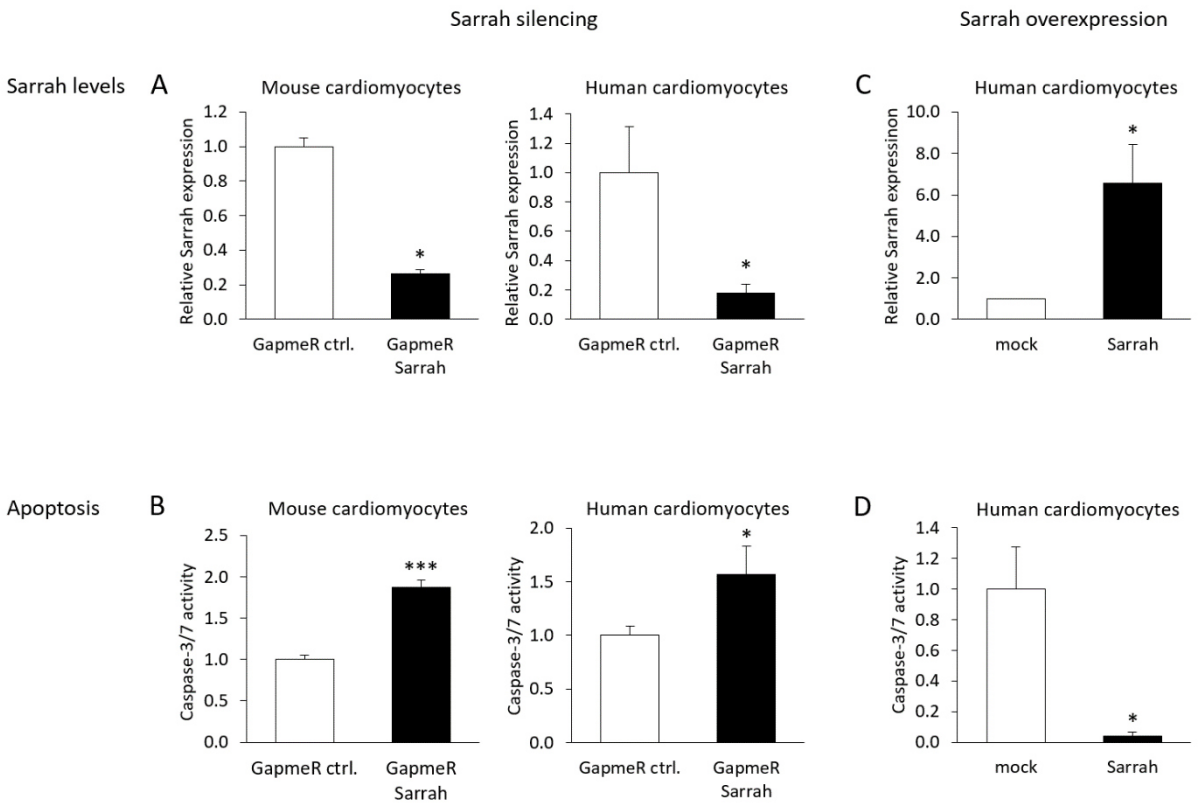

Figure 21: Sarrah can be silenced by GapmeRs, overexpressed with lentiviral particles and negatively correlates with caspase-3/7 activity. (A) Mouse HL-1 cardiomyocytes and primary human cardiomyocytes were transfected with LNA GapmeR control or LNA GapmeR targeting Sarrah. RNA was isolated and Sarrah levels were measured by qRT-PCR 48 h later (n = 3; SEM; * t-test $p < 0.05$). (B) Mouse HL-1 cardiomyocytes and primary human cardiomyocytes were transfected with LNA GapmeRs. Apoptosis was quantified by caspase-3/7 activity measurements 48 h later (n = 3; SEM; * t-test $p < 0.05$; * t-test $p < 0.001$). (C) Primary human cardiomyocytes were transduced with lentiviral particles containing a mock sequence or the human Sarrah sequence. RNA was isolated and Sarrah levels were measured by qRT-PCR ten days later (n = 4; SEM; * t-test $p < 0.05$). (D) Primary human cardiomyocytes were transduced with lentiviral particles. Apoptosis was quantified by caspase-3/7 activity measurements ten days later (n = 4; SEM; * t-test $p < 0.05$).

To verify that Sarrah depletion induces apoptosis rather than necrosis by using another cell death assay, LNA GapmeR-transfected mouse cardiomyocytes were stained with annexin V and 7-AAD followed by flow cytometry analysis (figure 22). During early apoptosis, phosphatidylserine is flipped from the inner to the outer plasma membrane leaflet, where it can be bound by the phospholipid-binding protein annexin V[319]. 24 hours after Sarrah knockdown, the amount of dieing annexin V-single-

positive cells increased. Another 24 hours later, a major proportion of cells turned double-positive for annexin V and 7-AAD, which stains dead cells that have become permeable.

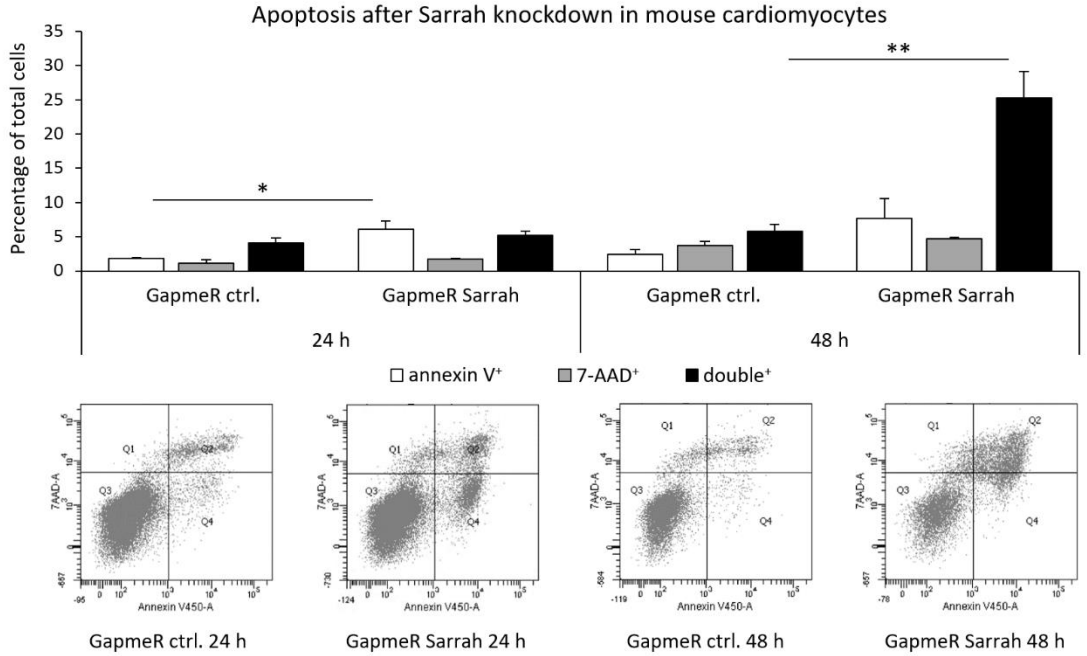

Figure 22: Sarrah silencing increases the amount of annexin V-positive cells. Mouse HL-1 cardiomyocytes were transfected with LNA GapmeRs and stained with annexin V-450 and 7-AAD 24 h or 48 h later. Annexin V specifically stains apoptotic cells, 7-AAD stains all dead cells regardless of the cell death type. Early apoptosis manifests as annexin V-single-positive cells, late apoptosis as double-positive cells. The staining was quantified by flow cytometry (top), representative images are shown (bottom; n = 3; SEM; * t-test $p < 0.05$; ** t-test $p < 0.01$).

Based on the increase in caspase-3/7 activity and in the annexin V-positive cardiomyocyte proportion upon Sarrah silencing, it can be concluded that the cell-protective effect of Sarrah is anti-apoptotic rather than anti-necrotic.

4.4 Sarrah Is Required for Contractility of Rat and Human Cardiomyocytes

Cardiac contractile function is diminished both after AMI and upon HFpEF. Since Sarrah expression is reduced by both conditions *in vivo*, an interesting question was to examine whether Sarrah depletion also diminishes cardiomyocyte contractility *in vitro*. Therefore, cardiomyocytes were isolated from neonatal rats, plated on coated glass coverslips and treated with LNA GapmeR control or LNA GapmeR targeting Sarrah, respectively, to establish a Sarrah knockdown in primary rat cells (figure 23 A). Adding high concentrations of LNA GapmeRs directly to the culture medium without any transfection reagent resulted in a solid Sarrah knockdown. Contractility measurements were performed on individual, viable, beating cardiomyocytes, thereby selecting for cells in which Sarrah depletion had not induced apoptosis yet. Upon Sarrah knockdown, cardiomyocytes exhibited a reduced contraction amplitude

and slower maximal contraction and relaxation velocities compared with LNA GapmeR control-treated cells, which reflects the AMI and HFpEF phenoytpes (figure 23 B).

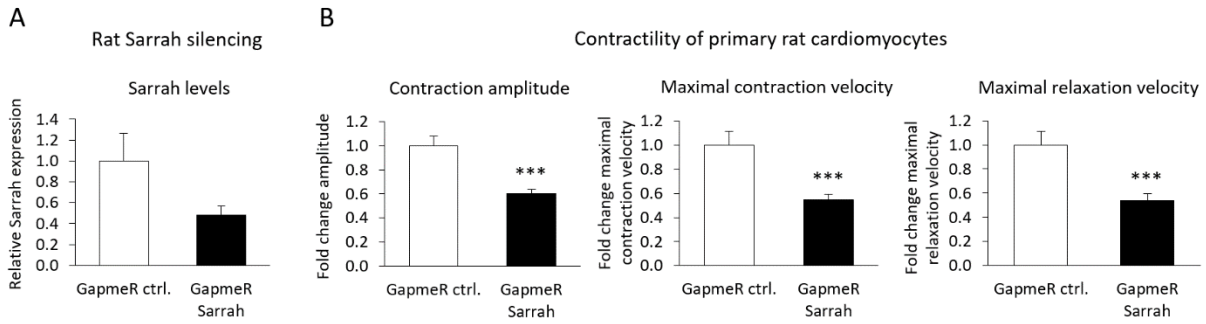

Figure 23: Sarrah silencing reduces contractility of primary rat cardiomyocytes. Primary rat cardiomyocytes were isolated from neonatal rats, plated on coated glass coverslips and treated with 325 nM LNA GapmeR. Cells were harvested from the coverslips for RNA isolation and quantification by qRT-PCR (A) after being subjected to contractility measurements using the IonOptix Myocyte Contractility Recording System (B). Cells were warmed to 37 °C during the measurements. The results were analyzed using the IonWizard software (n = 43-46; SEM; *** t-test $p < 0.001$).

In order to translate the results about Sarrah effects on cardiomyocyte apoptosis and contractility from rodent cells to human tissue, spontaneously beating human engineered heart tissue (EHT) organoids were used. For generation of EHT organoids, human induced pluripotent stem cells (hiPSCs) obtained by fibroblast reprogramming were differentiated into cardiomyocytes and embedded in a basement membrane together with human umbilical vein endothelial cells (HUVECs; figure 24).

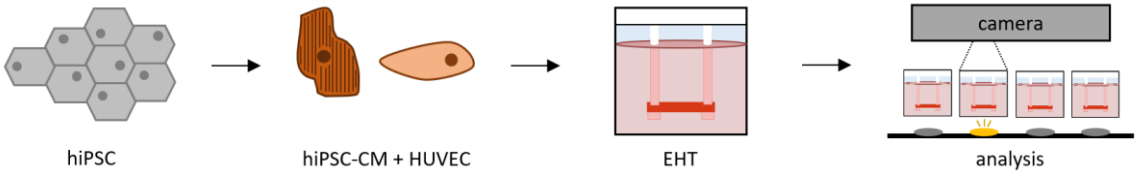

Figure 24: Scheme illustrating the generation and analysis of engineered heart tissue (EHT) organoids. EHT organoids were generated from 1,000,000 hiPSC-cardiomyocytes (CMs) and 300,000 HUVECs each and embedded in a basement membrane matrix. After onset of coherent beating on day 6, organoid contractility parameters were recorded three times per week.

Contractile force development in EHT organoids in which Sarrah was silenced by LNA GapmeRs was delayed by seven days (day 12 vs. day 5) and less pronounced than in organoids treated with an LNA GapmeR control. Fractional shortening, a parameter of contractility, was also reduced by 35 percent on day 10 compared with control organoids (figure 25 A). After contractility analysis, EHT organoids were fixed for histology and stained by TdT-mediated dUTP-biotin nick end labeling (TUNEL), which revealed significantly more apoptotic nuclei in Sarrah-silenced organoids (figure 25 B) than in controls.

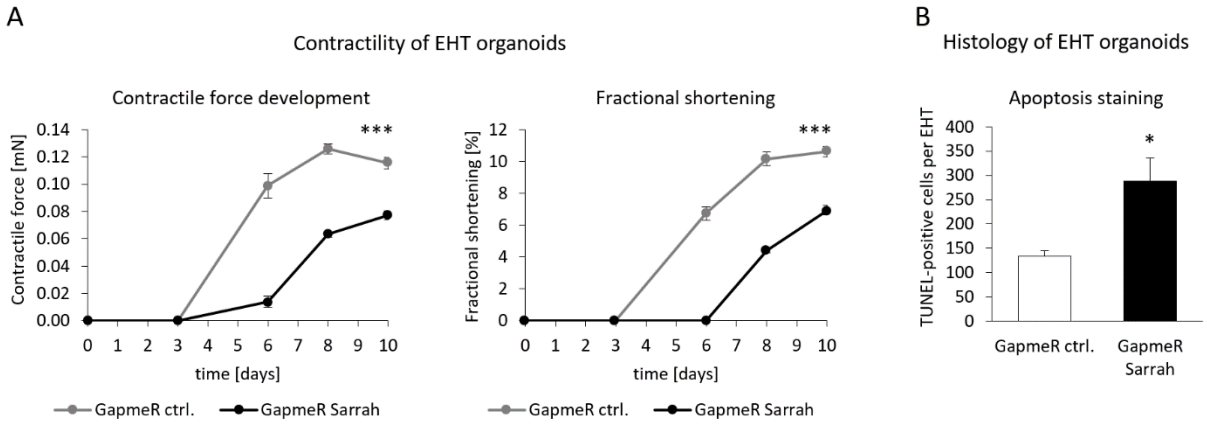

Figure 25: Sarrah-silenced EHT organoids exhibit reduced contractility and increased apoptosis. (A) EHT organoids consisting of cardiomyocytes and HUVECs were treated with LNA GapmeRs at a final concentration of 4 µM for 2 days. Contractile force development and fractional shortening of EHT organoids were recorded on days 0, 3, 6, 8 and 10 by the EHT contractility analysis instrument from EHT Technologies and analyzed using the corresponding software (n = 8; SEM; *** two-way ANOVA treatment $p < 0.0001$, $F = 44.39$; *** two-way ANOVA time $p < 0.0001$, $F = 221.22$). (B) After 22 days in culture, EHT organoids were fixed and stained by TUNEL as whole specimens to assess apoptosis (n = 4; SEM; * t-test $p < 0.05$).

The findings from primary rat cardiomyocytes and human engineered heart tissue demonstrate that Sarrah plays a crucial role for cardiomyocyte contractility and further consolidate the evidence suggesting that Sarrah is anti-apoptotic.

4.5 Sarrah Does not Influence Genes in *cis*

To elucidate the mechanism via which Sarrah affects apoptosis and contractility, the effect of Sarrah silencing on nearby genes was investigated. *Cis* gene regulation has been reported for several lncRNAs and is recognized as a common mechanism, especially for lncRNAs that are transcribed antisense to a protein-coding gene[320]. Beside overlapping with the gene locus of OXCT1, from which the enzyme succinyl-CoA:acetoacetate transferase 1 (SCOT1) is transcribed, Sarrah is located in proximity of the gene encoding F-box protein 4 (FBXO4) and, in humans, the annotated open reading frame c5orf51 (figure 26).

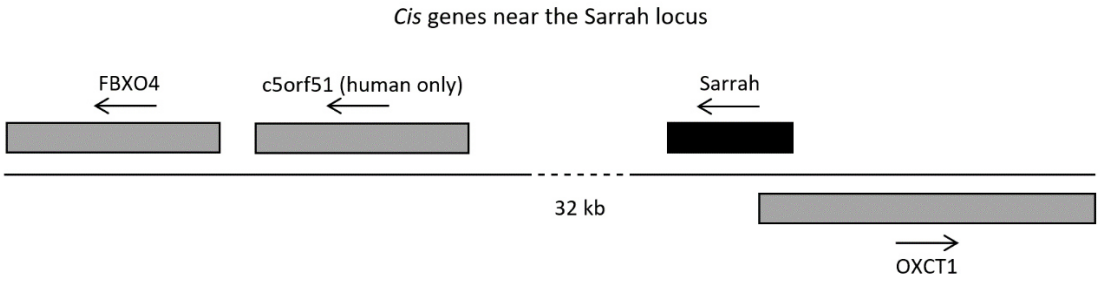

Figure 26: Scheme depicting the Sarrah gene locus with neighboring genes. The gene encoding Sarrah is transcribed antisense to the OXCT1 gene, which encodes the enzyme SCOT1, and overlaps with its transription start site. Two nearby protein-coding genes transcribed from the same strand are FBXO4 and, in humans only, c5orf51 (kb: kilobases).

In human cardiomyocytes, neither OXCT1 nor FBXO4 nor c5orf51 were significantly affected by Sarrah knockdown on mRNA level (figure 27 A), but OXCT1 mRNA levels exhibited a slight reduction that can likely be attributed to shared regulatory elements of Sarrah and OXCT1. In mouse cardiomyocytes, FBXO4 mRNA levels were unaltered upon Sarrah knockdown, whereas OXCT1 mRNA was downregulated, even though not as efficiently as upon treatment with an siRNA taregting OXCT1 that was transfected as a positive control (figure 27 B).

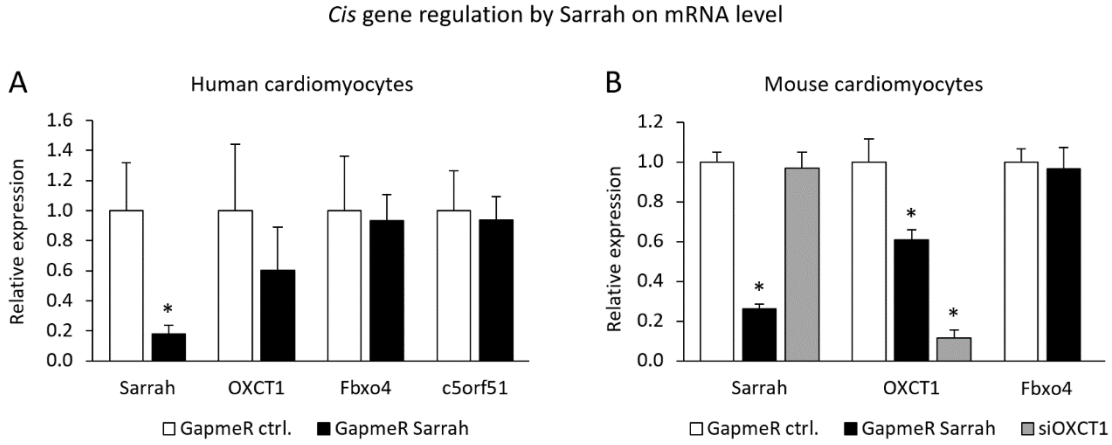

Figure 27: Effect of Sarrah knockdown on mRNA levels of *cis* genes. (A) Primary human cardiomyocytes were transfected with LNA GapmeRs. RNA was isolated and quantified by qRT-PCR 48 h later (n = 3; SEM; * t-test $p < 0.05$). (B) Mouse HL-1 cardiomyocytes were transfected with LNA GapmeRs or siRNA targeting OXCT1. RNA was isolated and quantified by qRT-PCR 48 h later (n = 4; SEM; * t-test $p < 0.05$).

To determine whether the modest reduction on mRNA level was sufficient to exert an effect on the enzymatic level, SCOT1 activity was measured after Sarrah knockdown in mouse cardiomyocytes (figure 28 A). The assay revealed that the substrate conversion rate of SCOT1 was very comparable between cells treated with an LNA GapmeR targeting Sarrah and a control LNA GapmeR while being significantly impeded by siRNA knockdown of OXCT1, indicating that Sarrah does not regulate SCOT1 enzymatic activity. An apoptosis assay with mouse cardiomyocytes allowed to ultimately exclude the possibilty that Sarrah functions via *cis* gene regulation as caspase-3/7 activity did not increase upon OXCT1 silencing (figure 28 B).

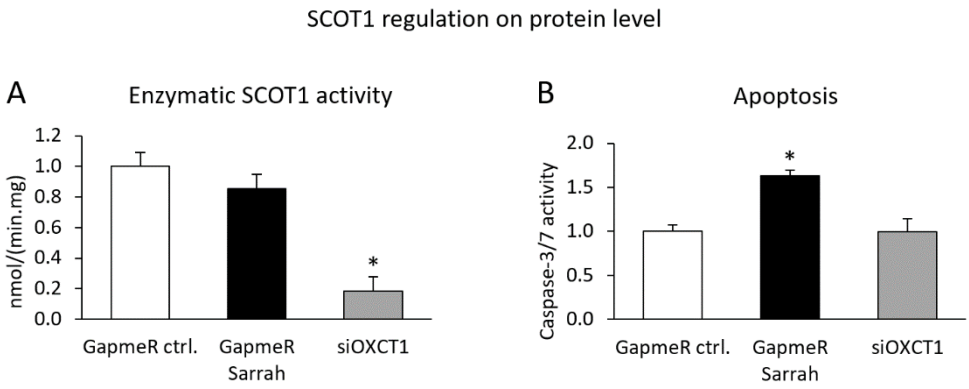

Figure 28: SCOT1 enzymatic activity and impact on apoptosis. (A) Mouse HL-1 cardiomyocytes were transfected and homogenized 48 h later for SCOT1 activity assay. SCOT1 enzymatic activity was measured as succinate-induced decrease in absorbance at 303 nm. SiRNA knockdown of SCOT1 was performed as a positive control (n = 5; SEM; * t-test $p < 0.05$). (B) Apoptosis was assessed by caspase-3/7 activity measurements in mouse HL-1 cardiomyocytes 48 h after transfection. SiRNA knockdown of SCOT1 was performed as a positive control (n = 3; SEM; * t-test $p < 0.05$).

In conclusion, Sarrah does not regulate mRNA levels of neighboring genes or SCOT1 activity in cardiomyocytes. The anti-apoptotic effects of Sarrah cannot be reproduced by SCOT1 silencing, either. Sarrah therefore does not seem to act via *cis* gene regulation.

4.6 Sarrah Impacts Apoptosis-Related Gene Expression

Genes regulated by Sarrah were globally identified in a microarray analysis of RNA from human cardiomyocytes transfected with an LNA GapmeR control or an LNA GapmeR targeting Sarrah, respectively. The analysis revealed that 501 genes were downregulated and 961 genes were upregulated after Sarrah silencing with a significance level of a p-value less than 0.05 in Student's t-test (figure 29 A). Enrichment analysis of down- and upregulated gene sets showed that pathways induced by Sarrah knockdown are mostly related to apoptosis, p53 signaling and DNA repair. Pathways repressed after Sarrah knockdown include among others myogenesis (figure 29 B).

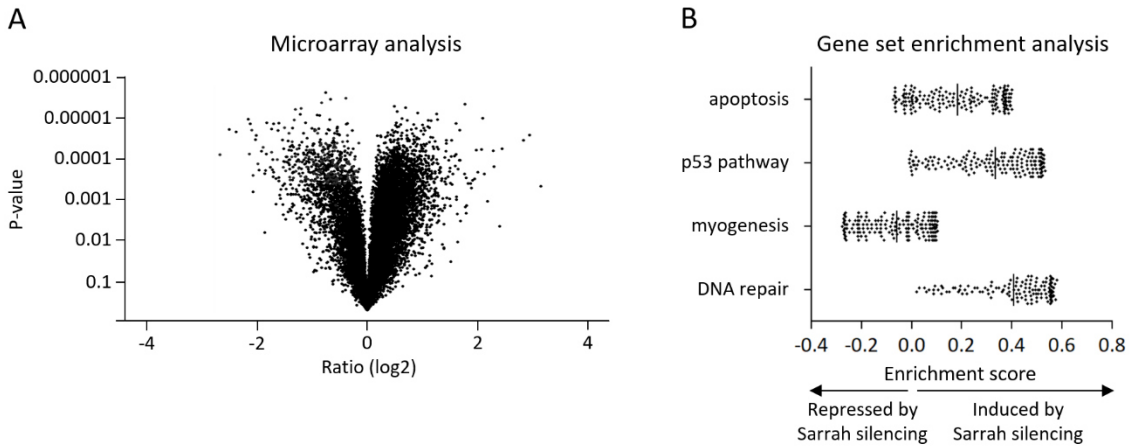

Figure 29: Microarray analysis reveals apoptosis-related genes affected by Sarrah knockdown. (A) A microarray analysis was performed with RNA of primary human cardiomyocytes. A volcano plot shows all genes measured in the microarray that are down- or upregulated more than -2-fold or 2-fold, respectively, in LNA GapmeR Sarrah-treated samples compared with LNA GapmeR control-treated samples (n = 3). (B) Gene set enrichment analysis with genes up- and downregulated after Sarrah silencing in the microarray reveals differentially regulated pathways.

Regulation of some of the most profoundly up- and downregulated genes in the microarray analysis was validated by qRT-PCR in three separate sets of transfected samples (figure 30).

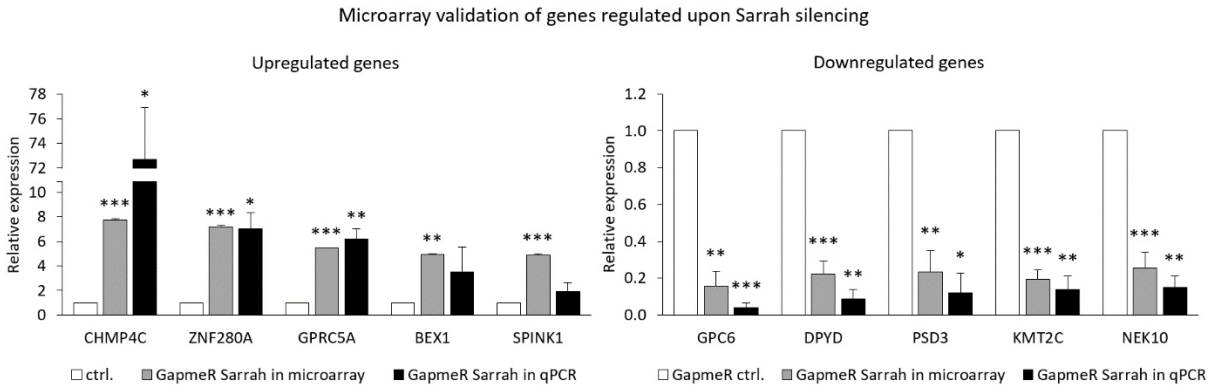

Figure 30: Validation of genes regulated upon Sarrah silencing using qRT-PCR. Regulation of some of the most significantly up- (left) and downregulated (right) genes from the microarray analysis was confirmed by qRT-PCR in primary human cardiomyocytes (n = 3; SEM; * t-test $p < 0.05$; ** t-test $p < 0.01$; *** t-test $p < 0.001$).

Overall, genome-wide identification of genes regulated by Sarrah yields several affected gene sets that confirm the anti-apoptotic function of the lncRNA.

4.7 Sarrah Forms Triplexes with Genomic DNA of Gene Promoters

Since Sarrah is located in the nucleus and has profound effects on gene expression, it was hypothesized that it might be associated with chromatin to regulate transcription. This eventuality was first estimated by an RNA immunoprecipitation (RIP) of histone H3 and quantification of co-precipitated Sarrah by qRT-PCR (figure 31). An 8.4-fold enrichment of Sarrah in histone H3-precipitated samples compared with immunoglobulin G (IgG) control samples indicated a significant localization to chromatin in human cardiomyocytes and underpinned the possibility that Sarrah may act as a transcriptional regulator in *trans*.

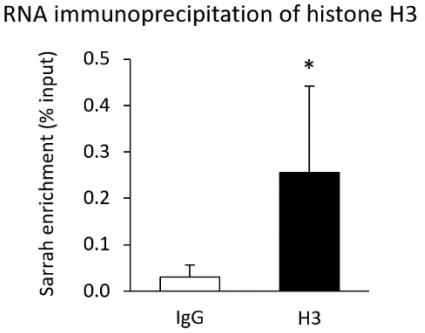

Figure 31: RNA immunoprecipitation of histone H3 indicates Sarrah association with chromatin. Sarrah levels were quantified by qRT-PCR in samples from RNA immunoprecipitation experiments using an IgG control antibody and a total histone H3 antibody in primary human cardiomyocytes (n = 3; SEM; * t-test $p < 0.05$).

Some lncRNAs that regulate transcription of distant genes have been reported to do so by forming triplexes with genomic DNA, preferentially promoters, and recruiting histone modifiers to these loci. To test whether Sarrah is capable of triplex formation, the Triplex Domain Finder software[321] was used. In a first step, the human and mouse Sarrah sequences were scanned for triple helix-prone motifs. In both human and mouse Sarrah, a pyrimidine-rich stretch of 22 or 34 nucleotides, respectively, was identified that is predicted to form parallel triplexes with double-stranded DNA (figure 32 and table 26).

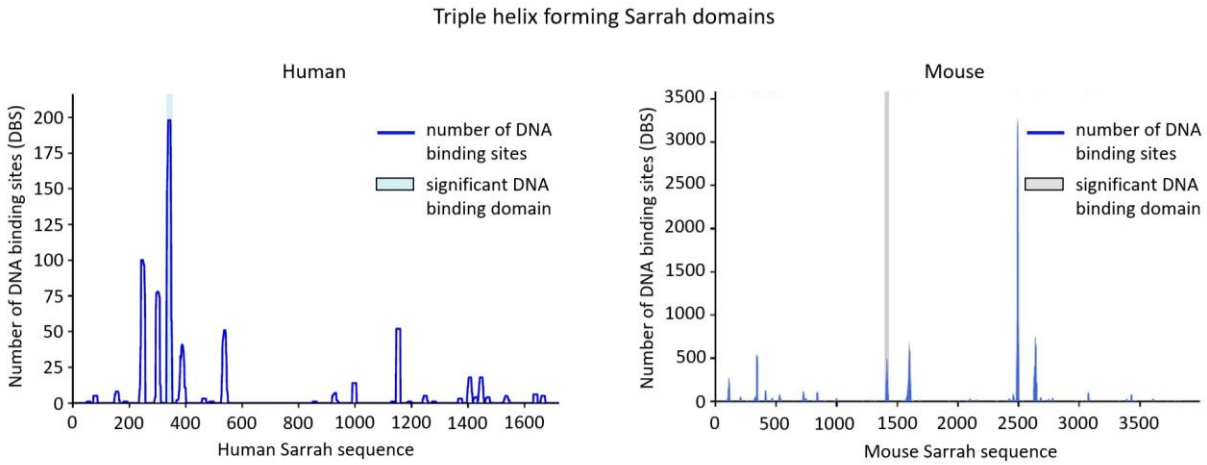

Figure 32: Triplex Domain Finder predicts Sarrah to contain triplex-prone motifs. The human (left) and mouse (right) Sarrah sequences were analyzed using the Triplex Domain Finder software to identify regions capable of DNA binding via triple helix formation (significance level: t-test $p < 0.05$).

In a next step, the genes up- and down-regulated by Sarrah silencing that had been identified in the microarray were analyzed with regard to sequence motifs capable to bind the predicted triple helix forming region in human and mouse Sarrah, respectively (figure 33).

Figure 33: Flow chart illustrating the procedure of predicting triple helix formation by Sarrah. The genes that had been identified as up- or downregulated by Sarrah in the microarray analysis of primary human cardiomyocyte RNA and the pyrimidine-rich Sarrah motifs that had been detected to be capable of triple helix formation in the first step of the Triplex Domain Finder analysis were used in the second step of triplex prediction by the Triplex Domain Finder. The software found an enrichment of Sarrah binding regions in promoters of downregulated, but not upregulated genes.

In both species, a significant enrichment of Sarrah binding sites was detected in promoters of downregulated genes (human: $p = 0.0033$; mouse: $p = 0.0012$). No interaction was found for upregulated genes (human: $p = 0.31$; mouse: $p = 0.99$). The human genome was predicted to harbour

134 Sarrah binding sites, while 162 Sarrah binding sites were identified in the mouse genome (table 26, appendices A-C), which represents 27 and 32 percent of downregulated genes, respectively. 54 triplex forming genes including glypican 6 (GPC6), the most profoundly downregulated gene from the microarray, overlap in both species to be targeted by Sarrah, constituting a share of 40 percent, which is within the same range as target conservation of microRNAs[322]. Gene ontology analysis of the 134 human genes presumably forming triple helices using the Database for Annotation, Visualization and Integrated Discovery (DAVID) revealed that associated disease categories were “cardiovascular” ($p = 5.8x10^{-8}$) and “aging” ($p = 0.0032$), further corroborating the proposed triplex formation by the cardiac, aging-regulated lncRNA Sarrah.

Table 26: Triplex Forming Sarrah Motifs and Corresponding DNA Binding Sites in Human and Mouse

Species	Sarrah region	Sarrah sequence	P-value	Number of targets
Human	332-353	GCCCCCTTCTCTTCTCCCGCCT	0.0033	134
Mouse	1399-1432	GTGTCTGTCTCCTCTCCTCCTCGTCCTTGTCCAT	0.0012	162

The exclusive prevalence of predicted Sarrah binding sites in downregulated gene promoters suggests that Sarrah interacts with DNA to activate gene expression. To experimentally validate that this interaction can indeed occur between the given sequences, binding between Sarrah and the GPC6 promoter was tested *in vitro* (figure 34 A). To this end, nuclear magnetic resonance (NMR) spectra of the Sarrah triplex motifs as single-stranded RNA oligonucleotides and the corresponding GPC6 promoter binding sites as double-stranded DNA oligonucleotides were recorded (figure 34 B).

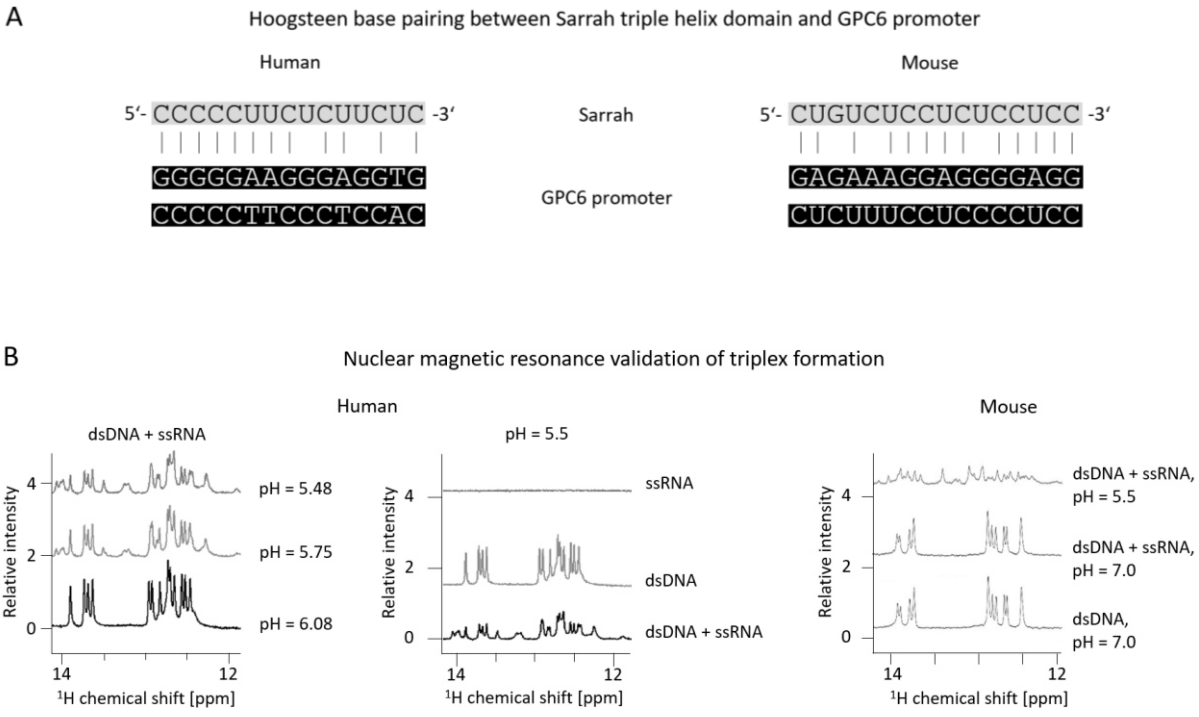

Figure 34: Nuclear magnetic resonance confirms triplex formation between Sarrah and the GPC6 promoter. (A) Scheme depicting triplex formation between Sarrah and the GPC6 promoter in human (left) and mouse (right). Vertical lines indicate Hoogsteen hydrogen bonding. (B) ^{1}H spectra of the Sarrah triplex motif as 15 nucleotides long ssRNA and the Sarrah binding site in the GPC6 promoter as 15 nucleotides long dsDNA in equal molar ratios for human (left and middle) and mouse sequences (right). Spectra were recorded in a solution with 100 µM nucleic acid at 288 K.

NMR spectra of ssRNA and dsDNA confirmed that Sarrah can bind the GPC6 promoter in human and mouse. In detail, the spectra show imino proton peaks indicative of Watson-Crick base pairing within DNA duplexes between 12 and 14 ppm. At neutral pH, no additional peaks were observed upon addition of ssRNA. However, at lower pH, several new peaks appeared (figure 34 B, left panel, upper two spectra and right panel, uppermost spectrum). These peaks are consistent with Hoogsteen hydrogen bonding between dsDNA and ssRNA, which indicates triplex formation. Their occurrence requires slightly acidic conditions *in vitro* for cytosine protonation at the N3 position[323], which facilitates cytosine-rich RNA binding to DNA duplexes[216] to form C^{+}-GC triplex structures[324]. To verify that the new peaks are specific to triplex structures rather than being the result of secondary structure formation by ssRNA or dsDNA alone, NMR spectra of isolated RNA and isolated DNA were recorded at acidic conditions as controls, but no peaks suggestive of triplex formation or any other structures like RNA hairpins, RNA-RNA duplexes or unique DNA conformations were observed (figure 34 B, middle panel and bottom spectrum in right panel).

These findings confirm that both the human and murine Sarrah sequences are able to interact with dsDNA by forming parallel triplexes via the proposed triplex motifs with the predicted gene promoters.

To further verify that Sarrah forms triplexes in cells, triplex formation in human cardiomyocytes was investigated. Therefore, downregulation of five selected genes – GPC6, PDE3A, ITPR2, PARP8 and SSBP2 – whose promoters are predicted to interact with Sarrah and that are involved in apoptosis was validated by qRT-PCR (figure 35). All genes were observed to be significantly downregulated in three separate sets of Sarrah-silenced human cardiomyocytes compared with control cells.

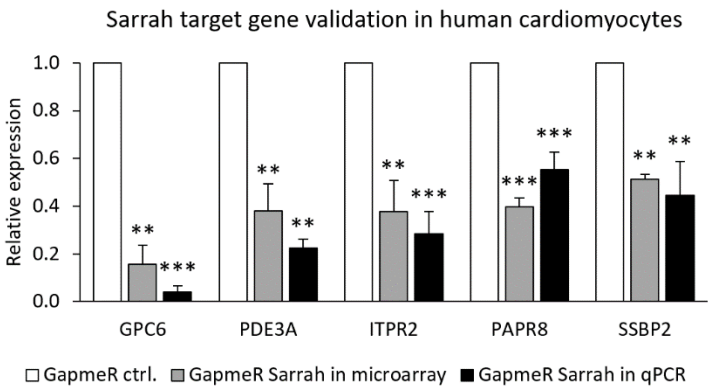

Figure 35: Sarrah target gene validation in human cardiomyocytes. From the 134 human genes predicted to be modulated by Sarrah triplex formation in their promoters, five were selected based on profound reduction in the microarray analysis

and implication in apoptosis. Downregulation was confirmed by qRT-PCR in primary human cardiomyocytes (n = 3; SEM, * t-test $p < 0.05$; ** t-test $p < 0.01$, *** t-test $p < 0.001$).

Physical interaction of Sarrah with genomic DNA in human cardiomyocytes was corroborated by RNA immunoprecipitation using an antibody that recognizes DNA-RNA hybrids[297] (figure 36 A). In contrast to U4 snRNA that was measured as a negative control, Sarrah was significantly enriched over IgG control, indicating that Sarrah interacts with genomic DNA in human cardiomyocytes. Furthermore, in a chromatin immunoprecipitation (ChIP) with the same antibody, fragments of genomic DNA that interact with RNA were precipitated. Among them, the promoter regions of GPC6, PDE3A, ITPR2, PARP8 and SSBP2 containing predicted Sarrah binding sites were significantly enriched over IgG control in contrast to negative control GAPDH promoter fragments (figure 36 B). The experiment was repeated with an additional RNase H digestion step, which degrades some DNA-RNA structures such as R loops, but which DNA-RNA triplexes are insensitive to[298]. After RNase H digestion, promoters of four out of five predicted Sarrah target genes were still enriched over IgG control in precipitated DNA samples with only ITPR2 promoter levels being affected by RNase H. This indicates that the majority of Sarrah target genes forms triple helices in their promoters.

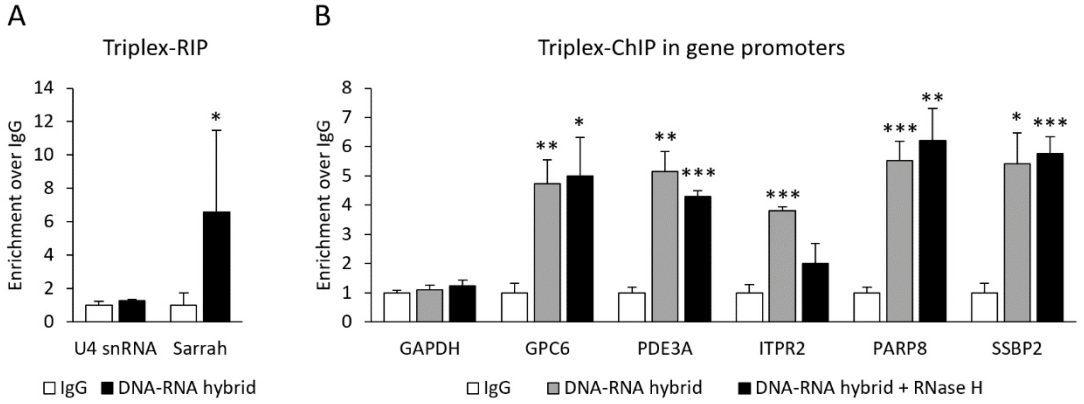

Figure 36: Immunoprecipitation experiments with a DNA-RNA hybrid-binding antibody indicate association of Sarrah and most target gene promoters with triplex structures. (A) Levels of U4 snRNA as negative control and Sarrah were measured by qRT-PCR in immunoprecipitates of crosslinked primary human cardiomyocyte RNA using an S9.6 anti-DNA-RNA hybrid antibody (n = 3; SEM, * t-test $p < 0.05$). (B) Levels of the GAPDH promoter as negative control and five Sarrah target gene promoters were measured by qRT-PCR in immunoprecipitates of crosslinked and sonicated primary human cardiomyocyte genomic DNA using an S9.6 anti-DNA-RNA hybrid antibody and protocols with and without RNase H digestion, respectively (n = 4; SEM, * t-test $p < 0.05$; ** t-test $p < 0.01$, *** t-test $p < 0.001$).

Eventually, functional importance of triplex formation by Sarrah was evaluated using a clustered regularly interspaced short palindromic repeats (CRISPR) / CRISPR-associated protein 9 (Cas9)-mediated approach to excise the endogenous triplex forming motif of Sarrah in the murine HL-1 cell line (figure 37 A). After transduction of the cells with virus particles containing mock single guide RNAs (sgRNAs) or sgRNAs guiding the Sarrah triplex motif deletion, the cells were used for an apoptosis assay and RNA isolation (figure 37 B).

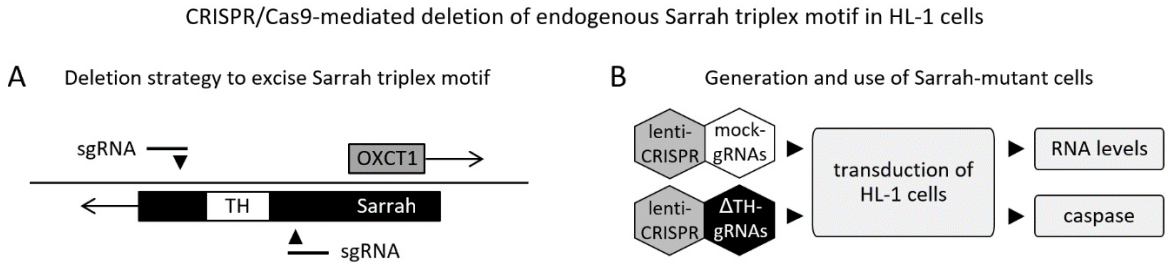

Figure 37: Scheme illustrating the Sarrah triplex motif deletion strategy and experimental work flow. (A) The triple helix (TH) motif of Sarrah was targeted by sgRNAs flanking the region without affetcing the OXCT1 gene. (B) Mouse HL-1 cardiomyocytes were transduced with a mix of virus particles for expression of the Cas9 nuclease and mock or Sarrah triple helix domain-targeting sgRNAs. Six days after transduction, cells were used for RNA isolation and seeded for an apoptosis assay.

Successful deletion of the triple helix forming domain within Sarrah (SarrahΔTH) was confirmed on RNA level by qRT-PCR using primers that bind within the excised region (figure 38 A). Cardiomyocytes with mutated Sarrah lacking the triplex motif exhibited significantly increased baseline apoptosis compared with mock-transduced cells, providing evidence for the fuctional importance of the triple helix forming domain (figure 38 B). However, of the five selected Sarrah target genes, only ITPR2 mRNA levels decreased significantly (figure 38 C). The other four genes displayed a slight, but statistically not significant tendency towards downregulation, suggesting that other effectors contribute to the anti-apoptotic function of Sarrah.

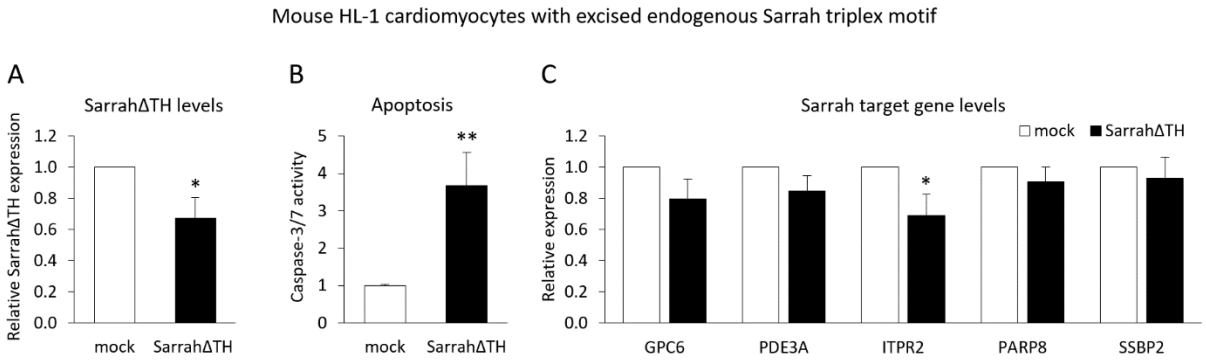

Figure 38: RNA levels and caspase activity in HL-1 cells lacking the endogenous Sarrah triplex motif. (A) Deletion of the Sarrah triplex motif in mouse HL-1 cardiomyocytes by sgRNAs was confirmed by qRT-PCR using primers binding within the deleted region. Cells were not selected for the deletion resulting in a cell pool of wildtype and mutant cells (n = 7; SEM; * t-test $p < 0.05$). (B) Apoptosis in mock-transduced and Sarrah-mutant mouse HL-1 cardiomyocytes was quantified as caspase-3/7 acitivity (n = 3; SEM; ** t-test $p < 0.01$). (C) Levels of Sarrah target gene mRNAs in mock-transduced and Sarrah-mutant mouse HL-1 cardiomyocytes were determined by qRT-PCR (n = 7; SEM; * t-test $p < 0.05$).

Similarly, simultaneous silencing of all five selected target genes in human cardiomyocytes did not affect apoptosis (figure 39). This again suggests that the anti-apoptotic effect of Sarrah is not conferred by only a subpopulation of target genes, but rather by a collective regulation of the majority of target genes.

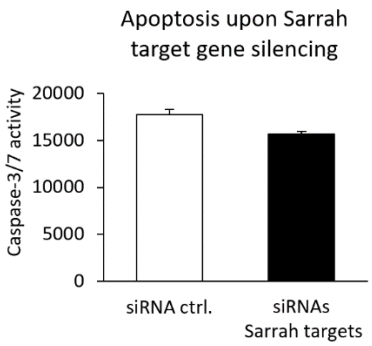

Figure 39: Apoptosis upon Sarrah target gene silencing in human cardiomyocytes. Primary human cardiomyocytes were transfected with 250 nM control siRNA or siRNAs against the Sarrah target genes GPC6, PDE3A, ITPR2, PARP8 and SSBP2 at a final concentration of 50 nM for each siRNA. Apoptosis was quantified as caspase-3/7 acitivity.

In summary, the bioinformatical prediction and the validation experiments show that triplex formation is a conserved mechanism of Sarrah to activate gene expression of target gene sets relevant in the contexts of cardiovascular aging and apoptosis in both mouse and human. Anti-apoptotic effects of Sarrah are likely to be conferred by a majority of target genes together rather than only by a subset of target genes.

4.8 Sarrah Interacts with CRIP2 and P300

Most long non-coding RNAs that have been reported to act via triplex formation with genomic DNA interact with transcription factors or histone modifiers and direct them to specific gene loci to silence or activate transcription. In order to identify such protein interaction partners of Sarrah that contribute to gene regulation of anti-apoptotic genes, an RNA affinity purification followed by mass spectrometry was performed. Antisense probes that specifically bind endogenous Sarrah were selected in an RNA accessibility assay in mouse HL-1 cardiomyocytes (figure 40). To this end, eight probes and the LNA GapmeR sequence known to target Sarrah at an accessible region as positive control were added to HL-1 cell lysate as DNA oligonucleotides. RNase H digestion degraded all RNA regions bound to double-stranded DNA, indicating that the region was accessible for the DNA probes and not occupied by protein or other interaction partners. Probes 5 and 8 yielded the most efficient RNA degradation and were used for the actual RNA affinity purification assay.

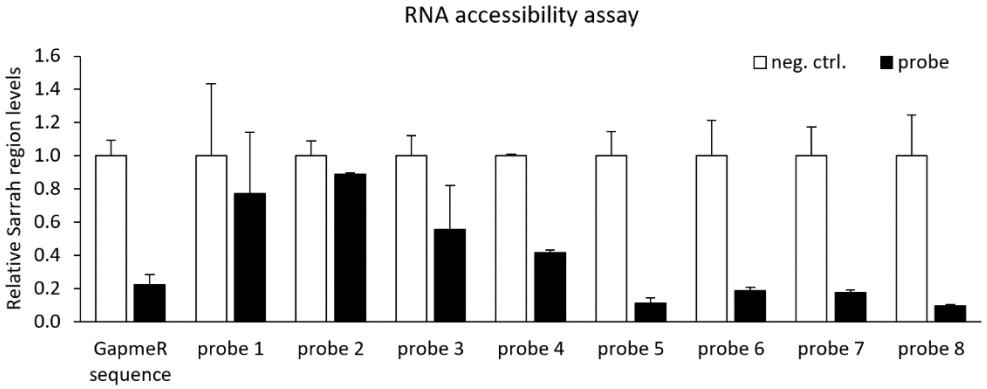

Figure 40: RNA accessibility assay to select antisense probes for Sarrah affinity purification. The sequences of the LNA GapmeR targeting mouse Sarrah as well as eight Sarrah antisense probes designed with the Stellaris Probe Designer were purchased as DNA oligonucleotides and incubated with lysate of mouse HL-1 cardiomyocytes. Samples without any oligonucleotide were included as negative controls. RNase H digestion was induced to degrade all RNA regions bound by double-stranded DNA. Levels of respective Sarrah regions targeted by the DNA oligonucleotides were quantified by qRT-PCR using primers flanking the DNA oligonucleotide binding sites (n = 2; SEM).

For RNA affinity purification, the two Sarrah antisense probe sequences as biotin-coupled, methylated RNA oligonucleotides were used to capture endogenous Sarrah from mouse cardiomyocyte lysate. Sarrah-bound proteins were purified and analyzed by mass spectrometry analysis (figure 41).

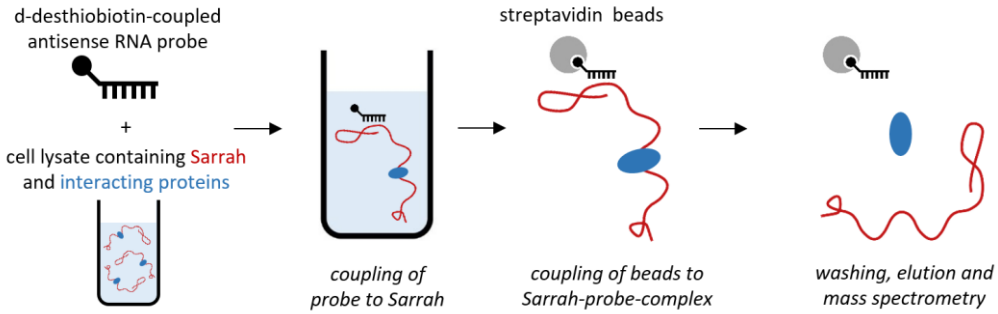

Figure 41: Scheme illustrating the procedure of Sarrah affinity purification. Sarrah antisense probes 5 and 8 selected in figure 40 were used as biotin-coupled, methylated RNA oligonucleotides for Sarrah pulldown from mouse HL-1 cardiomyocyte lysate. A probe of a scrambled sequence was used as control. Probe-Sarrah-protein complexes were captured with streptavidin beads. Sarrah-bound proteins were washed and eluted twice before being used for silver staining or mass spectrometry. Eluted RNA was used for qRT-PCR.

Eluates with an at least 5-fold enrichment of Sarrah in RNA eluted from Sarrah antisense probes over RNA eluted from scrambled probes were subjected to mass spectrometry analysis. In washing, repeated elution and bead fractions, Sarrah was not or only negligibly enriched (figure 42 A). Also a silver staining of proteins from two elution fractions and the beads indicated that the major portion of proteins is eluted during the first elution rather than the second and that the beads contained high background unspecific to Sarrah (figure 42 B).

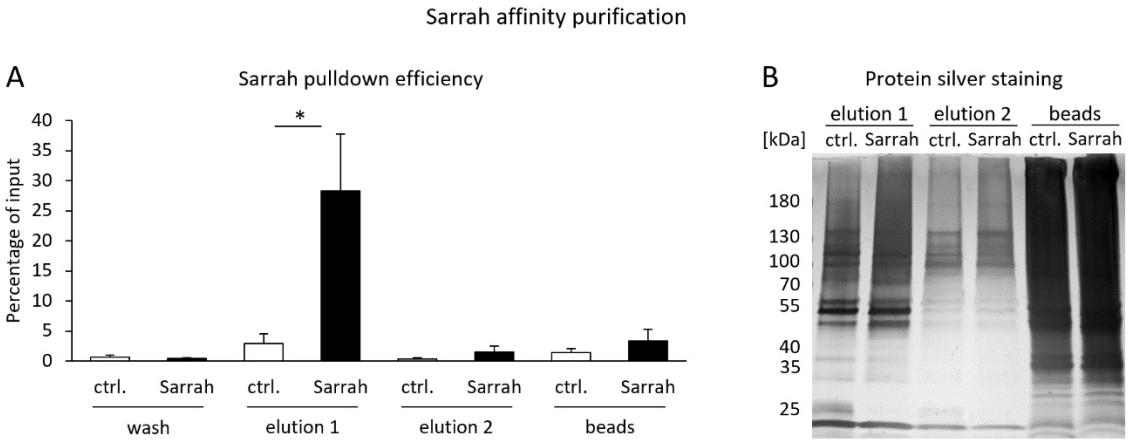

Figure 42: Efficiency of Sarrah affinity purification and staining of purified proteins. (A) During Sarrah affinity purification, supernatants from washing, two elution and bead fractions were collected for RNA isolation. Sarrah was quantified in all fractions by qRT-PCR (n = 5; SEM; * t-test $p < 0.05$). (B) Representative silver staining of proteins from both elution fractions and beads from Sarrah affinity purification on a sodium dodecyl sulfate (SDS) gel.

Mass spectrometry analysis of the first elution fraction identified six proteins to be significantly enriched in eluates from Sarrah antisense probes over those from scrambled probes (table 27), an unusually low number indicating high specificity and low background[325].

Table 27: Mass Spectrometry Results of Sarrah Affinity Purification

Protein	Fold enrichment	P-value
Cysteine-rich protein 2 (CRIP2)	26.18	0.0047
60S ribosomal protein L27a (RPL27A)	3.53	0.0492
Nuclease-sensitive element-binding protein 1 (YBX1)	2.15	0.0038
Interleukin enhancer-binding factor 3 (ILF3)	2.10	0.0190
Nucleolin (NCL)	1.94	0.0343
DnaJ homolog subfamily A member 1 (DNAJA1)	1.79	0.0175

The highest and most significantly enriched protein was the cardiac transcription factor cysteine-rich protein 2 (CRIP2; table 27, figure 43 A)[326,327]. In line with Sarrah regulation, CRIP2 has been reported to be lower expressed in patients with HFpEF[328] and after AMI[329]. Physical interaction between Sarrah and CRIP2 was verified by RNA immunoprecipitation with a CRIP2 antibody in human cardiomyocytes (figure 43 B). Additionally, since CRIP2 had been reported to interact with the transcriptional co-activator p300 in cardiomyocytes[330], Sarrah association with p300 was tested by RNA immunoprecipitation as well. The experiment demonstrated an interaction between Sarrah and p300 (figure 43 B), which acts as an acetyltransferase on lysine 27 at histone H3 (H3K27ac) to activate gene transcription[331]. Consistently, Sarrah also co-localizes to H3K27ac histone marks indicative of open chromatin as shown by another RNA immunoprecipitation (figure 43 B).

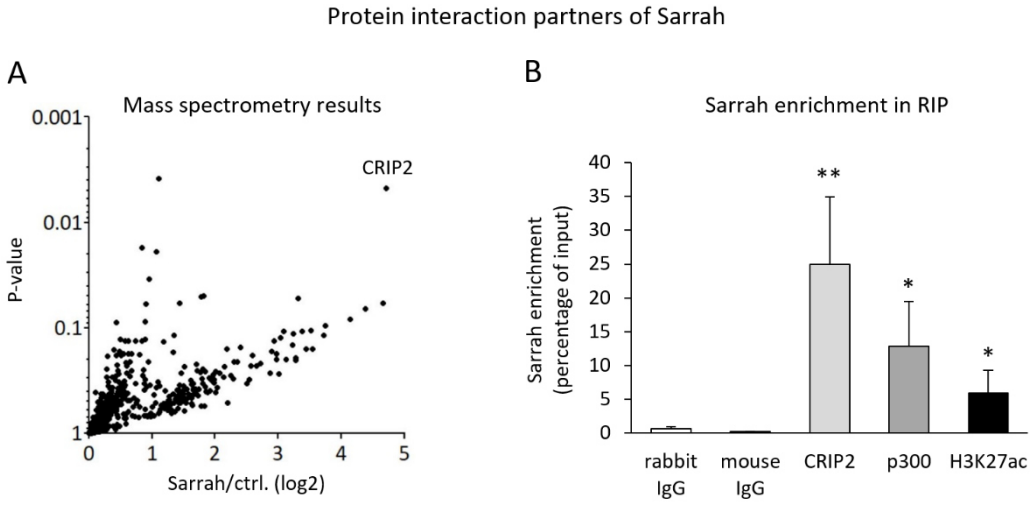

Figure 43: Identification and validation of protein interaction partners of Sarrah. (A) Volcano plot showing all proteins from Sarrah affinity purification identified by mass spectometry analysis. Highest and most significantly enriched hit CRIP2 is labeled. (B) RNA immunoprecipitation experiments with antibodies against CRIP2 (rabbit), p300 (mouse) and histone mark H3K27ac (rabbit) were performed in primary human cardiomyocytes. Sarrah was quantified by qRT-PCR (n = 4-8; SEM; * t-test $p < 0.05$; ** t-test $p < 0.01$).

The results reinforce the hypothesis that Sarrah regulates gene expression by recruiting proteins to triplexes formed with target gene promoters. Based on the presented findings, the following mechanistic model emerges: Sarrah acts via triplex formation with promoters of cardiac survival genes that are activated by Sarrah-guided recruitment of CRIP2 and p300, two proteins that enhance chromatin accessibility and facilitate transcription.

4.9 Sarrah Augments Recovery from Acute Myocardial Infarction in Mice

Finally, to explore the function of Sarrah *in vivo*, an acute myocardial infarction (AMI) model was employed. Sarrah or green fluorescent protein (GFP) as control were overexpressed in mouse hearts using adeno-associated virus serotype 9 (AAV9) particles. Two weeks later, mice were subjected to AMI surgery by ligation of the left anterior coronary artery (LAD). Cardiac parameters were evaluated by echocardiography only on days 1, 7 and 14 after AMI in one cohort and by echocardiography on day 1 and by magnetic resonance imaging (MRI) on day 14 after AMI in another cohort (figure 44 A). After the last echocardiographic or MRI recording, mice were sacrificed and hearts were collected for RNA isolation and histology. Sarrah levels in the myocardium reached 6.7-fold enrichment in AAV9-Sarrah-treated mice over GPF control mice (figure 44 B).

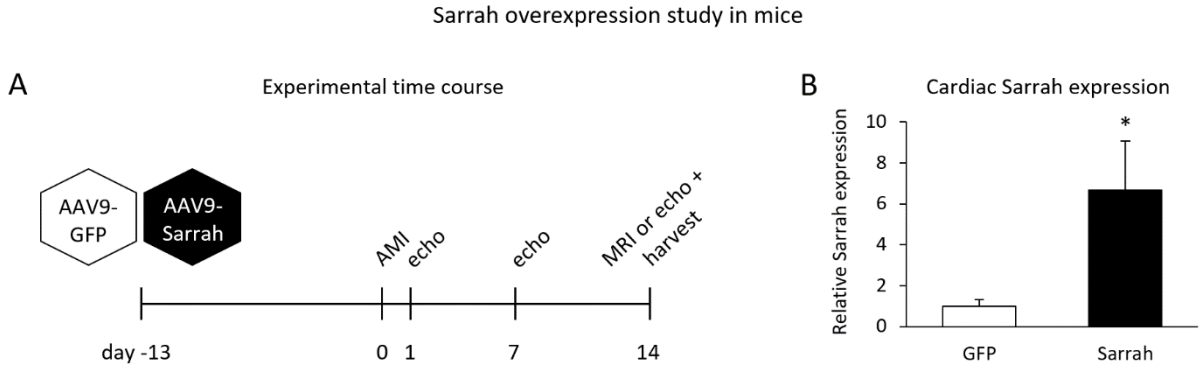

Figure 44: AMI study with Sarrah overexpressing mice. (A) Scheme depicting the time course of the study: $6x10^{11}$ AAV9 particles were injected into the tail vein of mice for overexpression of GFP or Sarrah before AMI surgery was performed two weeks later and cardiac parameters were measured by echocardiography and MRI for two more weeks. (B) Mouse hearts were collected four weeks after AAV9 injection, Sarrah levels were quantified by qRT-PCR (n = 15-16; SEM; * t-test $p < 0.05$).

Measurements of ejection fraction were very comparable between the two imaging techniques and showed that in both animal cohorts, recovery of contractile function was significantly enhanced in Sarrah overexpressing mice compared with GFP control mice already at day 7 and even more pronounced at day 14 after AMI (figure 45 A). Also stroke volumes at day 14 were significantly higher in the Sarrah overexpressing group than in the GFP control group as measured by echocardiography and MRI (figure 45 B), indicating higher heart contractility. Representative images of echocardiographic (figure 45 C) and MRI (figure 45 D) recordings illustrate that Sarrah overexpressing mouse hearts contain a smaller portion of stiffened left ventricular wall and therefore contract perceptibly more pronounced.

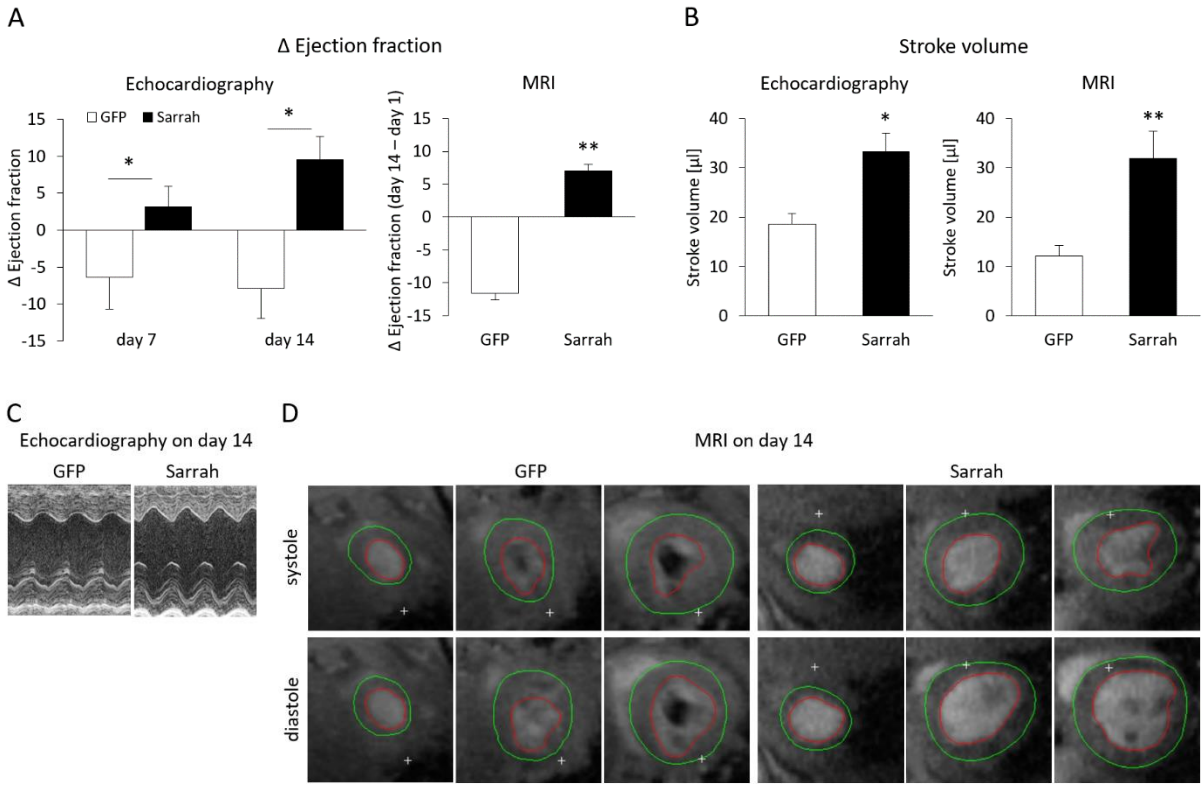

Figure 45: Sarrah overexpression in mouse hearts improves recovery from acute myocardial infarction. (A) Ejection fraction was measured in one animal cohort by echocardiography on days 1, 7 and 14 (n = 6-9) and in a second cohort by echocardiography on day 1 and by MRI on day 14 (n = 7-8; SEM; * t-test p < 0.05; ** t-test p < 0.01). (B) Stroke volume was measured by echocardiography (n = 6-9) or by MRI (n = 7-8) on day 14 after AMI and calculated as the difference between end diastolic volume and end systolic volume (SEM; * t-test p < 0.05; ** t-test p < 0.01). (C) Representative M mode echocardiography images on day 14. (D) Representative images from MRI on day 14 after AMI during end systole and end diastole from apical (left) to basal (right) heart segments.

Furthermore, the wall motion score index (WMSI), a parameter that reflects contractile function in 16 individual heart segments, showed significantly improved cardiac contractile recovery in the Sarrah overexpressing group compared with the control group at day 14 (figure 46 A). Matching Sarrah levels from the GFP and Sarrah overexpressing group with the difference in WMSI between days 1 and 14 revealed a significant correlation between Sarrah expression and contractile function as assessed by WMSI (figure 46 B). Consistently, the left ventricular wall was significantly thicker in Sarrah overexpressing mice than in control mice (figure 46 C).

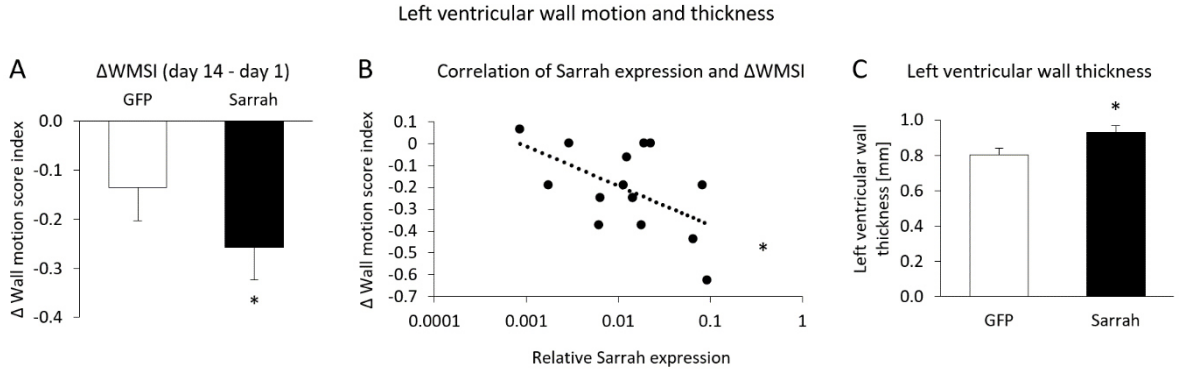

Figure 46: Sarrah overexpression in mouse hearts increases left ventricular wall contractility and thickness. (A) The WMSI was assessed from echocardiographic measurements on days 1 and 14 after AMI (n = 6-9; SEM; * t-test p < 0.05). (B) Changes in WMSI were correlated with Sarrah expression levels in combined data from GFP and Sarrah overexpressing mouse hearts (n = 6-9; SEM; * Spearman correlation p < 0.05). (C) Left ventricular wall thickness was assessed from MRI at day 14 after AMI surgery (n = 7-8; SEM; * t-test p < 0.05).

For a more thorough assessment of phenotypic changes in the Sarrah overexpressing mouse heart, histological stainings were performed on heart sections. The results corroborated the findings from echocardiography and MRI recordings. Specifically, sirius red staining, which visualizes fibrotic tissue, attested a reduced infarct size upon Sarrah overexpression (figure 47 A). Apoptosis was stained by TUNEL and DAPI co-staining. Quantification of TUNEL-positive nuclei revealed a reduction of apoptotic nuclei in the infarct zone upon Sarrah overexpression suggesting a higher rate of cardiomyocyte survival (figure 47 B). No difference in apoptotic cell number was detected in the border zone. DNA damage was quantified by staining H2AXγ, a DNA double strand break marker, but showed no change between GFP and Sarrah overexpressing mice (figure 47 C). To determine whether Sarrah overexpression induced hypertrophic changes, cardiomyocyte cell membranes were stained to measure cardiomyocyte size. No difference between the groups was observed (figure 47 D). Finally, to

test whether cardiomyocyte proliferation could be enhanced by Sarrah overexpression, mitosis marker phospho-histone H3 (PH3) was stained and quantified in cardiomyocytes and remaining cell types. While cardiomyocyte proliferation remained unaltered upon Sarrah overexpression, an unexpected rise in proliferation of non-cardiomyocytes was noticed (figure 47 E). Since it was hypothesized that the proliferating cells were endothelial cells, a co-staining of PH3 and an endothelial cell marker was performed. Indeed, the staining confirmed that the increase in proliferation upon Sarrah overexpression could be attributed to endothelial cells (figure 47 F).

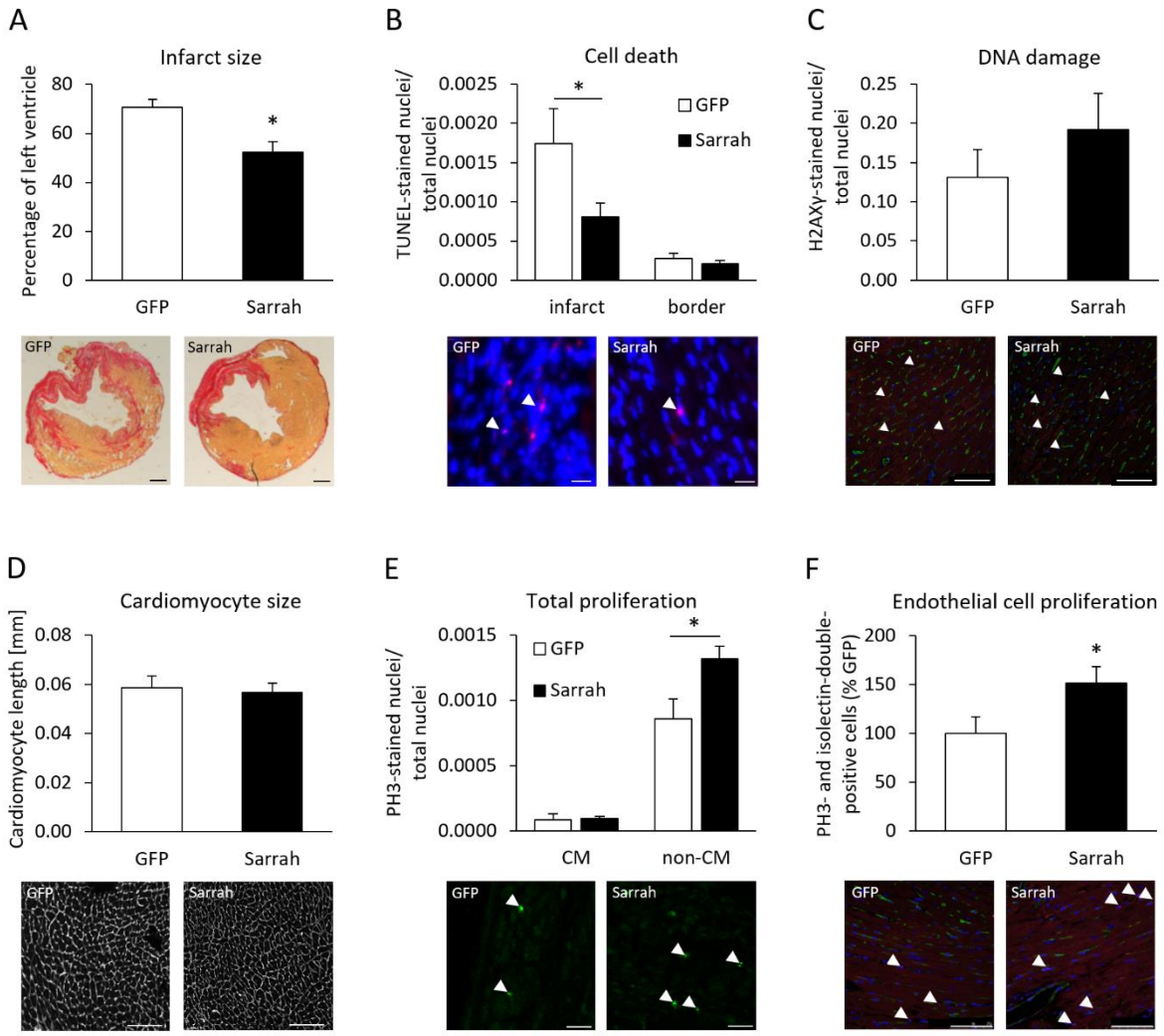

Figure 47: Histological stainings of Sarrah overexpressing AMI mouse hearts. (A) - (F) Quantification and representative images of histological stainings on paraffin sections from mouse hearts, which were collected two weeks after acute myocardial infarction from the mouse cohort evaluated by echocardiography only (n = 6-9; SEM; * t-test $p < 0.05$). (A) Infarct size was stained by sirius red and calculated as circumference of the infarcted region as percentage of the left ventricle. Scale bars are 1 mm. (B) Apoptosis was quantified by TUNEL-positive nuclei per total number of nuclei. Scale bars are 100 µm. (C) DNA damage was quantified by H2AXγ-positive nuclei per total number of nuclei. Scale bars are 75 µm. (D) Cardiomyocyte cell membranes were stained using wheat germ agglutinin. Cardiomyocyte width was measured in two different regions for 20 cells per region for each animal. Scale bars are 100 µm. (E) Total proliferation was quantified by PH3-positive nuclei per total number of nuclei. Cardiomyocytes (CM) were distinguished from non-cardiomyocytes by morphology. Scale bars are 20 µm. (F) Endothelial cell proliferation was quantified by PH3- and isolection-double-positive nuclei. Scale bars are 75 µm.

Together, the AMI study in GFP or Sarrah overexpressing mice demonstrated a substantial enhancement of cardiac contractile function as assessed from ejection fraction, stroke volume, wall motion score index, left ventricular wall thickness and infarct size. Additional histological stainings confirm the anti-apoptic function of Sarrah *in vivo* and suggest a role for Sarrah in stimulating endothelial cell proliferation. These beneficial effects of Sarrah on AMI recovery reveal unexplored therapeutic potential.

4.10 Sarrah Induces Endothelial Cell Proliferation *in vitro*

Adeno-associated virus-mediated overexpression of Sarrah in the heart resulted in an increase in endothelial cells proliferation, although AAV9 particles do not target endothelial cells, but only cardiomyocytes at the injected concentration[332]. To confirm that the effect that stimulates endothelial cell proliferation is indirectly conferred from cardiomyocytes to endothelial cells, an *in vitro* co-culture setting of both cell types was applied, in which human cardiomyocytes were treated to either overexpress or deplete Sarrah before being transferred into a dish with human umbilical vein endothelial cells (HUVECs). After 48 hours of co-culture, HUVECs were used for a cell proliferation assay (figure 48).

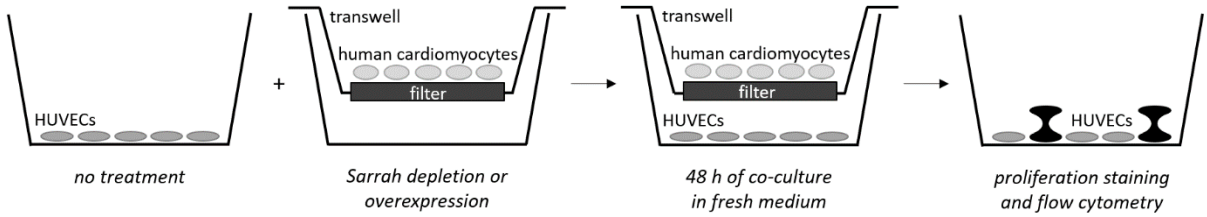

Figure 48: Scheme illustrating the co-culture setup of human cardiomyocytes with HUVECs and experimental work flow. Primary HUVECs were seeded in a cell culture dish without treatment. Primary human cardiomyocytes were seeded in a separate dish on a transwell filter and either transfected with LNA GapmeRs or transduced with lentivirus to deplete or overexpress Sarrah, respectively. 24 h after treatment, human cardiomyocytes were washed and transferred onto HUVECs for co-culture in fresh endothelial basal medium for 48 h. HUVECS were subsequently used for BrdU staining and flow cytometry analysis.

Flow cytometry analysis of BrdU-stained HUVECs revealed that Sarrah-depletion in human cardiomyocytes inhibits proliferation of co-cultured HUVECs compared with LNA GapmeR control treatment of cardiomyocytes (figure 49 A). Conversely, when HUVECs were co-cultured with human cardiomyocytes overexpressing human Sarrah, flow cytometry analysis showed that HUVEC proliferation was increased compared with cells co-cultured with mock-transduced cardiomyocytes (figure 49 B).

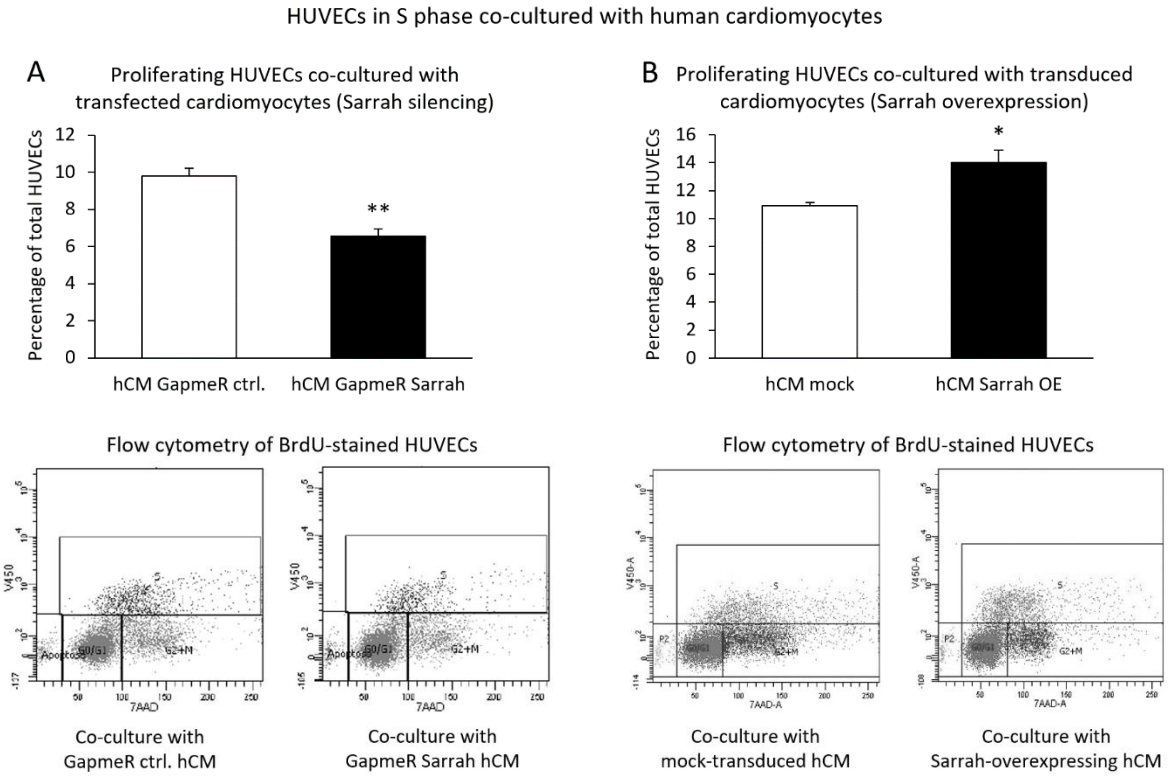

Figure 49: Sarrah in cardiomyocytes stimulates proliferation of co-cultured endothelial cells *in vitro*. Primary human cardiomyocytes were (A) transfected with LNA GapmeR control or LNA GapmeR Sarrah (n = 4) or (B) transduced with mock-lentivirus or Sarrah-lentivirus (n = 3) for Sarrah depletion or overexpression, respectively, and co-cultured with untreated primary HUVECs, which were stained with BrdU and analyzed by flow cytometry (top), representative images are shown (bottom). HUVECs in S phase were quantified a percentage of total HUVECs (OE: overexpression; SEM; * t-test $p < 0.05$; ** t-test $p < 0.01$).

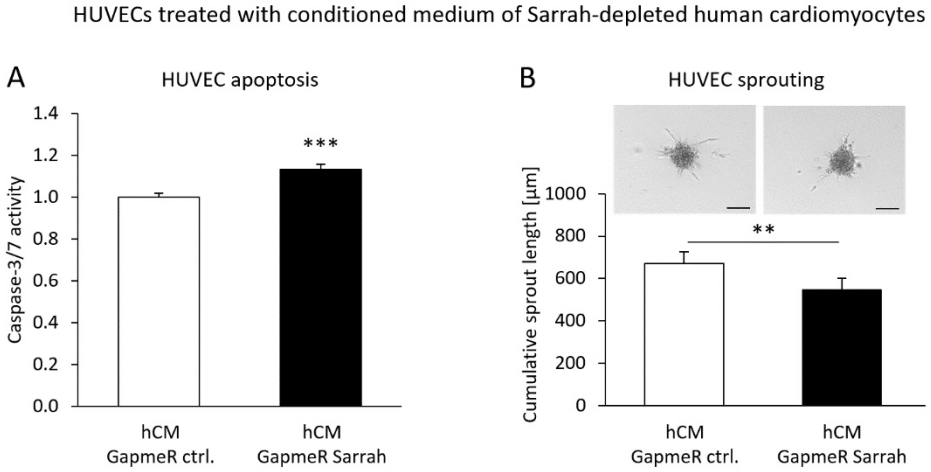

Figure 50: HUVEC treatement with conditioned medium from Sarrah-depleted human cardiomyocytes increases apoptosis and reduces sprouting capacity. (A) Apoptosis was quantified as caspase-3/7 activity in primary HUVECs cultured in conditioned medium from LNA GapmeR-transfected primary human cardiomyocytes that did not contain any LNA GapmeRs anymore (n = 29; SEM; *** t-test $p < 0.001$). (B) Sprouting of primary HUVEC spheroids cultured in conditioned medium from LNA GapmeR-transfected primary human cardiomyocytes that did not contain any LNA GapmeRs anymore was quantified as cumulative sprout length (bottom). Representative images are shown (top); scale bars are 100 µm (n = 39-46; SEM; ** t-test $p < 0.01$).

Consistently, when using conditioned medium from human cardiomyocytes that had been transfected with LNA GapmeRs, HUVECs treated with medium from Sarrah-depleted cells exhibited an increase in apoptosis (figure 50 A). Furthermore, Sarrah depletion in human cardiomyocytes reduced the *in vitro* sprouting capacity of HUVECs treated with conditioned medium compared with medium from control-transfected cardiomyocytes (figure 50 B).

Thus, the results from co-cultured and conditioned medium-treated HUVECs demonstrate that Sarrah confers pro-proliferative, anti-apoptotic and pro-angiogenic stimuli from cardiomyocytes to endothelial cells *in vitro*, features that correspond to the induced endothelial cell proliferation observed upon Sarrah overexpression *in vivo* and that pave the way for angiogenesis and revascularization, two processes beneficial for recovery from acute myocardial infarction.

In summary, this study identified the conserved, anti-apoptotic long non-coding RNA Sarrah in the heart whose expression diminishes during aging and upon myocardial ischemia. In the young and healthy heart, Sarrah is expressed at sufficient levels to form triplexes at promoters of all its target genes and recruits transcription factor CRIP2 and acetyltransferase p300 in order to activate transcription of cardiac survival genes, which ensure proper cardiac function and recovery. In contrast, in the aging and diseased heart, Sarrah levels decrease, which leads to insufficient target gene transcription, further decline of cardiac function and reduced recovery from ischemic events. Cardiac overexpression of Sarrah in mice substantially augments myocyte survival and stimulates endothelial cell proliferation, which significantly improves recovery from acute myocardial infarction, thereby highlighting the therapeutic potential of Sarrah (figure 51).

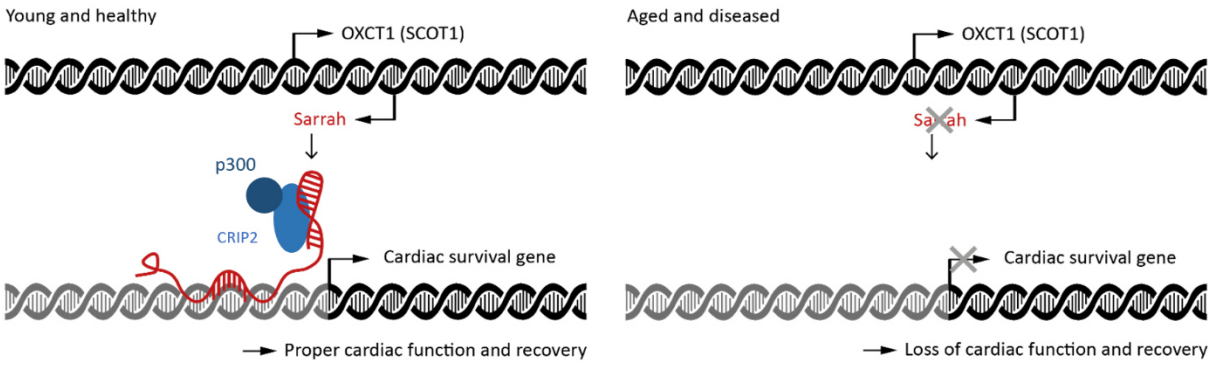

Figure 51: Scheme illustrating the model proposed for Sarrah function. Under physiological conditions, Sarrah contributes to proper cardiac function via triplex formation as well as CRIP2 and p300 recruitment to cardiac survival gene promoters. Downregulation of Sarrah during aging and ischemia withdraws it from promoters of target genes, which in turn are insufficiently transcribed, thereby deteriorating cardiac function.

5. Discussion

Aging and heart disease have been studied since long and associated with various structural alterations and cellular processes. During the last two decades, another layer of pathophysiologic changes modulated by long non-coding RNAs has been added on top of what had been known and challenged the understanding of molecular mechanistics, gene regulation and fine-tuning of proteins and RNA in the aging heart. The presented study contributes to this expanding understanding by identifying the lncRNA Sarrah in the heart and providing insights into its role in cardiomyocytes. The outlined findings evidence that Sarrah is a potential candidate for further therapeutic considerations with regard to ischemic heart conditions, but still, several open questions remain to be addressed.

5.1 Upstream of Sarrah

Sarrah has been identified by comparing the transcriptomes of young and aged mice. Its expression has been found to decrease not only upon aging, but also during heart conditions that are likely to occur during aging and that involve an ischemic environment, like acute myocardial infarction and heart failure with preserved ejection fraction. In cell culture, this has been modeled by exposure to hypoxia and DFO treatement. However, the precise mechanism of downregulation remains to be elucidated. Epigenetic alterations that typically occur during aging and affect gene expression globally[43] are a plausible explanation how Sarrah expression is reduced, possibly due to DNA methylation or post-translational histone modifications.

During ischemic heart events, a transient way of downregulation is more likely, for example by altered transcription factor binding at the Sarrah promoter. Annotations in the UCSC genome browser[333] exhibit a binding site for serum response factor (SRF), a transcription factor controlling cell growth and differentiation that is best characterized in the myocardium[334,335]. Publicly available ChIP-sequencing data demonstrate an interaction between SRF and the Sarrah promoter in the murine myoblast cell line C2C12[336]. However, SRF and its co-factors have been reported to induce rather than to silence gene expression upon hypoxia[337,338]. It is thus conceivable that physiologically, SRF activates Sarrah, but is withdrawn from the Sarrah promoter to other loci upon ischemic events, thereby contributing to Sarrah downregulation. When considering the time course of Sarrah levels after AMI in the infarct zone, which displays a delayed downregulation of Sarrah that is significant on day 3, but not yet on day 1 after AMI, it appears possible that hypoxia-responsive transcription factors contribute to an initial enhancement of Sarrah expression directly following AMI before being withdrawn from the locus.

As indicated by mRNA level measurements after Sarrah knockdown in mouse cardiomyocytes, the gene located antisense to Sarrah, OXCT1, might be co-regulated. OXCT1 encodes the enzyme SCOT1 that catalyzes the rate-limiting step of ketone body metabolism. It is highest expressed in heart, brain and kidney, preferentially only during periods of starvation[339]. Several studies have shown that like Sarrah, also OXCT1 is downregulated during hypoxia in cardiomyocytes[340] and neurons[341]. This suggests that transcription factors regulating OXCT1, although little is known about their identity, might modulate Sarrah expression, too. Co-localization and -regulation as well as cardiac expression common to both genes imply a similar demand of both gene products. In accordance, a cardiac OXCT1 knockout in mice increases susceptibility to pathological cardiac remodeling[342]. Another study reports a decrease in ketone body metabolism during heart failure, which has been proposed to protect the heart against oxidative stress[343]. This indicates that Sarrah might be downregulated in the failing heart as a secondary effect of OXCT1 regulation in order to compensate for the deleterious effects of reactive oxygen species. However, the considerations ascribing a role in Sarrah regulation to SRF or to OXCT1 regulating factors remain to be verified experimentally.

5.2 Linking Sarrah to Apoptosis and Contractility

Caspase- and annexin V-based *in vitro* assays with human and murine cells as well as histological stainings of human engineered heart tissue organoids and mouse heart sections have attested the anti-apoptotic role of Sarrah. While it can be regarded as certain that Sarrah does interfere with apoptosis, two related issues remain obscure: first, it cannot be excluded that Sarrah, additionally to inhibiting apoptosis, also influences necrosis, and secondly, the exact point that Sarrah intervenes at with one or both of the major apoptotic pathways still has to be explored. DNA double strand break stainings of H2AXγ in infarcted mouse hearts indicate that DNA damage is not the apoptotic trigger affected by Sarrah as no difference in staining quantifications was observed between Sarrah overexpressing mice and controls. Given the fact that Sarrah activates a whole set of anti-apoptotic genes, among them the five genes selected for triplex validation – GPC6, PDE3A, ITPR2, PARP8 and SSBP2 – but also MAPK10, DPYD, TAOK1, RBMS1 and others, it can be assumed that Sarrah itself does not directly modulate signaling of neither the extrinsic nor the intrinsic apoptotic pathway, but delegates this task to its target genes that each exert their specific anti-apoptotic function.

For instance, glypicans such as GPC6 and mitogen-associated protein (MAP) kinases such as MAPK10 influence apoptosis via SMAD signaling[344,345]. Smad2, Smad3 and Smad4 have been shown to act as co-transcriptional regulators upon transforming growth factor β (TGF-β) signaling and to drive the expression of the death-associated protein (DAP) kinase, a calcium/calmodulin-regulated serine/threonine kinase that triggers the release of cytochrome c from mitochondria[346] and that cross-

talks to MAP kinases to induce apoptosis[347]. Of note, Smad2 and Smad3 have been predicted as murine Sarrah target genes by the Triplex Domain Finder themselves. Therefore, SMAD proteins and the DAP kinase might act as mediators of the anti-apoptotic function of Sarrah. Interestingly, DAP kinases have been implicated both in cardiomyocyte apoptosis[348] and in muscle contractility[349], thereby constituting a possible link between the two cardiomyocyte phenotypes impacted by Sarrah: inhibition of apoptosis and promotion of contractility, the latter of which is described in primary rat cardiomyocytes and human engineered heart tissue organoids in this study.

SMAD-dependent apoptosis has been specifically described in cardiomyocytes[350]. In this context, Smad3 and Smad4 act downstream of the transcription factor AP-1. Both the SMAD signaling stimulators TGF-β and AP-1[351] and SMAD proteins[352] are elevated after AMI. Remarkably, in addition to having been implicated in AMI and apoptotsis, AP-1 also drives hypertrophic cardiomyocyte growth[353], a process which diminishes cardiac contractility and constitutes the most frequent structural abnormality of the myocardium in HFpEF[354]. However, the AP-1-driven induction of cardiomyocyte hypertrophy is, unlike AP-1-driven cardiomyocyte apoptosis, independent of SMAD proteins.

These studies suggest that Sarrah might mediate its anti-apoptotic function via activation of target genes that interfere with SMAD-dependent cardiomyocyte apoptosis, an event that is linked to cardiomyocyte contractility via DAP kinase and AP-1. It is conceivable that Sarrah participates in this interplay to modulate contractility by activating another distinct subset of target genes, for example calcium ion handling proteins like PDE3A or, in humans, CAMK2D and PRKG1 that are also predicted to form triplexes with Sarrah in their promoters. Regulation of cardiomyocyte contractility and differential expression in HFpEF indirectly associate Sarrah with hypertrophy, although no direct effect on cardiomyocyte growth has been observed upon Sarrah overexpression in mice. An interesting approach would be to investigate whether Sarrah overexpression rescues or attenuates the phenotype of hypertrophy induction in an *in vivo* model and if it does so via regulation of the suggested target genes.

The postulated link between apoptosis and contractility explains how Sarrah can affect two such different conditions as AMI and HFpEF, where cardiomyocyte apoptosis and cardiomyocyte stiffness play a major role, respectively. The explanation can be complemented by the common feature of ischemia that occurs in both diseases[355]. Based on these insights, it is presumable that Sarrah is also dysregulated in other heart diseases that exhibit cardiomyocyte apoptosis and diminished contractility, for instance in ischemic heart disease, other types of heart failure and arrhythmias.

5.3 Triplex Formation as the Mechanism of Sarrah Action

Triplex formation with genomic DNA in promoter regions of target genes is proposed as the mechanism of Sarrah action. Initially, this mechanism was identified by a bioinformatical prediction and exemplarily validated *in vitro* using RNA and DNA oligonucleotides for recording nuclear magnetic resonance spectra. However, a definite proof that triplex formation between Sarrah and its target gene promoters occurs *in vivo* cannot be deduced from this study. Immunoprecipitation experiments using a DNA-RNA hybrid binding antibody[297] have indeed corroborated that both Sarrah and the proposed DNA regions do associate with triplex structures, but still there is no experimental evidence that the triplexes detected in the RNA immunoprecipitates and the chromatin immunoprecipitates are the same ones. Nevertheless, the presented findings and further indications from the literature outlined below justify the conclusion that Sarrah forms triple helices with the identified target gene promoters to activate transcription.

Despite the use of acidic conditions to validate the interaction between Sarrah and the GPC6 promoter, it is likely that the interaction can occur at a physiological pH *in vivo*. An acidic environment has been reported to facilitate *in vitro* formation of parallel triplexes when measured by NMR, especially for pyrimidine-rich RNA oligonucleotides[356]. But when triplex formation is validated *in vitro* by electrophoretic mobility shift assay (EMSA), the structure can form at a pH of 7.5 as reported for lncRNA Khps1[298]. Besides, many RNAs are expected to be methylated at cytosine residues *in vivo*[357]. Modeling these physiological conditions using oligonucleotides containing 5-methyl-cytosine *in vitro* revealed that, especially for pyrimidine-rich sequences, thermodynamic stability of triplexes was increased by the oligonucleotide modification and even the optimal pH for triplex formation was shifted from below 6 to the neutral pH range[358,359,360]. Accordingly, triplex forming oligonucleotides containing 5-methyl-2'-deoxycytidine bases have been shown to increase stability of triple helices *in vivo* as well[361]. Although the referenced studies use single-stranded DNA as third strand, similar effects on stability can be expected with methylated RNA as third strand. Notably, also genomic DNA cytosine residues are oftentimes methylated *in vivo*[362]. This suggests that also the pyrimidine-rich triplex motif within Sarrah is able to engage in stable intracellular triplexes *in vivo* at a physiological pH.

Furthermore, pyrimidine-rich motifs are expected to be more relevant under *in vivo* circumstances than purine-rich triplex motifs because the latter often contain long guanine tracts that compete with quadruplex formation[363] and thereby limit efficient triplex formation *in vivo*[364]. Another Sarrah feature supporting its probability of triplex formation is its occurence near transcription start sites of actively transcribed genes as genomic regions with triplex formation have been identified to mostly be located within open chromatin[365]. This fits the function postulated for Sarrah and surprisingly contrasts the majority of lncRNAs that have been described to form triplexes to date, as six out of seven (pRNAs of

DHFR and rRNA genes, PARTICLE, MEG3, HOTAIR and Fendrr) of them lead to transcriptional silencing rather than activation of their respective loci. Only two lncRNAs, Khps1 and, depending on the genomic context, Fendrr have been described to activate gene expression in the literature.

To more reliably confirm that also Sarrah belongs to these lncRNAs, a number of methods are available. For example, electrophoretic mobility shift assays can be used. In contrast to NMR recordings, EMSAs do not require an acidic pH for detecting triplex formation and are therefore suitable to provide supporting evidence that Sarrah forms triplexes *in vivo*. For a definitive record of Sarrah interaction with the proposed target genes, chromatin isolation by RNA purification (ChIRP)-sequencing would be ideal to globally identify all Sarrah target sites in the genome. Functionally, a caspase activity assay with cells overexpressing wildtype Sarrah versus Sarrah lacking the triplex motif could provide further evidence that the particular sequence element is essential for the anti-apoptotic action of Sarrah. A rescue of the Sarrah overexpression phenotype would be expected upon overexpression of the mutated Sarrah variant, resulting in more apoptosis compared with cells overexpressing wildtype Sarrah.

But even solid experimental validation of triplex formation by Sarrah does not exclude the possibility that Sarrah confers its function via other mechanisms as well. Both human (1,731 nucleotides) and mouse Sarrah (3,990 nucleotides) belong to the larger representatives of the class of lncRNAs. It is thus conceivable that Sarrah contains more than one functional domain as shown for other lncRNAs[180]. Along this vein, chromatin immunoprecipitation and RNase H digestion of DNA-RNA hybrids from human cardiomyocytes suggests that Sarrah may engange in DNA-RNA configurations other than triplex structures. As presented above, fragments of all five target gene promoters could be detected in the precipitate, four of them being insensitive to RNase H, indicating possible triplex conformations. One of the target gene promoters though, namely the ITPR2 promoter, was precipitated, but not significantly enriched after RNase H digestion, suggesting that RNase H-sensitive DNA-RNA hybrids are formed in the ITPR2 promoter. Again, ChIRP-sequencing could clarify whether it is Sarrah or another RNA that partipicates in these structures. However, this also implies that if Sarrah indeed forms more than one kind of DNA-RNA hybrid structures, ChIRP-sequencing cannot definitively determine the type of DNA-RNA hybrid in a given region, but further experiments involving for instance RNase H digestion and high-resolution molecular imaging will be necesssary as DNA-RNA hybrid structures have not been comprehensively described yet.

The characterization of additional functional Sarrah domains, whether forming DNA-RNA hybrids or not, is also of interest with respect to the regulated genes identified in the microarray analysis that are not predicted to form triple helices. As stated above, 27 percent of human and 32 percent of mouse downregulated genes contain triplex motifs. The way of regulation that affects the other genes

remains obscure. Possibly, an interplay of two or more mechanisms conferred by different Sarrah domains ensures a robust regulation of all target genes, an explanation that would also account for the fact that the majority of examined target genes were not significantly downregulated in mouse cardiomyocytes upon excision of the Sarrah triplex motif. Alternatively, the remaining downregulated and the upregulated genes might be influenced by secondary effects mediated by the primary target gene products. Further investigations are required to address these questions.

5.4 Beneficial Effects of Sarrah on Cardiac Contractility in Mice

Overexpressing GFP or Sarrah in mouse hearts using an adeno-associated viral system revealed enhanced recovery of cardiac contracile function after acute myocardial infarction upon Sarrah overexpression as evaluated from left ventricular ejection fraction, stroke volume, wall motion score index and left ventricular wall thickness. Histological analysis confirmed the anti-apoptotic effect of Sarrah *in vivo*. Thus, both contractility and cell survival are beneficially influenced by Sarrah. It is arguable that the increase in contractility might be a secondary consequence of a reduction in apoptosis. Several findings, however, point to the conclusion that Sarrah promotes contractility irrespective of apoptosis. First, measuring contractility of individual rat cardiomyocytes and thereby selecting for viable cells supports this notion. Second, several contractility-related genes such as PDE3A, CAMK2D and PRKG1 are among the direct target genes of Sarrah. Third, as discussed above, apoptosis and contractility in cardiomyocytes are interconnected via several molecular pathways and factors like DAP kinase and AP-1. Last, in accordance with the notion that Sarrah promotes contractility, histological measurements of cardiomyocyte size indicated no hypertrophic cell enlargement upon Sarrah overexpression. Thus, the beneficial outcome of Sarrah overexpression does not merely rely on a short term improvement due to hypertrophic heart remodeling, which underpins the enhancement of cardiac contractility induced by Sarrah.

Another interesting and therapeutically relevant approach would be to study aged mice or a prematurely aged mouse model and determine whether Sarrah overexpression can either rescue the increased susceptibility to ischemic heart events or augment recovery from AMI also in this context. Finally, the effects of Sarrah deficiency that are expected to impair cardiac contractile function and specifically recovery after AMI remain to be investigated. A Sarrah knockdown model using LNA GapmeRs *in vivo* represents an appropriate model for this purpose. However, although LNA GapmeR injection has been reported to successfully induce lncRNA silencing in mice[264], *in vivo* tests of Sarrah LNA GapmeRs using different protocols and two different sequences within the scope of this study failed to achieve a proper knockdown. Alternatively, a knockout mouse model targeting the Sarrah transcription start site without affecting exonic regions of OXCT1 could be applied.

5.5 Sarrah-Stimulated Endothelial Cell Proliferation

One of the most surprising incidental findings of this study constituted the increased endothelial cell proliferation rate upon Sarrah overexpression in mouse hearts, which was insofar unexpected as the applied overexpression strategy targeted only cardiomyocytes, but not endothelial cells at the administered dose[332]. Cell culture experiments with human umbilical vein endothelial cells and human cardiomyocytes that either overexpressed Sarrah or that had been depleted of Sarrah confirmed the *in vivo* finding that Sarrah stimulates endothelial cell proliferation both in co-culture settings and when using conditioned medium. The observed *in vitro* results point to some type of cardiomyocyte-endothelial cell cross-talk rather than to a secondary effect due to the increased number of surviving cardiomyocytes that augments oxygen and nutrient demand of the myocardium and therefore enhances angiogenesis and perfusion.

This implies a paracrine signaling pathway from cardiomyocytes to cardiac endothelial cells that is induced or modulated by Sarrah. Paracrine signaling has been described in both homotypic and heterotypic cell interactions in the heart[32]. Factors secreted from cardiomyocytes include growth factors, hormones, cytokines, extracellular matrix proteins and peptides[366], for example the well-characterized natriuretic peptides A and B that also affect endothelial cells[367]. Stimulation of endothelial cell proliferation has been reported upon secretion of placental growth factor[368], fibroblast growth factor 9[369], angiopoietin-1[370] as well as vascular endothelial growth factors B[371] and C[372] from cardiomyocytes. This identifies the mentioned molecules as potential mediators of the pro-proliferative effect that cardiomyocytal Sarrah exerts on endothelial cells. In consistence, two of these factors, angiopoietin-1 and VEGF-C, were downregulated upon Sarrah silencing in the microarray analysis. Interestingly, myocardial overexpression of VEGF-B improves cardiac contractility after acute myocardial infarction[373], an effect that strikingly resembles Sarrah overexpression and highlights VEGF-B as a candidate of special interest in the search of Sarrah-induced signaling molecules secreted from cardiomyocytes.

Despite the plausibility of soluble factor secretion as the means of Sarrah-dependent communication between cardiomyocytes and endothelial cells, the possibility that Sarrah regulates extracellular vesicle content should not be excluded. Extracellular vesicles are divided into three subtypes based on their size, which are exosomes, microvesicles and apoptotic bodies in growing order[374]. Although lncRNAs can be transferred between cells in extracellular vesicles[375], Sarrah is unlikely to be transported out of cardiomyocytes itself as it is localized in the nucleus and associated with chromatin. However, a detailed analysis of conditioned medium composition from Sarrah overexpressing or Sarrah-silenced cardiomyocytes is required to shed light on the identity and the vehicle of the secreted messengers that induce endothelial cell proliferation. Acute myocardial infarction has been reported

to augment the amounts of both exosomes and microvesicles released from cardiomyocytes[376]. Extracellular vesicles from HL-1 cells have been found to enhance endothelial cell migration and proliferation[377]. A study using human induced pluripotent stem cell-derived cells showed that endothelial cells treated with extracellular vesicles isolated from conditioned medium of cardiomyocytes express increased levels of pro-angiogenic growth factors and exhibit enhanced angiogenesis[378]. These findings demonstrate that secretion of extracellular vesicles is equally likely to confer the proliferation stimulating effects of Sarrah.

It is also conceivable that Sarrah activates expression of target genes that participate in paracrine signaling more directly. For instance, GPC6 represents a potential direct candiate. Glypicans are attached to the cell membrane and contain extracellular domains. They have been shown to interact with secreted growth factors[379] on the one hand, but also to be cleaved and their parts to be secreted into the extracellular matrix[380] on the other hand. Notably, glypican 1 is known to promote myogenic satellite cell proliferation[381]. However, the effects of glypican cleavage products on endothelial cell proliferation have not been studied to date.

Overall, the findings indicating that Sarrah induces paracrine signaling from cardiomyocytes to endothelial cells in order to stimulate proliferation of the latter are in line with a range of studies that reveal cardiomyocytes to be regulators of angiogenesis by secreting molecules and extracellular vesicles. The identity of the secreted factors and the exact set of Sarrah target genes that modulate them directly or via auxiliary messengers remain to be investigated.

5.6 Therapeutic Potential of Sarrah

The acute myocardial infarction study in mice revealed that Sarrah overexpression promotes a clearly improved outcome of cardiac contractile function. This improvement can be attributed to the combination of three distinct effects that are induced by Sarrah, which are inhibition of cardiomyocyte apoptosis, enhancement of cardiomyocyte contractility and stimulation of endothelial cell proliferation.

Cardiomyocyte apoptosis was verified to be attenuated by Sarrah in both human and murine cells as well as in human engineered heart tissue and in mouse hearts. Gene set enrichment analysis of genes regulated upon Sarrah silencing in human cardiomyocytes corroborated these findings, so that the anti-apoptotic function appears to constitute the main effect of Sarrah. Inhibiting apoptosis in cardiomyocytes in the context of AMI has been shown to protect the myocardium during ischemia for example by blocking caspase activity[382,383], overexpression of C1q/TNF-related protein 9 that alleviates

ER stress[384] or administration of cyclic helix B peptide whose anti-apoptotic mechanism has not been dissected yet[385].

Cardiac contractile function that relies on contractility of individual myocytes as the contracting elements of the myocardium is decreased after acute myocardial infarction[386], but rarely has been addressed pharmacologically to date. In this work, Sarrah loss was shown to deteriorate contractility in two *ex vivo* settings using either isolated rat cardiomyocytes or human engineered heart tissue organoids. Several studies point to reduced calcium ion content in the sarcoplasmic reticulum[387] and myofilament hypersensitivity to calcium ions[388,389] as the causative effectors of reduced cardiac contractility. Voluntary exercise has been demonstrated as one of only few means to increase contractility after AMI in mice via a reduction of myofilament sensitivity to calcium ions[390].

Endothelial cell proliferation and migration are essential for initiation of angiogenesis, which in turn is indispensible for revascularization of damaged tissue following acute myocardial infarction[391], but on the downside drives tumor neovascularization[392]. A variety of therapeutic strategies to promote angiogenesis including administration of growth factors as peptides, gene delivery or stem cell-based therapy have been tested in clinical trials[393,394]. Although some of these studies have yielded ambiguous outcomes, the results overall support the idea that induction of angiogenesis is beneficial for the treatment of ischemic heart events such as myocardial infarction, particularly when using bone marrow cell-based approaches[395] or acitvating VEGF signaling[396].

Since Sarrah has the capacity to advantageously impact all three outlined aspects of AMI recovery, it is of substantial therapeutic interest to translate the findings from this work to a clinical context in humans. Two difficulties come along with Sarrah as a therapeutic compound. These are, first, the fact that for a beneficial patient outcome, Sarrah levels need to be augmented rather than diminished, and, second, the appropriate timing.

Silencing RNAs in a therapeutic context is, especially for miRNAs[397], better established than delivery of RNA molecules and can be achieved by using synthetic antisense oligonucleotides that can be both single- or double-stranded and usually are between 12 and 30 nucleotides long. Their mechanistic functions can be divided into promotion of RNA cleavage and degradation or steric blocking[398,399]. An exemplary lncRNA that has been proposed to be silenced for therapeutic purposes is MALAT1 in prostate cancer[400], multiple myeloma[401] and neuronal tissue[402]. In contrast, upregulation of gene expression is a scarcely used therapeutic approach. It can be achieved by immediate administration of the molecule of interest, by plasmid transfection, by carrier-mediated gene delivery or by targeting RNAs that repress transcription of their antisense protein-coding genes to induce protein expression[403,404]. For therapeutic purposes, the latter method could be modified by targeting a protein that represses Sarrah transcription. Also gene delivery strategies are continuously being advanced to

treat various human diseases such as enzyme deficiencies[405] or cancers[406] and are an option for Sarrah upregulation in the future.

Carrier-mediated gene delivery approaches can be divided into viral and non-viral techniques and utilize plasmids or minicircles encoding a gene for the factor to be upregulated as cargo[407]. Some constructs have been reported to be active for months or even years after delivery[408], but then again contain the risk of insertional mutagenesis by recombination with cellular DNA. Viral strategies benefit from natural viral features as gene delivery vehicles that include binding to the cell membrane, internalization and endosomal escape. Major drawbacks of viral delivery are low cargo capacity, high immune responses and limitations to the production scale. For therapeutic purposes, the vectors are depleted of all viral genes except for those needed for genome replication and packaging and supplemented with the gene to be expressed including regulatory sequences. AAV vectors as used in this study in mice are the leading method in the field of viral gene delivery[409], although their clinical efficacy still requires some improvement[410]. Their tissue specificity depends on the serotype, with serotype 9 exhibiting the best tropism for cardiomyocytes[410]. Additionally, lenti-, adeno- or Herpes simplex viral vectors are being investigated in therapeutic contexts[411]. Non-viral gene delivery methods include methods based on proteins, lipids or synthetic materials, for example virus-like protein particles, lipid micelles, synthetic polymers and carbon, metal or silane nanoparticles[403].

Several difficulties need to be overcome when delivering nucleic acids to a cell type or tissue, such as the fact that they are very unstable in extra- and intracellular fluids[410] and easily degraded by nucleases, which is a problem especially when directly administering an RNA molecule, but which nonetheless entails the advantage that the construct does not have to be transcribed. The short half-life can be counteracted by chemical modifications of the backbone or covalent linker molecules[412,413]. Another major challenge constitutes the cell-specific targeting, which can be improved by conjugation of the vector with targeting molecules to increase selectivity towards a particular cell type[414]. For instance, membrane proteins can be recognized by aptamers or antibodies[415,416]. Gene delivery can also be regulated spatially by ultrasound-triggered release[417]. Crossing the plasma membrane, evading immune cell and endosomal clearance and hijacking the cellular transcription machinery are further challenges that are addressed by a variety of technologies that are currently under development[414]. Both viral and non-viral gene delivery strategies could become an option for therapeutic Sarrah upregulation in the future, given that the postulated beneficial effects of Sarrah are confirmed in primate models and clinical trials.

To circumvent the challenges of RNA or gene delivery, the mechanistic Sarrah feature of activating a specific set of target genes by triplex formation could be exploited more directly. To this end, the sequence of the Sarrah triplex domain would be employed as triplex forming oligonucleotide and

coupled to factors able to initiate transcription[418]. Here again though, triplex forming oligonucleotides have only been used for gene repression[419,420], but not upregulation to date, so that the technology for transcriptional activation remains to be established before separate functional Sarrah domains can be applied therapeutically under the premise that the therapeutically relevant effect of Sarrah is conferred via triplex formation rather than another mechanism exerted by a different Sarrah domain.

However, as mentioned above, beside delivery issues, therapeutic utilization of Sarrah inevitably stumbles over an issue of timing because Sarrah decreases in the aging mouse heart. If this temporal expression pattern turns out to be conserved in humans, the problem arises that Sarrah levels ideally need to be restored before or within minutes to hours after acute myocardial infarction to yield any therapeutic benefit. This is not feasible with current tools that are available in the clinics. Therefore, patients at risk of Sarrah level-related AMI have to be identified in advance, which raises the question whether Sarrah is detectable in body fluids, which allowed for its use as a diagnostic tool and, given that Sarrah causally contributes to AMI, Sarrah delivery as a preventive measure rather than a therapeutic approach that requires precise timing within a narrow time window after myocardial infarction. Since a number of other lncRNAs are measurable in urine or blood[421] with some of them being proposed as biomarkers for heart failure[239], it is conceivable that also Sarrah could serve as a biomarker for heart disease if it is detectable and differentially regulated during aging or early disease stages in for example blood.

Taken together, Sarrah is a lncRNA of promising therapeutic potential in the context of myocardial ischemia, particularly after AMI, as its impacts a combination of three processes beneficial for cardiac regeneration. Restoring Sarrah levels that drop after AMI and during aging is expected to mitigate the deleterious effects of ischemic events and to decrease the risk for their occurrence. Therapeutic approaches to augment Sarrah levels are challenging at present, but will become increasingly realistic as gene therapeutic strategies advance. The possibility to utilize circulating Sarrah levels as biomarker remains to be investigated.

5.7 Outlook

Within the scope of this work, Sarrah has been identified in cardiac tissue, functionally and mechanistically characterized in cardiomyocytes and implicated in cardiac function in a rodent model. What remains to be unraveled is whether Sarrah acts via other mechanisms than triplex formation using different molecule domains, potentially in the cytoplasm, where a small fraction, especially in human cardiomyocytes, is localized; which role Sarrah plays in other cardiac cell types as it is also present in endothelial cells and fibroblasts; how it functions and is regulated in other organs such as

brain, placenta or bladder, where Sarrah sequencing reads are detectable in a genome viewer. For a more comprehensive understanding of cardiac Sarrah function, expression profiles and *in vivo* studies in additional disease contexts such as ischemic heart disease, different types of heart failure or arrythmias are interesting. Identification of an aging-regulated, locus-conserved homologue in a model organism of high regenerative heart capacity, like zebrafish or killifish, would allow to further study the contribution of Sarrah to heart regeneration and inspire its therapeutic use. The next steps towards therapeutic application in humans are, for instance, testing Sarrah overexpression in a pig model.

6. Conclusion

Cardiovascular diseases are a leading cause of morbidity and mortality worldwide. Aging inflicts structural and molecular changes on the heart that oftentimes involve ischemic events, cardiomyocyte apoptosis and cardiac stiffening, which makes it a major risk factor for cardiovascular disease. After being disregarded as transcriptional noise for a long time, long non-coding RNAs have lately emerged as key regulators of many cellular processes in physiology and disease of virtually all tissues and organs, with some of them being differentially regulated during aging.

This study identified a long non-coding transcript antisense to the OXCT1 gene locus, Sarrah, to be downregulated in the heart during aging, after acute myocardial infarction and upon heart failure with preserved ejection fraction. Sarrah is expressed in several cardiac cell types with highest levels in cardiomyocytes, where it is predominantly localized in the nucleus. In mouse and human cardiomyocytes, Sarrah levels are reduced upon exposure to hypoxia or treatment with hypoxia-mimetic agents *in vitro*.

Sarrah exerts an anti-apoptotic function in mouse and human cardiomyocytes as assessed from caspase activity and annexin V staining. Histological stainings of Sarrah-depleted human engineered heart tissue organoids and Sarrah overexpressing infarcted mouse hearts confirmed its anti-apoptotic function. Sarrah also plays a role in cardiomyocyte contractility, which is substantially impaired upon Sarrah silencing in human engineered heart tissue and neonatal rat cardiomyocytes. Additionally, cardiomyocytal Sarrah stimulates endothelial cell proliferation via paracrine effects as observed after Sarrah overexpression in mouse hearts as well as in co-culture settings with human endothelial cells and Sarrah-depleted or Sarrah overexpressing human cardiomyocytes.

A microarray analysis revealed that silencing Sarrah in human cardiomyocytes induced apoptosis-related gene expression. Mechanistically, Sarrah was predicted to form triplexes in human and mouse with promoters of genes downregulated, but not upregulated after Sarrah knockdown, suggesting that Sarrah interacts with target genes to activate their transcription. This interaction was confirmed *in vitro* using nucleic acid oligonucleotides containing the sequences of the Sarrah triplex motif and the Sarrah binding site of the exemplary target gene GPC6 of both human and mouse. RNA immunoprecipitation experiments in human cells demonstrated that Sarrah is associated with open chromatin, transcription factor CRIP2, transcriptional co-activator p300 and DNA-RNA hybrid structures that also occur in Sarrah target gene promoters, which indicated that Sarrah activates gene expression by triplex formation and recruitment of protein interaction partners. Deleting the triplex

motif of endogenous Sarrah in mouse cardiomyocytes augmented apoptosis, showing that triplex formation is of functional relevance for Sarrah action.

Finally, overexpressing Sarrah in an acute myocardial infarction mouse model improved recovery of cardiac contractile function as assessed from ejection fraction, stroke volume, wall motion and wall thickness measured by echocardiography and magnetic resonance imaging. Infarct size was substantially reduced in Sarrah overexpressing mice compared with controls. This *in vivo* study implies that restoring Sarrah levels in the aged or infarcted heart bears significant therapeutic potential, which can be attributed to the combination of three Sarrah effects: increased cardiomyocytes survival, enhanced contractility of individual cardiomyocytes and paracrine stimulation of endothelial cell proliferation likely contributing to increased angiogenesis and tissue perfusion.

In summary, cardiac lncRNA Sarrah is evolutionary conserved with regard to its genomic locus, function and molecular mechanism. Via triplex formation with gene promoters, it is capable to activate a set of target genes that together mediate the anti-apoptotic and pro-contractile function of Sarrah in cardiomyocytes and that confer angiogenic effects to endothelial cells. A therapeutic utilization of Sarrah in the context of myocardial ischemia is conceivable in the future if Sarrah upregulation proves to be beneficial in further studies.

7. Summary in German

Das Herz-Kreislauf-System in Säugetieren besteht aus dem Herzen, einem muskulären Hohlorgan, welches alle Organe mit Blut versorgt, und aus drei Gefäßkreisläufen, über die das Blut an seine Zielorte gelangt. Der linke Herzventrikel pumpt sauerstoffreiches Blut durch den Koronarkreislauf und den systemischen Kreislauf, von wo aus es den rechten Herzventrikel in sauerstoffarmem Zustand erreicht und weiter in den Lungenkreislauf befördert wird, wo es wieder mit Sauerstoff angereichert wird. Das Herz selbst besteht hauptsächlich aus Endothelzellen, Kardiomyozyten und Fibroblasten, die jeweils circa die Hälfte, ein Drittel bzw. ein Sechstel aller Herzzellen stellen.

Alter ist der größte Risikofaktor für kardiovaskuläre Erkrankungen, die in westlichen Ländern die häufigste Todesursache darstellen. Der menschliche Alterungsprozesses geht mit einer Reihe struktureller und zellulärer Veränderungen des Herzens einher. Zwei der Pathologien, für die das Herz mit zunehmendem Alter besonders anfällig wird, sind der akute Myokardinfarkt sowie Herzinsuffizienz mit erhaltener systolischer linksventrikulärer Funktion. Als Myokardinfarkt bezeichnet man jedes Auftreten von nekrotischem Herzgewebe, das kausal im Zusammenhang mit Ischämie steht. Der resultierende Verlust von Kardiomyozyten durch Nekrose und Apoptose sowie das während der Heilung entstehende fibrotische Narbengewebe beeinträchtigen die Herzfunktion auf unumkehrbare Weise, da das Herz unter anderem aufgrund der postmitotischen Identität von Kardiomyozyten nur über eine sehr geringfügige regenerative Kapazität verfügt. Die führende Ursache für Myokardinfarkte ist korornare Herzkrankheit. Herzinsuffizienz mit erhaltener systolischer linksventrikulärer Funktion dagegen ist die häufigste Form der Herzinsuffizienz und zeichnet sich durch linksventrikuläre diastolische Dysfunktion aus, die zu einem drastisch reduziertem Schlagvolumen führt. Als Sekundärfolge kommt es wie beim Myokardinfarkt auch zur Ischämie. Auf Zellebene ist eine hypertrophe Vergrößerung der Kardiomyozyten charakteristisch.

Nur zwei Prozent des menschlichen Genoms kodieren für Proteine. Der Großteil des Genoms wird in funktionelle RNA-Moleküle transkribiert, zu denen auch lange nicht-kodierende RNAs (LncRNAs) gehören. Sie sind über 200 Nukleotide lang, überwiegend gering und äußerst gewebespezifisch exprimiert, selten in Bezug auf die Sequenz, dafür meist in Bezug auf den Lokus konserviert und überdurschnittlich oft mit Chromatin assoziiert. Das wissenschaftliche Interesse an LncRNAs ist erst vor zwei Jahrzehnten merklich erwacht, sodass eine systematische Charakterisierung und funktionelle Klassifizierung bisher nicht vorgenommen wurde und LncRNAs deshalb basierend auf ihrem Genlokus im Verhältnis zu Protein kodierenden Nachbargenen als intergenisch, intronisch, strängig oder gegensträngig eingeteilt werden. Mechanistisch können LncRNAs mit anderen RNAs, Proteinen oder

DNA interagieren und sich an einer Vielzahl von zellulären Prozessen wie Genregulation, genomischer Prägung, Translation oder Spleißen beteiligen, indem sie beispielsweise als Schwamm, Köder oder Gerüst dienen. Für einige wenige LncRNAs wurde Triplexformation mit genomischer DNA beschrieben, die durch Rekrutierung entsprechender Histonmodifikatoren oder Transkriptionsfaktoren der Genregulation benachbarter oder entfernter Genloci dient. In Triplices bindet eine einzelsträngige Nukleinsäure per Hoogsteen-Wasserstoffbrücken sequenzspezifisch an die große Furche eines DNA-Moleküls, wobei sich pyrimidinreiche Einzelstränge vorzugsweise parallel und purinreiche antiparallel zum Doppelstrang ausrichten.

Es hat sich herausgestellt, dass zahlreiche LncRNAs in einer Vielzahl von Organen, darunter auch im kardiovaskulären System, in pathologische Prozesse involviert und therapeutisch relevant sind. Da die Mehrzahl aller krankheitsassoziierter Genloci innerhalb nicht-kodierender Regionen des Genoms liegt, stellen RNAs vielversprechende Ansatzpunkte für neuartige Therapien dar.

Im Rahmen dieser Arbeit wurden RNA-Expressionsprofile von acht Wochen und 18 Monate alten Herzzellen aus Mäusen verglichen. Eine bisher unbeschriebene LncRNA, die gegensträngig zum OXCT1-Gen liegt, wurde als im Alter herunterreguliert identifiziert und „Sarrah“ genannt. Sarrah ist in Bezug auf den Lokus und teilweise die Sequenz evolutionär konserviert und in kardialen Myozyten, Endothelzellen und Fibroblasten exprimiert, wobei die Expression in Myozyten am höchsten ist und Sarrah dort größtenteils im Nukleus auftritt. Akuter Myokardinfarkt im Mausmodell sowie Herzinsuffizienz mit erhaltener systolischer linksventrikulärer Funktion im Ratenmodell verringern die Expression von Sarrah im Herzen. Diese Herunterregulierung kann in kultivierten humanen und murinen Kardiomyozyten durch Exposition mit Hypoxie sowie durch Behandlung mit dem Eisenchelator Deferoxamin nachgebildet werden.

Quantifizierung von Caspaseaktivität und Färbungen mit Annexin V zeigen, dass die pharmakologische Hemmung von Sarrah mit LNA-GapmeRs in humanen und murinen Kardiomyozyten zu einem Anstieg von Apoptose führt, wohingegen lentivirale Überexpression von humanem Sarrah in humanen Kardiomyozyten Apoptose reduziert. Diese Ergebnisse charakterisieren Sarrah deutlich als antiapoptotische LncRNA. Kontraktilitätsmessungen an isolierten Kardiomyozyten aus neonatalen Ratten belegen, dass Inhibition von Sarrah die Kontraktilität mindert. Bestätigt werden diese Befunde durch Kontraktilitätsaufnahmen von Organoiden aus Herzgewebe, welches aus Endothelzellen und Kardiomyozyten aus induziert pluripotenten Stammzellen gezüchtet wurde. Diese Organoide fangen zeitlich verzögert an, zu schlagen, wenn Sarrah in den Kardiomyozyten inhibiert wird, und erreichen eine gegenüber Kontrollorganoiden verringerte Schlagkraft. Histologische Färbungen demonstrieren, dass Sarrah inhibierte Organoide mehr apoptotische Zellen enthalten als Kontrollorganoide.

Um den Mechanismus, über den Sarrah wirkt, zu entschlüsseln, wurde zunächst die Regulation benachbarter Gene durch Sarrah untersucht, da dieser Wirkmechanismus für einige LncRNAs bekannt ist. Auf mRNA-Ebene waren weder FBXO4 noch c5orf51, ein Nachbargen, das nur im humanen Genom in der Nähe des Sarrahlokus' gelegen ist, in humanen oder murinen Kardiomyozyten von Sarrahinhibition beeinflusst. OXCT1, das Gen, das mit dem Sarrahlokus überlappt, war in humanen Zellen unbetroffen, in murinen Zellen jedoch durch Sarrahinhibition leicht herunterreguliert. Um festzustellen, ob diese Regulation der mRNA-Expression einen funktionellen Einfluss hat, wurde die Aktivität des Enzyms SCOT1, das von OXCT1 kodiert wird, in Sarrah inhibierten murinen Kardiomyozyten gemessen. Eine Veränderung gegenüber Kontrollzellen war nicht zu verzeichnen. In Übereinstimmung erhöhte die Hemmung der OXCT1-mRNA nicht die Apoptoserate von murinen Kardiomyozyten, sodass eine Funktionalität von Sarrah über OXCT1 ausgeschlossen werden kann.

In einem Microarray mit RNA aus humanen Kontroll- und Sarrah inhibierten Kardiomyozyten wurden Gene identifiziert, die von Sarrah reguliert werden. Eine Analyse der Anreicherung von Gensets unter den regulierten Genen ergab, dass Sarrahinhibition die Expression von Genen, die mit apoptotischen Signalwegen assoziert sind, induziert. Da Sarrah im Nukleus lokalisiert ist, wurde gemutmaßt, dass es als Genregulator fungiert. Eine Immunopräzipitation von Histon H3 aus humanen Kardiomyozyten mit anschließender Detektion von Sarrah deutete damit in Übereinstimmung auf eine Assoziation mit Chromatin hin. Bioinformatisch wurde sowohl in der humanen als auch in der murinen Sarrahsequenz ein pyrimidinreiches Motiv identifiziert, dass in der Lage ist, DNA mithilfe von Triplexformation zu binden. In einer weiteren bioinformatischen Berechnung wurde in den Promotoren von 134 humanen sowie 162 murinen Genen, die in der Microarray-Analyse herunterreguliert waren, eine Triplexformation mit dem entsprechenden Sarrahmotiv vorhergesagt. In Promotoren von in der Microarray-Analyse hochregulierten Genen wurde keine Triplexformation ermittelt. Eine Gen-Ontologie-Analyse der 134 humanen Zielgene von Sarrah ergab deren Verwicklung in kardiovaskuläre und Alterungsprozesse.

Die Vorhersage der Triplices wurde mittels Kernspinresonanz bestätigt. Hierfür wurden die Sarrahmotive aus beiden Spezies als einzelsträngige RNA mit den entsprechenden Promotor-Abschnitten des am stärksten herunterregulierten Gens, GPC6, als doppelsträngige DNA zusammengebracht und die Kernspinresonanzspektren gemessen. Die Spektren deuten in beiden Spezies auf Hoogsteen-Wasserstoffbrücken zwischen RNA und DNA hin. Um die Triplexformation auch *in vivo* zu bestätigen, wurde ein Antikörper, der DNA-RNA-Hybride erkennt, für Immunopräzipitationen verwendet. Zunächst wurde dafür die Regulation von fünf aus 54 Zielgenen von Sarrah, die sowohl in Mensch als auch Maus vorhergesagt worden waren und mit Apoptose in Verbindung stehen, in humanen Kardiomyozyten per quantitativer Echtzeit-PCR validiert. Die Level von GPC6, PDE3A, PARP8,

ITPR2 und SSBP2 waren nach Sarrahinhibition allesamt vermindert. RNA- beziehungsweise Chromatinimmunopräzipitationen mit dem DNA-RNA-Hybrid bindenden Antikörper ergaben eine Anreicherung sowohl von Sarrah als auch von Genpromotorfragmenten aller fünf ausgewählter Zielgene an DNA-RNA-Hybriden in humanen Kardiomyozyten. Für vier der fünf Zielgene waren die DNA-RNA-Hybride in den präzipitierten Promotoren RNase-H-insensitiv, was auf Triplexformation verweist. Lediglich die Hybride im ITPR2-Promotor waren nach RNase-H-Verdau nicht mehr signifikant gegenüber der Kontrolle angereichert, was suggeriert, dass Sarrah eventuell auch andere Arten von DNA-RNA-Interaktionen eingehen kann, um Genexpression zu regulieren.

Um die Bedeutung der Triplexformation durch Sarrah funktionell zu untersuchen, wurde mittels eines CRISPR/Cas9-basierten Verfahrens das Triplexmotiv aus endogenem Sarrah in murinen Kardiomyozyten deletiert. Die Mutation wurde mittels quantitativer Echtzeit-PCR mit Primern, die innerhalb der Deletion binden, bestätigt. Erhöhte Caspaseaktivität in den mutanten Zellen zeugte von einer funktionellen Bedeutung der Triplexformation für die antiapoptotische Wirkung von Sarrah. Die Expression der fünf näher untersuchten Zielgene war nach Deletion des Triplexmotivs zwar leicht, aber nur für ITPR2 signifikant herunterreguliert. In Übereinstimmung damit führte eine gleichzeitige Inhibition aller fünf Zielgene in humanen Kardiomyozyten nicht zu einem Anstieg der Caspaseaktivität, was darauf schließen lässt, dass für eine effiziente Funktionalität von Sarrah die Mehrheit aller Zielgene angesteuert werden muss.

Da andere Triplex bildende LncRNAs mit Histon modifizierenden Proteinen und Transkriptionsfaktoren interagieren, um Genexpression zu regulieren, wurde eine RNA-Affinitätsreinigung für Sarrah vorgenommen. Endogenes Sarrah wurde mit zwei komplementären Methyl-RNA-Sonden aus murinen Kardiomyozyten isoliert und die gebundenen Proteine wurden mittels Massenspektrometrie identifiziert. Die Analyse ergab eine physische Interaktion zwischen Sarrah und dem Transkriptionsfaktor CRIP2, der in Kardiomyozyten bekannterweise mit der Histonacetylase p300 interagiert. Beide Interaktionen wuren mittels RNA-Immunopräzipitation mit Antikörpern gegen die beiden Proteine validiert. In einer zusätzlichen RNA-Immunopräzipitation wurde eine Assoziation zwischen Sarrah und der Histonmarkierung H3K27ac gezeigt, die von p300 gesetzt wird und Chromatin für Transkription öffnet.

Schließlich wurde in einer Mausstudie die Rolle von Sarrah *in vivo* untersucht. Intravenöse Injektion von Adeno-assoziierten Viruspartikeln des Serotyps 9 mit der murinen Sarrahsequenz führte zu einer 6,7-fachen Sarrah-Überexpression in Kardiomyozyten, bevor zwei Wochen später ein akuter Myokardinfarkt mittels Ligation der Koronararterie *Ramus interventricularis anterior* herbeigeführt wurde. Eine Mauskohorte wurde an den Tagen 1, 7 und 14 nach Infarkt mittels Echokardiographie untersucht, eine zweite Mauskohorte an Tag 1 mittels Echokardiographie und an Tag 14 mittels

Magnetresonanztomographie. An Tag 14 wurden die Herzen für RNA-Isolierung und histologische Färbungen entnommen. Die Studie offenbarte, dass Sarrah überexprimierende Mäuse sich erheblich besser von einem Myokardinfarkt erholen als Kontrollmäuse. Erstere wiesen eine erhöhte Ejektionsfraktion sowie ein vergrößertes Schlagvolumen auf, die mit beiden Messtechniken sehr vergleichbar ausfielen. Wandbewegung und -dicke des linken Herzventrikels waren mit Sarrah-Überexpression ebenfalls gesteigert, wobei die Wandbewegung positiv mit den Expressionsleveln von Sarrah korrelierte.

Histologische Färbungen auf Paraffinschnitten der infarzierten Mausherzen von fibrotischem Gewebe, fragmentierter DNA, DNA-Doppelstrangbrüchen, Kardiomyozytenmembranen, PH3-positiven Zellkernen bzw. PH3- sowie Isolektin-positiven Zellkernen offenbarten nach Sarrah-Überexpression eine reduzierte Infarktgröße, weniger Apoptose, keine Unterschiede in der Quantität von DNA-Schäden oder der Größe von Kardiomyozyten, eine höhere absolute Anzahl proliferierender Zellen bzw. mehr proliferierende Endothelzellen. Um diesen überraschenden letzten Befund *in vitro* zu bestätigen, wurden humane Kardiomyozyten transfiziert, um Sarrah zu inhibieren, oder transduziert, um Sarrah überzuexprimieren. 24 Stunden nach Behandlung wurden die Zellen auf einem Filter für weitere 48 Stunden mit humanen Nabelschnurendothelzellen co-kultiviert, bevor die Endothelzellen mit BrdU gefärbt und im Durchflusszytometer analysiert wurden. Die Proliferationsrate der Endothelzellen korrelierte in beiden Versuchen mit der Expression von Sarrah in Kardiomyozyten. Zusätzlich wiesen Endothelzellen, die mit konditioniertem Medium von Sarrah inhibierten Kardiomyozyten behandelt worden waren, eine höhere Apoptose- und geringere Sprießrate auf.

Insgesamt wurde in dieser Studie die evolutionär konservierte LncRNA Sarrah in Kardiomyozyten identifiziert, die im Alter sowie bei Auftreten altersbedingter kardialer Pathologien herunterreguliert wird. Die Wirkung von Sarrah in Kardiomyozyten ist vor allem antiapoptotisch und prokontraktil. Zusätzlich stimuliert Sarrah die Proliferation von Endothelzellen über parakrine Effekte von Kardiomyozyten. Mechanistisch wird die Formation einer Tripelhelix mit Genpromotoren postuliert. Die Transkription der Zielgene wird im Zusammenspiel mit den Proteinen CRIP2 und p300 aktiviert, was in Mäusen zu einer substanziell verbesserten Genesung von einem Myokardinfarkt führt. Die Ergebnisse verweisen auf ein hohes therapeutisches Potential der LncRNA Sarrah, das durch Erhöhung der kardialen Sarrahlevel nach Myokardinfarkt in Zukunft von Nutzen sein kann.

8. References

1. Bautch, V. L. & Caron, K. M. Blood and Lymphatic Vessel Formation. *Cold Spring Harb Perspect Biol.* 1–13 (2015).
2. Guyton, A. C. & Hall, J. E. *Textbook of Medical Physiology*. (Elsevier, 2011).
3. Andall, R. G. *et al. Surgical and Radiologic Anatomy*. (Springer France, 2016).
4. Adams, R. H. & Alitalo, K. Molecular regulation of angiogenesis and lymphangiogenesis. *Nat. Rev. Mol. Cell Biol.* 8, 464–478 (2007).
5. Kaufmann, Mike LeMaster, Philip Matern, Katie Morrison-Graham, Devon Quick, J. R. A. edited and created by L. W. *Anatomy & Physiology*. (Open Oregon State, Oregon State University, 2019).
6. Nandi, S. S. & Mishra, P. K. Harnessing fetal and adult genetic reprograming for therapy of heart disease. *J Nat Sci.* 1, 4–6 (2015).
7. Tam, P. P. L., Parameswaran, M., Kinder, S. J. & Weinberger, R. P. The allocation of epiblast cells to the embryonic heart and other mesodermal lineages : the role of ingression and tissue movement during gastrulation. *Development.* 1642, 1631–1642 (1997).
8. Xin, M., Olson, E. N. & Bassel-duby, R. Mending broken hearts: cardiac development as a basis foradult heart regeneration and repair. *Nat Rev Mol Cell Biol.* 14, 529–541 (2013).
9. Meijler, F. L. & Meijler, T. D. Archetype , adaptation and the mammalian heart. *Neth Hear. J* 142–148 (2011). doi:10.1007/s12471-011-0086-4
10. Chetrit, M., Xu, B., Verma, B. R., Klein, A. L. & Xu, B. Multimodality Imaging for the Assessment of Pericardial Diseases. *Curr. Cardiol. Rep.* (2019).
11. Charles Molnar & Gair, J. *Concepts of Biology*. (OpenStax College, 2012).
12. Shi, J. *et al.* Early Assessment of Left Ventricular Function by Layer-Specific Strain and Its Relationship to Pulsatile Arterial Load in Patients with Coronary Slow Flow. *Int. Heart J.* 1–7 (2019). doi:10.1536/ihj.18-495
13. Tyrrell, C. *et al.* The neuropeptide galanin promotes an anti-thrombotic phenotype onendocardial endothelial cells from heart failure patients. *Aut. Neurosci.* 206, 35–42 (2017).
14. Association, A. H. High Blood Pressure. *All About Heart Rate (Pulse)*
15. Pollock, J. D. & Makaryus., A. N. Cardiac Cycle. in *Physiology* (StatPearls Publishing, 2018).
16. George, S. A. *et al.* Clinical Arrhythmias At the Atrioventricular Crossroads : Dual Pathway Electrophysiology in the Atrioventricular Node and its Underlying Heterogeneities Clinical Arrhythmias. *Arrhythm Electrophysiol Rev.* 179–185 (2017). doi:10.15420/aer.2017.30.1
17. Banerjee, I. *et al.* Determination of cell types and numbers during cardiac development in the neonatal and adult rat and mouse. *Am J Physiol Hear. Circ Physiol.* 29209, 1883–1891 (2019).
18. Pinto, A. R. *et al.* Revisiting Cardiac Cellular Composition. *Circ Res.* 118, 400–409 (2016).
19. Fleischmann, B. K., Jovinge, S., Walsh, S. & Ponte, A. Cardiomyocyte cell cycle control and growth estimation in vivo — an analysis based on cardiomyocyte nuclei. *Cardiovasc Res.* 365–373 (2010). doi:10.1093/cvr/cvq005

20. Heart, H. *et al.* Dynamics of Cell Generation and Turnover in the Article Dynamics of Cell Generation and Turnover in the Human Heart. *Cell* 1566–1575 (2015). doi:10.1016/j.cell.2015.05.026

21. Alberts, B. *et al. Molecular Biology of the Cell*. (Garland Science, 2002).

22. Shadrin, I., Khodabukus, A. & Bursac, N. Striated Muscle Function, Regeneration, and Repair. *Cell Mol Life Sci.* 73, 4175–4202 (2017).

23. Zhu, Y. *et al.* Cholesterol is required for maintaining T-tubule integrity and intercellular connections at intercalated discs in cardiomyocytes. *J Mol Cell Cardiol.* 204–212 (2017). doi:10.1016/j.yjmcc.2016.05.013.Cholesterol

24. Gray, G. A., Toor, I. S., Castellan, R. F. P., Crisan, M. & Meloni, M. Resident cells of the myocardium: more than spectators in cardiac injury, repair and regeneration. *Curr. Opin. Physiol.* 1, 46–51 (2018).

25. Zhou, P. & Pu, W. T. Recounting cardiac cellular composition. *Circ Res.* 118, 368–370 (2017).

26. Turner, N. A. In flammatory and fibrotic responses of cardiac fibroblasts to myocardial damage associated molecular patterns (DAMPs). *J. Mol. Cell. Cardiol.* 94, 189–200 (2016).

27. Epelman, S. *et al.* Embryonic and Adult-Derived Resident Cardiac Macrophages Are Maintained through Distinct Mechanisms at Steady State and during Inflammation. *Immunity* 40, 91–104 (2014).

28. Hulsmans, M. *et al.* Macrophages Facilitate Electrical Conduction in the Heart. *Cell* 169, 510–522 (2018).

29. Teichert, M. *et al.* Pericyte-expressed Tie2 controls angiogenesis and vessel maturation. *Nat. Commun.* 8, 1–12 (2017).

30. Tattersall, I. W. *et al.* In vitro modeling of endothelial interaction with macrophages and pericytes demonstrates Notch signaling function in the vascular microenvironment. *Angiogenesis* 19, 201–215 (2017).

31. Spencer, H. L. *et al.* Role of TPBG (Trophoblast Glycoprotein) Antigen in Human Pericyte Migratory and Angiogenic Activity. *Arter. Thromb Vasc Biol* 1–12 (2019). doi:10.1161/ATVBAHA.119.312665

32. Talman, V. & Kivelä, R. Cardiomyocyte- Endothelial Cell Interactions in Cardiac Remodeling and Regeneration. *Front. Cardiovasc. Med.* 5, 1–8 (2018).

33. Colliva, A., Braga, L., Giacca, M. & Zacchigna, S. Endothelial cell-cardiomyocyte crosstalk in heart development and disease. *J Physiol* 0, 1–17 (2019).

34. Sluijter, J. P. G., Verhage, V., Deddens, J. C., Akker, F. Van Den & Doevendans, P. A. Microvesicles and exosomes for intracardiac communication. *Cardiovasc. Res.* 302–311 (2014). doi:10.1093/cvr/cvu022

35. Noireaud, J. & Andriantsitohaina, R. Recent Insights in the Paracrine Modulation of Cardiomyocyte Contractility by Cardiac Endothelial Cells. *Biomed Res Int.* 2014, (2014).

36. Doroudgar, S. & Glembotski, C. The Cardiomyokine Story Unfolds: Investigating Stress-inducedProtein Secretion in the Heart. *Trends Mol Med.* 17, 207–214 (2012).

37. Olsson, A., Dimberg, A., Kreuger, J. & Claesson-Welsh, L. VEGF receptor signalling — in control of vascular function. *Nat Rev Mol Cell Biol.* 7, 359–371 (2006).

38. Mlih, M., Khericha, M., Birdwell, C., West, A. P. & Karpac, J. A virus-acquired host cytokine

controls systemic aging by antagonizing apoptosis. *PLoS Biol.* (2018).

39. Sen, P., Shah, P. P., Nativio, R. & Berger, S. L. Epigenetic Mechanisms of Longevity and Aging. *Cell* 166, 822–839 (2016).

40. Kirkwood, T. B. L. Understanding the Odd Science of Aging. *Cell* 120, 437–447 (2005).

41. Krut, V. N., Dontsov, V. I., Khalyavkin, A. V & Markova, A. M. Natural aging as as a sequential poly-systemic syndrome. *Front Biosci* 909–920 (2018).

42. Sahin, E. & DePinho, R. A. Linking functional decline of telomeres, mitochondria and stem cells during ageing. *Nature* 464, (2010).

43. López-Otín, C., Blasco, M. A., Partridge, L., Serrano, M. & Kroemer, G. The Hallmarks of Aging. *Cell* (2013). doi:10.1016/j.cell.2013.05.039

44. Gonçalves de Carvalho, C. & Ribeiro, S. Aging, low-grade systemic inflammation and vitamin D: a mini-review. *Eur. JournalSM Clin. Nutr.* (2017).

45. Blackburn, E. H., Greider, C. W. & Szostak, J. W. Telomeres and telomerase : the path from maize , Tetrahymena and yeast to human cancer and aging. *Nat Med* 12, 1133–1138 (2006).

46. Katewa, S. D. & Kapahi, P. Dietary restriction and aging, 2009. *Aging Cell* 9, 105–112 (2011).

47. Nelson, G. *et al.* A senescent cell bystander effect: senescence-induced senescence. *Aging Cell* 345–349 (2012). doi:10.1111/j.1474-9726.2012.00795.x

48. North, B. & Sinclair, D. The Intersection Between Aging and Cardiovascular Disease. *Circ. Res.* 19, 161–169 (2015).

49. Dhingra, R. & Vasan, R. S. Age as a Cardiovascular Risk Factor. *Med Clin North Am.* 96, 87–91 (2013).

50. WHO. WHO Cardiovascular diseases (CVDs) leading death cause. (2017). Available at: http://www.who.int/mediacentre/factsheets/fs317/en/.

51. World Economic Forum. Which countries have the most deaths from heart disease? (2019).

52. Benjamin, E. *et al.* Heart Disease and Stroke Statistics - 2018 Update A Report From the American Heart Association. *Circulation.* 67–492 (2018). doi:10.1161/CIR.0000000000000558

53. Statistisches Bundesamt. Todesursachen in Deutschland 2016. (2019).

54. Xu, J., Murphy, S. L., Kochanek, K. D. & Bastian, B. *National Vital Statistics Reports on Deaths: Final Data for 2016*. 67, (2016).

55. Takeshita, K., Fujimori, T., Kurotaki, Y. & Honjo, H. Sinoatrial Node Dysfunction and Early Unexpected Death of Mice With a Defect of Klotho Gene Expression. *Circulation.* 1776–1782 (2004). doi:10.1161/01.CIR.0000124224.48962.32

56. Lakatta, E. G. & Levy, D. Arterial and Cardiac Aging: Major Shareholders in Cardiovascular Disease Enterprises Part II : The Aging Heart in Health : Links to Heart Disease. *Circulation.* 346–354 (2003). doi:10.1161/01.CIR.0000048893.62841.F7

57. Lakatta, E. G. & Levy, D. Arterial and Cardiac Aging: Major Shareholders in Cardiovascular Disease Enterprises Part I : Aging Arterie : A " Set Up " for Vascular Disease. *Circulation.* 139–146 (2003). doi:10.1161/01.CIR.0000048892.83521.58

58. Schulman, S. *et al.* Age-related decline in left ventricular filling at rest and exercise. *Am J Physiol.* (1992).

59. Fleg, J. *et al.* Impact upright of age on the cardiovascular response exercise in healthy men and women to dynamic. *J Appl Physiol* 890–900 (1995).

60. Levy, D. *et al.* Echocardiographically detected left ventricular hypertrophy: prevalence and risk factors. The Framingham Heart Study. *Ann Intern Med.* (1988).

61. Antelmi, I. *et al.* Influence of age, gender, body mass index, and functional capacity on heart rate variability in a cohort of subjects without heart disease. *Am J Cardiol.* 381–385 (2004). doi:10.1016/j.amjcard.2003.09.065

62. Akazawa, H. & Komuro, I. Roles of cardiac transcription factors in cardiac hypertrophy. *Circ Res.* 1–8 (2003). doi:10.1161/01.RES.0000072977.86706.23

63. Goldspink, D. F., Burniston, J. G. & Tan, L. Cardiomyocyte death and the ageing and failing heart. *Exp Physiol.* (2003).

64. Childs, B. G., Sluis, B. Van De, Kirkland, J. L. & Deursen, J. M. Van. Clearance of p16Ink4a-positive senescent cells delays ageing-associated disorders. *Nature* 479, 232–236 (2012).

65. Fagagna, F. d'Adda di. Living on a break: cellular senescence as a DNA-damage response. *Nat. Rev. Cancer* 8, 512–522 (2008).

66. Volkova, M., Garg, R., Dick, S. & Boheler, K. R. Aging-associated changes in cardiac gene expression. *Circ Res.* 66, 194–204 (2005).

67. Lakatta, E. G. & Sollott, S. J. Perspectives on mammalian cardiovascular aging: humans to molecules. *Comp. Biochem. Physiol.* 132, 699–721 (2002).

68. Lee, C., Allison, D. B., Brand, J., Weindruch, R. & Prolla, T. A. Transcriptional profiles associated with aging and middle age-onset caloric restriction in mouse hearts. *Proc Natl Acad Sci USA.* (2002).

69. Ames, B. Delaying the mitochondrial decay of aging. *Ann N Y Acad Sci.* 7–12 (2004).

70. Lesnefsky, E. J., Moghaddas, S., Tandler, B., Kerner, J. & Hoppel, C. L. Mitochondrial Dysfunction in Cardiac Disease: Ischemia – Reperfusion, Aging, and Heart Failure. *J Mol Cell Cardiol.* 1089, 1065–1089 (2001).

71. Carrier, L. *et al.* Expression of the sarcomeric actin isogenes in the rat heart with development and senescence. *Circ Res.* (1992).

72. Bodyak, N. *et al.* Gene expression profiling of the aging mouse cardiac myocytes. *Nucleic Acids Res.* 30, 3788–3794 (2002).

73. Anderson, J. L. & Morrow, D. A. Acute Myocardial Infarction. *N Engl J Med.* 2053–2064 (2017). doi:10.1056/NEJMra1606915

74. Herzstiftung, D. *Deutscher Herzbericht 2018*. (2019).

75. Thygesen, K., Alpert, J. S., Jaffe, A. S., Simoons, M. L. & Chaitman, B. R. Third universal definition of myocardial infarction. *Nat. Rev. Cardiol.* 9, 620–633 (2012).

76. K, T., JS, A. & HD, W. Universal definition of myocardial infarction. *Eur Hear. J.* 2525–2538 (2007). doi:10.1093/eurheartj/ehm355

77. Krijnen, P. A. J. *et al.* Apoptosis in myocardial ischaemia and infarction. *J Clin Pathol* 801–811 (2002).

78. Dispersyn, G. D. *et al.* Dissociation of cardiomyocyte apoptosis and dedifferentiation in infarct border zones. *Eur Hear. J.* 849–857 (2002). doi:10.1053/euhj.2001.2963

79. Larroza, A. *et al.* Differentiation between acute and chronic myocardial infarction by means of texture analysis of late gadolinium enhancement and cine cardiac magnetic resonance imaging. *Eur. J. Radiol.* 92, 78–83 (2017).

80. Sandoval, Y. & Jaffe, A. S. Type 2 Myocardial Infarction: JACC Review Topic of the Week. *J Am Coll Cardiol.* (2019).

81. Saleh, M. & Ambrose, J. A. Understanding myocardial infarction. *F1000Res.* 7, 1–8 (2018).

82. Flachskampf, F. A. *et al.* Cardiac imaging after myocardial infarction. *Eur Hear. J.* 272–283 (2011). doi:10.1093/eurheartj/ehq446

83. Sinn, M. *et al.* Acute versus Chronic Myocardial Infarction: Diagnostic Accuracy of Quantitative Native T1 and T2 Mapping versus Assessment of Edema on Standard T2-weighted Cardiovascular MR Images for Differentiation. *Radiology* 285, 83–91 (2017).

84. Beek, A. M. & Rossum, A. C. Van. Cardiovascular magnetic resonance imaging in patients with acute myocardial infarction. *Heart* (2010). doi:10.1136/hrt.2009.172296

85. Sjöblom, J., Muhrbeck, J., Witt, N., Alam, M. & Frykman-Kull, V. Evolution of Left Ventricular Ejection Fraction After Acute. *Circulation.* 743–748 (2014). doi:10.1161/CIRCULATIONAHA.114.009924

86. Sidebotham, D. & Grice, I. J. Le. Physiology and Pathophysiology. in *Cardiothoracic Critical Care* 621–628 (Elsevier, 2007). doi:https://doi.org/10.1016/B978-0-7506-7572-7.X5001-2

87. Anderson, J. ST-elevation acute myocardial infarction and complications of myocardial infarction. in *Goldman's Cecil medicine* (eds. Goldman, L. & Schafer, A.) 441–456 (Elsevier Saunders, 2016).

88. Kajstura, J. *et al.* Apoptotic and necrotic myocyte cell deaths are independent contributing variables of infarct size in rats. *Lab Invest.* (1996).

89. Dorn, G. I. Molecular Mechanisms That Differentiate Apoptosis from Programmed Necrosis. *Toxicol Pathol.* 227–234 (2013). doi:10.1177/0192623312466961

90. Whelan, R. S., Kaplinskiy, V. & Kitsis, R. N. Cell Death in the Pathogenesis of Heart Disease: Mechanisms and Significance. *Annu Rev Physiol.* (2010). doi:10.1146/annurev.physiol.010908.163111

91. Henriquez, M., Armisén, R., Stutzin, A. & Quest, A. F. G. Cell Death by Necrosis , a Regulated Way to Go. *Curr Mol Med.* 187–206 (2008).

92. Degterev, A. *et al.* Chemical inhibitor of nonapoptotic cell death with therapeutic potential for ischemic brain injury. *Nat Chem Biol.* 1, (2013).

93. Kerr, J. F. R. Shrinkage necrosis: a distinct mode of cellular death. *J. Pathol.* 105, (1971).

94. Scorrano, L. *et al.* A Distinct Pathway Remodels Mitochondrial Cristae and Mobilizes Cytochrome c during Apoptosis. *Dev. Cell* 2, 55–67 (2002).

95. Scorrano, L. *et al.* BAX and BAK Regulation of Endoplasmic Reticulum Ca2+: A Control Point for Apoptosis. *Science (80-.).* 300, 135–140 (2003).

96. Saraste, A. & Pulkki, K. Morphologic and biochemical hallmarks of apoptosis. *Cardiovasc. Res.* 45, 528–537 (2000).

97. Hochhauser, E. *et al.* Bax Deficiency Reduces Infarct Size and Improves Long-Term Function After Myocardial Infarction. *Cell Biochem Biophys.* 47, 11–19 (2007).

98. Lee, P. *et al.* Fas pathway is a critical mediator of cardiac myocyte death and MI during ischemia-reperfusion in vivo. *Am. J. Physiol. Hear. Circ. Physiol.* 10461, 456–463 (2003).

99. Bacmeister, L. *et al. Inflammation and fibrosis in murine models of heart failure*. *Basic Research in Cardiology* (Springer Berlin Heidelberg, 2019). doi:10.1007/s00395-019-0722-5

100. Lindsey, M. L. *et al.* Guidelines for experimental models of myocardial ischemia and infarction. *Am J Physiol Hear. Circ Physiol.* 812–838 (2018). doi:10.1152/ajpheart.00335.2017

101. Lutgens, E. *et al.* Chronic myocardial infarction in the mouse: cardiac structural and functional changes. *Cardiovasc Res.* (1999).

102. Gladden, J. D., Chaanine, A. H. & Redfield, M. M. Heart Failure with Preserved Ejection Fraction. *Annu Rev Med.* (2018).

103. Dunlay, S., Roger, V. & Redfield, M. Epidemiology of heart failure with preserved ejection fraction. *Nat Rev Cardiol.* (2017).

104. Krittanawong, C. & Kukin, M. Current Management and Future Directions of Heart Failure With Preserved Ejection Fraction: a Contemporary Review. *Curr Treat Options Cardiovasc Med.* (2018). doi:10.1007/s11936-018-0623-1

105. Oktay, A. A., Rich, J. D. & Shah, S. J. The Emerging Epidemic of Heart Failure with Preserved Ejection Fraction. *Curr Hear. Fail Rep.* 10, 1–17 (2014).

106. Shah, S. *et al.* Baseline characteristics of patients in the treatment of preserved cardiac function heart failure with an aldosterone antagonist trial. *Circ Hear. Fail.* 6, 184–192 (2013).

107. Bharathi, U. & Kitzman, D. W. Heart Failure With Preserved Ejection Fraction in Older Adult. *Hear. Fail Clin.* 13, 485–502 (2018).

108. Ponikowski, P. *et al.* 2016 ESC Guidelines for the diagnosis and treatment of acute and chronic heart failure. *Eur Hear. J.* 2129–2200 (2016). doi:10.1093/eurheartj/ehw128

109. Lam, C. S. P., Voors, A. A., Boer, R. A. De, Solomon, S. D. & Veldhuisen, D. J. Van. Heart failure with preserved ejection fraction: from mechanisms to therapies. *Eur Hear. J.* 2780–2792 (2018). doi:10.1093/eurheartj/ehy301

110. Ito, S. *et al.* Prediction of Hospitalization, Inpatient Events, and Post-Discharge Outcomes for Heart Failure: Novel Approaches. in *Stroke Volume and Cardiovascular Event Risk in Heart Failure With Preserved Ejection Fraction* (2015).

111. Lifesciences, E. *Normal Hemodynamic Parameters and Laboratory Values*. (2009).

112. Farris, S. D., Moussavi-Harami, F. & Stempien-Otero, A. Heart failure with preserved ejection fraction and skeletal muscle physiology. *Hear. Fail Rev.* 22, 141–148 (2018).

113. Reddy, Y. *et al.* Arterial Stiffening With Exercise in Patients With Heart Failure and Preserved Ejection Fraction. *J Am Coll Cardiol.* 70, 136–148 (2018).

114. Hasenfuß, G. *et al.* A transcatheter intracardiac shunt device for heart failure with preserved ejection fraction (REDUCE LAP-HF): a multicentre, open-label, single-arm, phase 1 trial. *Lancet.* 387, 1298–1304 (2016).

115. Gorter, T. M. *et al.* Right ventricular dysfunction in heart failure with preserved ejection fraction: a systematic review and meta-analysis. *Eur J Hear. Fail.* 472–487

116. Borlaug, B. A. & Obokata, M. Is it time to recognize a new phenotype? Heart failure with preserved ejection fraction with pulmonary vascular disease. *Eur Hear. J.* 2874–2878 (2017). doi:10.1093/eurheartj/ehx184

117. Maurer, M. S., King, D. L., Rumbarger, L. E., Packer, M. & Burkhoff, D. Left Heart Failure With a Normal Ejection Fraction: Identification of Different Pathophysiologic Mechanisms. *J Card Fail.* 11, (2005).

118. Obokata, M., Reddy, Y., Pislaru, S., Melenovsky, V. & Borlaug, B. Evidence Supporting the Existence of a Distinct Obese Phenotype of Heart. *Circulation.* 6–19 (2017). doi:10.1161/CIRCULATIONAHA.116.026807

119. Adamson, P. B. *et al.* Wireless pulmonary artery pressure monitoring guides management to reduce decompensation in heart failure with preserved ejection fraction. *Circ Hear. Fail.* 935–944 (2014). doi:10.1161/CIRCHEARTFAILURE.113.001229

120. Bayeva, M., Gheorghiade, M. & Ardehali, H. Mitochondria as a therapeutic target in heart failure. *J Am Coll Cardiol.* 61, 599–610 (2013).

121. Neubauer, S. *et al.* Myocardial phosphocreatine-to-ATP ratio is a predictor of mortality in patients with dilated cardiomyopathy. *Circulation.* (1997).

122. Hasenfuss, G. & Teerlink, J. R. Clinical update Cardiac inotropes: current agents and future directions. *Eur Hear. J.* 1838–1845 (2011). doi:10.1093/eurheartj/ehr026

123. Krüger, M. *et al.* Protein kinase G modulates human myocardial passive stiffness by phosphorylation of the titin springs. *Circ Res.* (2009). doi:10.1161/CIRCRESAHA.108.184408

124. Zile, M. R. *et al.* Myocardial stiffness in patients with heart failure and a preserved ejection fraction: contributions of collagen and titin. *Circulation.* 131, 1247–1259 (2015).

125. Heerebeek, L. Van *et al.* Molecular and Cellular Basis for Diastolic Dysfunction. *Curr Hear. Fail Rep.* 293–302 (2012). doi:10.1007/s11897-012-0109-5

126. Kakkar, R. & Lee, R. Intramyocardial fibroblast myocyte communication. *Circ Res.* 106, 47–57 (2010).

127. Paulus, W. J. & Tschöpe, C. A novel paradigm for heart failure with preserved ejection fraction: comorbidities drive myocardial dysfunction and remodeling through coronary microvascular endothelial inflammation. *J Am Coll Cardiol.* 62, (2013).

128. Savvatis, K., Escher, F., Schlippenbach, J. Von, Skurk, C. & Steendijk, P. Cardiac Inflammation Contributes to Changes in the Extracellular Matrix in Patients With Heart Failure and Normal Ejection Fraction. *Circ Hear. Fail.* 44–52 (2011). doi:10.1161/CIRCHEARTFAILURE.109.931451

129. Upadhya, B., Taffet, G. E., Cheng, C. P. & Kitzman, D. W. Heart Failure with Preserved Ejection Fraction in the Elderly: Scope of the Problem. *J Mol Cell Cardiol.* 73–87 (2017). doi:10.1016/j.yjmcc.2015.02.025.Heart

130. Ramasamy, R. *et al.* Advanced glycation end products and RAGE: a common thread in aging, diabetes, neurodegeneration, and inflammation. *Glycobiology* 15, (2005).

131. Tschöpe, C. & Westermann, D. Heart Failure with Normal Ejection Fraction. Pathophysiology, diagnosis, and treatment. *Herz.* 89–96 (2009). doi:10.1007/s00059-009-3197-6

132. Shah, S. J. Evolving Approaches to the Management of Heart Failure with Preserved Ejection Fraction in Patients with Coronary Artery Disease. *Curr Treat Options Cardiovasc Med.* 58–75 (2010). doi:10.1007/s11936-009-0060-2

133. Valero-Muñoz, Backman, W. & Sam, F. Murine Models of Heart Failure With Preserved Ejection Fraction. *JACC Basic Transl Sci.* 2, (2017).

134. Tofovic, S. P., Kusaka, H., Kost, C. K. J. & Bastacky, S. Renal function and structure in diabetic,

hypertensive, obese ZDFxSHHF-hybrid rats. *Ren Fail.* 6049, (2009).

135. Hamdani, N. *et al.* Myocardial Titin Hypophosphorylation Importantly Contributes to Heart Failure With Preserved Ejection Fraction in a Rat Metabolic Risk ModelClinical Perspective. *Circ. Hear. Fail.* 6, (2013).

136. Mohanan, A. *et al.* TRC120038, a Novel Dual AT(1)/ET(A) Receptor Blocker for Control of Hypertension, Diabetic Nephropathy, and Cardiomyopathy in ob-ZSF1 Rats. *Int J Hypertens.* 2011, (2011).

137. van Dijk, C. G. M. *et al.* Distinct Endothelial Cell Responses in the Heart and Kidney Microvasculature Characterize the Progression of Heart Failure With Preserved Ejection Fraction in the Obese ZSF1 Rat With Cardiorenal Metabolic Syndrome. *Circ Hear. Fail.* 1–13 (2016). doi:10.1161/CIRCHEARTFAILURE.115.002760

138. Montarras, D. *et al.* Direct Isolation of Satellite Cells for Skeletal Muscle Regeneration. *Science (80-.).* 309, 2064–2068 (2005).

139. Tzahor, E. & Poss, K. D. Cardiac regeneration strategies: Staying young at heart. *Science (80-.).* 356, 1035–1039 (2017).

140. Hashimoto, H. *et al.* Therapeutic approaches for cardiac regeneration and repair. *Nat Rev Cardiol.* 15, 585–600 (2018).

141. Porrello, E. R. *et al.* Transient regenerative potential of the neonatal mouse heart. *Science (80-.).* 331, 1078–1080 (2011).

142. Bergmann, O. *et al.* Evidence for Cardiomyocyte Renewal in Humans. *Science (80-.).* 835, 98–103 (2009).

143. Burridge, P., Keller, G., Gold, J. & Wu, J. Production of de novo cardiomyocytes: human pluripotent stem cell differentiation and direct reprogramming. *Cell Stem Cell.* 10, 16–28 (2013).

144. Yang, L. *et al.* Human cardiovascular progenitor cells develop from a KDR 1 embryonic-stem-cell-derived population. *Nature* 453, 3–8 (2008).

145. Heineke, J. & Molkentin, J. D. Regulation of cardiac hypertrophy by intracellular signalling pathways. *Nat Rev Mol Cell Biol.* 7, (2006).

146. Laflamme, M. A., Myerson, D., Saffitz, J. E. & Murry, C. E. Evidence for Cardiomyocyte Repopulation by Extracardiac Progenitors in Transplanted Human Hearts. *Circ Res.* 634–640 (2002). doi:10.1161/01.RES.0000014822.62629.EB

147. Samak, M. *et al.* Cardiac Hypertrophy: An Introduction to Molecular and Cellular Basis. *Med Sci Monit Basic Res.* 75–79 (2016). doi:10.12659/MSMBR.900437

148. Hsieh, P. C. *et al.* Evidence from a genetic fate-mapping study that stem cells refresh adult mammalian cardiomyocytes after injury. *Nat Med* 13, 970–974 (2007).

149. van Berlo, J. *et al.* c-kit+ cells minimally contribute cardiomyocytes to the heart. *Nature* 509, 337–341 (2014).

150. Uygur, A. & Lee, R. T. Mechanisms of Cardiac Regeneration. *Dev Cell.* 36, 362–374 (2016).

151. Yahalom-Ronen, Y., Rajchman, D., Sarig, R., Geiger, B. & Tzahor, E. Reduced matrix rigidity promotes neonatal cardiomyocyte dedifferentiation, proliferation and clonal expansion. *Elife.* 1–18 (2015). doi:10.7554/eLife.07455

152. Ieda, M. *et al.* Direct reprogramming of fibroblasts into functional cardiomyocytes by defined

factors. *Cell* 142, 375–386 (2010).

153. Tani, H., Taketaro, S. & Masaki, I. Direct Cardiac Reprogramming : A Novel Approach for Heart Regeneration. *Int J Mol Sci.* 1–13 (2018). doi:10.3390/ijms19092629

154. Srivastava, D. & Dewitt, N. Review In Vivo Cellular Reprogramming: The Next Generation. *Cell* 166, 1386–1396 (2016).

155. Gourdie, R. G., Dimmeler, S. & Kohl, P. Novel therapeutic strategies targeting fibroblasts and fibrosis in heart disease. *Nat. Rev Drug Discov.* 15, 620–638 (2016).

156. Moon, J. *et al.* Blockade to pathological remodeling of infarcted heart tissue using a porcupine antagonist. *Proc Natl Acad Sci USA.* (2017). doi:10.1073/pnas.1621346114

157. Eschenhagen, T. *et al.* Cardiomyocyte Regeneration: A Consensus Statement. 136, 680–686 (2018).

158. Lin, Z. & Pu, W. T. Strategies for Cardiac Regeneration and Repair. *Sci Transl Med.* 6, 1–12 (2014).

159. Chong, J. *et al.* Human embryonic-stem-cell-derived cardiomyocytes regenerate non-human primate hearts. *Nature* 510, 273–277 (2014).

160. Shiba, Y. *et al.* Allogeneic transplantation of iPS cell-derived cardiomyocytes regenerates primate hearts. *Nature* 538, 388–391 (2016).

161. Ogle, B. M. *et al.* Distilling complexity to advance cardiac tissue engineering. *Sci Transl Med.* (2016).

162. Pasumarthi, K. B. S., Nakajima, H., Nakajima, H. O., Soonpaa, M. H. & Field, L. J. Targeted Expression of Cyclin D2 Results in Cardiomyocyte DNA Synthesis and Infarct Regression in Transgenic Mice. *Circ Res.* 110–118 (2005). doi:10.1161/01.RES.0000152326.91223.4F

163. Tao, G. *et al.* Pitx2 promotes heart repair by activating the antioxidant response after cardiac injury. *Nature* 534, 119–123 (2016).

164. Lenihan, D. J. *et al.* A Phase I, Single Ascending Dose Study of Cimaglermin Alfa (Neuregulin 1β3) in Patients With Systolic Dysfunction and Heart Failure. *JACC Basic Transl Sci.* 1, (2016).

165. Nakada, Y. *et al.* Hypoxia induces heart regeneration in adult mice. *Nature* 541, 222–227 (2017).

166. Barile, L. *et al.* Extracellular vesicles from human cardiac progenitor cells inhibit cardiomyocyte apoptosis and improve cardiac function after myocardial infarction. *Cardiovasc Res.* 530–541 (2014). doi:10.1093/cvr/cvu167

167. Gallet, R. *et al.* Exosomes secreted by cardiosphere-derived cells reduce scarring, attenuate adverse remodelling , and improve function in acute and chronic porcine myocardial infarction. *Eur Hear. J.* 201–211 (2017). doi:10.1093/eurheartj/ehw240

168. Zangi, L. *et al.* Modified mRNA directs the fate of heart progenitor cells and induces vascular regeneration after myocardial infarction. *Nat Biotechnol.* 31, 898–907 (2013).

169. Collins, F. S., Green, E. D., Guttmacher, A. E. & Guyer, M. S. A vision for the future of genomics research. *Nature* 422, 15–17 (2003).

170. Collins, F. S., Morgan, M. & Patrinos, A. The Human Genome Project: Lessons from Large-Scale Biology. *Science (80-.).* 300, 286–291 (2003).

171. Pertea, M. & Salzberg, S. L. Between a chicken and a grape: estimating the number of human genes. *Genome Biol.* (2010).

172. Dunham, I. & Kundaje, A. An integrated encyclopedia of DNA elements in the human genome. *Nature* (2012). doi:10.1038/nature11247

173. Mattick, J. S. Non-coding RNAs: the architects of eukaryotic complexity. *EMBO Rep.* 2, 986–991 (2001).

174. Pertea, M. The Human Transcriptome: An Unfinished Story. *Genes (Basel)* 344–360 (2012). doi:10.3390/genes3030344

175. Uchida, S. & Dimmeler, S. Long Noncoding RNAs in Cardiovascular Diseases. *Circ. Res.* 116, (2015).

176. Chan, P. P. & Lowe, T. M. GtRNAdb 2.0: an expanded database of transfer RNA genes identified in complete and draft genomes. *Nucleic Acids Res.* 44, 184–189 (2016).

177. Pan, T. Modifications and functional genomics of human transfer RNA. *Cell Res.* 1–10 (2018). doi:10.1038/s41422-018-0013-y

178. Karijolich, J. & Yu, Y.-T. Spliceosomal snRNA modifications and their function. *RNA Biol.* 7, 192–204 (2014).

179. Bohnsack, M. T. & Sloan, K. E. Modifications in small nuclear RNAs and their roles in spliceosome assembly and function. *Biol Chem.* 399, 1265–1276 (2018).

180. Cech, T. R. & Steitz, J. A. The Noncoding RNA Revolution — Trashing Old Rules to Forge New Ones. *Cell* 157, 77–94 (2014).

181. Dieci, G., Preti, M. & Montanini, B. Eukaryotic snoRNAs: A paradigm for gene expression fl exibility. *Genomics* 94, 83–88 (2009).

182. Kufel, J. & Grzechnik, P. Small Nucleolar RNAs Tell a Different Tale. *Trends Genet.* 35, 104–117 (2018).

183. Dupuis-Sandoval, F., Poirier, M. & Scott, M. S. The emerging landscape of small nucleolar RNAs in cell biology. *Wiley Interdiscip Rev RNA.* 6, (2015).

184. Treiber, T., Treiber, N. & Meister, G. Regulation of microRNA biogenesis and its crosstalk with other cellular pathways. *Nat. Rev. Mol. Cell Biol.* 20, (2019).

185. Gebert, L. F. R. & MacRae, I. J. Regulation of microRNA function in animals. *Nat Rev Mol Cell Biol.* 20, (2019).

186. Mello, C. C. & Conte, D. J. Revealing the world of RNA interference. *Nature* 431, (2004).

187. Lippman, Z. & Martienssen, R. The role of RNA interference in heterochromatic silencing. *Nature* 431, 10–13 (2004).

188. Dana, H. *et al.* Molecular Mechanisms and Biological Functions of siRNA. *Int J Biomed Sci.* 13, 48–57 (2017).

189. Sloan, K. E. *et al.* Tuning the ribosome: The influence of rRNA modification on eukaryotic ribosome biogenesis and function. *RNA Biol.* 6286, (2016).

190. Li, W., Notani, D. & Rosenfeld, M. Enhancers as non-coding RNA transcription units: recent insights and future perspectives. *Nat Rev Genet.* (2016).

191. Li, X., Yang, L. & Chen, L. The Biogenesis, Functions, and Challenges of Circular RNAs. *Mol Cell.* (2018).

192. Xu, S. *et al.* A comprehensive review of circRNA: from purification and identification to disease

marker potential. *Peer J* 1–28 (2018). doi:10.7717/peerj.5503

193. Frankish, A. *et al.* GENCODE reference annotation for the human and mouse genomes ıa Gir on. *Nucleic Acids Res.* 47, 766–773 (2019).

194. Dhanoa, J. K., Sethi, R. S., Verma, R., Arora, J. S. & Mukhopadhyay, C. S. Long non-coding RNA: its evolutionary relics and biological implications in mammals: a review. *J Anim Sci Technol.* 7, 1–10 (2018).

195. Cabili, M. N. *et al.* Integrative annotation of human large intergenic noncoding RNAs reveals global properties and specific subclasses. *Genes Dev.* 1915–1927 (2011). doi:10.1101/gad.17446611.

196. Sigova, A. A. *et al.* Divergent transcription of long noncoding RNA/mRNA gene pairs in embryonic stem cells. *Proc Natl Acad Sci USA.* 1–6 (2013). doi:10.1073/pnas.1221904110/-/DCSupplemental.www.pnas.org/cgi/doi/10.1073/pnas.1221904110

197. Derrien, T. *et al.* The GENCODE v7 catalog of human long noncoding RNAs: Analysis of their gene structure, evolution, and expression. *Genome Res.* 1775–1789 (2012). doi:10.1101/gr.132159.111.

198. Diederichs, S. The four dimensions of noncoding RNA conservation. *Trends Genet.* 30, 121–123 (2014).

199. Guttman, M. *et al.* Chromatin signature reveals over a thousand highly conserved large non-coding RNAs in mammals. *Nature* 457, 223–227 (2009).

200. Managadze, D., Rogozin, I. B., Chernikova, D., Shabalina, S. A. & Koonin, E. V. Negative Correlation between Expression Level and evolutionary rate of long intergenic noncoding RNAs. *Genome Biol Evol.* 3, 1390–1404 (2011).

201. Penny, G. D., Kay, G. F., Sheardown, S. A., Rastan, S. & Brockdorff, N. Requirement for Xist in X chromosome inactivation. *Nature* 379, 131–137 (1996).

202. da Rocha, S. T. & Heard, E. Novel players in X inactivation: insights into Xist -mediated gene silencing and chromosome conformation. *Nat Struct Mol Biol.* 24, 197–204 (2017).

203. Carrieri, C. *et al.* translation through an embedded SINEB2 repeat. *Nature* 491, 454–457 (2012).

204. Tsai, M. *et al.* Long Noncoding RNA as Modular Scaffold of Histone Modification Complexes. *Science (80-.).* 689–694 (2010).

205. Szczepanska, J. & Blasiak, J. The Long Noncoding RNA HOTAIR in Breast Cancer: Does Autophagy Play a Role? *Int J Mol Sci.* (2017). doi:10.3390/ijms18112317

206. Wang, K. C. *et al.* A long noncoding RNA maintains active chromatin to coordinate homeotic gene expression. *Nature* 472, 120–124 (2011).

207. Fox, A. H. & Lamond, A. I. Paraspeckles. *Cold Spring Harb Perspect Biol.* 1–15 (2010).

208. West, J. A. *et al.* Resource The Long Noncoding RNAs NEAT1 and MALAT1 Bind Active Chromatin Sites. *Mol. Cell* 55, 791–802 (2014).

209. Beltran, M. *et al.* A natural antisense transcript regulates Zeb2/Sip1 gene expression during Snail1-induced epithelial-mesenchymal transition. *Genes Dev.* 756–769 (2008). doi:10.1101/gad.455708.in

210. Cesana, M. *et al.* A Long Noncoding RNA Controls Muscle Differentiation by Functioning as a Competing Endogenous RNA. *Cell* 147, 358–369 (2011).

211. Lee, S. *et al.* Noncoding RNA NORAD Regulates Genomic Stability by Sequestering PUMILIO Proteins. *Cell* 164, 69–80 (2016).

212. Telomerase, Y. & Secondary, R. N. A. RNA as a Flexible Scaffold for Proteins: Yeast Telomerase and Beyond. *Cold Spring Harb Symp Quant Biol.* LXXI, (2006).

213. Kino, T., Hurt, D. E., Ichijo, T., Nader, N. & Chrousos, G. P. Noncoding RNA Gas5 Is a Growth Arrest- and Starvation-Associated Repressor of the Glucocorticoid Receptor. *Sci Signal.* 3, 1–16 (2010).

214. Hoogsteen, K. The structure of crystals containing a hydrogen-bonded complex of 1-methylthymine and 9-methyladenine. *Acta Cryst.* 822–823 (1959). doi:10.1107/S0365110X59002389

215. Pasternack, L. B. *et al.* Proton NMR Studies of 5'-d-(TC)3 (CT)3 (AG)3-3' — A Paperclip Triplex: The Structural Relevance of Turns. *Biophys. J.* 82, 3170–3180 (2002).

216. Li, Y., Syed, J. & Sugiyama, H. RNA-DNA Triplex Formation by Long Noncoding RNAs. *Cell Chem. Biol.* 23, 1325–1333 (2016).

217. Agazies, Y. M., Lee, J. S. & Burkholderll, G. D. Characterization of a New Monoclonal Antibody to Triplex DNA and Immunofluorescent Staining of Mammalian Chromosomes *. *J Biol Chem.* (1994).

218. Lubitz, I., Zikich, D. & Kotlyar, A. Specific High-Affinity Binding of Thiazole Orange to Triplex and G-Quadruplex DNA. *Biochemistry* 3567–3574 (2010). doi:10.1021/bi1000849

219. Buske, F. A., Bauer, D. C., Mattick, J. S. & Bailey, T. L. Triplexator: Detecting nucleic acid triple helices in genomic and transcriptomic data. *Genome Res.* 1372–1381 (2012). doi:10.1101/gr.130237.111.1372

220. Jalali, S., Singh, A., Maiti, S. & Scaria, V. Genome‐wide computational analysis of potential long noncoding RNA mediated DNA: DNA:RNA triplexes in the human genome. *J Transl Med.* 1–17 (2017). doi:10.1186/s12967-017-1282-9

221. Martianov, I., Ramadass, A., Barros, A. S., Chow, N. & Akoulitchev, A. Repression of the human dihydrofolate reductase gene by a non-coding interfering transcript. *Nature* 445, (2007).

222. Schmitz, K., Mayer, C., Postepska, A. & Grummt, I. Interaction of noncoding RNA with the rDNA promoter mediates recruitment of DNMT3b and silencing of rRNA genes. *Genes Dev.* 1, 2264–2269 (2010).

223. O'Leary, V. B. *et al.* PARTICLE, a Triplex-Forming Long ncRNA , Regulates Locus-Specific Methylation in Response to Low-Dose Irradiation. *Cell Rep.* 474–485 (2015). doi:10.1016/j.celrep.2015.03.043

224. Grote, P. & Herrmann, B. G. The long non-coding RNA Fendrr links epigenetic control mechanisms to gene regulatory networks in mammalian embryogenesis. *RNA Biol.* 1579–1585 (2013).

225. Mondal, T. *et al.* MEG3 long noncoding RNA regulates the TGF- b pathway genes through formation of RNA-DNA triplex structures. *Nat Commun.* (2015). doi:10.1038/ncomms8743

226. Kalwa, M. *et al.* The lncRNA HOTAIR impacts on mesenchymal stem cells via triple helix formation. *Nucleic Acids Res.* 44, 10631–10643 (2016).

227. Postepska-Igielska, A. *et al.* LncRNA Khps1 Regulates Expression of the Proto- oncogene SPHK1 via Triplex-Mediated Changes in Chromatin Structure Article LncRNA Khps1 Regulates Expression of the Proto-oncogene SPHK1 via Triplex-Mediated Changes in Chromatin Structure.

Mol. Cell 60, 626–636 (2015).

228. Chu, C., Qu, K., Zhong, F. L., Artandi, S. E. & Chang, H. Y. Genomic Maps of Long Noncoding RNA Occupancy Reveal Principles of RNA-Chromatin Interactions. *Mol. Cell* 44, 667–678 (2011).

229. Manolio, T. A. *et al.* Finding the missing heritability of complex diseases. *Nature* 461, 747–753 (2009).

230. Hindorff, L. A. *et al.* Potential etiologic and functional implications of genome-wide association loci for human diseases and traits. *Proc Natl Acad Sci USA.* (2009).

231. Yang, K. *et al.* Deep RNA Sequencing Reveals Dynamic Regulation of Myocardial Noncoding RNAs in Failing Human Heart and Remodeling With Mechanical Circulatory Support. *Circulation.* 1009–1021 (2014). doi:10.1161/CIRCULATIONAHA.113.003863

232. Ishii, N. *et al.* Identification of a novel non-coding RNA, MIAT, that confers risk of myocardial infarction. *J Hum Genet.* 1087–1099 (2006). doi:10.1007/s10038-006-0070-9

233. Kallen, A. N. *et al.* The imprinted H19 lncRNA antagonizes let-7 microRNAs. *Mol Cell.* 52, 101–112 (2013).

234. Gao, W. *et al.* Association of polymorphisms in long non-coding RNA H19 with coronary artery disease risk in a Chinese population. *Mutat Res.* 772, 15–22 (2015).

235. Yap, K. *et al.* Article Molecular Interplay of the Noncoding RNA ANRIL and Methylated Histone H3 Lysine 27 by Polycomb CBX7 in Transcriptional Silencing of INK4a. *Mol Cell.* 662–674 (2010). doi:10.1016/j.molcel.2010.03.021

236. McPherson, R. *et al.* A Common Allele on Chromosome 9 Associated with Coronary Heart Disease. *Science (80-.).* 1488–1492 (2007).

237. Tang, S. *et al.* Association of lincRNA-p21 Haplotype with Coronary Artery Disease in a Chinese Han Population. *Dis Markers.* 2016, (2016).

238. Korostowski, L., Sedlak, N. & Engel, N. The Kcnq1ot1 Long Non-Coding RNA Affects Chromatin Conformation and Expression of Kcnq1, but Does Not Regulate Its Imprinting in the Developing Heart. *PLoS Genet.* 8, (2012).

239. Vausort, M., Wagner, D. R. & Devaux, Y. Long Noncoding RNAs in Patients With Acute Myocardial Infarction. *Circ Res.* 668–677 (2014). doi:10.1161/CIRCRESAHA.115.303836

240. Zolk, O., Solbach, T. F., Eschenhagen, T., Weidemann, A. & Fromm, M. F. Activation of negative regulators of the hypoxia-inducible factor (HIF) pathway in human end-stage heart failure. *Biochem Biophys Res Commun.* 376, 315–320 (2008).

241. Yan, Y. *et al.* Circulating Long Noncoding RNA UCA1 as a Novel Biomarker of Acute Myocardial Infarction. *BioMed Res. Int.* 2016, 1–8 (2016).

242. Liu, Y. *et al.* Long Non Coding RNA-UCA1 Contributes to Cardiomyocyte Apoptosis by Suppression of p27 Expression. *Cell Physiol Biochem.* 150001, 1986–1998 (2015).

243. Zangrando, J. *et al.* Identification of candidate long non-coding RNAs in response to myocardial infarction. *BMC Genomics.* (2014).

244. Pattingre, S. *et al.* Bcl-2 Antiapoptotic Proteins Inhibit Beclin 1-Dependent Autophagy. *Cell* 122, 927–939 (2005).

245. Wang, K. *et al.* APF lncRNA regulates autophagy and myocardial infarction by targeting miR-188-3p. *Nat. Commun.* 6, 1–11 (2015).

246. Wang, K. *et al.* CARL lncRNA inhibits anoxia-induced mitochondrial fission and apoptosis in cardiomyocytes by impairing miR-539-dependent PHB2 downregulation. *Nat. Commun.* 5, 1–13 (2014).

247. Wu, H. *et al.* Long noncoding RNA Meg3 regulates cardiomyocyte apoptosis in myocardial infarction. *Gene Ther.* (2018).

248. Long, C. *et al.* Circulating long noncoding RNA, LIPCAR, predicts survival in patients with heart failure. *Circ Res.* 1569–1575 (2014). doi:10.1161/CIRCRESAHA.114.303915

249. Qu, X. *et al.* MIAT Is a Pro-fibrotic Long Non-coding RNA Governing Cardiac Fibrosis in Post-infarct Myocardium. *Sci Rep.* 1–11 (2017). doi:10.1038/srep42657

250. Tao, H. *et al.* Long noncoding RNA H19 controls DUSP5/ERK1/2 axis in cardiac fibroblast proliferation and fibrosis. *Cardiovasc. Pathol.* 25, 381–389 (2016).

251. Jiang, X., Zhang, F. & Ning, Q. Losartan reverses the down-expression of long noncoding RNA-NR024118 and Cdkn1c induced by angiotensin II in adult rat cardiac fibroblasts. *Pathol. Biol.* 63, 122–125 (2015).

252. Han, P. *et al.* A long noncoding RNA protects the heart from pathological hypertrophy. *Nature* (2014). doi:10.1038/nature13596

253. Viereck, J. *et al.* Long noncoding RNA Chast promotes cardiac remodeling. *Sci Transl Med.* 8, 1–13 (2016).

254. Wang, Z. *et al.* The long noncoding RNA Chaer defines an epigenetic checkpoint in cardiac hypertrophy. *Nat Med* 22, (2016).

255. Lee, J. *et al.* Analysis of Transcriptome Complexity Through RNA Sequencing in Normal and Failing Murine Hearts. *Circ Res.* 1332–1341 (2011). doi:10.1161/CIRCRESAHA.111.249433

256. Wang, K. *et al.* The long noncoding RNA CHRF regulates cardiac hypertrophy by targeting miR-489. *Circ Res. Res* 1377–1388 (2014). doi:10.1161/CIRCRESAHA.114.302476

257. Klattenhoff, C. A. *et al.* Braveheart, a Long Noncoding RNA Required for Cardiovascular Lineage Commitment. *Cell* 152, 570–583 (2013).

258. Grote, P. *et al.* The tissue-specific lncRNA Fendrr is an essential regulator of heart and body wall development in the mouse. *Dev Cell.* 24, 206–214 (2013).

259. Holdt, L. M. *et al.* ANRIL expression is associated with atherosclerosis risk at chromosome 9p21. *Arter. Thromb Vasc Biol.* 620–627 (2010). doi:10.1161/ATVBAHA.109.196832

260. Helgadottir, A. *et al.* The same sequence variant on 9p21 associates with myocardial infarction , abdominal aortic aneurysm and intracranial aneurysm. *Nat Genet.* 40, 217–224 (2008).

261. Li, D. Y. *et al.* H19 Induces Abdominal Aortic Aneurysm Development and Progression. *Circulation.* 1551–1568 (2018). doi:10.1161/CIRCULATIONAHA.117.032184

262. Han, D. K. M., Khaing, Z. Z., Pollock, R. A., Haudenschild, C. C. & Liau, G. H19, a Marker of Developmental Transition, Is Reexpressed in Human Atherosclerotic Plaques and Is Regulated by the Insulin Family of Growth Factors in Cultured Rabbit Smooth Muscle Cells. *J Clin Invest.* (1996).

263. Hadji, F. *et al.* Altered DNA Methylation of Long Noncoding RNA. *Circulation.* 1848–1862 (2016). doi:10.1161/CIRCULATIONAHA.116.023116

264. Michalik, K. M. *et al.* Long noncoding RNA MALAT1 regulates endothelial cell function and vessel growth. *Circ. Res.* 114, 1389–97 (2014).

265. Cremer, S. *et al.* Hematopoietic Deficiency of the Long Noncoding RNA MALAT1 Promotes Atherosclerosis and Plaque Inflammation. *Circ. Res.* 1320–1334 (2019). doi:10.1161/CIRCULATIONAHA.117.029015

266. Wang, G., Li, Y., Peng, Y., Tang, J. & Li, H. Association of polymorphisms in MALAT1 with risk of coronary atherosclerotic heart disease in a Chinese population. *Lipids Heal. Dis.* 2, 1–7 (2018).

267. Zhuo, Y. *et al.* Functional polymorphism of lncRNA MALAT1 contributes to pulmonary arterial hypertension susceptibility in Chinese people. *Clin Chem Lab Med.* (2017).

268. Wu, Z. *et al.* Long noncoding RNA MEG3 suppressed endothelial cell proliferation and migration through regulating miR-21. *Am J Transl Res.* 9, 3326–3335 (2017).

269. Sun, Z. *et al.* Long Non-Coding RNA MEG3 Downregulation Triggers Human Pulmonary Artery Smooth Muscle Cell Proliferation and Migration via the p53 Signaling Pathway. *Cell Physiol Biochem.* 2569–2581 (2017). doi:10.1159/000480218

270. Wu, G. *et al.* LincRNA-p21 regulates neointima formation, vascular smooth muscle cell proliferation, apoptosis, and atherosclerosis by enhancing p53 activity. *Circulation.* 1452–1465 (2014). doi:10.1161/CIRCULATIONAHA.114.011675

271. Çekin, N. *et al.* Decreased FENDRR and LincRNA-p21 expression in atherosclerotic plaque. *Anatol J Cardiol.* 131–136 (2018). doi:10.14744/AnatolJCardiol.2017.8081

272. Hu, W., Wang, Z., Wang, J., Li, L. & Jiang, G. Upregulation of lincRNA-p21 in thoracic aortic aneurysms is involved in the regulation of proliferation and apoptosis of vascular smooth muscle cells by activating TGF - β 1 signaling pathway. *J Cell Biochem.* 4113–4120 (2019). doi:10.1002/jcb.27696

273. Shen, Z. & She, Q. Association Between the Deletion Allele of Ins/Del Polymorphism (Rs145204276) in the Promoter Region of GAS5 with the Risk of Atherosclerosis. *Cell Physiol Biochem.* 400010, 1431–1443 (2018).

274. Wang, Y.-N.-Z. *et al.* Long Noncoding RNA-GAS5: A Novel Regulator of Hypertension-Induced Vascular Remodeling. *Hypertension.* 736–748 (2016). doi:10.1161/HYPERTENSIONAHA.116.07259

275. Li, F., Lin, D. & Gao, L. LncRNA TUG1 promotes proliferation of vascular smooth muscle cell and atherosclerosis through regulating miRNA-21/PTEN axis. *Eur Rev Med Pharmacol Sci.* 7439–7447 (2018).

276. Shi, L., Tian, C., Sun, L., Cao, F. & Meng, Z. The lncRNA TUG1/miR-145-5p/FGF10 regulates proliferation and migration in VSMCs of hypertension. *Biochem Biophys Res Commun.* (2018).

277. Bao, M. *et al.* Long non-coding RNAs in ischemic stroke. *Cell Death Dis.* (2018). doi:10.1038/s41419-018-0282-x

278. Abdelmohsen, K. *et al.* Senescence-associated lncRNAs: senescence-associated long noncoding RNAs. *Aging Cell.* 890–900 (2013). doi:10.1111/acel.12115

279. Yoon, J. *et al.* Scaffold function of long non-coding RNA HOTAIR in protein ubiquitination. *Nat. Commun.* 4, 1–14 (2013).

280. Kotake, Y. *et al.* Long non-coding RNA ANRIL is required for the PRC2 recruitment to and silencing of p15 INK4B tumor suppressor gene. *Oncogene* 30, 1956–1962 (2011).

281. Hofmann, P. *et al.* Long non-coding RNA H19 regulates endothelial cell aging via inhibition of STAT3 signalling. *Circ Res.* 230–242 (2019). doi:10.1093/cvr/cvy206

282. Boon, R. *et al.* Long Noncoding RNA Meg3 Controls Endothelial Cell Aging and Function: Implications for Regenerative Angiogenesis. *J Am Coll Cardiol.* 68, 2589–2591 (2016).

283. Johnson, R. Neurobiology of Disease Long non-coding RNAs in Huntington's disease neurodegeneration. *Neurobiol. Dis.* 46, 245–254 (2012).

284. Meier, I., Fellini, L., Jakovcevski, M., Schachner, M. & Morellini, F. Expression of the snoRNA Host Gene gas5 in the Hippocampus Is Upregulated by Age and Psychogenic Stress and Correlates with Reduced Novelty-Induced Behavior in C57BL/6 Mice. *Hippocampus.* 1036, 1027–1036 (2010).

285. Cuomo, D. *et al.* Transcriptional landscape of mouse-aged ovaries reveals a unique set of non-coding RNAs associated with physiological and environmental ovarian dysfunctions. *Cell Death Discov.* (2018). doi:10.1038/s41420-018-0121-y

286. Tripathi, V. *et al.* Long Noncoding RNA MALAT1 Controls Cell Cycle Progression by Regulating the Expression of Oncogenic Transcription Factor B-MYB. *PLoS Genet.* 9, (2013).

287. Kumar, P. P. *et al.* Coordinated control of senescence by lncRNA and a novel T-box3 co-repressor complex. *Elife.* 1–28 (2014). doi:10.7554/eLife.02805

288. Bao, X. *et al.* The p53-induced lincRNA-p21 derails somatic cell reprogramming by sustaining H3K9me3 and CpG methylation at pluripotency gene promoters. *Cell Res.* 25, 80–92 (2015).

289. Khalil, A. M. *et al.* Many human large intergenic noncoding RNAs associate with chromatin-modifying complexes and affect gene expression. *Proc Natl Acad Sci USA.* 106, (2009).

290. Degirmenci, U. & Lei, S. Role of lncRNAs in Cellular Aging. *Front Endocrinol* 7, 1–10 (2016).

291. Bink, D. I., Lozano-vidal, N. & Boon, R. A. Long Non-Coding RNA in Vascular Disease. *Noncoding RNA.* (2019). doi:10.3390/ncrna5010026

292. He, J., Tu, C. & Liu, Y. Role of lncRNAs in aging and age-related diseases. *Ageing Res Rev.* 158–175 (2018). doi:10.1002/agm2.12030

293. Breckwoldt, K. *et al.* Differentiation of cardiomyocytes and generation of human engineered heart tissue. *Nat. Protoc.* 12, 1177–1197 (2017).

294. Neuhauser, N., Michalski, A., Scheltema, R. A., Olsen, J. V & Mann, M. Andromeda: A Peptide Search Engine Integrated into the MaxQuant Environment. *J. Proteome Res.* 1794–1805 (2011). doi:10.1021/pr101065j

295. Cox, J. & Mann, M. MaxQuant enables high peptide identification rates, individualized p.p.b.-range mass accuracies and proteome-wide protein quantification. *Nat Biotechnol.* 26, 1367–1372 (2008).

296. Tyanova, S. *et al.* The Perseus computational platform for comprehensive analysis of (prote)omics data. *Nat Methods.* 13, (2016).

297. Boguslawski, S. J. *et al.* Characterization of monoclonal antibody to DNA • RNA and its application to immunodetection of hybrids. *J. Immunol. Methods* 89, 123–130 (1986).

298. Postepska-igielska, A. *et al.* LncRNA Khps1 Regulates Expression of the Proto- oncogene SPHK1 via Triplex-Mediated Changes in Chromatin Structure Article LncRNA Khps1 Regulates Expression of the Proto-oncogene SPHK1 via Triplex-Mediated Changes in Chromatin Structure. *Mol. Cell* 60, 626–636 (2015).

299. Jeong, J. *et al.* Rapid and Versatile Cloning Method for Functional Genomics. 78, 5440–5443 (2012).

300. Doench, J. G. *et al.* Optimized sgRNA design to maximize activity and minimize off-target effects of CRISPR-Cas9. *Nat Biotechnol.* 34, 184–191 (2016).

301. Tzelepis, K. *et al.* A CRISPR Dropout Screen Identifies Genetic Vulnerabilities and Therapeutic Targets in Acute Myeloid Leukemia. *Cell Rep.* 17, 1193–1205 (2016).

302. Sassi, Y. *et al.* Cardiac myocyte miR-29 promotes pathological remodeling of the heart by activating Wnt signaling. *Nat. Commun.* 8, 1–11 (2017).

303. Gagnon, K. T., Li, L., Janowski, B. A. & Corey, D. R. NIH Public Access. *Nat Protoc.* 9, 2045–2060 (2015).

304. Hirt, M. N. *et al.* Increased afterload induces pathological cardiac hypertrophy: A new in vitro model. *Basic Res. Cardiol.* 107, (2012).

305. Korff, T. & Augustin, H. G. Integration of Endothelial Cells in Multicellular Spheroids Prevents Apoptosis and Induces Differentiation. *Basic Res Cardiol.* 143, 1341–1352 (1998).

306. Miltenyi Biotec. Neonatal Heart Dissociation Kit Protocol (mouse and rat). 1–2 (2012).

307. Wang, L. *et al.* CPAT: Coding-Potential Assessment Tool using an alignment-free logistic regression model. *Nucleic Acids Res.* 41, 1–7 (2013).

308. Takagawa, J. *et al.* NIH Public Access. 102, 2104–2111 (2009).

309. Subramanian, A. *et al.* Gene set enrichment analysis: A knowledge-based approach for interpreting genome-wide expression profiles. *Proc. Natl. Acad. Sci.* 102, 15545–15550 (2005).

310. Huang, D. W., Sherman, B. T. & Lempicki, R. A. Systematic and integrative analysis of large gene lists using DAVID bioinformatics resources. *Nat. Protoc.* (2008). doi:10.1038/nprot.2008.211

311. Huang, D. W., Sherman, B. T. & Lempicki, R. A. Bioinformatics enrichment tools : paths toward the comprehensive functional analysis of large gene lists. *Nucleic Acids Res.* 37, 1–13 (2009).

312. Kuo, C. *et al.* Detection of RNA – DNA binding sites in long noncoding RNAs. *Nucleic Acids Res.* 47, (2019).

313. Frankish, A. *et al.* GENCODE reference annotation for the human and mouse genomes ıa Gir on. *Nucleic Acids Res.* 47, 766–773 (2019).

314. Saraste, A. & Pulkki, K. Morphologic and biochemical hallmarks of apoptosis. *Cardiovasc Res.* 45, 528–537 (2000).

315. Xiang, J., Wan, C., Guo, R. & Guo, D. Is Hydrogen Peroxide a Suitable Apoptosis Inducer for All Cell Types ? *Biomed Res Int.* 2016, (2016).

316. Schofield, C. J. & Ratcliffe, P. J. Oxygen sensing by HIF hydroxylases. *Nat Rev Mol Cell Biol.* 5, (2004).

317. Forsythe, J. O. A. *et al.* Activation of Vascular Endothelial Growth Factor Gene Transcription by Hypoxia-Inducible Factor 1. *Mol Cell Biol.* 16, 4604–4613 (1996).

318. Kurreck, J., Wyszko, E., Gillen, C. & Erdmann, V. A. Design of antisense oligonucleotides stabilized by locked nucleic acids. *Nucleic Acids Res.* 30, 1911–1918 (2002).

319. Vermes, I., Haanen, C., Steffens-Nakken, H. & Reutelingsperger, C. A novel assay for apoptosis Flow cytometric detection of phosphatidylserine expression on early apoptotic cells using fluorescein labelled Annexin V. *J Immunol Methods.* 184, 39–51 (1995).

320. Kopp, F. & Mendell, J. T. Functional Classification and Experimental Dissection of Long

Noncoding RNAs. *Cell* 172, 393–407 (2018).

321. Kuo, C.-C. *et al.* Detection of RNA-DNA binding sites in long noncoding RNAs. *Nucleic Acids Res.* 47, (2019).

322. Lewis, B. P., Burge, C. B. & Bartel, D. P. Conserved Seed Pairing, Often Flanked by Adenosines, Indicates that Thousands of Human Genes are MicroRNA Targets We predict regulatory targets of vertebrate microRNAs. *Cell* 120, 15–20 (2005).

323. Petrov, A. S., Lamm, G. & Pack, G. R. The triplex-hairpin transition in cytosine-rich DNA. *Biophys. J.* 87, 3954–3973 (2004).

324. Nikolova, E. N., Goh, G. B., Brooks, C. L. & Al-Hashimi, H. M. Characterizing the Protonation State of Cytosine in Transient G•C Hoogsteen Base Pairs in Duplex DNA. *J Am Chem Soc.* 6, 247–253 (2013).

325. Tacheny, A., Dieu, M., Arnould, T. & Renard, P. Mass spectrometry-based identification of proteins interacting with nucleic acids. *J. Proteomics* 94, 89–109 (2013).

326. Wei, T., Lin, H., Lu, C., Chen, C. & You, L. Gene Expression Patterns Expression of Crip2 , a LIM-domain-only protein , in the mouse cardiovascular system under physiological and pathological conditions. *Gene Expr. Patterns* 11, 384–394 (2011).

327. Kim, J., Kim, H., Koun, S., Ham, H. & Kim, M. Zebrafish Crip2 Plays a Critical Role in Atrioventricular Valve Development by Downregulating the Expression of ECM Genes in the Endocardial Cushion. *Mol. Cells* 37, 406–411 (2014).

328. Zhao, Q., Wu, K. E., Li, N., Li, Z. & Jin, F. Identification of potentially relevant genes for myocardial infarction using RNA sequencing data analysis. *Exp Ther Med.* 1456–1464 (2018). doi:10.3892/etm.2017.5580

329. Das, S. *et al.* Transcriptomics of cardiac biopsies reveals differences in patients with or without diagnostic parameters for heart failure with preserved ejection fraction. *Sci. Rep.* 1–14 (2019). doi:10.1038/s41598-019-39445-2

330. Chang, D. F., Belaguli, N. S., Chang, J. & Schwartz, R. J. LIM-only protein , CRP2 , switched on smooth muscle gene activity in adult cardiac myocytes. *Proc Natl Acad Sci U S A* (2007).

331. Raisner, R. *et al.* Enhancer Activity Requires CBP / P300 Report Enhancer Activity Requires CBP / P300. *CellReports* 24, 1722–1729 (2018).

332. Ramanujam, D., Sassi, Y., Laggerbauer, B. & Engelhardt, S. Viral Vector-Based Targeting of miR-21 in Cardiac Nonmyocyte Cells Reduces Pathologic Remodeling of the Heart. *Mol. Ther.* 24, 1939–1948 (2016).

333. Kent, W. J. *et al.* The Human Genome Browser at UCSC. *Genome Res.* 996–1006 (2002). doi:10.1101/gr.229102.

334. Chai, J. & Tarnawski, A. Serum response factor: discovery, biochemistry, biological roles and implications for tissue injury healing. *J Physiol Pharmacol.* 147–157 (2002).

335. McDonough, P. M., Hanford, D. S., Sprenkle, A. B., Mellon, N. R. & Glembotski, C. C. Collaborative Roles for c-Jun N-terminal Kinase, c-Jun, Serum Response Factor, and Sp1 in Calcium-regulated Myocardial Gene Expression. *J Biol Chem.* 272, 24046–24053 (1997).

336. Johnson, D. S., Mortazavi, A. & Myers, R. M. Genome-wide mapping of in vivo protein-DNA interactions. *Science (80-.).* 1497–1503 (2007).

337. Chiu, C., Wang, B., Chung, T. & Shyu, K. Angiotensin II and the ERK pathway mediate the

induction of myocardin by hypoxia in cultured rat neonatal cardiomyocytes. *Clin Sci.* 282, 273–282 (2010).

338. Ding, X. *et al.* Upregulation of SRF Is Associated With Hypoxic Pulmonary Hypertension by Promoting Viability of Smooth Muscle Cells via Increasing Expression of Bcl-2. *J Cell Biochem.* 2738, 2731–2738 (2017).

339. Zhang, S. & Xie, C. The role of OXCT1 in the pathogenesis of cancer as a rate-limiting enzyme of ketone body metabolism. *Life Sci.* 183, 110–115 (2017).

340. Cheng, Y., Song, J., Hu, P. & Zhu, Y. Tetrahydroxystilbene Glucoside (TSG) Restores the Effect of Transient Hypoxia on Reperfusion Injury in Senescent H9c2 Cells by Regulating Mitochondrial Energy Metabolism. *Evid Based Complement Altern. Med.* 2018, 1–7 (2018).

341. Maurer, G. D. *et al.* Differential utilization of ketone bodies by neurons and glioma cell lines: a rationale for ketogenic diet as experimental glioma therapy. *BMC Cancer* 11, (2011).

342. Schugar, R. C. *et al.* Cardiomyocyte-specific deficiency of ketone body metabolism promotes accelerated pathological remodeling. *Mol Metab.* 3, 754–769 (2014).

343. Karwi, Q. G., Uddin, G. M., Ho, K. L. & Lopaschuk, G. D. Loss of Metabolic Flexibility in the Failing Heart. *Front. Cardiovasc. Med.* 5, 1–19 (2018).

344. Miyazono, K., Kamiya, Y. & Morikawa, M. Bone morphogenetic protein receptors and signal transduction. *J Biochem.* 147, 35–51 (2010).

345. Tgf-, U., Sun, C. K., Chua, M., He, J. & So, S. K. Suppression of Glypican 3 Inhibits Growth of Hepatocellular Carcinoma Cells through up-regulation of TGF-β2. *Neoplasia* 13, 735–747 (2011).

346. Jang, C. *et al.* TGF-β induces apoptosis through Smad-mediated expression of DAP-kinase. *Nat Cell Biol.* 4, (2002).

347. Elbadawy, M., Usui, T., Yamawaki, H. & Sasaki, K. Novel Functions of Death-Associated Protein Kinases through Mitogen-Activated Protein Kinase-Related Signals. *Int J Mol Sci.* (2018). doi:10.3390/ijms19103031

348. Guo, X. *et al.* Death Associated Protein Kinase Mediates Myofibril Degeneration and Myocyte Apoptosis Induced by Beta-adrenergic Receptors. in *Apoptosis, Necrosis, and Autophagy* (Circulation, 2016).

349. Kuo, J., Lin, J., Staddon, J. M., Hosoya, H. & Chen, R. Uncoordinated regulation of stress fibers and focal adhesions by DAP kinase. *J Cell Sci.* (2003). doi:10.1242/jcs.00794

350. Schneiders, D., Heger, J., Best, P., Piper, H. M. & Taimor, G. SMAD proteins are involved in apoptosis induction in ventricular cardiomyocytes. *Cardiovasc Res.* 67, 87–96 (2005).

351. Shimizu, N. *et al.* Activation of mitogen-activated protein kinases and activator protein-1 in myocardial infarction in rats. *Cardiovasc Res.* 116–124 (1998).

352. Hao, J. *et al.* Elevation of Expression of Smads 2, 3, and 4, Decorin and TGF-b in the Chronic Phase of Myocardial Infarct Scar Healing. *J Mol Cell Cardiol.* 678, 667–678 (1999).

353. Taimor, G., Schlüter, K., Best, P., Helmig, S. & Piper, H. M. Transcription activator protein 1 mediates alpha- but not beta-adrenergic hypertrophic growth responses in adult cardiomyocytes. *Am J Physiol Hear. Circ Physiol.* 2369–2375 (2019).

354. Heinzel, F. R., Hohendanner, F., Jin, G., Sedej, S. & Edelmann, F. Myocardial hypertrophy and its role in heart failure with preserved ejection fraction. *J Appl Physiol* 1233–1242 (2015).

doi:10.1152/japplphysiol.00374.2015

355. Oktay, A. & Shah, S. J. Diagnosis and Management of Heart Failure with Preserved Ejection Fraction : 10 Key Lessons. *Curr Cardiol Rev.* 42–52 (2015).

356. Santos, C. de los, Rosen, M. & Patel, D. NMR studies of DNA (R+)n.(Y-)n.(Y+)n triple helices in solution: imino and amino proton markers of T.A.T and C.G.C+ base-triple formation. *Biochemistry.* (1989).

357. Motorin, Y., Lyko, F., Helm, M., Poincare, H. & Aiguillettes, B. 5-methylcytosine in RNA: detection, enzymatic formation and biological functions. *Nucleic Acids Res.* 38, 1415–1430 (2010).

358. Lee, J. S., Woodsworth, M. L., Latimer, L. J. P. & Morgan, A. R. Poly(pyrimidine).poly(purine) synthetic DNAs containing 5-methylcytosine form stable triplexes at neutral pH. *Nucleic Acids Res.* 12, 6603–6614 (1984).

359. Xodo, L. E., Manzini, G., Quadrifoglio, F., Marel, G. A. Van Der & Boom, J. H. Van. Effect of 5-methylcytosine on the stability of triple-stranded DNA-a thermodynamic study. *Nucleic Acids Res.* 19, 5625–5631 (1991).

360. Povsic, T. J. & Dervan, P. B. Triple helix formation by oligonucleotides on DNA extended to the physiological pH range. *J. Am. Chem. Soc.* 3059–3061 (1989). doi:10.1021/ja00190a047

361. Novopashina, D., Fokina, A. A. & Boutorine, A. S. Monitoring DNA triplex formation using multicolor fluorescence and application to insulin-like growth factor I promoter downregulation. *FEBS J.* 281, 1417–1431 (2014).

362. Lan, J., Hua, S., He, X. & Zhang, Y. DNA methyltransferases and methyl-binding proteins of mammals. *Acta Biochim Biophys Sin (Shanghai).* (2010). doi:10.1093/abbs/gmq015.Advance

363. Olivas, W. M. & Maher, L. J. Competitive Triplex/Quadruplex Equilibria Involving Guanine-Rich Oligonucleotides. *Biochemistry.* 278–284 (1995). doi:10.1021/bi00001a034

364. Alunni-fabbroni, M., I, G. M., Quadrifogli, F. & Xodo, L. E. Guanine-rich oligonucleotides targeted to a critical R.Y site located in the Ki-ras promoter. The effect of competing self-structures on triplex formation. *Eur J Biochem.* 151, 143–151 (1996).

365. Cetin, N. S. *et al.* Isolation and genome-wide characterization of cellular DNA:RNA triplex structures. *Nucleic Acids Res.* 47, 2306–2321 (2019).

366. Shimano, M., Ouchi, N. & Walsh, K. Cardiokines: recent progress in elucidating the cardiac secretome. *Circulation.* (2012). doi:10.1161/CIRCULATIONAHA.112.150656

367. Kuhn, M. Endothelial actions of atrial and B-type natriuretic peptides. *Br J Pharmacol.* (2012). doi:10.1111/j.1476-5381.2012.01827.x

368. Accornero, F. & Molkentin, J. D. Placental Growth Factor as a Protective Paracrine Effector in the Heart. *Trends Cardiovasc Med.* 21, 220–224 (2011).

369. Itoh, N., Ohta, H., Nakayama, Y. & Konishi, M. Roles of FGF Signals in Heart Development, Health, and Disease. *Front Cell Dev Biol.* 4, 1–11 (2016).

370. Arita, Y. *et al.* Myocardium-derived angiopoietin-1 is essential for coronary vein formation in the developing heart. *Nat. Commun.* 5, 1–14 (2014).

371. Bry, M., Kivelä, R., Leppänen, V. & Alitalo, K. Vascular Endothelial Growth Factor-B in Physiology and Disease. *Physiol Rev.* 779–794 (2014). doi:10.1152/physrev.00028.2013

372. Chen, H. I. *et al.* VEGF-C and aortic cardiomyocytes guide coronary artery stem development

Find the latest version : VEGF-C and aortic cardiomyocytes guide coronary artery stem development. 124, 4899–4914 (2014).

373. Zentilin, L. *et al.* Cardiomyocyte VEGFR-1 activation by VEGF-B induces compensatory hypertrophy and preserves cardiac function after myocardial infarction. *FASEB J.* (2010).

374. Thum, T. & Condorelli, G. Long Noncoding RNAs and MicroRNAs in Cardiovascular Pathophysiology. *Circ Res.* 751–762 (2015). doi:10.1161/CIRCRESAHA.116.303549

375. Hinger, S. A. *et al.* Diverse Long RNAs Are Differentially Sorted into Extracellular Vesicles Secreted by Colorectal Cancer Cells Article Diverse Long RNAs Are Differentially Sorted into Extracellular Vesicles Secreted by Colorectal Cancer Cells. *Cell Rep.* 25, 715-725.e4 (2018).

376. Loyer, X. *et al.* Intra-Cardiac Release of Extracellular Vesicles Shapes Inflammation Following Myocardial Infarction. *Circ Res.* 100–106 (2018). doi:10.1161/CIRCRESAHA.117.311326

377. Rodriguez, J. A. *et al.* Selective increase of cardiomyocyte derived extracellular vesicles after experimental myocardial infarction and functional effects on the endothelium. *Thromb Res.* (2018).

378. Dougherty, J. A. *et al.* Extracellular Vesicles Released by Human Induced-Pluripotent Stem Cell-Derived Cardiomyocytes Promote Angiogenesis. *Front Physiol.* 9, 1–14 (2018).

379. Desbordes, S. C. & Sanson, B. The glypican Dally-like is required for Hedgehog signalling in the embryonic epidermis of Drosophila. *Develop* 6245–6255 (2003). doi:10.1242/dev.00874

380. Velleman, S. G., Song, Y., Shin, J. & Mcfarland, D. C. Comparative Biochemistry and Physiology , Part A Modulation of turkey myogenic satellite cell differentiation through the shedding of glypican-1. *Comp Biochem Physiol A Mol Integr Physiol.* 164, 36–43 (2013).

381. Velleman, S. G., Liu, C., Coy, C. S. & McFarland, D. C. Effects of glypican-1 on turkey skeletal muscle cell proliferation , differentiation and fibroblast growth factor 2. *Dev Growth Differ.* 271–276 (2006). doi:10.1111/j.1440-169x.2006.00860.x

382. Yaoita, H., Ogawa, K., Maehara, K. & Maruyama, Y. Attenuation of Ischemia/Reperfusion Injury in Rats by a Caspase Inhibitor. *Circulation.* 276–281 (1998).

383. Laugwitz, K.-L. *et al.* Blocking Caspase-Activated Apoptosis Improves Contractility in Failing Myocardium. *Hum Gene Ther.* 12, (2004).

384. Zhao, D. *et al.* Cardiac-derived CTRP9 protects against myocardial ischemia/reperfusion injury via calreticulin-dependent inhibition of apoptosis. *Cell Death Dis.* (2018). doi:10.1038/s41419-018-0726-3

385. Yang, C. *et al.* Cyclic helix B peptide ameliorates acute myocardial infarction in mice by inhibiting apoptosis and in fl ammatory responses. *Cell Death Discov.* (2019). doi:10.1038/s41420-019-0161-y

386. Gao, H. *et al.* Changes and classification in myocardial contractile function in the left ventricle following acute myocardial infarction. *J R Soc Interface.* (2017).

387. Hasenfuss, G. & Pieske, B. Calcium Cycling in Congestive Heart Failure. *J Mol Cell Cardiol.* 969, (2002).

388. Velden, J. Van Der *et al.* Increased Ca2+-sensitivity of the contractile apparatus in end-stage human heart failure results from altered phosphorylation of contractile proteins. *Cardiov* 57, 37–47 (2003).

389. Stienen, G. J. M., Lamers, J. M. J. & Duncker, D. J. Alterations in Myofilament Function

Contribute to Left Ventricular Dysfunction in Pigs Early After Myocardial Infarction. *Circ Res.* (2004). doi:10.1161/01.RES.0000149531.02904.09

390. Schober, T. & Knollmann, B. C. Exercise After Myocardial Infarction Improves Contractility and Decreases Myofilament Ca2+ Sensitivity. *Circ Res.* 937–939 (2007). doi:10.1161/01.RES.0000265138.06052.08

391. Cochain, C., Channon, K. M. & Silvestre, J.-S. Angiogenesis in the Infarcted Myocardium. *Antioxid Redox Signal.* 18, 1100–1113 (2013).

392. Folkman, J. Tumor angiogenesis: therapeutic implications. *N Engl J Med.* (1971).

393. Losordo, D. W. & Dimmeler, S. Therapeutic Angiogenesis and Vasculogenesis for Ischemic Disease Part II: Cell-Based Therapies. *Circulation.* 2692–2697 (2004). doi:10.1161/01.CIR.0000128596.49339.05

394. Disease, I., Losordo, D. W. & Dimmeler, S. Therapeutic Angiogenesis and Vasculogenesis for Ischemic Disease Part I: Angiogenic Cytokines. *Circulation.* 2487–2491 (2004). doi:10.1161/01.CIR.0000128595.79378.FA

395. Laan, A. M. Van Der, Piek, J. J. & Royen, N. Van. reviews Targeting angiogenesis to restore the microcirculation after reperfused Mi. *Nat. Publ. Gr.* 6, 515–523 (2009).

396. Kobayashi, K., Maeda, K., Takefuji, M., Kikuchi, R. & Morishita, Y. Dynamics of angiogenesis in ischemic areas of the infarcted heart. *Sci. Rep.* 1–13 (2017). doi:10.1038/s41598-017-07524-x

397. Christopher, A. F. *et al.* MicroRNA therapeutics: Discovering novel targets and developing specific therapy. *Perspect Clin Res.* 68–74 (2016). doi:10.4103/2229-3485.179431

398. Bennett, C. F. Therapeutic Antisense Oligonucleotides Are Coming of Age. *Annu Rev Med.* (2019).

399. Shen, X. & Corey, D. R. Chemistry, mechanism and clinical status of antisense oligonucleotides and duplex RNAs. *Nucleic Acids Res.* 46, 1584–1600 (2019).

400. Chang, J., Xu, W., Hou, X. & Junqing, D. MALAT1 silencing suppresses prostate cancer progression by upregulating miR-1 and downregulating KRAS. *Onco Targets Ther.* (2018).

401. Amodio, N. *et al.* Drugging the lncRNA MALAT1 via LNA gapmeR ASO inhibits gene expression of proteasome subunits and triggers anti-multiple myeloma activity. *Leukemia.* 1948–1957 (2018). doi:10.1038/s41375-018-0067-3

402. Wu, Q. & Yi, X. Down-regulation of Long Noncoding RNA MALAT1 Protects Hippocampal Neurons Against Excessive Autophagy and Apoptosis via the PI3K / Akt Signaling Pathway in Rats with Epilepsy. *J Mol Neurosci.* 234–245 (2018).

403. Lostalé-Seijo, I. & Montenegro, J. Synthetic materials at the forefront of gene delivery. *Nat. Rev. Chem.* 2, 258–277 (2018).

404. Wahlestedt, C. Targeting long non-coding RNA to therapeutically upregulate gene expression. *Nat Rev Drug Discov.* 12, 433–446 (2013).

405. Melchiorri, D. *et al.* Regulatory evaluation of Glybera in Europe — two committees, one mission. *Nat. Rev. Drug Discov.* 12, 719–719 (2013).

406. Peng, Z. Current Status of Gendicine in China: Recombinant Human Ad-p53 Agent for Treatment of Cancers. *Hum Gene Ther.* (2005).

407. Kaczmarek, J. C., Kowalski, P. S. & Anderson, D. G. Advances in the delivery of RNA therapeutics: From concept to clinical reality. *Genome Med.* 9, 1–16 (2017).

408. Hil, A. B. *et al.* Overcoming Gene-Delivery Hurdles: Physiological Considerations for Nonviral Vector. *Trends Biotechnol.* 34, 91–105 (2016).

409. Wang, D., Tai, P. W. L. & Gao, G. Adeno-associated virus vector as a platform for gene therapy delivery. *Nat. Rev. Drug Discov.* 18, 358–378 (2019).

410. Zincarelli, C., Soltys, S., Rengo, G. & Rabinowitz, J. E. Analysis of AAV serotypes 1-9 mediated gene expression and tropism in mice after systemic injection. *Mol. Ther.* 16, 1073–1080 (2008).

411. Nayerossadat, N., Maedeh, T. & Ali, P. A. Viral and nonviral delivery systems for gene delivery. *Adv Biomed Res.* (2012).

412. Jia, F. *et al.* Depth-Profiling the Nuclease Stability and the Gene Silencing Efficacy of Brush-Architectured Poly(ethylene glycol)-DNA Conjugates. *J Am Chem Soc.* (2017).

413. Stein, C. A. & Castanotto, D. FDA-Approved Oligonucleotide Therapies in 2017. *Mol. Ther.* 25, 1069–1075 (2017).

414. Juliano, R. L. The delivery of therapeutic oligonucleotides. *Nucleic Acids Res.* 44, 6518–6548 (2016).

415. James O McNamara II, Eran R Andrechek, Yong Wang, Kristi D Viles, Rachel E Rempel, Eli Gilboa, Bruce A Sullenger & Paloma H Giangrande James O McNamara II, Eran R Andrechek, Yong Wang, Kristi D Viles, Rachel E Rempel, Eli Gilboa, B. A. S. P. H. G. Cell type–specific delivery of siRNAs with aptamer-siRNA chimeras. *Nat Biotechnol.* (2006).

416. Erwei Song, Pengcheng Zhu, Sang-Kyung Lee, Dipanjan Chowdhury, Steven Kussman, Derek M Dykxhoorn, Yi Feng, Deborah Palliser, David B Weiner, Premlata Shankar, Wayne A Marasco & Judy LiebermaErwei Song, Pengcheng Zhu, Sang-Kyung Lee, Dipanjan Chowdhury, St, W. A. M. & J. L. Antibody mediated in vivo delivery of small interfering RNAs via cell-surface receptors. *Nat Biotechnol.* (2005).

417. Anderson, C. D., Moisyadi, S., Avelar, A., Walton, C. B. & Shohet, R. V. Ultrasound-targeted hepatic delivery of factor IX in hemophiliac mice. *Gene Ther.* 23, 510–519 (2016).

418. Wu, Q. *et al.* High-affinity triplex-forming oligonucleotide target sequences in mammalian genomes. *Mol Carcinog.* 806, 797–806 (2007).

419. Jain, A., Wang, G. & Vasquez, K. M. DNA triple helices: Biological consequences and therapeutic potential. *Biochimie* 90, 1117–1130 (2008).

420. Cooney, M., Czernuszewicz, G., Postel, E., Flint, S. & Hogan, M. Site-Specific Oligonucleotide Binding Represses Transcription of the Human c-myc Gene in vitro. *Science (80-.).* 241, 456–459 (1988).

421. Jiang, X. & Ning, Q. The emerging roles of long noncoding RNAs in common cardiovascular diseases. *Hypertens Res.* 1–5 (2015). doi:10.1038/hr.2015.26

9. Abbreviations

AAV9	adeno-associated virus serotype 9
AMI	acute myocardial infarction
ANOVA	analysis of variance
ATP	adenosine triphosphate
BrdU	bromodeoxyuridine
Cas9	CRISPR-associated protein 9
cDNA	complementary DNA
ChIP	chromatin immunoprecipitation
ChIRP	chromatin isolation by RNA purification
circRNA	circular RNA
CM	cardiomyocyte
CMI	chronic myocardial infarction
CMV	cytomegalovirus
CPAT	Coding Potential Assessment Tool
CRIP2	cysteine rich protein 2
CRISPR	clustered regularly interspaced short palindromic repeats
ctrl.	control
DAP	death-associated protein
DAVID	Database for Annotation, Visualization and Integrated Discovery
DBD	DNA binding domain
DBS	DNA binding site
DFO	desferrioxamine
DMEM	Dulbecco's Modified Eagle's Medium
DNA	deoxyribonucleic acid
dsDNA	double-stranded DNA
E	embryonic day
EBM	endothelial basal medium
EC	endothelial cell
ECM	extracellular matrix
EF	ejection fraction
EHT	engineered heart tissue
EMSA	electrophoretic mobility shift assay

ER	endoplasmic reticulum
eRNA	enhancer RNA
et al.	et alii (Latin; “and others”)
FB	fibroblast
FBS	fetal bovine serum
GAPDH	glyceraldehyde-3-phosphate dehydrogenase
gDNA	genomic DNA
GFP	green fluorescent protein
GPC6	glypican 6
GSEA	gene set enrichment analysis
H2AXγ	phosphorylated histone H2AX
hCM	human cardiomyocyte
HEK	human embryonic kidney cell
HFpEF	heart failure with preserved ejection fraction
HIF1A	hypoxia-inducible factor 1-alpha
hiPSC	human induced pluripotent stem cell
HS	horse serum
HPRT1	hypoxanthine-guanine phosphoribosyltransferase 1
HUVEC	human umbilical vein endothelial cell
ICD	International Classification of Diseases
kb	kilobase
LAD	left anterior descending
LNA	locked nucleic acid
lncRNA	long non-coding RNA
MAP	mitogen-associated protein
MI	myocardial infarction
miRNA	microRNA
MRI	magnetic resonance imaging
mRNA	messenger RNA
MYH7	myosin heavy chain 7
NMR	nuclear magnetic resonance
OXCT1	3-oxoacid CoA-transferase 1
p300	histone acetyltransferase p300
PBS	phosphate-buffered saline
PBS-T	phosphate-buffered saline with 0.1 % Tween 20

PCR	polymerase chain reaction
PH3	phospho-histone H3
PRC2	polycomb repressive complex 2
pRNA	promoter-associated RNA
qRT-PCR	quantitative real-time polymerase chain reaction
RIP	RNA immunoprecipitation
RNA	ribonucleic acid
RPKM	reads per kilobase million
RPLP0	ribosomal protein, large, P0
rpm	rotations per minute
rRNA	ribosomal RNA
RT	room temperature
Sarrah	SCOT1-antisense RNA regulated during aging in the heart
SCOT1	succinyl-CoA:acetoacetate transferase 1
SDS	sodium dodecyl sulfate
SERCA2	sarco-/endoplasmic reticulum calcium ATPase 2
sgRNA	single guide RNA
shRNA	small hairpin RNA
siRNA	small interfering RNA
snoRNA	small nucleolar RNA
SNP	single-nucleotide polymorphism
snRNA	small nuclear RNA
SRF	serum response factor
ssRNA	single-stranded RNA
TDF	Triplex Domain Finder
TGF-β	transforming growth factor β
tRNA	transfer RNA
TSS	transcription start site
TUNEL	TdT-mediated dUTP-biotin nick end labeling
USA	United States of America
UTR	untranslated region
VEGF	vascular endothelial growth factor
WMSI	wall motion score index
ZSF1	Zucker fatty spontaneously hypertensive heart failure F1 hybrid

10. Appendix

Appendix A: Human Sarrah target genes predicted by Triplex Domain Finder

AAMDC	CAMKMT	FAT4	KCND2	NCOA1	PRR16	SCD	TNS1
ABCA1	CCDC158	FHIT	KIAA0100	NFE2L2	PRUNE2	SCFD2	TRIM2
ACADM	CDC73	GAS7	KMT2A	NFIA	PTPRG	SETD2	TTBK2
ACADVL	CELF2	GIP	LAMC1	NLGN1	PTPRM	SLC35F5	TTLL5
ALS2	CLYBL	GLG1	LHFP	NNMT	R3HDM2	SLCO3A1	TWSG1
ANTXR1	CNTN1	GLS	LMOD1	NRP1	RABGAP1L	SOD2	UBE4B
ANXA4	COG5	GPC6	LOXL2	NSD1	RBMS1	SP110	USP34
AP2B1	CSAD	GPR137B	LPGAT1	PAPPA	RBMS3	SPG11	WASF2
AP3B1	CYBRD1	HACE1	MAGI1	PARD3	REV3L	SPTBN1	XYLT1
ARHGAP10	DHX32	HLCS	MAP4	PARP4	RIN2	SSBP2	ZBTB20
ARHGEF11	DOCK1	HMBOX1	MAPK10	PARP8	ROR1	TAOK1	ZC3H14
ARHGEF12	DPYD	IGFBP3	MCM8	PDE3A	RPS28	TAPT1	ZHX2
ASH1L	EPB41L4A	IKZF5	MED13L	PDSS2	RPS6KC1	TBC1D5	ZKSCAN3
BCKDHB	EPHA5	ITGA11	MGAT5	PHKB	RSRC1	TCF12	ZMIZ1
BTBD9	ETV1	ITGAV	MICAL2	PICALM	RTN4IP1	TCF7L2	ZNF800
CACNA1A	EVI5	ITPR2	MTCL1	PLCL1	SAMD3	THBS1	
CALD1	FAM120B	JARID2	MYO1D	PRKG1	SAPCD1	TNFSF18	

Appedix B: Mouse Sarrah target genes predicted by Triplex Domain Finder

AAMDC	CMSS1	FBN1	KCND2	MEIS2	PDSS2	SCD	TSC22D1
ADAMTS12	CMYA5	FBN2	KCNMA1	MMAB	PLAGL1	SGCD	TSHZ2
AKT3	CNTN1	FBXL7	KMT2A	MMP14	PLCB1	SH3YL1	TWSG1
ANK3	COL6A3	FGGY	LDB2	MTHFD1L	PLEKHH2	SLC7A14	UBE4B
ANO4	COL8A1	FRMD5	LDLR	MTSS1	PPAP2A	SLC8A1	UBR5
ARHGAP10	CYBRD1	GATAD2B	LHFP	MYO1E	PPAP2B	SLC9A9	USP34
ARL13B	CYP1B1	GBF1	LPHN2	NAV3	PPFIBP1	SLCO3A1	USP53
ASH1L	DAB2	GIP	LPHN3	NCOA2	PPP3CA	SMAD2	WASF2
ATP2B4	DMXL1	GK2	LRBA	NEGR1	PRKCA	SMAD3	WDR26
BAZ2B	DOCK5	GPC6	LRCH2	NEK11	PRR16	SOD2	WWTR1
BDKRB2	DPYD	GPR137B	LRGUK	NFIA	PTP4A2	SPAST	XYLT1
BIRC6	EBF2	GPR155	LRRC16A	NLGN1	PTPRG	SPG11	ZBTB20
CACNA1A	EDIL3	HERC3	MAGI1	NR3C2	RARS2	SRGAP1	ZC3H14
CASK	EFEMP1	HIVEP1	MALL	NTM	RBMS1	SSBP2	ZCCHC7
CBLN3	EMB	HMCN1	MAP4	NTRK2	RCAN2	SUGCT	ZKSCAN3
CCDC158	ENOX1	HMGA2	MAP4K4	NUMB	REV3L	SYNJ2	
CDC73	ETV1	HYDIN	MAPK10	PAMR1	RIN2	TCF7L2	
CELF2	EVI5	INSR	MAPKAP1	PAPPA	RPS6KC1	TET2	

CEP128	FAM110B	ITGA8	MBD5	PARP8	RSRC1	TGFBI	
CLSTN1	FAM120A	ITGAV	MCPH1	PDE3A	RTN4IP1	TMEM245	
CLYBL	FARS2	ITPR2	MED13L	PDGFD	SAPCD1	TNFSF18	

Appendix C: Sarrah target gene overlap between Human and Mouse

AAMDC	CLYBL	GPC6	MAGI1	PARP8	RIN2	SOD2	USP34
ARHGAP10	CNTN1	GPR137B	MAP4	PDE3A	RPS6KC1	SPG11	WASF2
ASH1L	CYBRD1	ITGAV	MAPK10	PDSS2	RSRC1	SSBP2	XYLT1
CACNA1A	DPYD	ITPR2	MED13L	PRR16	RTN4IP1	TCF7L2	ZBTB20
CCDC158	ETV1	KCND2	NFIA	PTPRG	SAPCD1	TNFSF18	ZC3H14
CDC73	EVI5	KMT2A	NLGN1	RBMS1	SCD	TWSG1	
CELF2	GIP	LHFP	PAPPA	REV3L	SLCO3A1	UBE4B	

11. Declaration on Oath

Hiermit versichere ich, dass ich die vorliegende Dissertation selbstständig und nur unter Zuhilfenahme der hier angegebenen Quellen und Hilfsmittel verfasst habe.

Die Dissertation wurde bisher keiner anderen Fakultät vorgelegt. Ich erkläre, dass ich bisher kein Promotionsverfahren erfolglos beendet habe und dass keine Aberkennung eines bereits erworbenen Doktorgrades vorliegt.

Frankfurt am Main, 18.06.2019

12. Acknowledgements

The story of Sarrah is, like many other PhD projects, a story of defeat and perseverance. Perseverance would have never overcome the moments of defeat without the following people who I am highly indebted to and whom I would hereby like to express my sincere gratitude:

- Reinier Boon – for the opportunity of pursuing my PhD, the exciting topic, the awe-inspiring expertise, the advice on drafting the manuscript for publication and performing experiments, the possibility to visit international conferences and learn a lot about making and presenting science and for being open to discuss personal issues;
- Stefanie Dimmeler – for the valuable scientific input, the network, the convenience of having a wide variety of devices, experts and collaborators at hand, the support in presenting and visiting conferences and the motivation to gather even more energy and determination than thought possible;
- Michaela Müller-McNicoll – for agreeing to be my second referee, the tips for drafting my thesis and the kind and uncomplicated communication;
- our collaboration partners, especially Ilka Wittig, Manuel Kaulich, Marc Hirt, Christoph Schürmann and Ivan Costa – for being utterly helpful, for making it possible to advance the project in diverse directions and for providing valuable expertise;
- my group: Janina, Denise, Noelia, Diewertje, Kosta, Ellen, Patrick, Laura, Phát, Theresa, Caro, Luisa, Silvia, Lupo and the Amsterdam people – for the close technical assistance, the critical look at cells, statistics and slides, the exchange of protocols and chemicals, the personal support and all the fun moments we shared;
- the administration team, especially both Claudias and Heike – for arranging contracts, parcels, travel expenses and plenty of other bureaucratic operations;
- the technicians, especially Ariane, Marion, Andrea, Felix, Astrid, Marius, Christina and Tina – for being the experts on animal handling, histology or molecular biology and for helping me out whenever I needed advice and additional work force, even on short notice;
- my fellow PhD candidates, especially Simone, Eva, Julian, Youssef, Andi, Philipp and Shemsi – for facing the same challenges, looking forward to the same hallmarks, being confronted with the same expectations; I am grateful for the comfort that gave me;
- the postdocs, especially Tamer, Yosif, Wesley, Tina and Larissa – for sharing not only knowledge, but also your stories about your PhD and the future;

- the PIs, especially Phillip and Manolis – for your kindness, your cooperative attitude, your input and engagement for my project;
- the Fraunhofer people: Hiromi, Tatjana, Nadine, Verena, Sylvia, Christine, Nhu – for sharing reagents, devices and the office key, for a lot of encouragement and audacious ideas;
- Jes-Niels Boeckel – for inciting my initial thrill about science and introducing me to the depths of genome browsers;
- Nicolas Jaé – for investing plenty of time, kindness and extraordinary scientific expertise; for the extra effort you have taken to help me without expecting anything in return; for being so incredibly supportive when PhD life took a twist; without you, not the pulldown would have come to an end, but my hope and confidence; thank you so much for all the encouragement and support that I needed so urgently;
- my friends, especially Nathan and Colin – for being ever so helpful and reminding me of life beyond life science;
- my parents – for believing in me, for logistic support and for sharing excitement, disappointment, hopes and doubts;
- Jonas and Adrianek – for you, it was worth all the trouble.